TU Clausthal
Clausthal University of Technology

Transverse Isotropic and Orthotropic Composites: Experiments, Identification and Finite Element Analysis

Doctoral Thesis
(Dissertation)

to be awarded the degree of

Doctor in Engineering (Dr.-Ing.)

submitted by

Ali Kheiri Marghzar

approved by the Faculty of
Mathematics/Computer Science and Mechanical Engineering,
Clausthal University of Technology

Date of oral examination
31.05.2021

Chairperson of the Board of Examiners
Prof. Dr.-Ing. Gunther Brenner

Supervising Tutor and Reviewer
Prof. Dr.-Ing. Stefan Hartmann

Reviewer
Prof. Dr.-Ing. Holm Altenbach

Foreword

The work presented in this thesis was carried out over the last three years at the Institute of Applied Mechanics, Clausthal University of Technology (Institut für Technische Mechanik, Technische Universität Clausthal). This project was funded by a coordinated program of the *Campus Funktionswerkstoffe und –strukturen* which is an institution of the Technical University of Clausthal (TUC). I would like to thank the Campus Funktionswerkstoffe und –strukturen for the financial support of this work.

I would like to take this opportunity and express my sincere gratitude to my supervisor Professor Stefan Hartmann for giving me the chance to be a part of his research group. I would like to thank him for his permanent and infinite support, for his valuable advices and his recommendations. Further, I am deeply indebted to Professor Holm Altenbach, who agreed to be the co-examiner of this thesis.

I want to thank my colleagues at the working group of Solid Mechanics Matthias Grafenhorst, Jithin Mohan, Maria Angeles Martinez Page, Chris Leistner, Rose Rogin Gilbert, Pranav Kumar Dileep, and Lutz Müller-Lohse for creating a supportive and friendly working atmosphere. I am grateful to Matthias Grafenhorst for every possible assistance. I am deeply indebted to him for his help regarding numerical implementations. I would like to thank Maria Angeles Martinez Page and Stephan Krämer for helpful recommendations and all the valuable discussions we had. I am particularly thankful to Rose Rogin Gilbert for the valuable discussions we had, especially on material parameter identification. I would like to thank Chris Leistner for the time he spent with me in the laboratory. A special thanks to Pranav Kumar Dileep for all the valuable discussions regarding different aspects of modeling. I would also like to thank Lutz Müller-Lohse for our discussions about FEM modeling and I thank my office mate Jithin Mohan for the cooperative, friendly, and pleasant working atmosphere in the office.

Finally, a word of thanks goes out to my family, who supported me continuously through the whole process. I would like to thank my brother for his support and his advice. I owe many thanks to my father for his unconditional support and encouragement. I would especially like to thank my mother for her love, her patience, and her prayers, which are always with me and inspire me.

Clausthal-Zellerfeld, June 2020 Ali Kheiri Marghzar

Abstract

In today's engineering industry, constitutive modeling and numerical analysis of the behavior of composite materials, particularly transversely isotropic and orthotropic materials, have gained a lot of attention. This is mainly due to the usage of composites for a wide range of applications in different industries. Moreover, the advantages of composites such as high strength and flexibility in design make these materials attractive.

Due to many factors in the design of composites, holes in laminates are unavoidable. Fibers are usually cut by drilling a hole into laminates. Alternatively, fiber can be bypassed around holes in order to reduce the fracture tendency around a hole, or to achieve different stress distributions. One of the goals of this work is to compare these cases: In one case, fibers were bypassed around the hole while fibers were cut in the other case by drilling a hole. In order to compare these cases and to get a deeper insight into the process using simulations, a constitutive model of transverse isotropic for the small strain case is applied based on large strain theory. The model is implemented in the in-house finite element program TASAFEM. One major challenge of this simulation is to determine the fiber orientations. To begin with, the circumplacement of fibers is modeled using the streamline function to obtain the inhomogeneous fiber direction for finite element simulations. In order to increase the precision of simulations, the B-spline method is used to model the fiber directions according to the experimental observations. In the broad field of geometric modeling and computer-aided design (CAD), it is common to use B-splines to describe curves and surfaces which is mainly due to their mathematical properties and their flexibility. Another challenge regarding the simulations is to identify the required parameters for the presented material model. Several different experiments are carried out in this regard. Finally, the whole process of modeling, simulation, and material parameter identification is validated by means of validation tests.

Orthotropic laminates belong to the most commonly used laminates in industrial applications. The investigation is extended to orthotropy laminates, where we have fibers in two directions, and our aim is to predict the behavior of orthotropy laminates based on the calculated parameters. A constitutive model of orthotropy for the small strain case is applied and implemented in the in-house code TASAFEM. Another challenge in this work is to calculate the material parameters of orthotropy laminates as a basis for finite element simulations. The material parameters are identified within a least-square approach with the help of optical results of a digital image correlation system. For this purpose, different experiments such as tensile, three rail shear, lap shear and compression tests are carried out. Nine material parameters of linear elastic for orthotropy case are identified. In the next step, it is necessary to validate the numerical approach with experimental observations. The validation examples are performed as theses samples have fibers in two perpendicular directions, where the hole is drilled after the production process. Finally, a comparison between the finite element simulations and the experimental results is provided.

Contents

1 Introduction

Composite materials are combinations of two or more materials with different properties, with the aim of obtaining properties that cannot be achieved with any of the materials alone. Composites have two parts, the reinforcing part and the matrix part. The reinforcing part is in the form of fibers, particles or sheets which is combined with the other part, the matrix. Reinforced concrete is an example of fiber-reinforced composites. It is known that fibers are stronger and stiffer than the matrix part. Using composites has advantages such as high strength and light weight. In addition, design flexibility is another advantage of composites since composites can be formed in any shapes. Fiber composites have a wide range of applications, from racing car bodies and building constructions to pipes and bicycle frames. Fibers made from glass are manufactured in many different ways and for specific uses. Glass fiber is a material consisting of fine fibers of glass. In this work, E-glass fiber composite is used to make samples as it is the cheapest and the most common type of glass fiber.

1.1 Motivation

Nowadays, it is common to use numerical simulations for different investigations as these calculations become more and more significant. Further, experimental investigation of large-scale samples or prototypes are very expensive and time consuming. Thus, applying mathematical models to predict the behavior of a material is valuable and can reduce the work.

Due to the common usage of fiber composites in the industry, see e.g. (Hufenbach et al., 2011), (Holbery and Houston, 2006), (Böhlke et al., 2019), and (Bronzino, 2006), it is important to have the ability to model and simulate these structures. Over the years, constitutive modeling and numerical analysis of anisotropic materials, especially transversely isotropic and orthotropic materials, gained greater attention and emphasis because of the wide range of applications of this type of fiber composites.

Due to the design, holes in laminates are unavoidable. Fibers can be cut by drilling a hole into laminates, see Fig. 1.1(a). Alternatively, fiber can be bypassed around the hole, see Fig. 1.1(b). This case can be utilized in the production process of fiber-reinforced composites to obtain different stress distributions around a hole, for instance, and to minimize the fracture tendency. One of the goals of this work is to compare the stress and strain state of these cases. In one case, fibers are bypassed around the hole, while the fibers are cut by drilling a hole in the other case, see (Hartmann and Kheiri Marghzar, 2018). In order to compare these two cases, suitable parameters have to be obtained for the transversal isotropy model where continuous functions have to be used to determine the fiber orientation in the material model. Commonly, the works treat fiber direction defined with piece-wise functions, see (Zhu et al., 2017), or by element-wise

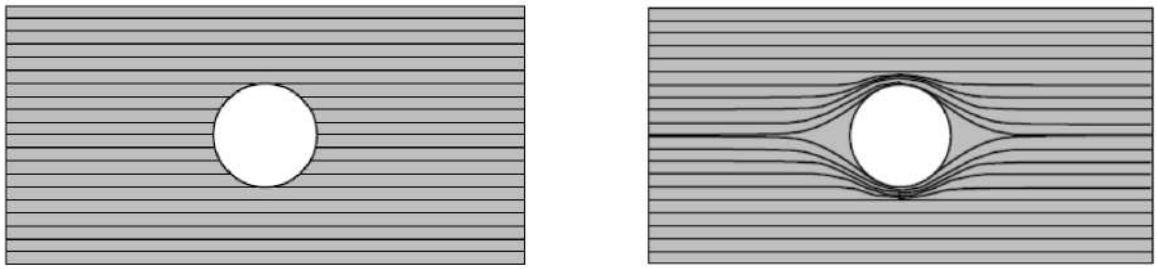

(a) Transversal isotropy laminates (b) Bypassed fibers around the hole

Figure 1.1: Sketch of transversal isotropy laminate and bypassing the fibers around the hole in the laminate during the production process, (Hartmann and Kheiri Marghzar, 2018)

formulations, see (Huang and Haftka, 2005; Hyer and Lee, 1991). However, in this thesis, spatially inhomogeneous transversal isotropy is formulated on the basis of patches using B-spline approaches to obtain the fiber orientation. B-spline methods are very popular in computer-aided geometric design because of their prominent advantages. Despite the worldwide popularity and usage of the B-spline, the possibility to define and control the parameters within B-spline is still a challenging task and an ongoing field of research.

In the field of small deformation of orthotropy, the hyperelastic behavior is well investigated, and numerous constitutive models can be found in the literature, see Sec. 1.2. On the other hand, according to my knowledge, material parameter identification in this case has not been adequately addressed. This work therefore intends to address this topic as well. Hence, one of the tasks in this work is to obtain parameters for the case of orthotropy, and according experiments have been carried out. Experiments, identification process, and modeling are closely connected to each other, see Fig. 1.2. Furthermore, it is necessary to evaluate the final results since the numerical solutions have to fulfill the requirements of reliability and efficiency. Thus, validation examples should be provided to compare the difference between experiments and simulations in the case of transversal isotropy and orthotropy.

1.2 Literature Review

One of the goal of this work is to perform calculations and investigations for uni-directional or transversal isotropic laminates. It is convenient to assume linear elasticity for such kind of uni-directional laminates, see, for instance, (Fiolka, 2008; Kaliske, 1999), and, for a brief overview, (Weise and Meyer, 2003). A fundamental work in this area is (Spencer, 1984). An introduction to laminates and sandwich materials, including the aspects of anisotropic elasticity and modeling of laminates, can be found in (Altenbach and Altenbach, 2004). The theory of invariants for different kind of composites is discussed in (Itskov, 2007; Spencer, 1984). Modeling aspects of laminate and sandwich composites are discussed in details in (Altenbach and Becker, 2003).

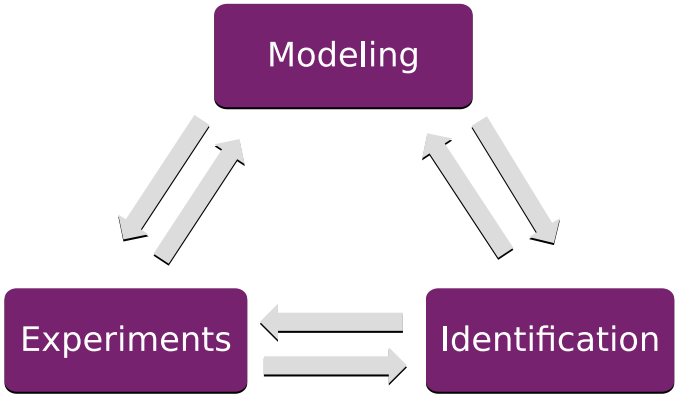

Figure 1.2: Modeling procedure

In this work, we restrict ourselves to the elastic material model. This can be formulated by an invariant theory, for example (Itskov and Aksel, 2004; Schröder, 1996; Schröder and Neff, 2003; Spencer, 1984). Invariants for materials exhibiting transversely isotropic behavior were also discussed in (Criscione et al., 2001). A model for nearly incompressible transversely isotropic materials over reinforced rubber-like materials is given in (Rüter and Stein, 2000). Further, the following contributions can provide more information regarding the field of small deformation: (Aboudi, 2013; Aboudi et al., 2012; Agarwal et al., 2006; Gibson, 2011; Parton and Kudryavtsev, 1993; Vogler et al., 2007).

There is another area of applications for transversal isotropy since soft tissues show this kind of anisotropic behavior, (Balzani et al., 2006; Itskov and Aksel, 2004; Schröder and Neff, 2003; Schröder et al., 2005; Weiss et al., 1996a). The behavior of biological joints is explored by (Almeida and Spilker, 1998), focusing on the modeling of soft tissues as an incompressible transversely isotropic material. The mathematical models treating the constitutive modeling of the behavior of arteries over anisotropic soft tissues were investigated and summarized by (Holzapfel and Ogden, 2010). A constitutive model to highlight the behavior of arteries was suggested by (Holzapfel et al., 2000). A transversely isotropic hyperelastic material model that can be used for blood vessels is presented in (Prot et al., 2007). For s specific illustration, see (Sansour, 2008; Zdunek et al., 2014). Since there are only a very few analytical solutions, numerical methods have to be chosen. The finite element method is the most common approach. For information on possible numerical difficulties, see (Sepahia et al., 2018; Wriggers et al., 2016). Fine meshes and quadratic shape functions are used in this work to reduce numerical issues.

There are also contributions concerning the development of material models to analyze hyperelastic orthotropy materials. The construction of polyconvex orthotropic free-energy functions, for instance, is discussed in (Schröder and Neff, 2003).

Strain energy functions that are polyconvex and proven to be coercive are discussed for orthotropic materials in (Itskov and Aksel, 2004). A model to represent the hyperelastic material behavior of pneumatic membranes reinforced with roven-woven fibers can be found in (Reese

et al., 2001). Coated fabrics as an orthotropic material were modeled in a plane stress framework, see (Colasante, 2014). An elastic–plastic constitutive model was developed for paper and paperboard, see (Mäkelä and Östlund, 2003). Multi-layer plates with orthotropic behavior are discussed in (Altenbach, 2000b). Moreover, a comparison between different proposals for the transverse shear stiffnesses with values based on a deformable directed surface theory can be found in (Altenbach, 2000a). An orthotropic model was also discussed, for instance in (Bischoff et al., 2002; Reddy, 2003; Schmid et al., 2006; Schröder et al., 2005; Spencer, 1971). An orthotropic hyperelastic constitutive model that can be used for reinforced structures and biological soft tissues was proposed by (Itskov, 2001). A new polyconvex orthotropic hyperelastic model for the geometrically nonlinear simulations of tensile membrane structures is provided in (Motevalli et al., 2019). In (Itskov, 2001), the strain energy function of the orthotropy model is formulated in terms of three isotropic tensor functions coupled with the associated structural tensor which is usuable for anisotropic materials and particularly biological soft tissues. A new constitutive orthotropic model for the simulation of arterial walls was proposed in (Holzapfel et al., 2000), where each layer of the artery is considered as a fiber-reinforced material.

Different methods have been developed to determine fiber orientation to analyze different aspects of laminates with a hole. Laminates with deformed fibers can lead to a change of loading paths, resulting in favorable stress distributions within the laminate and, thus, improving the structural performance. (Banichuk, 1981; Duvaut et al., 2000; Pedersen, 1991) are some examples for theoretical and numerical studies of fiber orientation, aiming to determine the fiber direction within the domain of a composite panel in order to improve structural performance measures (e.g. buckling) through design optimization. For the stiffening of laminates and investigations to achieve variable stiffness in specimens see (Lozano et al., 2016; Niu et al., 2016). Further, see (Huang and Haftka, 2005; Peeters et al., 2015; Zhu et al., 2017) for detailed research on ways to optimize the fiber direction near a hole in laminates, on path optimization for laminated composite structures, and on how to determine the optimal fiber angle distribution. Regarding difficulties in buckling, failure, and vibration in laminates reinforced by curvilinear fibers see (Hyer and Lee, 1991; Ribeiro et al., 2014). Wall et al. (2008) have developed a strategy for shape optimal design based on the isogeometric approach. Studies and research on stress, strain, fracture and the influence of the thickness distribution in a ply with different fiber angles can be found in (Blom et al., 2010; Koricho et al., 2015; Malakhov and Polilov, 2016, 2013; Nagendra et al., 1995; Rowlands et al., 1973; Skordos et al., 2002; Toubal et al., 2005). An approximation of fiber pathways after forming process in fiber textiles is presented in (Roth et al., 2020). Here, a practical tailoring of fiber orientations is considered for laminates with circular holes. (Yau and Chou, 1988) is one of the first works in this area which improves the compressive load-carrying capability of composite laminates. The work of (Hyer and Charette, 1991) is among the first works that study the effect of the fiber direction angle around a cutout for a flat plate with a circular hole. They suggested that improved designs can be obtained by aligning the fibers with the principal directions of the stress field. Furthermore, an improvement with respect to material failure load levels can be seen in their finite element simulations. In this work, a spatially continuous formulation of the fiber orientation using B-spline is used, see (Hartmann et al., 2020), although fiber orientation is commonly defined by piece-wise functions, see (Zhu et al., 2017), or by element-wise formulations, see (Huang and Haftka, 2005; Hyer and Lee, 1991).

B-spline is a powerful tool to generate any curve or surface. B-spline attracts the researchers due to its flexibility and ability in representing the complex geometry. There is a vast investigation on this topic. Definition and basis of B-spline is presented mainly in (Catmull and Clark, 1978; Piegl and Tiller, 1987, 1997, 2000a; Rogers and Fog, 1989a; Rogers, 2001). B-spline is defined using different parameters. There are different approaches to these parameters discussed in, for example, (Li et al., 2005; Lyche and Mørken, 1987; Sapidis and Farin, 1990a). B-splines can be used for a representation of different surfaces such as turbine blades, for example, see (Auger et al., 2018; Van Oosterom et al., 2019). Another application is image interpolation in medical imaging (Lehmann, 2001), where it is shown that a high-degree of B-spline interpolation has superior properties, exhibiting smallest interpolation errors and reasonable computing times in the scope of medical imaging. A method to generate a skinned B-spline surface for wings is presented by (Bentamy et al., 2005). Here, due to the flexibility of this geometric modeling using B-spline, it was shown that it is well-suited to represent a smooth geometry of the complex surface of a wing with a restricted number of parameters, see also (Brakhage and Lamby, 2008a). The problem of fitting curves and surfaces to known data sets has been studied by numerous researchers see, for example, (Gordon and Riesenfeld, 1974; Grossman, 1971; Rogers, 1977; Rogers and Fog, 1989b).

Identifying the material parameters of a material model is one of the main steps to make subsequent predictions. The identification process for transversal isotropy was discussed in (Christensen, 2005). Digital image correlation (DIC) systems are a very useful measurement tool, as was shown by full-field measurements of the displacements and strains over an area in the center of a specimen, compared to finite element computations. The idea and the theory behind it are discussed in (Andresen et al., 1996; Mahnken and Stein, 1996). Other Works use this concept with the help of gradient-based optimization methods, see (Benedix et al., 1998; Cooreman et al., 2007; Krämer, 2016; Kreissig et al., 2001), where gradient-based optimization methods were used. In this work, a least-square method is chosen to minimize the residual between the experimental data and the numerical results. For a gradient-free scheme see (Hartmann et al., 2003), where the numerical algorithm of (Powell, 1998) is addressed, or (Huber and Tsakmakis, 1999a,b) regarding a neural network method. The basis and fundamental theory of parameter identification using finite elements is treated in (Hartmann, 2017). In addition, for the aspect of purely elastic material, see (Hartmann and Gilbert, 2018; Hartmann et al., 2018). An inverse method was proposed to determine the four elastic parameters of an orthotropic material, see (Lecompte et al., 2005). Moreover, a method is proposed which is based on a finite element calculated strain field of a perforated specimen under tension and on the displacement field measured using an Electronic Speckle Pattern Interferometer. In (Huang et al., 2004), parameter identification was studied for two-dimensional orthotropic material bodies. Identification of orthotropic material was also discussed in (Frederiksen, 1997a,b; Mäkelä and Östlund, 2003).

1.3 Layout of the Thesis

The motivation of this work and a literature review were already presented in this chapter. *Chapter 2* provides a brief overview fundamental of Continuum Mechanics. This includes the kine-

matics as well as the introduction of the stress tensor and the strain tensor. In addition, balance equations are introduced, which are the balance of mass, linear and angular momentum, energy and entropy. Additionally, the fundamentals of constitutive modeling are given in the last section.

Chapter 3 discusses the constitutive model. The first aspect is matrix notation, which is related to the term in Voigt-notation. Second, the constitutive model of isotropy is discussed. The elasticity tensor stands for all materials that are modeled with linear isotropic elasticity. Third, the formulation for transversal isotropy is presented and invariants for this case are studied. Moreover, the constitutive relations for the stress-state are derived. In the next step, the constitutive equations for materials reinforced with two families of fibers are discussed, which lead us to the orthotropic case. A constitutive model of orthotropy for small strain case is derived from large strain theory and the relation between the invariants of the Green strain and right Cauchy-Green tensor is shown. The derivation of a constitutive serves to simplify the stress state. Finally, the stress state is obtained for the orthotropy case.

Chapter 4 focuses on the experimental investigation for the purpose of identification. To begin with, the production process of samples using vacuum assisted resin infusion (VARI) is explained. Important aspects regarding the experimental setup, dimension of samples, and data evaluation of the results are discussed, and tensile tests for dog-bone specimens are examined. Regarding transverse isotropic samples, tensile, three rail shear, and computational compression tests are performed. Additionally, tensile, three rail shear, lap shear and compression tests for the orthotropy case are accomplished. The goal of these experiments is to find the required parameters for the models, which is discussed in *Chapter 3*. Another topic in this chapter is to derive a concept of material parameter identification. Here, the procedure, the basic definitions and concepts for the identification problem are presented. Based on the experimental results and the defined material model, the parameters for isotropy, transverse isotropy and orthotropy are calculated. The identified parameters serve to make predictions, as we are interested in comparing the experiments and simulations.

Chapter 5 addresses the aspect of determining the fiber orientation. We would like to bypass the fibers around a hole in order to improve the performance of structures. Addressing the fiber direction is of interest for our computations in *Chapter 6*. For this aim, a streamline approach is provided as the first approach to define the fiber direction. In the next step, a interpolation concept to describe continuously the fiber orientations on the basis of B-spline is introduced which is a more flexible way to describe the fiber direction in our composite laminates. We will start with the B-spline curve, and the properties of the B-spline curve will be discussed. Furthermore, the parameters to define the B-spline curve such as knot vector and control points are discussed. Since a unit tangent vector is needed for our material models, derivatives of the B-spline curve are obtained. We will extend the B-spline curve to the B-spline surface while the parameters and derivatives of the B-spline surface are discussed. In order to carry out any computations, input data is required to generate a surface using the B-spline interpolation concept. For this purpose, it is explained how the data points are obtained from the experiments. Finally, an application based on the interpolation concept for fiber bypassing around a hole is presented.

Chapter 6 addresses the finite element computations starting with finite element studies using the streamline approach with the obtained parameters for transversal isotropy in *Chapter 4*. First, finite element studies using the streamline approach with obtained parameters for in *Chapter 4*

transversal isotropy can be seen. The details of the modeling are provided, followed by a comparison between the behavior of a plate with bypassed fibers with a plate with cut fibers. In the following, we will carry out finite element simulations using the obtained material parameters for transverse isotropy, to gain a better understanding of the effects of rivets on the performance of laminates with hole. In the next step, we aim to validate the whole process of material parameter identification process using the results of experiments, and we would like to find out how well the material model can predict the behavior of transversal isotropy plates. In order to do so, we carry out computations using the obtained parameters in *Chapter 4* for transverse isotropy so as, with the help of the B-spline approach, to obtain the distributed fiber directions in *Chapter 5*. FEM computations are again performed with the help of the streamline approach since it is of interest to compare the results of computations using B-spline and streamline methods with respect to the experimental data. In addition, the details on samples, experiments, the projection of FEM simulation to DIC results and models are explained. Further, a comparison of experimental results and simulations is presented.

For the next step, validation samples regarding the samples with orthogonal fiber distributions are discussed and the details of experiments are provided. A comparison of simulations using the obtained parameters in *Chapter 4* with the material model in *Chapter 3* and experiments using DIC observations is given.

Chapter 7 summarizes the main aspects of the work, followed by an outlook on possible future research work.

2 Fundamentals of Continuum Mechanics

Continuum Mechanics is the basic analysis of the kinematics of material bodies and the balance relations describing the behavior of internal and extern effects. These are completed with the relations of the theory of materials by introducing constitutive equations. This chapter is based on Continuum Mechanics textbooks such as (Altenbach, 2012; Altenbach and Altenbach, 1994; Haupt, 2000; Holzapfel, 2008; Malvern, 1969; Ogden, 1984; Truesdell and Noll, 1965). The goal of this chapter is to present the main relations in Continuum Mechanics.

2.1 Kinematics

Kinematics deals with the description of the motion of a material body without considering external forces. In addition, strain measures with the help of a deformation gradient will be introduced.

2.1.1 Configuration and Motion

A material body is composed of a set of material points $\mathcal{B} = \{\mathcal{P}\}$. The configuration $\boldsymbol{\mathcal{R}}$ which does not change over time is called reference configuration

$$\boldsymbol{\mathcal{R}}\colon \begin{cases} \mathcal{B} & \to \boldsymbol{\mathcal{R}}[\mathcal{B}] \subset \mathbb{V}^3 \\ \mathcal{P} & \mapsto \boldsymbol{\mathcal{R}}(\mathcal{P}) = \boldsymbol{X} \Longleftrightarrow \mathcal{P} = \boldsymbol{\mathcal{R}}^{-1}(\boldsymbol{X}). \end{cases} \tag{2.1}$$

The material body $\mathcal{B}$ deforms and moves and it generates a new configuration called current configuration $\boldsymbol{\chi}_t$

$$t \mapsto \boldsymbol{\chi}_t\colon \begin{cases} \mathcal{B} & \to \boldsymbol{\chi}_t[\mathcal{B}] \subset \mathbb{V}^3 \\ \mathcal{P} & \mapsto (\boldsymbol{x}) = \boldsymbol{\chi}_t(\mathcal{P}) \Longleftrightarrow \mathcal{P} = \boldsymbol{\chi}_t^{-1}(\boldsymbol{x}). \end{cases} \tag{2.2}$$

Then, $\boldsymbol{X}$ and $\boldsymbol{x}$ are assigned to a material point $\mathcal{P}$, representing the position in the reference configuration $\boldsymbol{\mathcal{R}}$, and in the current configuration $\boldsymbol{\chi}_t$ as shown in Fig. 2.1. The motion is defined by

$$\boldsymbol{x} = \boldsymbol{\chi}_{\mathrm{R}}(\boldsymbol{X}, t). \tag{2.3}$$

The difference, see also Fig. 2.2

$$\boldsymbol{u}(\boldsymbol{X}, t) = \boldsymbol{x} - \boldsymbol{X} = \boldsymbol{\chi}_{\mathrm{R}}(\boldsymbol{X}, t) - \boldsymbol{X} \tag{2.4}$$

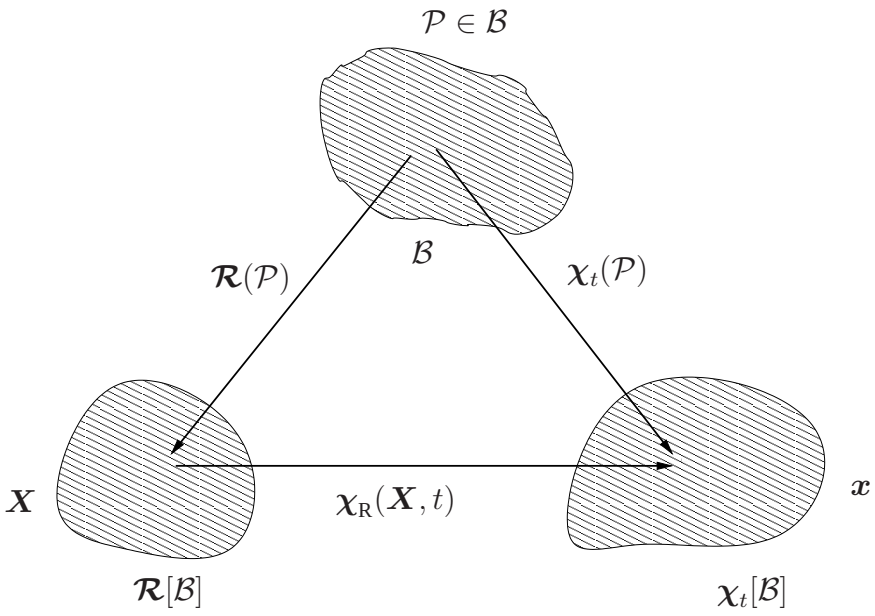

Figure 2.1: Reference and current configurations

represents the displacement vector. The deformation gradient describes the local change of motion and is defined by

$$\mathbf{F}(\boldsymbol{X}, t) = \operatorname{Grad} \boldsymbol{\chi}_{\mathrm{R}}(\boldsymbol{X}, t). \tag{2.5}$$

It follows

$$\mathbf{F} = \operatorname{Grad}(\boldsymbol{u} + \boldsymbol{X}) = \operatorname{Grad} \boldsymbol{u} + \mathbf{I}, \tag{2.6}$$

where $\mathbf{I}$ is the second order identity tensor. The displacement gradient tensor can be written as $\mathbf{H}(\boldsymbol{X}, t) := \operatorname{Grad} \boldsymbol{u}(\boldsymbol{X}, t)$ and the deformation gradient can be described as $\mathbf{F} = \mathbf{H} + \mathbf{I}$.

The deformation gradient has the property to map material line elements $\mathrm{d}\boldsymbol{X}$ in the reference configuration to material line elements $\mathrm{d}\boldsymbol{x}$ in the current configuration

$$\mathrm{d}\boldsymbol{x} = \mathbf{F}\, \mathrm{d}\boldsymbol{X}. \tag{2.7}$$

The inverse of $\mathbf{F}$ must exist where the existence is guaranteed by the determinant of $\mathbf{F}$ denoted by J, i.e.

$$J := \det \mathbf{F} \neq 0. \tag{2.8}$$

Regarding all deformations, J is required to be greater than zero, $J > 0$, since the body can not interpenetrate itself. Moreover, the deformation gradient transforms material surface elements from the reference to the current configuration

$$\mathrm{d}\boldsymbol{a} = (\det \mathbf{F})\, \mathbf{F}^{-\mathrm{T}}\, \mathrm{d}\boldsymbol{A} \tag{2.9}$$

and material volume elements are transformed by

$$\mathrm{d}v = (\det \mathbf{F})\, \mathrm{d}V = J\, \mathrm{d}V. \tag{2.10}$$

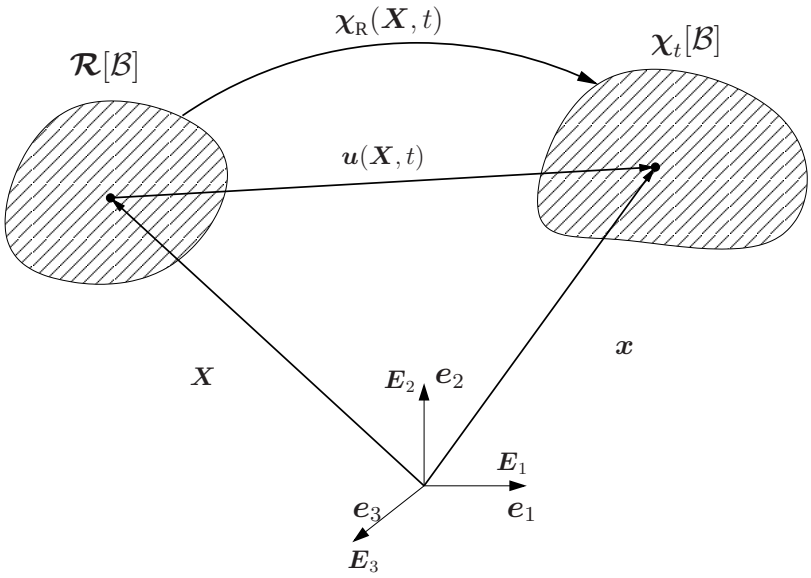

Figure 2.2: Displacement vector

It is necessary to have measures that are independent of rigid body motions. The deformation gradient does not have this property. Thus, the right and left Cauchy-Green tensors are introduced

$$\mathbf{C} = \mathbf{F}^{\mathrm{T}}\mathbf{F} \quad \text{and} \quad \mathbf{B} = \mathbf{F}\mathbf{F}^{\mathrm{T}}. \tag{2.11}$$

The Green strain tensor

$$\mathbf{E} = \frac{1}{2}\left(\mathbf{C} - \mathbf{I}\right) \tag{2.12}$$

is of interest, which can be expressed by the displacement gradient

$$\mathbf{E} = \tfrac{1}{2}(\mathbf{H} + \mathbf{H}^{\mathrm{T}} + \mathbf{H}^{\mathrm{T}}\mathbf{H}). \tag{2.13}$$

In the case of small strain theory, which is used in this work, the quadratic term is neglected,

$$\boldsymbol{\varepsilon} := \tfrac{1}{2}(\mathbf{H} + \mathbf{H}^{\mathrm{T}}) = \tfrac{1}{2}(\mathrm{Grad}\,\boldsymbol{u} + \mathrm{Grad}^{T}\,\boldsymbol{u}). \tag{2.14}$$

Furthermore, it is assumed that there is no distinction between the spatial coordinates $\boldsymbol{x}$ and the coordinates in the reference configuration $\boldsymbol{X}$ (due to theory of small displacements which is assumed in this thesis).

Principal strains are of interest and can be defined by

$$\epsilon_{\alpha}^{(\mathrm{m})} = \begin{cases} \dfrac{1}{m}(\lambda_{\alpha}^{m} - 1) & \text{if } m \neq 0 \\ \ln \lambda_{\alpha} & \text{if } m = 0, \end{cases} \tag{2.15}$$

for more details, see (Ogden, 1984).

2.1.2 Strain Energy Function

$\psi(\mathbf{F}, \boldsymbol{X})$ is called strain energy function when ψ depends only on deformation gradient $\mathbf{F}$. The strain energy function relies on the deformation gradient $\mathbf{F}$ and the position of a point when we are dealing with heterogeneous materials, $\psi(\mathbf{F}, \boldsymbol{X})$.

A significant constraint of the strain energy function is that it is assumed to be *objective*. This means that after a translation or a rotation in space, the amount of stored energy has to be unchanged

$$\psi(\mathbf{F}) = \psi(\mathbf{QF}) \tag{2.16}$$

where $\mathbf{Q}$ is an orthogonal tensor. If $\mathbf{Q} = \mathbf{R}^T$, Eq.(2.16) leads to

$$\psi(\mathbf{F}) = \psi(\mathbf{R}^T\mathbf{F}) = \psi(\mathbf{R}^T\mathbf{RU}) = \psi(\mathbf{U}). \tag{2.17}$$

Thus, we may write

$$\psi(\mathbf{F}) = \hat{\psi}(\mathbf{C}) = \bar{\psi}(\mathbf{E}). \tag{2.18}$$

2.1.3 Deformation Velocities

In Continuum Mechanics, the temporal rate of change over line, surface, and volume elements is of interest. The temporal rate of change of line elements is described by

$$(\mathrm{d}\boldsymbol{x})^{\cdot} = (\mathbf{F}\,\mathrm{d}\boldsymbol{X})^{\cdot} = \dot{\mathbf{F}}\mathbf{F}^{-1}\,\mathrm{d}\boldsymbol{x} = \mathbf{L}\,\mathrm{d}\boldsymbol{x}, \tag{2.19}$$

along with the change of surface elements as

$$(\mathrm{d}\boldsymbol{a})^{\cdot} = \left(J\mathbf{F}^{-\mathrm{T}}\,\mathrm{d}\boldsymbol{A}\right)^{\cdot} = \left[(\operatorname{div}\boldsymbol{v})\mathbf{I} - \mathbf{L}^{\mathrm{T}}\right]\mathrm{d}\boldsymbol{a}, \tag{2.20}$$

and the change of material volume elements

$$(\mathrm{d}v)^{\cdot} = \dot{J}\,\mathrm{d}V = (\operatorname{div}\boldsymbol{v})\,\mathrm{d}v. \tag{2.21}$$

In Eq.(2.19), the spatial velocity gradient tensor

$$\mathbf{L} = \operatorname{grad}\boldsymbol{v}(\boldsymbol{x}, t) = \dot{\mathbf{F}}\mathbf{F}^{-1} \tag{2.22}$$

is defined. The spatial velocity gradient $\mathbf{L}$ can be decomposed additively into a symmetric part $\mathbf{D}$ and a skew symmetric part $\mathbf{W}$,

$$\mathbf{L} = \mathbf{D} + \mathbf{W}, \tag{2.23}$$

with

$$\mathbf{D} = \frac{1}{2}\left(\mathbf{L} + \mathbf{L}^T\right). \tag{2.24}$$

and

$$\mathbf{W} = \frac{1}{2}\left(\mathbf{L} - \mathbf{L}^T\right). \tag{2.25}$$

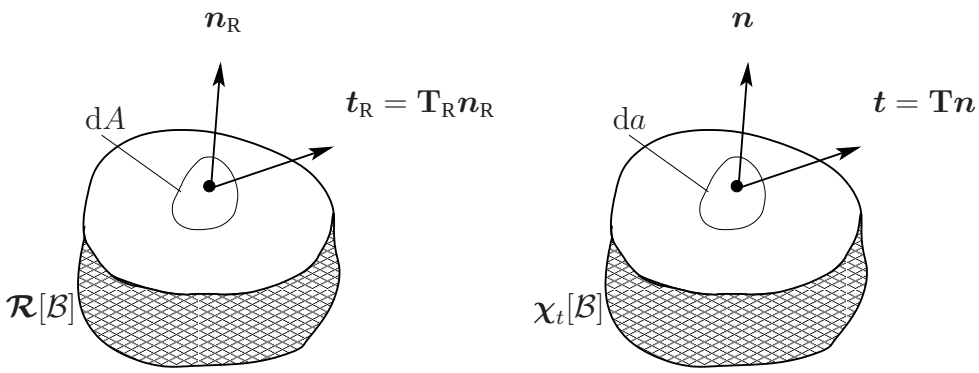

(a) Reference configuration (b) Current configuration

Figure 2.3: Stress vectors and normal unit vectors

2.2 Stress Tensors

Stresses are generated by a deformation inside a body which generates a body interaction. The generated stresses are a significant quantity in Continuum Mechanics, (Holzapfel, 2008). Regarding constitutive modeling, different stress tensors can be introduced depending on their definition.

A traction is applied over a material body and if the body is considered in two parts cut by a plane surface, see Fig. 2.3, this results in forces on the surfaces. The surface element can be written as

$$\mathrm{d}\boldsymbol{f} = \boldsymbol{t}\,\mathrm{d}a = \mathbf{T}\,\mathrm{d}\boldsymbol{a}, \tag{2.26}$$

where $\mathrm{d}\boldsymbol{a} = \boldsymbol{n}\,\mathrm{d}a$, see Fig. 2.3. The Cauchy stress vector is represented by the vector $\boldsymbol{t}$ and $\mathbf{T}$ represents the Cauchy stress tensor which is also called true stress tensor due to the fact that it acts on material surface elements in the current configuration. According to Cauchy's theorem, the stress tensor $\mathbf{T}$ is connected with the surface traction $\boldsymbol{t}$,

$$\boldsymbol{t} = \mathbf{T}\boldsymbol{n}. \tag{2.27}$$

The first Piola-Kirchhoff stress tensor $\mathbf{T}_{\mathrm{R}}$ can be introduced by

$$\mathrm{d}\boldsymbol{f} = \boldsymbol{t}_{\mathrm{R}}\,\mathrm{d}A = \mathbf{T}_{\mathrm{R}}\,\mathrm{d}\boldsymbol{A}, \tag{2.28}$$

where $\mathrm{d}\boldsymbol{A} = \boldsymbol{n}_{\mathrm{R}}\,\mathrm{d}A$. Furthermore, vector $\boldsymbol{n}_{\mathrm{R}}$ represents the unit normal vector in the reference configuration. Cauchy's theorem can also be expressed with quantities related to the reference configuration following

$$\boldsymbol{t}_{\mathrm{R}} = \mathbf{T}_{\mathrm{R}}\boldsymbol{n}_{\mathrm{R}}. \tag{2.29}$$

The Cauchy and the first Piola-Kirchhoff stress tensors are related to each other using the transformation relation for the material surface element (2.9) as

$$\mathbf{T}_{\mathrm{R}} = (\det\mathbf{F})\mathbf{T}\mathbf{F}^{-\mathrm{T}}. \tag{2.30}$$

The second Piola-Kirchhoff tensor is another significant stress tensor operating on the reference configuration. It is defined as

$$\tilde{\mathbf{T}} := (\det \mathbf{F})\, \mathbf{F}^{-1}\mathbf{T}\mathbf{F}^{-\mathrm{T}}. \tag{2.31}$$

Furthermore, the Kirchhoff stress tensor is another stress tensor that operates in the current configuration and it is related to the Cauchy stress tensor by

$$\mathbf{S} := (\det \mathbf{F})\, \mathbf{T}. \tag{2.32}$$

Considering Eq.(2.31) and Eq.(2.32), the Kirchhoff stress tensor and the second Piola-Kirchhoff tensor are connected to each other using

$$\mathbf{S} = \mathbf{F}\tilde{\mathbf{T}}\mathbf{F}^{T}. \tag{2.33}$$

2.3 Balance Equations

This section serves to introduce balance equations and principles that are applicable to any material. These principles are the conservation of mass, the momentum balance principles and the balance of energy. These principles are discussed in the following subsections.

2.3.1 Balance of Mass

This principle shows that the mass remains constant with respect to time. This means that the mass of a body $\mathcal{B}$ remains unchanged during the deformation, and the mass of the body in the current configuration is equal to the mass of the body in the reference configuration as

$$m(\mathcal{B}, t) = \int_{\omega} \varrho(\boldsymbol{x}, t)\, \mathrm{d}v = \int_{\Omega} \varrho_{\mathrm{R}}(\boldsymbol{X}, t)\, \mathrm{d}V \tag{2.34}$$

which leads to

$$\frac{\mathrm{d}m}{\mathrm{d}t} = \frac{\mathrm{d}}{\mathrm{d}t} \int_{\omega} \varrho(\boldsymbol{x}, t)\, \mathrm{d}v = \frac{\mathrm{d}}{\mathrm{d}t} \int_{\Omega} \varrho_{\mathrm{R}}(\boldsymbol{X}, t)\, \mathrm{d}V = 0 \tag{2.35}$$

In the reference configuration, the local form can be calculated by

$$\frac{\partial}{\partial t}\varrho_{\mathrm{R}}(\boldsymbol{X}, t) = 0 \Longleftrightarrow \varrho_{\mathrm{R}} = \varrho_{\mathrm{R}}(\boldsymbol{X}) \tag{2.36}$$

In the current configuration, the local form can also be written using Eq.(2.10) and Eq.(2.35) as

$$\dot{\varrho} + \varrho \mathrm{div}\, \boldsymbol{v} = 0 \tag{2.37}$$

and

$$\varrho_{\mathrm{R}} = \varrho \det \mathbf{F} \tag{2.38}$$

can be concluded where ϱ_{R} is the mass density in the reference configuration and ϱ represents the mass in the current configuration .

2.3.2 Balance of Linear Momentum

The linear momentum of the material body $\mathcal{B}$ is defined as the volume integral of the product of the mass density with its velocity

$$\boldsymbol{J}(\mathcal{B},t) = \int\limits_{\omega} \boldsymbol{v}(\boldsymbol{x},t)\,\varrho(\boldsymbol{x},t)\,\mathrm{d}v = \int\limits_{\Omega} \boldsymbol{v}(\boldsymbol{X},t)\,\varrho_{\mathrm{R}}(\boldsymbol{X})\,\mathrm{d}V. \tag{2.39}$$

The balance of linear momentum in the reference configuration

$$\frac{\mathrm{d}\boldsymbol{J}}{\mathrm{d}t} = \frac{\mathrm{d}}{\mathrm{d}t}\int\limits_{\Omega} \boldsymbol{v}\left(\boldsymbol{X},t\right)\varrho_{\mathrm{R}}\left(\boldsymbol{X},t\right)\mathrm{d}V = \int\limits_{\partial\Omega} \boldsymbol{t}_{\mathrm{R}}\left(\boldsymbol{X},t\right)\mathrm{d}A + \int\limits_{\Omega} \boldsymbol{k}\left(\boldsymbol{X},t\right)\varrho_{\mathrm{R}}\left(\boldsymbol{X}\right)\mathrm{d}V \tag{2.40}$$

and in the current configuration

$$\frac{\mathrm{d}\boldsymbol{J}}{\mathrm{d}t} = \frac{\mathrm{d}}{\mathrm{d}t}\int\limits_{\omega} \boldsymbol{v}\left(\boldsymbol{x},t\right)\varrho\left(\boldsymbol{x},t\right)\mathrm{d}v = \int\limits_{\partial\omega} \boldsymbol{t}\left(\boldsymbol{x},t\right)\mathrm{d}a + \int\limits_{\omega} \boldsymbol{k}\left(\boldsymbol{x},t\right)\varrho\left(\boldsymbol{x},t\right)\mathrm{d}v, \tag{2.41}$$

demonstrate that the change of linear momentum with respect to time is equal to external forces resulting from surface tractions and specific volume forces. In order to obtaining the global balance momentum, we can use the divergence theorem and Eq.(2.10) together with Cauchy's theorem, see (Haupt, 2000),

$$\int\limits_{\omega} \frac{\mathrm{d}}{\mathrm{d}t}\left(\boldsymbol{v}\left(\boldsymbol{x},t\right)\varrho\left(\boldsymbol{x},t\right)J\right)\mathrm{d}v = \int\limits_{\omega} \operatorname{div}\mathbf{T}\,\mathrm{d}v + \int\limits_{\omega} \boldsymbol{k}\left(\boldsymbol{x},t\right)\varrho\left(\boldsymbol{x},t\right)\mathrm{d}v. \tag{2.42}$$

With the help of the local balance of mass (2.38) and Eq.(2.10), the local balance of momentum in current configuration can be presented as

$$\varrho\boldsymbol{v} = \operatorname{div}\mathbf{T} + \varrho\boldsymbol{k} \tag{2.43}$$

and regarding the reference configuration, it yields

$$\varrho_{\mathrm{R}}\boldsymbol{v} = \operatorname{Div}\mathbf{T}_{\mathrm{R}} + \varrho_{\mathrm{R}}\boldsymbol{k}. \tag{2.44}$$

2.3.3 Balance of Angular Momentum

The balance of angular momentum states that the change of rotational momentum

$$\boldsymbol{D}_{\boldsymbol{c}}(\mathcal{B},t) = \int\limits_{\omega} (\boldsymbol{x}-\boldsymbol{c})\times\boldsymbol{v}\varrho(\boldsymbol{x},t)\,\mathrm{d}v = \int\limits_{\Omega} (\boldsymbol{\chi}_{\mathrm{R}}(\boldsymbol{X},t)-\boldsymbol{c})\times\boldsymbol{v}\varrho_{\mathrm{R}}(\boldsymbol{X})\,\mathrm{d}V, \tag{2.45}$$

is equivalent to the moment generated by all forces acting on the material body.

$$\frac{\mathrm{d}\boldsymbol{D}_{\boldsymbol{c}}}{\mathrm{d}t} = \frac{\mathrm{d}}{\mathrm{d}t}\int\limits_{\omega} (\boldsymbol{x}-\boldsymbol{c})\times\boldsymbol{v}\varrho\,\mathrm{d}v = \int\limits_{\partial\omega} (\boldsymbol{x}-\boldsymbol{c})\times\boldsymbol{t}\,\mathrm{d}a + \int\limits_{\omega} (\boldsymbol{x}-\boldsymbol{c})\times\boldsymbol{k}\varrho\,\mathrm{d}v. \tag{2.46}$$

It can be shown that local form of this expression is given by

$$\mathbf{T} = \mathbf{T}^{\mathrm{T}}, \tag{2.47}$$

which refers to the symmetry of the Cauchy stress tensor, see (Haupt, 2000).

3 Theory of Transverse Isotropic and Orthotropic Composites

3.1 Introduction

Composites materials consist of two or more materials and these materials are combined to achieve specific properties. In engineering and the industry applications, thanks to the widespread use of fiber for reinforcement purposes, it is possible to create lightweight composite materials that are very robust. In this case, the material response is anisotropic, i.e. the materials exhibit different responses under applied loads in different directions. This means that composite materials show different physical properties and characteristic depending on the orientation of the fibers in the matrix. In this work, in the context of small strains, we assume isotropy, transversal isotropy, and orthotropy for linear elasticity. For this aim, material models are needed for each case in order to predict the behavior of isotropy, transversal isotropy and orthotropy.

3.2 Voigt-Notation

In this part, matrix notation is obtained from the tensorial notation which is related to the term *Voigt*-notation. This notation is widely used by researchers, see, for example, (Christensen, 2005; Hartmann, 2003; Lüth and Ibach, 2003; Reddy, 2003). The tensorial formulation, which has the advantage of being independent of the choice of the coordinate system, can be adjusted to cartesian coordinates or to curvilinear coordinates, (Weiss et al., 1996a), where several soft tissues show kind of anisotropic behavior. The property of symmetry of the stress and strain tensor have a significant influence in this regard. Furthermore, the scalar product in the principle of virtual displacements leads to a representation of the vector including the independent strain tensor components caused by a symmetric elasticity matrix. It is common to reformulate tensorial expressions into matrix equations, where the Voigt notation can be applied, see (Vannucci, 2018). The components of the stress and strain tensors are assembled in a (6×1) column vector, and the (6×6) elasticity matrix connects both quantities, which will be explained in more detail in the following. For this purpose, the stress and strain tensor are

$$\mathbf{T} = \begin{bmatrix} T_{11} & T_{12} & T_{31} \\ & T_{22} & T_{23} \\ \text{sym.} & & T_{33} \end{bmatrix} \boldsymbol{e}_i \otimes \boldsymbol{e}_j, \tag{3.1}$$

$$\mathbf{E} = \begin{bmatrix} \varepsilon_{11} & \varepsilon_{12} & \varepsilon_{31} \\ & \varepsilon_{22} & \varepsilon_{23} \\ \text{sym.} & & \varepsilon_{33} \end{bmatrix} \boldsymbol{e}_i \otimes \boldsymbol{e}_j, \tag{3.2}$$

which can be assembled into column vectors

$$\mathbf{T}^T = \{T_{11}\ T_{22}\ T_{33}\ T_{12}\ T_{23}\ T_{31}\}, \tag{3.3}$$

and

$$\tilde{\mathbf{E}}^T = \{\varepsilon_{11}\ \varepsilon_{22}\ \varepsilon_{33}\ \varepsilon_{12}\ \varepsilon_{23}\ \varepsilon_{31}\}. \tag{3.4}$$

For a better understanding of the process of changing the symmetry properties into matrix formulation, the tensorial quantities are represented by (9×1) and (9×9) matrices, see (Hartmann, 2003). Eq.(3.94) leads to

$$\begin{Bmatrix} T_{11} \\ T_{22} \\ T_{33} \\ T_{12} \\ T_{23} \\ T_{31} \\ T_{13} \\ T_{21} \\ T_{32} \end{Bmatrix} = \begin{bmatrix} C_{1111} & C_{1122} & C_{1133} & C_{1112} & C_{1123} & C_{1131} & C_{1113} & C_{1121} & C_{1132} \\ C_{2211} & C_{2222} & C_{2233} & C_{2212} & C_{2223} & C_{2231} & C_{2213} & C_{2221} & C_{2232} \\ C_{3311} & C_{3322} & C_{3333} & C_{3312} & C_{3323} & C_{3331} & C_{3313} & C_{3321} & C_{3332} \\ C_{1211} & C_{1222} & C_{1233} & C_{1212} & C_{1223} & C_{1231} & C_{1213} & C_{1221} & C_{1232} \\ C_{2311} & C_{2322} & C_{2333} & C_{2312} & C_{2323} & C_{2331} & C_{2313} & C_{2321} & C_{2332} \\ C_{3111} & C_{3122} & C_{3133} & C_{3112} & C_{3123} & C_{3131} & C_{3113} & C_{3121} & C_{3132} \\ C_{1311} & C_{1322} & C_{1333} & C_{1312} & C_{1323} & C_{1331} & C_{1313} & C_{1321} & C_{1332} \\ C_{2111} & C_{2122} & C_{2133} & C_{2112} & C_{2123} & C_{2131} & C_{2113} & C_{2121} & C_{2132} \\ C_{3211} & C_{3222} & C_{3233} & C_{3212} & C_{3223} & C_{3231} & C_{3213} & C_{3221} & C_{3232} \end{bmatrix} \begin{Bmatrix} \varepsilon_{11} \\ \varepsilon_{22} \\ \varepsilon_{33} \\ \varepsilon_{12} \\ \varepsilon_{23} \\ \varepsilon_{31} \\ \varepsilon_{13} \\ \varepsilon_{21} \\ \varepsilon_{32} \end{Bmatrix}. \tag{3.5}$$

Due to the symmetry of the stress tensor, equations 4 to 6 are equal to the last three equations 7 to 9. This results in

$$\begin{Bmatrix} T_{11} \\ T_{22} \\ T_{33} \\ T_{12} \\ T_{23} \\ T_{31} \end{Bmatrix} = \begin{bmatrix} C_{1111} & C_{1122} & C_{1133} & C_{1112} & C_{1123} & C_{1131} & C_{1113} & C_{1121} & C_{1132} \\ C_{2211} & C_{2222} & C_{2233} & C_{2212} & C_{2223} & C_{2231} & C_{2213} & C_{2221} & C_{2232} \\ C_{3311} & C_{3322} & C_{3333} & C_{3312} & C_{3323} & C_{3331} & C_{3313} & C_{3321} & C_{3332} \\ C_{1211} & C_{1222} & C_{1233} & C_{1212} & C_{1223} & C_{1231} & C_{1213} & C_{1221} & C_{1232} \\ C_{2311} & C_{2322} & C_{2333} & C_{2312} & C_{2323} & C_{2331} & C_{2313} & C_{2321} & C_{2332} \\ C_{3111} & C_{3122} & C_{3133} & C_{3112} & C_{3123} & C_{3131} & C_{3113} & C_{3121} & C_{3132} \end{bmatrix} \begin{Bmatrix} \varepsilon_{11} \\ \varepsilon_{22} \\ \varepsilon_{33} \\ \varepsilon_{12} \\ \varepsilon_{23} \\ \varepsilon_{31} \\ \varepsilon_{13} \\ \varepsilon_{21} \\ \varepsilon_{32} \end{Bmatrix}. \tag{3.6}$$

The symmetry of the strain tensor leads to

$$\varepsilon_{12} = \varepsilon_{21}, \quad \varepsilon_{23} = \varepsilon_{32}, \quad \varepsilon_{31} = \varepsilon_{13}. \tag{3.7}$$

Thus, the (6×9) matrix can be transferred to

$$\begin{Bmatrix} T_{11} \\ T_{22} \\ T_{33} \\ T_{12} \\ T_{23} \\ T_{31} \end{Bmatrix} = \begin{bmatrix} C_{1111} & C_{1122} & C_{1133} & C_{1112}+C_{1121} & C_{1123}+C_{1132} & C_{1131}+C_{1113} \\ C_{2211} & C_{2222} & C_{2233} & C_{2212}+C_{2221} & C_{2223}+C_{2232} & C_{2231}+C_{2213} \\ C_{3311} & C_{3322} & C_{3333} & C_{3312}+C_{3321} & C_{3323}+C_{3332} & C_{3331}+C_{3313} \\ C_{1211} & C_{1222} & C_{1233} & C_{1212}+C_{1221} & C_{1223}+C_{1232} & C_{1231}+C_{1213} \\ C_{2311} & C_{2322} & C_{2333} & C_{2312}+C_{2321} & C_{2323}+C_{2332} & C_{2331}+C_{2313} \\ C_{3111} & C_{3122} & C_{3133} & C_{3112}+C_{3121} & C_{3123}+C_{3132} & C_{3131}+C_{3113} \end{bmatrix} \begin{Bmatrix} \varepsilon_{11} \\ \varepsilon_{22} \\ \varepsilon_{33} \\ \varepsilon_{12} \\ \varepsilon_{23} \\ \varepsilon_{31} \end{Bmatrix}. \tag{3.8}$$

In other words, $\mathbf{T} = \tilde{\mathbf{C}}\tilde{\mathbf{E}}$, with $\mathbf{T} \in \mathbb{R}^6$, $\tilde{\mathbf{E}} \in \mathbb{R}^6$ and $\tilde{\mathbf{C}} \in \mathbb{R}^{6\times 6}$ is obtained. The positioning of the coefficients of a fourth order tensor into $\tilde{\mathbf{C}}$ is based on the actual calculation. For instance, a product of $\mathcal{C} = \mathbf{A} \otimes \mathbf{B}$ is considered, where $\mathbf{A} = \mathbf{A}^{\mathrm{T}}$ and $\mathbf{B} = \mathbf{B}^{\mathrm{T}}$ are symmetric tensors. The coefficients of $\mathcal{C}$ are pointed out by $c_{ijkl} = a_{ij}b_{kl}$. In this regard, the coefficient matrix (3.8) has the representation

$$\mathbf{C} = \begin{bmatrix} a_{11}b_{11} & a_{11}b_{22} & a_{11}b_{33} & 2a_{11}b_{12} & 2a_{11}b_{23} & 2a_{11}b_{31} \\ a_{22}b_{11} & a_{22}b_{22} & a_{22}b_{33} & 2a_{22}b_{12} & 2a_{22}b_{23} & 2a_{22}b_{31} \\ a_{33}b_{11} & a_{33}b_{22} & a_{33}b_{33} & 2a_{33}b_{12} & 2a_{33}b_{23} & 2a_{33}b_{31} \\ a_{12}b_{11} & a_{12}b_{22} & a_{12}b_{33} & 2a_{12}b_{12} & 2a_{12}b_{23} & 2a_{12}b_{31} \\ a_{23}b_{11} & a_{23}b_{22} & a_{23}b_{33} & 2a_{23}b_{12} & 2a_{23}b_{23} & 2a_{23}b_{31} \\ a_{31}b_{11} & a_{31}b_{22} & a_{31}b_{33} & 2a_{31}b_{12} & 2a_{31}b_{23} & 2a_{31}b_{31} \end{bmatrix}. \tag{3.9}$$

Regarding the transposition T_{23} of a fourth-order tensor, the product $T_{ij} = C_{ikjl}E_{kl}$ is considered,

$$\begin{Bmatrix} T_{11} \\ T_{22} \\ T_{33} \\ T_{12} \\ T_{23} \\ T_{31} \\ T_{13} \\ T_{21} \\ T_{32} \end{Bmatrix} = \begin{bmatrix} C_{1111} & C_{1212} & C_{1313} & C_{1112} & C_{1213} & C_{1311} & C_{1113} & C_{1211} & C_{1312} \\ C_{2121} & C_{2222} & C_{2323} & C_{2122} & C_{2223} & C_{2321} & C_{2123} & C_{2221} & C_{2322} \\ C_{3131} & C_{3232} & C_{3333} & C_{3132} & C_{3233} & C_{3331} & C_{3133} & C_{3231} & C_{3332} \\ C_{1121} & C_{1222} & C_{1323} & C_{1122} & C_{1223} & C_{1321} & C_{1123} & C_{1221} & C_{1322} \\ C_{2131} & C_{2232} & C_{2333} & C_{2132} & C_{2233} & C_{2331} & C_{2133} & C_{2231} & C_{2332} \\ C_{3111} & C_{3212} & C_{3313} & C_{3112} & C_{3213} & C_{3311} & C_{3113} & C_{3211} & C_{3312} \\ C_{1131} & C_{1232} & C_{1333} & C_{1132} & C_{1233} & C_{1331} & C_{1133} & C_{1231} & C_{1332} \\ C_{2111} & C_{2212} & C_{2313} & C_{2112} & C_{2213} & C_{2311} & C_{2113} & C_{2211} & C_{2312} \\ C_{3121} & C_{3222} & C_{3323} & C_{3122} & C_{3223} & C_{3321} & C_{3123} & C_{3221} & C_{3322} \end{bmatrix} \begin{Bmatrix} \varepsilon_{11} \\ \varepsilon_{22} \\ \varepsilon_{33} \\ \varepsilon_{12} \\ \varepsilon_{23} \\ \varepsilon_{31} \\ \varepsilon_{13} \\ \varepsilon_{21} \\ \varepsilon_{32} \end{Bmatrix}. \tag{3.10}$$

The indices 2 and 3 are exchanged in every column in comparison to (3.5). Using the symmetries and Eq.(3.7) the last three rows can be ignored, which leads to

$$\begin{Bmatrix} T_{11} \\ T_{22} \\ T_{33} \\ T_{12} \\ T_{23} \\ T_{31} \end{Bmatrix} = \begin{bmatrix} C_{1111} & C_{1212} & C_{1313} & C_{1112}+C_{1211} & C_{1213}+C_{1312} & C_{1311}+C_{1113} \\ C_{2121} & C_{2222} & C_{2323} & C_{2122}+C_{2221} & C_{2223}+C_{2322} & C_{2321}+C_{2123} \\ C_{3131} & C_{3232} & C_{3333} & C_{3132}+C_{3231} & C_{3233}+C_{3332} & C_{3331}+C_{3133} \\ C_{1121} & C_{1222} & C_{1323} & C_{1122}+C_{1221} & C_{1223}+C_{1322} & C_{1321}+C_{1123} \\ C_{2131} & C_{2232} & C_{2333} & C_{2132}+C_{2231} & C_{2233}+C_{2332} & C_{2331}+C_{2133} \\ C_{3111} & C_{3212} & C_{3313} & C_{3112}+C_{3211} & C_{3213}+C_{3312} & C_{3311}+C_{3113} \end{bmatrix} \begin{Bmatrix} \varepsilon_{11} \\ \varepsilon_{22} \\ \varepsilon_{33} \\ \varepsilon_{12} \\ \varepsilon_{23} \\ \varepsilon_{31} \end{Bmatrix}. \tag{3.11}$$

This idea can be applied to the tensors $\mathbf{I} \otimes \mathbf{I}$, $[\mathbf{I} \otimes \mathbf{M} + \mathbf{M} \otimes \mathbf{I}]^{T_{23}}$, $\mathbf{M} \otimes \mathbf{M}$, and $\mathbf{I} \otimes \mathbf{M} + \mathbf{M} \otimes \mathbf{I}$, and we obtain the following representations:

$$\mathbf{I} \otimes \mathbf{I} \longrightarrow \begin{bmatrix} 1 & 1 & 1 & 0 & 0 & 0 \\ 1 & 1 & 1 & 0 & 0 & 0 \\ 1 & 1 & 1 & 0 & 0 & 0 \\ 0 & 0 & 0 & 0 & 0 & 0 \\ 0 & 0 & 0 & 0 & 0 & 0 \\ 0 & 0 & 0 & 0 & 0 & 0 \end{bmatrix}, \quad \mathcal{I} = [\mathbf{I} \otimes \mathbf{I}]^{T_{23}} \longrightarrow \begin{bmatrix} 1 & 0 & 0 & 0 & 0 & 0 \\ 0 & 1 & 0 & 0 & 0 & 0 \\ 0 & 0 & 1 & 0 & 0 & 0 \\ 0 & 0 & 0 & 1 & 0 & 0 \\ 0 & 0 & 0 & 0 & 1 & 0 \\ 0 & 0 & 0 & 0 & 0 & 1 \end{bmatrix} \tag{3.12}$$

$$[\mathbf{I}\otimes\mathbf{M}+\mathbf{M}\otimes\mathbf{I}]^{T_{23}} \longrightarrow \begin{bmatrix} 2m_{11} & 0 & 0 & 2m_{12} & 0 & 2m_{31} \\ 0 & 2m_{22} & 0 & 2m_{12} & 2m_{23} & 0 \\ 0 & 0 & 2m_{33} & 0 & 2m_{23} & 2m_{31} \\ m_{12} & m_{12} & 0 & m_{11}+m_{22} & m_{31} & m_{23} \\ 0 & m_{23} & m_{23} & m_{31} & m_{22}+m_{33} & m_{12} \\ m_{31} & 0 & m_{31} & m_{23} & m_{12} & m_{11}+m_{33} \end{bmatrix} \tag{3.13}$$

$$\mathbf{M}\otimes\mathbf{M} \longrightarrow \begin{bmatrix} m_{11}^2 & m_{11}m_{22} & m_{11}m_{33} & 2m_{11}m_{12} & 2m_{11}m_{23} & 2m_{11}m_{31} \\ m_{11}m_{22} & m_{22}^2 & m_{22}m_{33} & 2m_{12}m_{22} & 2m_{22}m_{23} & 2m_{22}m_{31} \\ m_{11}m_{33} & m_{22}m_{33}^2 & m_{33}^2 & 2m_{12}m_{33} & 2m_{23}m_{33} & 2m_{31}m_{33} \\ m_{11}m_{12} & m_{12}m_{22} & m_{12}m_{33} & 2m_{12}^2 & 2m_{12}m_{23} & 2m_{12}m_{31} \\ m_{11}m_{23} & m_{22}m_{23} & m_{23}m_{33} & 2m_{12}m_{23} & 2m_{23}^2 & 2m_{23}m_{31} \\ m_{11}m_{31} & m_{22}m_{31} & m_{31}m_{33} & 2m_{12}m_{31} & 2m_{23}m_{31} & 2m_{31}^2 \end{bmatrix} \tag{3.14}$$

$$\mathbf{I}\otimes\mathbf{M}+\mathbf{M}\otimes\mathbf{I} \longrightarrow \begin{bmatrix} 2m_{11} & m_{11}+m_{22} & m_{11}+m_{33} & 2m_{12} & 2m_{23} & 2m_{31} \\ m_{11}+m_{22} & 2m_{22} & m_{22}+m_{33} & 2m_{12} & 2m_{23} & 2m_{31} \\ m_{11}+m_{33} & m_{22}+m_{33} & 2m_{33} & 2m_{12} & 2m_{23} & 2m_{31} \\ m_{12} & m_{12} & m_{12} & 0 & 0 & 0 \\ m_{23} & m_{23} & m_{23} & 0 & 0 & 0 \\ m_{31} & m_{31} & m_{31} & 0 & 0 & 0 \end{bmatrix} \tag{3.15}$$

using relations

$$(\mathbf{B}\cdot\mathbf{C})\mathbf{A} = (\mathbf{A}\otimes\mathbf{B})\mathbf{C}, \tag{3.16}$$

and

$$\mathbf{A}\mathbf{C}\mathbf{B}^{\mathrm{T}} = [\mathbf{A}\otimes\mathbf{B}]^{T_{23}}\,\mathbf{C}, \tag{3.17}$$

where the symbolic $\mathcal{A}^{T_{23}}$ implies the transposition of second and third index, i.e. for $\mathcal{A} = a_{ijkl}\boldsymbol{e}_i\otimes\boldsymbol{e}_j\otimes\boldsymbol{e}_k\otimes\boldsymbol{e}_l$, we obtain $\mathcal{A}^{T_{23}} = a_{ikjl}\boldsymbol{e}_i\otimes\boldsymbol{e}_j\otimes\boldsymbol{e}_k\otimes\boldsymbol{e}_l$. $\mathcal{I} = [\mathbf{I}\otimes\mathbf{I}]^{T_{23}} = \delta_{ik}\delta_{jl}\boldsymbol{e}_i\otimes\boldsymbol{e}_j\otimes\boldsymbol{e}_k\otimes\boldsymbol{e}_l$ is the fourth order identity tensor, $\mathbf{A} = \mathcal{I}\mathbf{A}$, elasticity relation (3.57) can be presented by a fourth order elasticity tensor $\mathcal{C}$ considering all aformentioned assumptions see, (de Boer, 1982; Hartmann, 2003; Itskov, 2007).

In Solid Mechanics, the shear angles

$$\gamma_{12} = 2\varepsilon_{12}, \quad \gamma_{23} = 2\varepsilon_{23}, \quad \gamma_{31} = 2\varepsilon_{31} \tag{3.18}$$

are proposed, implying that the product with 2 can be omitted. Hence, the last three columns of matrices $\tilde{\mathbf{C}}$ should be multiplied with a factor $1/2$, which yields that the matrices (3.12) - (3.15) become symmetric.

3.3 Constitutive Modeling

Chapter 2 introduces balance relations that hold for all materials. On the other hand, constitutive relations are relations that are specific to a material. Constitutive equations are mathematical relations which relate the response or behavior of a specific material subjected to a specific loading.

A path-independent material behavior with large reversible deformation is called hyperelastic (Aboudi, 2013; Aboudi et al., 2012; Schröder and Neff, 2003). Several researchers discussed hyperelastic material in a purely mechanical theory, see (Duong and Itskov, 2015; Krawietz, 2013). The stress tensors of homogeneous hyperelastic materials are directly derived from a strain energy function, (Holzapfel, 2008),

$$\mathbf{T}_{\mathrm{R}} = \rho_{\mathrm{R}} \frac{\partial \psi(\mathbf{F}, \boldsymbol{X})}{\partial \mathbf{F}}, \tag{3.19}$$

$$\mathbf{T} = J^{-1} \rho_{\mathrm{R}} \frac{\partial \psi(\mathbf{F}, \boldsymbol{X})}{\partial \mathbf{F}} \mathbf{F}^T = J^{-1} \mathbf{F} \left(\rho_{\mathrm{R}} \frac{\partial \psi(\mathbf{F}, \boldsymbol{X})}{\partial \mathbf{F}} \right)^T, \tag{3.20}$$

where $\mathbf{T}_{\mathrm{R}}$ is the first Piola-Kirchhoff stress tensor and $\mathbf{T}$ is the Cauchy stress tensor, as introduced in Sec. 2.2. These types of relations are known as constitutive equations.

An alternative relation gained for the second Piola-Kirchhoff stress tensor is

$$\tilde{\mathbf{T}} = 2\rho_{\mathrm{R}} \frac{\partial \psi(\mathbf{C})}{\partial \mathbf{C}} = \rho_{\mathrm{R}} \frac{\partial \psi(\mathbf{E})}{\partial \mathbf{E}}, \tag{3.21}$$

see (Holzapfel, 2008).

In this thesis, I would like to model and predict the behavior of isotropic material, the transverse isotropic and orthotropic laminates. For this aim, constitutive models of isotropy, transversal isotropy and orthotropy are discussed in following.

3.3.1 Isotropy

Isotropic materials behave the same way in every direction under an applied load, as these materials have the same physical properties in every direction. The hyperelastic material is isotropic when the strain energy function must satisfy

$$\psi(\mathbf{F}) = \psi(\mathbf{F}\mathbf{Q}^T), \tag{3.22}$$

or the following equation in terms of $\mathbf{C}$

$$\psi(\mathbf{C}) = \psi(\mathbf{Q}\mathbf{C}\mathbf{Q}^T), \tag{3.23}$$

must be fulfield for all symmetric tensors $\mathbf{C} = \mathbf{F}^T\mathbf{F}$ and orthogonal tensors $\mathbf{Q}$, (Holzapfel, 2008).

The strain energy function can be expressed in terms of the invariants

$$\psi(\mathbf{E}) = \psi(\mathrm{I}_{\mathbf{E}}, \mathrm{II}_{\mathbf{E}}, \mathrm{III}_{\mathbf{E}}) \tag{3.24}$$

or

$$\psi(\mathbf{C}) = \psi(\mathrm{I}_{\mathbf{C}}, \mathrm{II}_{\mathbf{C}}, \mathrm{III}_{\mathbf{C}}), \tag{3.25}$$

where the invariants are defined by

$$\mathrm{I}_{\mathbf{E}} = \mathrm{tr}\, \mathbf{E}, \quad \mathrm{II}_{\mathbf{E}} = \mathrm{tr}\, \mathbf{E}^2, \quad \mathrm{III}_{\mathbf{E}} = \mathrm{tr}\, \mathbf{E}^3, \tag{3.26}$$

or based on the right Cauchy-Green tensor *,

$$\mathrm{I}_{\mathbf{C}} = \mathrm{tr}\,\mathbf{C}, \quad \mathrm{II}_{\mathbf{C}} = \mathrm{tr}\,\mathbf{C}^2, \quad \mathrm{III}_{\mathbf{C}} = \mathrm{tr}\,\mathbf{C}^3. \tag{3.28}$$

Thus, the second Piola-Kirchhoff stress tensor is calculated from the derivative of the strain energy function with respect to $\mathbf{E}$ by

$$\tilde{\mathbf{T}} = \rho_{\mathrm{R}} \frac{\mathrm{d}\hat{\psi}(\mathrm{I}_{\mathbf{E}}, \mathrm{II}_{\mathbf{E}}, \mathrm{III}_{\mathbf{E}})}{\mathrm{d}\mathbf{E}}, \tag{3.29}$$

or based on the right Cauchy-Green strain

$$\tilde{\mathbf{T}} = 2\rho_{\mathrm{R}} \frac{\partial\hat{\bar{\psi}}(\mathrm{I}_{\mathbf{C}}, \mathrm{II}_{\mathbf{C}}, \mathrm{III}_{\mathbf{C}})}{\partial\mathbf{C}}. \tag{3.30}$$

Due to the construction of the constitutive model for small strains, the Green strain tensor $\mathbf{E}$ is considered. Applying the chain rule on Eq.(3.29) yields

$$\tilde{\mathbf{T}} = \rho_{\mathrm{R}} \left(\frac{\partial\hat{\psi}}{\partial \mathrm{I}_{\mathbf{E}}}\mathbf{I} + 2\frac{\partial\hat{\psi}}{\partial \mathrm{II}_{\mathbf{E}}}\mathbf{E} + 3\frac{\partial\hat{\psi}}{\partial \mathrm{III}_{\mathbf{E}}}\mathbf{E}^2 \right). \tag{3.31}$$

With regards to small strains, the stresses become equal, $\tilde{\mathbf{T}} \to \mathbf{T}$. Hence, the final stress can be written for the isotropic part like

$$\mathbf{T} = \Lambda \mathrm{I}_{\mathbf{E}}\mathbf{I} + 2\mu_T\mathbf{E}. \tag{3.32}$$

Regarding $\mathbf{T} = \mathcal{C}\mathbf{E}$, a fourth order elasticity tensor can be expressed by

$$\mathcal{C} = \Lambda\mathbf{I} \otimes \mathbf{I} + 2\mu_T\mathcal{I}, \tag{3.33}$$

for more details on this, see (Hartmann, 2003; Haupt, 2000). With the help of Sect. 3.2, it is possible to write

$$\begin{Bmatrix} T_{11} \\ T_{22} \\ T_{33} \\ T_{12} \\ T_{23} \\ T_{31} \end{Bmatrix} = \begin{bmatrix} \lambda + 2\mu_T & \Lambda & \Lambda & 0 & 0 & 0 \\ \Lambda & \Lambda + 2\mu_T & \Lambda & 0 & 0 & 0 \\ \Lambda & \Lambda & \Lambda + 2\mu_T & 0 & 0 & 0 \\ 0 & 0 & 0 & \mu_T & 0 & 0 \\ 0 & 0 & 0 & 0 & \mu_T & 0 \\ 0 & 0 & 0 & 0 & 0 & \mu_T \end{bmatrix} \begin{Bmatrix} \varepsilon_{11} \\ \varepsilon_{22} \\ \varepsilon_{33} \\ \gamma_{12} \\ \gamma_{23} \\ \gamma_{31} \end{Bmatrix}. \tag{3.34}$$

In this case, Λ and μ_T demonstrate the constants depending on the Young's modulus E and the Poisson's number ν by

$$\Lambda = \frac{\nu E}{(1+\nu)(1-2\nu)}, \qquad \mu_T = \frac{E}{2(1+\nu)}. \tag{3.35}$$

*It should be noted that invariants can also be presented as

$$\mathrm{I}_{\mathbf{C}} = \mathrm{tr}\,\mathbf{C}, \quad \mathrm{II}_{\mathbf{C}} = \frac{1}{2}[(\mathrm{tr}\,\mathbf{C})^2 - (\mathrm{tr}\,\mathbf{C}^2)], \quad \mathrm{III}_{\mathbf{C}} = det\mathbf{C} = J^2. \tag{3.27}$$

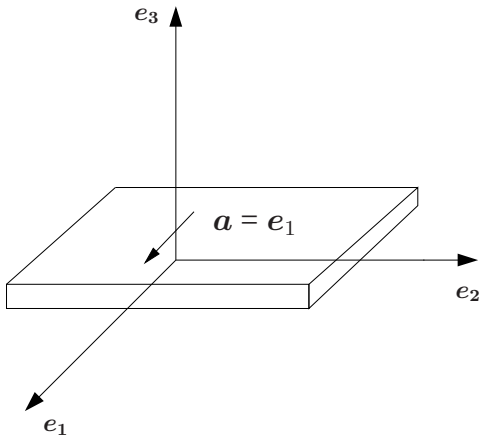

Figure 3.1: Schematic representation of fiber orientation in the transversal isotropic material

3.3.2 Transverse Isotropy

The mechanics of fiber-reinforced composites are based on the concept of anisotropic materials, in which the response of the material relies on the fiber direction. The most simple anisotropic material has one preferred direction. These materials are with physical properties that are symmetric about an axis. This type of material is known as transverse isotropic. This section addresses the modeling of laminates using one fiber direction.

A considerable amount of studies has been directed towards transversal isotropic materials. Linear elasticity is assumed for transverse isotropy laminates, see for example, (Fiolka, 2008; Spencer, 1971; Weiss et al., 1996b). Other works are, for example (Altenbach and Altenbach, 2004; Spencer, 1984). There are also publications focusing on the aspect of deformations, see for instance, (Aboudi, 2013; Aboudi et al., 2012; Agarwal et al., 2006; Gibson, 2011; Parton and Kudryavtsev, 1993; Reddy, 2003). There is also a new area of applications of transverse isotropic, in the field of biomechanics, due to the fact that several soft tissues show anisotropic behavior, (Itskov and Aksel, 2004; Schröder and Neff, 2003; Schröder et al., 2005; Weiss et al., 1996a).

Transversal isotropic laminates are characterized by a preferred direction, see Fig. 3.1. Constitutive equations for transversal isotropy of an elastic material are modeled using a strain-energy function depending on the Green strain tensor and a structural tensor $\mathbf{M} = \boldsymbol{a} \otimes \boldsymbol{a}$, where $\boldsymbol{a}(\boldsymbol{X})$ defines the fiber orientation with the properties $\|\boldsymbol{a}\| = 1$,

$$\tilde{\mathbf{T}} = \rho_{\mathrm{R}} \frac{\partial \psi(\mathbf{E}, \mathbf{M})}{\partial \mathbf{E}}, \tag{3.36}$$

or a strain-energy function can be written based on the right Cauchy-Green tensor $\mathbf{C} = \mathbf{F}^{\mathrm{T}}\mathbf{F}$ as

$$\tilde{\mathbf{T}} = 2\rho_{\mathrm{R}} \frac{\partial \overline{\psi}(\mathbf{C}, \mathbf{M})}{\partial \mathbf{C}}. \tag{3.37}$$

Regarding the structural tensor $\mathbf{M}$, some properties have to be mentioned:

$$\mathbf{M} = \mathbf{M}^T \tag{3.38}$$

$$\mathbf{M} = \mathbf{M}^2 = \mathbf{M}^3 = \ldots, \tag{3.39}$$

$$\det \mathbf{M} = 0, \tag{3.40}$$

$$\operatorname{adj} \mathbf{M} = \operatorname{cof} \mathbf{M} = 0, \tag{3.41}$$

where adj is the adjoint of a tensor field

$$\operatorname{adj}(\bullet) = \big(\det(\bullet)\big)(\bullet)^{-1} = \big(\operatorname{cof}(\bullet)\big)^{\mathrm{T}}. \tag{3.42}$$

According to (Itskov, 2007), the strain energy function can be expressed as a function of traces of the following tensors

$$\mathbf{E}, \quad \mathbf{E}^2, \quad \mathbf{E}^3, \quad \mathbf{M}, \quad \mathbf{M}^2, \quad \mathbf{M}^3, \quad \mathbf{E}\mathbf{M}, \quad \mathbf{E}^2\mathbf{M}, \quad \mathbf{E}\mathbf{M}^2, \quad \mathbf{E}^2\mathbf{M}^2. \tag{3.43}$$

i.e.

$$\operatorname{tr}(\mathbf{E}), \quad \operatorname{tr}(\mathbf{E}^2), \quad \operatorname{tr}(\mathbf{E}^3), \quad \operatorname{tr}(\mathbf{M}), \quad \operatorname{tr}(\mathbf{M}^2), \quad \operatorname{tr}(\mathbf{M}^3), \quad \operatorname{tr}(\mathbf{E}\mathbf{M}), \quad \operatorname{tr}(\mathbf{E}^2\mathbf{M}),$$

$$\operatorname{tr}(\mathbf{E}\mathbf{M}^2), \quad \operatorname{tr}(\mathbf{E}^2\mathbf{M}^2). \tag{3.44}$$

Since $\boldsymbol{a}$ is a unit vector*

$$\operatorname{tr} \mathbf{M} = \operatorname{tr}(\boldsymbol{a} \otimes \boldsymbol{a}) = \boldsymbol{a} \cdot \boldsymbol{a} = 1, \tag{3.45}$$

$$\operatorname{tr} \mathbf{M} = \operatorname{tr} \mathbf{M}^2 = \operatorname{tr} \mathbf{M}^3 = 1, \tag{3.46}$$

$$\operatorname{tr}(\mathbf{E}\mathbf{M}^2) = \mathbf{E} \cdot \mathbf{M}^2 = \mathbf{E} \cdot \mathbf{M}, \tag{3.47}$$

$$\operatorname{tr}(\mathbf{E}^2\mathbf{M}^2) = \mathbf{E}^2 \cdot \mathbf{M}^2 = \mathbf{E}^2 \cdot \mathbf{M}, \tag{3.48}$$

the set of invariants reduce to

$$\mathrm{I}_{\mathbf{E}} = \operatorname{tr} \mathbf{E}, \quad \mathrm{II}_{\mathbf{E}} = \operatorname{tr} \mathbf{E}^2, \quad \mathrm{III}_{\mathbf{E}} = \operatorname{tr} \mathbf{E}^3, \quad \mathrm{IV}_{\mathbf{E}} = \operatorname{tr}(\mathbf{E}\mathbf{M}) = \mathbf{E} \cdot \mathbf{M},$$

$$\mathrm{V}_{\mathbf{E}} = \operatorname{tr}(\mathbf{E}^2\mathbf{M}) = \mathbf{E}^2 \cdot \mathbf{M}. \tag{3.49}$$

Thus, a set of five invariants $\mathrm{I}_{\mathbf{E}}, \mathrm{II}_{\mathbf{E}}, \mathrm{III}_{\mathbf{E}}, \mathrm{IV}_{\mathbf{E}}$ and $\mathrm{V}_{\mathbf{E}}$ is required, for more details see also (Itskov, 2007; Spencer, 1971, 1984). The invariants can be also written based on the right Cauchy-Green tensor,

$$\mathrm{I}_{\mathbf{C}} = \operatorname{tr} \mathbf{C}, \quad \mathrm{II}_{\mathbf{C}} = \operatorname{tr} \mathbf{C}^2, \quad \mathrm{III}_{\mathbf{C}} = \operatorname{tr} \mathbf{C}^3, \quad \mathrm{IV}_{\mathbf{C}} = \operatorname{tr}(\mathbf{C}\mathbf{M}) = \mathbf{C} \cdot \mathbf{M},$$

$$\mathrm{V}_{\mathbf{C}} = \operatorname{tr}(\mathbf{C}^2\mathbf{M}) = \mathbf{C}^2 \cdot \mathbf{M}. \tag{3.50}$$

*Scalar product or dot product is defined by $\boldsymbol{a} \cdot \boldsymbol{b} = |\boldsymbol{a}||\boldsymbol{b}| cos\theta$ where θ, is the angle between the vectors $\boldsymbol{a}$ and $\boldsymbol{b}$.

Thus, the second Piola-Kirchhoff stress tensor reads

$$\tilde{\mathbf{T}} = 2\rho_{\mathrm{R}} \frac{\partial \hat{\overline{\psi}}(\mathrm{I}_{\mathbf{C}}, \mathrm{II}_{\mathbf{C}}, \mathrm{III}_{\mathbf{C}}, \mathrm{IV}_{\mathbf{C}}, \mathrm{V}_{\mathbf{C}})}{\partial \mathbf{C}}, \tag{3.51}$$

or based on $\mathbf{E}$

$$\tilde{\mathbf{T}} = \rho_{\mathrm{R}} \frac{\partial \hat{\psi}(\mathrm{I}_{\mathbf{E}}, \mathrm{II}_{\mathbf{E}}, \mathrm{III}_{\mathbf{E}}, \mathrm{IV}_{\mathbf{E}}, \mathrm{V}_{\mathbf{E}})}{\partial \mathbf{E}}. \tag{3.52}$$

The invariants of the Green strain and the right Cauchy-Green tensors are connected to each other, and they can be represented by

$$\mathrm{I}_{\mathbf{C}} = 2\mathrm{I}_{\mathbf{E}} + 3, \quad \mathrm{II}_{\mathbf{C}} = 4\mathrm{II}_{\mathbf{E}} + 4\mathrm{I}_{\mathbf{E}} + 3, \quad \mathrm{III}_{\mathbf{C}} = 8\mathrm{III}_{\mathbf{E}} + 8\mathrm{II}_{\mathbf{E}} + 6\mathrm{I}_{\mathbf{E}} + 3, \quad \mathrm{IV}_{\mathbf{C}} = 2\mathrm{IV}_{\mathbf{E}} + 1,$$

$$\mathrm{V}_{\mathbf{C}} = 4\mathrm{V}_{\mathbf{E}} + 4\mathrm{IV}_{\mathbf{E}} + 1, \tag{3.53}$$

or vice versa

$$\mathrm{I}_{\mathbf{E}} = \frac{1}{2}(\mathrm{I}_{\mathbf{C}} - 3), \quad \mathrm{II}_{\mathbf{E}} = \frac{1}{4}(\mathrm{II}_{\mathbf{C}} - 2\mathrm{I}_{\mathbf{C}} + 3), \quad \mathrm{III}_{\mathbf{E}} = \frac{1}{8}(\mathrm{III}_{\mathbf{C}} - 2\mathrm{II}_{\mathbf{C}} + \mathrm{I}_{\mathbf{C}}), \quad \mathrm{IV}_{\mathbf{E}} = \frac{1}{2}(\mathrm{IV}_{\mathbf{C}} - 1),$$

$$\mathrm{V}_{\mathbf{E}} = \frac{1}{4}(\mathrm{V}_{\mathbf{C}} - 2\mathrm{IV}_{\mathbf{C}} + 1). \tag{3.54}$$

Since the constitutive model is formulated for small strains, later on the Green strain tensor $\mathbf{E}$ is considered. Applying the chain rule on Eq.(3.52) leads to

$$\tilde{\mathbf{T}} = \rho_{\mathrm{R}} \left(\frac{\partial \hat{\psi}}{\partial \mathrm{I}_{\mathbf{E}}} \mathbf{I} + 2\frac{\partial \hat{\psi}}{\partial \mathrm{II}_{\mathbf{E}}} \mathbf{E} + 3\frac{\partial \hat{\psi}}{\partial \mathrm{III}_{\mathbf{E}}} \mathbf{E}^2 + \frac{\partial \hat{\psi}}{\partial \mathrm{IV}_{\mathbf{E}}} \mathbf{M} + \frac{\partial \hat{\psi}}{\partial \mathrm{V}_{\mathbf{E}}} (\mathbf{EM} + \mathbf{ME}) \right). \tag{3.55}$$

We take a strain energy function which quadratically depends on the strain tensor $\mathbf{E}$

$$\psi(\mathbf{E}, \mathbf{M}) = \frac{\Lambda}{2}\mathrm{I}_{\mathbf{E}}^2 + \mu_T \mathrm{II}_{\mathbf{E}} + \alpha \mathrm{I}_{\mathbf{E}} \mathrm{IV}_{\mathbf{E}} + 2(\mu_L - \mu_T)\mathrm{V}_{\mathbf{E}} + \frac{\beta}{2}\mathrm{IV}_{\mathbf{E}}^2. \tag{3.56}$$

Then, $\mathbf{T}$ depends linearly on the strain state $\mathbf{E}$, see (Fiolka, 2008; Spencer, 1984). In the case of small strains, the stresses become equal, $\tilde{\mathbf{T}} \to \mathbf{T}$, since the stresses have the tendency to become equal for very small strains. With respect to Eq.(3.52), the final stress can be expressed as

$$\mathbf{T} = \rho_{\mathrm{R}} \left((\Lambda \mathrm{I}_{\mathbf{E}} + \alpha \mathrm{IV}_{\mathbf{E}})\mathbf{I} + 2\mu_T \mathbf{E} + (\alpha \mathrm{I}_{\mathbf{E}} + \beta \mathrm{IV}_{\mathbf{E}})\mathbf{M} + 2(\mu_L - \mu_T)(\mathbf{EM} + \mathbf{ME}) \right). \tag{3.57}$$

The product of density in the reference configuration with the material parameters is usually not visible in the final version, so it is abbreviated by,

$$\Lambda \leftarrow \rho_{\mathrm{R}}\Lambda, \quad \mu_T \leftarrow \rho_{\mathrm{R}}\mu_T, \quad \mu_L \leftarrow \rho_{\mathrm{R}}\mu_L, \quad \alpha \leftarrow \rho_{\mathrm{R}}\alpha, \quad \beta \leftarrow \rho_{\mathrm{R}}\beta. \tag{3.58}$$

Thus,

$$\mathbf{T} = \mathcal{C}\mathbf{E} \tag{3.59}$$

where $\mathcal{C}$ can be written as

$$\mathcal{C} = \Lambda \mathbf{I} \otimes \mathbf{I} + 2\mu_T \mathcal{I} + \alpha[\mathbf{I} \otimes \mathbf{M} + \mathbf{M} \otimes \mathbf{I}] + \beta \mathbf{M} \otimes \mathbf{M} + 2(\mu_L - \mu_T)[\mathbf{I} \otimes \mathbf{M} + \mathbf{M} \otimes \mathbf{I}]^{T_{23}}. \quad (3.60)$$

In the case of transverse isotropy, fibers are directed in one direction. For example, the structural tensor can be expressed using $\boldsymbol{a} = \boldsymbol{e}_1$ which leads to $\mathbf{M} = \boldsymbol{a} \otimes \boldsymbol{a} = \boldsymbol{e}_1 \otimes \boldsymbol{e}_1$. Using matrix representation, $\mathbf{C}$ can be shown as,

$$\begin{Bmatrix} T_{11} \\ T_{22} \\ T_{33} \\ T_{12} \\ T_{23} \\ T_{31} \end{Bmatrix} = \begin{bmatrix} \Lambda + 2\alpha + 2\mu_T + 4(\mu_L - \mu_T) + \beta & \Lambda + \alpha & \Lambda + \alpha & 0 & 0 & 0 \\ \Lambda + \alpha & \Lambda + 2\mu_T & \Lambda & 0 & 0 & 0 \\ \Lambda + \alpha & \Lambda & \Lambda + 2\mu_T & 0 & 0 & 0 \\ 0 & 0 & 0 & \mu_L & 0 & 0 \\ 0 & 0 & 0 & 0 & \mu_T & 0 \\ 0 & 0 & 0 & 0 & 0 & \mu_L \end{bmatrix} \begin{Bmatrix} \varepsilon_{11} \\ \varepsilon_{22} \\ \varepsilon_{33} \\ \gamma_{12} \\ \gamma_{23} \\ \gamma_{31} \end{Bmatrix}, \quad (3.61)$$

which can also be seen in the literature as

$$\begin{Bmatrix} T_{11} \\ T_{22} \\ T_{33} \\ T_{12} \\ T_{23} \\ T_{31} \end{Bmatrix} = \begin{bmatrix} C_{11} & C_{12} & C_{12} & 0 & 0 & 0 \\ C_{12} & C_{22} & C_{23} & 0 & 0 & 0 \\ C_{12} & C_{23} & C_{22} & 0 & 0 & 0 \\ 0 & 0 & 0 & C_{66} & 0 & 0 \\ 0 & 0 & 0 & 0 & \frac{C_{22}-C_{23}}{2} & 0 \\ 0 & 0 & 0 & 0 & 0 & C_{66} \end{bmatrix} \begin{Bmatrix} \varepsilon_{11} \\ \varepsilon_{22} \\ \varepsilon_{33} \\ \gamma_{12} \\ \gamma_{23} \\ \gamma_{31} \end{Bmatrix}. \quad (3.62)$$

If $\mathbf{M} = \boldsymbol{a} \otimes \boldsymbol{a} = \boldsymbol{e}_2 \otimes \boldsymbol{e}_2$, it reads

$$\begin{Bmatrix} T_{11} \\ T_{22} \\ T_{33} \\ T_{12} \\ T_{23} \\ T_{31} \end{Bmatrix} = \begin{bmatrix} C_{22} & C_{12} & C_{23} & 0 & 0 & 0 \\ C_{12} & C_{11} & C_{12} & 0 & 0 & 0 \\ C_{23} & C_{12} & C_{22} & 0 & 0 & 0 \\ 0 & 0 & 0 & C_{66} & 0 & 0 \\ 0 & 0 & 0 & 0 & C_{66} & 0 \\ 0 & 0 & 0 & 0 & 0 & \frac{C_{22}-C_{23}}{2} \end{bmatrix} \begin{Bmatrix} \varepsilon_{11} \\ \varepsilon_{22} \\ \varepsilon_{33} \\ \gamma_{12} \\ \gamma_{23} \\ \gamma_{31} \end{Bmatrix}, \quad (3.63)$$

and if $\mathbf{M} = \boldsymbol{a} \otimes \boldsymbol{a} = (\frac{\boldsymbol{e_1}}{\sqrt{2}} + \frac{\boldsymbol{e_2}}{\sqrt{2}}) \otimes (\frac{\boldsymbol{e_1}}{\sqrt{2}} + \frac{\boldsymbol{e_2}}{\sqrt{2}})$, matrix $\mathbf{C}$ yields

$$\mathbf{C} = \begin{bmatrix} \frac{C_{11}+2C_{12}+C_{22}+4C_{66}}{4} & \frac{C_{11}+2C_{12}+C_{22}-4C_{66}}{4} & \frac{C_{12}+C_{23}}{2} & \frac{C_{11}-C_{22}}{4} & 0 & 0 \\ \frac{C_{11}+2C_{12}+C_{22}-4C_{66}}{4} & \frac{C_{11}+2C_{12}+C_{22}+4C_{66}}{4} & \frac{C_{12}+C_{23}}{2} & \frac{C_{11}-C_{22}}{4} & 0 & 0 \\ \frac{C_{12}+C_{23}}{2} & \frac{C_{12}+C_{23}}{2} & C_{22} & \frac{C_{12}-C_{23}}{2} & 0 & 0 \\ \frac{C_{11}-C_{22}}{4} & \frac{C_{11}-C_{22}}{4} & \frac{C_{12}-C_{23}}{2} & \frac{C_{11}-2C_{12}+C_{22}}{4} & 0 & 0 \\ 0 & 0 & 0 & 0 & \frac{C_{22}-C_{23}+2C_{66}}{4} & \frac{C_{23}-C_{22}+2C_{66}}{4} \\ 0 & 0 & 0 & 0 & \frac{C_{23}-C_{22}+2C_{66}}{4} & \frac{C_{22}-C_{23}+2C_{66}}{4} \end{bmatrix}. \quad (3.64)$$

3.3.3 Orthotropy

The constitutive equations for materials reinforced with two families of fibers are discussed in this section. It is possible to construct three structural tensors $\mathbf{M}_1$, $\mathbf{M}_2$, and $\mathbf{M}_3$ in three different directions, including the information of anisotropy. Thus, structural tensors can be represented as

$$\mathbf{M}_1 = \boldsymbol{a} \otimes \boldsymbol{a}, \quad \mathbf{M}_2 = \boldsymbol{b} \otimes \boldsymbol{b}, \quad \mathbf{M}_3 = \boldsymbol{c} \otimes \boldsymbol{c} \tag{3.65}$$

and the strain energy function is given by

$$\psi(\mathbf{C}, \mathbf{M}_1, \mathbf{M}_2, \mathbf{M}_3) = \psi(\mathbf{Q}\mathbf{C}\mathbf{Q}^T, \mathbf{Q}\mathbf{M}_1\mathbf{Q}^T, \mathbf{Q}\mathbf{M}_2\mathbf{Q}^T, \mathbf{Q}\mathbf{M}_3\mathbf{Q}^T), \tag{3.66}$$

where it must be fulfilled for all symmetric tensors $\mathbf{C}$ and orthogonal tensors $\mathbf{Q}$. On the other hand, the argument tensors are reducible due to the orthonormal basis $\boldsymbol{a}$, $\boldsymbol{b}$, and $\boldsymbol{c}$, see (Schröder, 1996). Considering the orthonormality condition,

$$\sum_{i=1}^{3}(\mathbf{M}_i\mathbf{C} + \mathbf{C}\mathbf{M}_i) = \mathbf{M}_1\mathbf{C} + \mathbf{M}_2\mathbf{C} + \mathbf{M}_3\mathbf{C} + \mathbf{C}\mathbf{M}_1 + \mathbf{C}\mathbf{M}_2 + \mathbf{C}\mathbf{M}_3 \tag{3.67}$$

$$= (\mathbf{M}_1 + \mathbf{M}_2 + \mathbf{M}_3)\mathbf{C} + \mathbf{C}(\mathbf{M}_1 + \mathbf{M}_2 + \mathbf{M}_3) = 2\mathbf{C}, \tag{3.68}$$

and, accordingly,

$$\sum_{i=1}^{3} \operatorname{tr}(\mathbf{M}_i\mathbf{C}) = \operatorname{tr}(\mathbf{M}_1\mathbf{C}) + \operatorname{tr}(\mathbf{M}_2\mathbf{C}) + \operatorname{tr}(\mathbf{M}_3\mathbf{C}) = \operatorname{tr}(\mathbf{C}(\mathbf{M}_1 + \mathbf{M}_2 + \mathbf{M}_3)) = \operatorname{tr}(\mathbf{C}\mathbf{I}) = \operatorname{tr}\mathbf{C},$$

$$\operatorname{tr}(\mathbf{M}_3\mathbf{C}) = \operatorname{tr}\mathbf{C} - \operatorname{tr}(\mathbf{M}_2\mathbf{C}) - \operatorname{tr}(\mathbf{M}_1\mathbf{C}), \tag{3.69}$$

the strain energy function depends on

$$\psi = \psi(\mathbf{C}, \mathbf{M}_1, \mathbf{M}_2), \tag{3.70}$$

see (Holzapfel, 2008; Schröder, 1996; Spencer, 1984). According to (Itskov, 2007), the strain energy function can be expressed as a function of traces of the tensors,

$$\begin{aligned} &\mathbf{E}, \quad \mathbf{E}^2, \quad \mathbf{E}^3, \quad \mathbf{M}_1, \quad \mathbf{M}_1^2, \quad \mathbf{M}_1^3, \quad \mathbf{M}_2, \quad \mathbf{M}_2^2, \quad \mathbf{M}_2^3, \quad \mathbf{E}\mathbf{M}_1, \quad \mathbf{E}\mathbf{M}_2, \\ &\mathbf{M}_1\mathbf{M}_2, \quad \mathbf{M}_1^2\mathbf{M}_2, \quad \mathbf{E}^2\mathbf{M}_1, \quad \mathbf{E}^2\mathbf{M}_2, \quad \mathbf{E}\mathbf{M}_1^2, \quad \mathbf{E}\mathbf{M}_2^2, \quad \mathbf{E}^2\mathbf{M}_1^2, \quad \mathbf{E}^2\mathbf{M}_2^2. \end{aligned} \tag{3.71}$$

Since $\boldsymbol{a}$ and $\boldsymbol{b}$ are unit vectors, we have the properties,

$$\operatorname{tr}\mathbf{M}_1 = \operatorname{tr}(\boldsymbol{a} \otimes \boldsymbol{a}) = \boldsymbol{a} \cdot \boldsymbol{a} = 1 \tag{3.72}$$

$$\operatorname{tr}\mathbf{M}_1 = \operatorname{tr}\mathbf{M}_1^2 = \operatorname{tr}\mathbf{M}_1^3 = 1 \tag{3.73}$$

$$\operatorname{tr}\mathbf{M}_2 = \operatorname{tr}(\boldsymbol{b} \otimes \boldsymbol{b}) = \boldsymbol{b} \cdot \boldsymbol{b} = 1 \tag{3.74}$$

$$\operatorname{tr}\mathbf{M}_2 = \operatorname{tr}\mathbf{M}_2^2 = \operatorname{tr}\mathbf{M}_2^3 = 1 \tag{3.75}$$

$$\operatorname{tr}(\mathbf{M}_1^2\mathbf{M}_2) = \operatorname{tr}(\mathbf{M}_1\mathbf{M}_2) = 0 \tag{3.76}$$

$$\operatorname{tr}(\mathbf{E}\mathbf{M}_1^2) = \mathbf{E} \cdot \mathbf{M}_1^2 = \mathbf{E} \cdot \mathbf{M}_1 \tag{3.77}$$

$$\operatorname{tr}(\mathbf{E}\mathbf{M}_2^2) = \mathbf{E} \cdot \mathbf{M}_2^2 = \mathbf{E} \cdot \mathbf{M}_2 \tag{3.78}$$

$$\operatorname{tr}(\mathbf{E}^2\mathbf{M}_1^2) = \mathbf{E}^2 \cdot \mathbf{M}_1^2 = \mathbf{E}^2 \cdot \mathbf{M}_1 \tag{3.79}$$

$$\operatorname{tr}(\mathbf{E}^2\mathbf{M}_2^2) = \mathbf{E}^2 \cdot \mathbf{M}_2^2 = \mathbf{E}^2 \cdot \mathbf{M}_2 \tag{3.80}$$

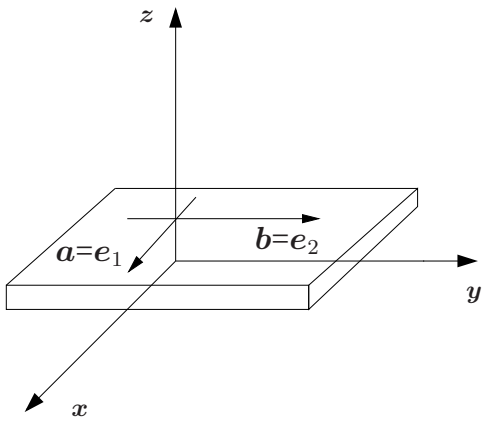

Figure 3.2: Schematic representation of fiber orientations in the orthotropic material

and the set of invariants reduces to

$$\mathrm{I}_{\mathbf{E}} = \operatorname{tr}\mathbf{E}, \quad \mathrm{II}_{\mathbf{E}} = \operatorname{tr}\mathbf{E}^2, \quad \mathrm{III}_{\mathbf{E}} = \operatorname{tr}\mathbf{E}^3, \quad \mathrm{IV}_{\mathbf{E}} = \operatorname{tr}(\mathbf{E}\mathbf{M}_1) = \mathbf{E}\cdot\mathbf{M}_1,$$

$$\mathrm{V}_{\mathbf{E}} = \operatorname{tr}(\mathbf{E}\mathbf{M}_2) = \mathbf{E}\cdot\mathbf{M}_2, \quad \mathrm{VI}_{\mathbf{E}} = \operatorname{tr}(\mathbf{E}^2\mathbf{M}_1) = \mathbf{E}^2\cdot\mathbf{M}_1, \quad \mathrm{VII}_{\mathbf{E}} = \operatorname{tr}(\mathbf{E}\mathbf{M}_2) = \mathbf{E}^2\cdot\mathbf{M}_2,$$

$$\mathrm{VIII}_{\mathbf{E}} = \operatorname{tr}(\mathbf{M}_1\mathbf{M}_2) = \mathbf{M}_1\cdot\mathbf{M}_2 = (\boldsymbol{a}\otimes\boldsymbol{a})\cdot(\boldsymbol{b}\otimes\boldsymbol{b}) = (\boldsymbol{a}\cdot\boldsymbol{b})^2 = 0. \tag{3.81}$$

The invariants can also be expressed based on the right Cauchy-Green tensor:

$$\mathrm{I}_{\mathbf{C}} = \operatorname{tr}\mathbf{C}, \quad \mathrm{II}_{\mathbf{C}} = \operatorname{tr}\mathbf{C}^2, \quad \mathrm{III}_{\mathbf{C}} = \operatorname{tr}\mathbf{C}^3, \quad \mathrm{IV}_{\mathbf{C}} = \operatorname{tr}(\mathbf{C}\mathbf{M}_1) = \mathbf{C}\cdot\mathbf{M}_1,$$

$$\mathrm{V}_{\mathbf{C}} = \operatorname{tr}(\mathbf{C}\mathbf{M}_2) = \mathbf{C}\cdot\mathbf{M}_2, \quad \mathrm{VI}_{\mathbf{C}} = \operatorname{tr}(\mathbf{C}^2\mathbf{M}_1) = \mathbf{C}^2\cdot\mathbf{M}_1, \quad \mathrm{VII}_{\mathbf{C}} = \operatorname{tr}(\mathbf{C}^2\mathbf{M}_2) = \mathbf{C}^2\cdot\mathbf{M}_2,$$

$$\mathrm{VIII}_{\mathbf{E}} = \operatorname{tr}(\mathbf{M}_1\mathbf{M}_2) = \mathbf{M}_1\cdot\mathbf{M}_2 = 0. \tag{3.82}$$

In the following, the model of orthotropy for linear elasticity and for a small strain theory will be introduced. The second Piola-Kirchhoff stress tensor $\tilde{\mathbf{T}}$ depends on the Green strain tensor and the two structural tensors

$$\tilde{\mathbf{T}} = \rho_{\mathrm{R}}\frac{\partial\psi(\mathbf{E},\mathbf{M}_1,\mathbf{M}_2)}{\partial\mathbf{E}}, \tag{3.83}$$

or alternatively, with the right Cauchy-Green tensor

$$\tilde{\mathbf{T}} = 2\rho_{\mathrm{R}}\frac{\partial\overline{\psi}(\mathbf{C},\mathbf{M}_1,\mathbf{M}_2)}{\partial\mathbf{C}}. \tag{3.84}$$

Using the invariants in Eq.(3.81), and since we are interested in a theory of small displacements, the most general quadratic form can be obtained for the strain energy function which is quadratic in $\mathbf{E}$, see also (Spencer, 1984). Then, $\mathbf{T}$ depends linearly on the strain state $\mathbf{E}$.

The invariants of the Green strain and the right Cauchy-Green tensor are related, see also Appendix 8.1,

$$\mathrm{I}_{\mathbf{C}} = 2\mathrm{I}_{\mathbf{E}} + 3, \quad \mathrm{II}_{\mathbf{C}} = 4\mathrm{II}_{\mathbf{E}} + 4\mathrm{I}_{\mathbf{E}} + 3, \quad \mathrm{III}_{\mathbf{C}} = 8\mathrm{III}_{\mathbf{E}} + 12\mathrm{II}_{\mathbf{E}} + 6\mathrm{I}_{\mathbf{E}} + 3, \quad \mathrm{IV}_{\mathbf{C}} = 2\mathrm{IV}_{\mathbf{E}} + 1,$$

$$\mathrm{V}_{\mathbf{C}} = 4\mathrm{V}_{\mathbf{E}} + 4\mathrm{IV}_{\mathbf{E}} + 1, \quad \mathrm{VI}_{\mathbf{C}} = 2\mathrm{VI}_{\mathbf{E}} + 1, \quad \mathrm{VII}_{\mathbf{C}} = 4\mathrm{VII}_{\mathbf{E}} + 4\mathrm{VI}_{\mathbf{E}} + 1 \tag{3.85}$$

or vice versa

$$\mathrm{I}_{\mathbf{E}} = \frac{1}{2}(\mathrm{I}_{\mathbf{C}}-3), \quad \mathrm{II}_{\mathbf{E}} = \frac{1}{4}(\mathrm{II}_{\mathbf{C}}-2\mathrm{I}_{\mathbf{C}}+3), \quad \mathrm{III}_{\mathbf{E}} = \frac{1}{8}(\mathrm{III}_{\mathbf{C}}-3\mathrm{II}_{\mathbf{C}}+3\mathrm{I}_{\mathbf{C}}-3), \quad \mathrm{IV}_{\mathbf{E}} = \frac{1}{2}(\mathrm{IV}_{\mathbf{C}}-1),$$

$$\mathrm{V}_{\mathbf{E}} = \frac{1}{4}(\mathrm{V}_{\mathbf{C}} - 2\mathrm{IV}_{\mathbf{C}} + 1), \quad \mathrm{VI}_{\mathbf{E}} = \frac{1}{2}(\mathrm{VI}_{\mathbf{C}} - 1), \quad \mathrm{VII}_{\mathbf{E}} = \frac{1}{4}(\mathrm{VII}_{\mathbf{C}} - 2\mathrm{VI}_{\mathbf{C}} + 1). \tag{3.86}$$

The second Piola-Kirchhoff stress tensor $\tilde{\mathbf{T}}$ can be written as

$$\tilde{\mathbf{T}} = \rho_{\mathrm{R}} \frac{\partial \hat{\psi}(\mathrm{I}_{\mathbf{E}}, \mathrm{II}_{\mathbf{E}}, \mathrm{III}_{\mathbf{E}}, \mathrm{IV}_{\mathbf{E}}, \mathrm{V}_{\mathbf{E}}, \mathrm{VI}_{\mathbf{E}}, \mathrm{VII}_{\mathbf{E}})}{\partial \mathbf{E}}, \tag{3.87}$$

or the strain-energy function can be written based on right Cauchy-Green tensor $\mathbf{C}$ as

$$\tilde{\mathbf{T}} = 2\rho_{\mathrm{R}} \frac{\partial \hat{\overline{\psi}}(\mathrm{I}_{\mathbf{C}}, \mathrm{II}_{\mathbf{C}}, \mathrm{III}_{\mathbf{C}}, \mathrm{IV}_{\mathbf{C}}, \mathrm{V}_{\mathbf{C}}, \mathrm{VI}_{\mathbf{C}}, \mathrm{VII}_{\mathbf{C}})}{\partial \mathbf{C}}. \tag{3.88}$$

We draw on the formulation using the Green strain tensor $\mathbf{E}$ for orthotropy materials, because we are again interested in formulating a constitutive model for small strains. Applying the chain rule on Eq.(3.87) yields, see also Appendix 8.2,

$$\tilde{\mathbf{T}} = \rho_{\mathrm{R}} \left(\frac{\partial \hat{\psi}}{\partial \mathrm{I}_{\mathbf{E}}}\mathbf{I} + 2\frac{\partial \hat{\psi}}{\partial \mathrm{II}_{\mathbf{E}}}\mathbf{E} + 3\frac{\partial \hat{\psi}}{\partial \mathrm{III}_{\mathbf{E}}}\mathbf{E}^2 + \frac{\partial \hat{\psi}}{\partial \mathrm{IV}_{\mathbf{E}}}\mathbf{M}_1 + \frac{\partial \hat{\psi}}{\partial \mathrm{V}_{\mathbf{E}}}(\mathbf{E}\mathbf{M}_1 + \mathbf{M}_1\mathbf{E}) + \right.$$
$$\left. \frac{\partial \hat{\psi}}{\partial \mathrm{VI}_{\mathbf{E}}}\mathbf{M}_2 + \frac{\partial \hat{\psi}}{\partial \mathrm{VII}_{\mathbf{E}}}(\mathbf{E}\mathbf{M}_2 + \mathbf{M}_2\mathbf{E}) \right). \tag{3.89}$$

Since we are interested in small strain theory, the strain energy function must depend quadratically on the strain tensor

$$\psi(\mathbf{E}, \mathbf{M}_1, \mathbf{M}_2) = \frac{\Lambda}{2}(\operatorname{tr}\mathbf{E})^2 + \mu \operatorname{tr}\mathbf{E}^2 + (\alpha_1 \mathbf{E}\cdot\mathbf{M}_1 + \alpha_2 \mathbf{E}\cdot\mathbf{M}_2)\operatorname{tr}\mathbf{E} + 2\mu_1 \mathbf{E}^2\cdot\mathbf{M}_1 +$$
$$2\mu_2 \mathbf{E}^2\cdot\mathbf{M}_2 + \frac{1}{2}\beta_1(\mathbf{E}\cdot\mathbf{M}_1)^2 + \frac{1}{2}\beta_2(\mathbf{E}\cdot\mathbf{M}_2)^2 + \beta_3(\mathbf{E}\cdot\mathbf{M}_1)(\mathbf{E}\cdot\mathbf{M}_2), \tag{3.90}$$

alternatively, this reads

$$\psi(\mathbf{E}, \mathbf{M}_1, \mathbf{M}_2) = \frac{\Lambda}{2}\mathrm{I}_{\mathbf{E}}^2 + \mu\mathrm{II}_{\mathbf{E}} + (\alpha_1\mathrm{IV}_{\mathbf{E}} + \alpha_2\mathrm{VI}_{\mathbf{E}})\mathrm{I}_{\mathbf{E}} + 2\mu_1\mathrm{V}_{\mathbf{E}} + 2\mu_2\mathrm{VII}_{\mathbf{E}} + \frac{1}{2}\beta_1\mathrm{IV}_{\mathbf{E}}^2$$
$$+ \frac{1}{2}\beta_2\mathrm{VI}_{\mathbf{E}}^2 + \beta_3\mathrm{IV}_{\mathbf{E}}\mathrm{VI}_{\mathbf{E}}. \tag{3.91}$$

The strain energy function can also be expressed in terms of $\mathbf{C}$ as

$$\psi(\mathbf{C}, \mathbf{M}_1, \mathbf{M}_2) = \frac{\Lambda}{8}(\mathrm{I}_{\mathbf{C}} - 3)^2 + \frac{\beta_3}{4}(\mathrm{IV}_{\mathbf{C}} - 1)(\mathrm{VI}_{\mathbf{C}} - 1) + \frac{\mu}{4}(\mathrm{II}_{\mathbf{C}} - 2\mathrm{I}_{\mathbf{C}} + 3)$$
$$+ \Big(\frac{\alpha_1}{2}(\mathrm{IV}_{\mathbf{C}} - 1) + \frac{\alpha_2}{4}(\mathrm{VI}_{\mathbf{C}} - 1)\Big)(\mathrm{I}_{\mathbf{C}} - 3) + \frac{\mu_1}{2}(\mathrm{V}_{\mathbf{C}} - 2\mathrm{IV}_{\mathbf{C}} + 1)$$
$$+ \frac{\mu_2}{2}(\mathrm{VII}_{\mathbf{C}} - 2\mathrm{VI}_{\mathbf{C}} + 1) + \frac{\beta_1}{8}(\mathrm{IV}_{\mathbf{C}} - 1)^2 + \frac{\beta_2}{8}(\mathrm{VI}_{\mathbf{C}} - 1)^2. \tag{3.92}$$

The final stress states using Eq.(3.87) can be obtained by applying the derivative in Eq.(3.89)

$$\mathbf{T} = \rho_{\mathrm{R}}\Bigg((\Lambda \mathrm{I}_{\mathbf{E}} + \alpha_1 \mathrm{IV}_{\mathbf{E}} + \alpha_2 \mathrm{VI}_{\mathbf{E}})\mathbf{I} + 2\mu\mathbf{E} + (\alpha_1 \mathrm{I}_{\mathbf{E}} + \beta_1 \mathrm{IV}_{\mathbf{E}} + \beta_3 \mathrm{VI}_{\mathbf{E}})\mathbf{M}_1 + 2\mu_1(\mathbf{E}\mathbf{M}_1 + \mathbf{M}_1\mathbf{E}) + 2\mu_2(\mathbf{E}\mathbf{M}_2 + \mathbf{M}_2\mathbf{E}) + (\alpha_2 \mathrm{I}_{\mathbf{E}} + \beta_2 \mathrm{VI}_{\mathbf{E}} + \beta_3 \mathrm{IV}_{\mathbf{E}})\mathbf{M}_2 \Bigg). \quad (3.93)$$

The relation can be expressed by the fourth order elasticity tensor $\mathcal{C}$

$$\mathbf{T} = \mathcal{C}\mathbf{E} \quad (3.94)$$

with

$$\mathcal{C} = \Lambda \mathbf{I}\otimes\mathbf{I} + \alpha_1\Big[\mathbf{I}\otimes\mathbf{M}_1 + \mathbf{M}_1\otimes\mathbf{I}\Big] + \alpha_2\Big[\mathbf{I}\otimes\mathbf{M}_2 + \mathbf{M}_2\otimes\mathbf{I}\Big] + 2\mu\mathcal{I} + \beta_1\mathbf{M}_1\otimes\mathbf{M}_1 + \beta_2\mathbf{M}_2\otimes\mathbf{M}_2 + \beta_3\Big[\mathbf{M}_1\otimes\mathbf{M}_2 + \mathbf{M}_2\otimes\mathbf{M}_1\Big] + 2\mu_1\Big[\mathbf{I}\otimes\mathbf{M}_1 + \mathbf{M}_1\otimes\mathbf{I}\Big]^{T_{23}} + 2\mu_2\Big[\mathbf{I}\otimes\mathbf{M}_2 + \mathbf{M}_2\otimes\mathbf{I}\Big]^{T_{23}}, \quad (3.95)$$

see also Appendix 8.3.

Using the *Voigt*-notation, which is discussed in Sect. 3.2, Eq.(3.94) can be expressed in matrix notation:

$$\begin{Bmatrix} T_{11} \\ T_{22} \\ T_{33} \\ T_{12} \\ T_{23} \\ T_{31} \end{Bmatrix} = \mathbf{C} \begin{Bmatrix} \varepsilon_{11} \\ \varepsilon_{22} \\ \varepsilon_{33} \\ \gamma_{12} \\ \gamma_{23} \\ \gamma_{31} \end{Bmatrix}. \quad (3.96)$$

If $\boldsymbol{a} = \boldsymbol{e}_1$ and $\boldsymbol{b} = \boldsymbol{e}_2$, $\mathbf{C}$ can for this case be represented using Eq.(3.95) as

$$\begin{bmatrix} \Lambda + 2\alpha_1 + \beta_1 + 2\mu + 4\mu_1 & \Lambda + \alpha_1 + \alpha_2 + \beta_3 & \Lambda + \alpha_1 & 0 & 0 & 0 \\ \Lambda + \alpha_1 + \alpha_2 + \beta_3 & \Lambda + 2\alpha_2 + \beta_2 + 2\mu + 4\mu_2 & \Lambda + \alpha_2 & 0 & 0 & 0 \\ \Lambda + \alpha_1 & \Lambda + \alpha_2 & \Lambda + 2\mu & 0 & 0 & 0 \\ 0 & 0 & 0 & \mu + \mu_2 & 0 & 0 \\ 0 & 0 & 0 & 0 & \mu + \mu_1 & 0 \\ 0 & 0 & 0 & 0 & 0 & \mu + \mu_1 + \mu_2 \end{bmatrix}. \quad (3.97)$$

Using Eq.(3.96) and Eq.(3.97), Eq.(3.94) can be expressed as

$$\begin{Bmatrix} T_{11} \\ T_{22} \\ T_{33} \\ T_{12} \\ T_{23} \\ T_{31} \end{Bmatrix} = \begin{bmatrix} C_{11} & C_{12} & C_{13} & 0 & 0 & 0 \\ C_{12} & C_{22} & C_{23} & 0 & 0 & 0 \\ C_{13} & C_{23} & C_{33} & 0 & 0 & 0 \\ 0 & 0 & 0 & C_{44} & 0 & 0 \\ 0 & 0 & 0 & 0 & C_{55} & 0 \\ 0 & 0 & 0 & 0 & 0 & C_{66} \end{bmatrix} \begin{Bmatrix} \varepsilon_{11} \\ \varepsilon_{22} \\ \varepsilon_{33} \\ \gamma_{12} \\ \gamma_{23} \\ \gamma_{31} \end{Bmatrix}. \quad (3.98)$$

The relation between the invariants of Eq.(3.97) and Eq.(3.98) can be written as

$$\mu_1 = C_{66} - C_{44} \tag{3.99}$$
$$\mu_2 = C_{66} - C_{55} \tag{3.100}$$
$$\mu = C_{55} + C_{44} - C_{66} \tag{3.101}$$
$$\Lambda = C_{33} + 2(C_{66} - C_{44} - C_{55}) \tag{3.102}$$
$$\alpha_1 = C_{13} - C_{33} - 2(C_{66} - C_{44} - C_{55}) \tag{3.103}$$
$$\alpha_2 = C_{23} - C_{33} - 2(C_{66} - C_{44} - C_{55}) \tag{3.104}$$
$$\beta_1 = C_{11} + C_{33} - 4C_{55} - 2C_{13} \tag{3.105}$$
$$\beta_2 = C_{22} + C_{33} - 4C_{44} - 2C_{23} \tag{3.106}$$
$$\beta_3 = C_{12} - C_{13} - C_{23} + C_{33} + 2(C_{66} - C_{44} - C_{55}) \tag{3.107}$$

The elasticity stiffness matrix which is presented in Eq.(3.97) can also be obtained using elastic constants such as Poisson's ratio, Young's modulus, and shear modulus. For this aim, we reverse Eq.(3.94) to

$$\mathbf{E} = \mathbf{ST}, \tag{3.108}$$

$\mathbf{S}$ is called the compliance matrix, and $\mathbf{C}$ is equal to $\mathbf{S}^{-1}$. Eq.(3.108) leads to

$$\begin{Bmatrix} \varepsilon_{11} \\ \varepsilon_{22} \\ \varepsilon_{33} \\ \gamma_{12} \\ \gamma_{23} \\ \gamma_{31} \end{Bmatrix} = \begin{bmatrix} S_{11} & S_{12} & S_{13} & 0 & 0 & 0 \\ S_{12} & S_{22} & S_{23} & 0 & 0 & 0 \\ S_{13} & S_{23} & S_{33} & 0 & 0 & 0 \\ 0 & 0 & 0 & S_{44} & 0 & 0 \\ 0 & 0 & 0 & 0 & S_{55} & 0 \\ 0 & 0 & 0 & 0 & 0 & S_{66} \end{bmatrix} \begin{Bmatrix} T_{11} \\ T_{22} \\ T_{33} \\ T_{12} \\ T_{23} \\ T_{31} \end{Bmatrix}, \tag{3.109}$$

where the relation between elastic coefficients of Eq.(3.98) and Eq.(3.109) can be shown as

$$\begin{aligned} C_{11} &= \frac{S_{22}S_{33} - S_{23}^2}{S}, & C_{12} &= \frac{S_{13}S_{23} - S_{12}S_{33}}{S}, & C_{13} &= \frac{S_{12}S_{23} - S_{13}S_{22}}{S}, \\ C_{22} &= \frac{S_{33}S_{11} - S_{13}^2}{S}, & C_{33} &= \frac{S_{11}S_{22} - S_{12}^2}{S}, & C_{23} &= \frac{S_{12}S_{13} - S_{23}S_{11}}{S}, \\ C_{44} &= \frac{1}{S_{44}}, & C_{55} &= \frac{1}{S_{55}}, & C_{66} &= \frac{1}{S_{66}}, \end{aligned} \tag{3.110}$$

with

$$S = S_{11}S_{22}S_{33} - S_{11}S_{23}^2 - S_{22}S_{13}^2 - S_{33}S_{12}^2 + 2S_{12}S_{23}S_{13}, \tag{3.111}$$

see (Reddy, 2003).

The extensional strain $\varepsilon_{11}^{(1)}$ in the material coordinate direction $\boldsymbol{e}_1$ due to the stress T_{11} in the same direction is $\frac{T_{11}}{E_1}$, where E_1 represents the Young's modulus of the material in $\boldsymbol{e}_1$ direction. The extensional strain $\varepsilon_{11}^{(2)}$ due to the stress T_{22} in the same direction $\boldsymbol{e}_2$ is $-\frac{T_{22}\nu_{21}}{E_2}$, where ν_{21} is the Poisson ratio

$$\nu_{21} = -\frac{\varepsilon_{11}}{\varepsilon_{22}} \tag{3.112}$$

and E_2 represents the Young's modulus of the material in $\boldsymbol{e}_2$ direction, see (Reddy, 2003). Similarly, T_{33} generates a strain $\varepsilon_{11}^{(3)}$ equal to $-\frac{T_{33}\nu_{31}}{E_3}$, where E_3 represents the Young's modulus of the material in $\boldsymbol{e}_3$ direction. The total strain ε_{11} due to the stresses in all directions is

$$\varepsilon_{11} = \varepsilon_{11}^{(1)} + \varepsilon_{11}^{(2)} + \varepsilon_{11}^{(3)} = \frac{T_{11}}{E_1} - \frac{T_{22}\nu_{21}}{E_2} - \frac{T_{33}\nu_{31}}{E_3}, \tag{3.113}$$

and similarly for ε_{22}

$$\varepsilon_{22} = -\frac{T_{11}\nu_{12}}{E_1} + \frac{T_{22}}{E_2} - \frac{T_{33}\nu_{32}}{E_3}, \tag{3.114}$$

and for ε_{33}

$$\varepsilon_{33} = -\frac{T_{11}\nu_{13}}{E_1} - \frac{T_{22}\nu_{23}}{E_2} + \frac{T_{33}}{E_3}. \tag{3.115}$$

Regarding the shear behavior for orthotropic material, it follows that

$$\gamma_{12} = \frac{T_{12}}{G_{12}}, \quad \gamma_{23} = \frac{T_{23}}{G_{23}}, \quad \gamma_{31} = \frac{T_{31}}{G_{31}}, \tag{3.116}$$

where G_{12}, G_{23}, and G_{31} are shear moduli in three different directions. Thus, Eq.(3.109) can be reformulated as

$$\begin{Bmatrix} \varepsilon_{11} \\ \varepsilon_{22} \\ \varepsilon_{33} \\ \varepsilon_{12} \\ \varepsilon_{23} \\ \varepsilon_{31} \end{Bmatrix} = \begin{bmatrix} \frac{1}{E_1} & -\frac{\nu_{21}}{E_2} & -\frac{\nu_{31}}{E_3} & 0 & 0 & 0 \\ -\frac{\nu_{12}}{E_1} & \frac{1}{E_2} & -\frac{\nu_{32}}{E_3} & 0 & 0 & 0 \\ -\frac{\nu_{13}}{E_1} & -\frac{\nu_{23}}{E_2} & \frac{1}{E_3} & 0 & 0 & 0 \\ 0 & 0 & 0 & \frac{1}{2G_{12}} & 0 & 0 \\ 0 & 0 & 0 & 0 & \frac{1}{2G_{23}} & 0 \\ 0 & 0 & 0 & 0 & 0 & \frac{1}{2G_{31}} \end{bmatrix} \begin{Bmatrix} T_{11} \\ T_{22} \\ T_{33} \\ T_{12} \\ T_{23} \\ T_{31} \end{Bmatrix}, \tag{3.117}$$

which can be written as

$$\begin{Bmatrix} \varepsilon_{11} \\ \varepsilon_{22} \\ \varepsilon_{33} \\ \gamma_{12} \\ \gamma_{23} \\ \gamma_{31} \end{Bmatrix} = \begin{bmatrix} \frac{1}{E_1} & -\frac{\nu_{21}}{E_2} & -\frac{\nu_{31}}{E_3} & 0 & 0 & 0 \\ -\frac{\nu_{12}}{E_1} & \frac{1}{E_2} & -\frac{\nu_{32}}{E_3} & 0 & 0 & 0 \\ -\frac{\nu_{13}}{E_1} & -\frac{\nu_{23}}{E_2} & \frac{1}{E_3} & 0 & 0 & 0 \\ 0 & 0 & 0 & \frac{1}{G_{12}} & 0 & 0 \\ 0 & 0 & 0 & 0 & \frac{1}{G_{23}} & 0 \\ 0 & 0 & 0 & 0 & 0 & \frac{1}{G_{31}} \end{bmatrix} \begin{Bmatrix} T_{11} \\ T_{22} \\ T_{33} \\ T_{12} \\ T_{23} \\ T_{31} \end{Bmatrix}, \tag{3.118}$$

In Eq.(3.98), matrix $\mathbf{C}$ is a symmetric matrix and the inverse of a symmetric matrix is symmetric. Hence, $\mathbf{S}^{-1}$ (inverse of $\mathbf{C}$) in Eq.(3.118) is also symmetric. The matrix $\mathbf{S}^{-1}$ implies that

$$\frac{\nu_{21}}{E_2} = \frac{\nu_{12}}{E_1}, \quad \frac{\nu_{31}}{E_3} = \frac{\nu_{13}}{E_1}, \quad \frac{\nu_{32}}{E_3} = \frac{\nu_{23}}{E_2}. \tag{3.119}$$

Finally, comparing Eq.(3.118) and Eq.(3.109), it follows

$$
\begin{aligned}
S_{11} &= \frac{1}{E_1}, & S_{12} &= -\frac{\nu_{12}}{E_1}, & S_{13} &= -\frac{\nu_{13}}{E_1}, \\
S_{22} &= \frac{1}{E_2}, & S_{23} &= -\frac{\nu_{23}}{E_2}, & S_{33} &= \frac{1}{E_3}, \\
S_{44} &= \frac{1}{G_{23}}, & S_{55} &= \frac{1}{G_{13}}, & S_{66} &= \frac{1}{G_{12}}.
\end{aligned}
\tag{3.120}
$$

Consequently, elastic coefficients of Eq.(3.98) for an orthotropic material are represented by 9 independent material coefficients in Eq.(3.109) which can also be expressed by Eq.(3.118). Working with engineering constants has advantages, since they have physical meanings. For this reason, in the next chapter, we will identify the parameters using Eq.(3.118) which leads us to calculate the parameters in Eq.(3.109) and subsequently the parameters in Eq.(3.98).

To this end, alternative expressions of the components of the elasticity matrix $\mathbf{C}$, can be expressed using the parameter sets,

$$\boldsymbol{\kappa}_{\mathrm{SP}} = \{\Lambda, \alpha_1, \alpha_2, \mu, \mu_1, \mu_2, \beta_1, \beta_2, \beta_3\}, \tag{3.121}$$

$$\boldsymbol{\kappa}_{\mathrm{C}} = \{C_{11}, C_{12}, C_{13}, C_{22}, C_{23}, C_{33}, C_{44}, C_{55}, C_{66}\}, \tag{3.122}$$

$$\boldsymbol{\kappa}_{\mathrm{S}} = \{E_1, E_2, E_3, \nu_{12}, \nu_{13}, \nu_{32}, G_{12}, G_{23}, G_{13}\}. \tag{3.123}$$

Alternative expressions of the components $\boldsymbol{\kappa}_{\mathrm{C}}$ based on $\boldsymbol{\kappa}_{\mathrm{S}}$ components are

$$
\begin{aligned}
C_{11} &= \frac{\frac{1}{E_2E_3} - (\frac{\nu_{23}}{E_2})^2}{\omega}, & C_{12} &= \frac{\frac{\nu_{13}\nu_{23}}{E_2E_1} + \frac{\nu_{12}}{E_1E_3}}{\omega}, & C_{13} &= \frac{\frac{\nu_{12}\nu_{23}}{E_1E_2} + \frac{\nu_{13}}{E_1E_2}}{\omega}, \\
C_{22} &= \frac{\frac{E_3}{E_1} - (\frac{\nu_{13}}{E_1})^2}{\omega}, & C_{33} &= \frac{\frac{1}{E_2E_1} - (\frac{\nu_{12}}{E_1})^2}{\omega}, & C_{23} &= \frac{\frac{\nu_{12}\nu_{13}}{E_1^2} + \frac{\nu_{23}}{E_2E_1}}{\omega}, \\
C_{44} &= G_{23}, & C_{55} &= G_{13}, & C_{66} &= G_{12},
\end{aligned}
\tag{3.124}
$$

with

$$\omega = \frac{\nu_{13}\nu_{12}}{E_1^3} - \frac{1}{E_1}(\frac{\nu_{23}}{E_2})^2 - \frac{1}{E_2}(\frac{\nu_{13}}{E_1})^2 - \frac{\nu_{12}}{E_3}(\frac{\nu_{12}}{E_1})^2 - 2\frac{\nu_{12}\nu_{23}\nu_{13}}{E_1^2E_2}. \tag{3.125}$$

Another possibility is to represent components of $\boldsymbol{\kappa}_{\mathrm{SP}}$ using $\boldsymbol{\kappa}_{\mathrm{S}}$ by

$$\begin{aligned}
\mu_1 &= G_{12} - G_{23} \\
\mu_2 &= G_{12} - G_{13} \\
\mu &= G_{13} + G_{23} - G_{12} \\
\Lambda &= \frac{\frac{1}{E_2E_1} - (\frac{\nu_{12}}{E_1})^2}{\omega} + 2(G_{12} - G_{23} - G_{13}) \\
\alpha_1 &= \frac{\frac{\nu_{12}\nu_{23}}{E_1E_2} + \frac{\nu_{13}}{E_1E_2}}{\omega} - \frac{\frac{1}{E_2E_1} - (\frac{\nu_{12}}{E_1})^2}{\omega} - 2(G_{12} - G_{23} - G_{13}) \\
\alpha_2 &= \frac{\frac{\nu_{12}\nu_{13}}{E_1^2} + \frac{\nu_{23}}{E_2E_1}}{\omega} - \frac{\frac{1}{E_2E_1} - (\frac{\nu_{12}}{E_1})^2}{\omega} - 2(G_{12} - G_{23} - G_{13}) \\
\beta_1 &= \frac{\frac{1}{E_2E_3} - (\frac{\nu_{23}}{E_2})^2}{\omega} + \frac{\frac{1}{E_2E_1} - (\frac{\nu_{12}}{E_1})^2}{\omega} - 4G_{13} - 2\frac{\frac{\nu_{12}\nu_{23}}{E_1E_2} + \frac{\nu_{13}}{E_1E_2}}{\omega} \\
\beta_2 &= \frac{\frac{E_3}{E_1} - (\frac{\nu_{13}}{E_1})^2}{\omega} + \frac{\frac{1}{E_2E_1} - (\frac{\nu_{12}}{E_1})^2}{\omega} - 4G_{23} - 2\frac{\frac{\nu_{12}\nu_{13}}{E_1^2} + \frac{\nu_{23}}{E_2E_1}}{\omega}
\end{aligned} \tag{3.126}$$

$$\beta_3 = \frac{\frac{\nu_{13}\nu_{23}}{E_2E_1} + \frac{\nu_{12}}{E_1E_3}}{\omega} - \frac{\frac{\nu_{12}\nu_{23}}{E_1E_2} + \frac{\nu_{13}}{E_1E_2}}{\omega} - \frac{\frac{\nu_{12}\nu_{13}}{E_1^2} + \frac{\nu_{23}}{E_2E_1}}{\omega} + \frac{\frac{1}{E_2E_1} - (\frac{\nu_{12}}{E_1})^2}{\omega} + 2(G_{12} - G_{23} - G_{13}) \tag{3.127}$$

with

$$\omega = \frac{\nu_{13}\nu_{12}}{E_1^3} - \frac{1}{E_1}(\frac{\nu_{23}}{E_2})^2 - \frac{1}{E_2}(\frac{\nu_{13}}{E_1})^2 - \frac{\nu_{12}}{E_3}(\frac{\nu_{12}}{E_1})^2 - 2\frac{\nu_{12}\nu_{23}\nu_{13}}{E_1^2E_2}. \tag{3.128}$$

It is also possible to represent components of $\boldsymbol{\kappa}_{\mathrm{S}}$ with the help of $\boldsymbol{\kappa}_{\mathrm{C}}$ by

$$\begin{aligned}
S_{11} &= \frac{C_{23}^2 - C_{22}C_{33}}{C_{13}^2C_{22} - 2C_{12}C13C23 + C_{12}^2C_{33}}, & S_{12} &= \frac{C_{23} + \Gamma}{-C_{13}C_{22} + C_{12}C_{23}}, \\
S_{13} &= \frac{1 - \frac{C_{12}+\Gamma}{-C_{13}C_{22}+C_{12}C_{23}}}{C_{13}}, & S_{22} &= \frac{C_{13}(-1 + \frac{C_{12}(C_{23}+\Gamma)}{-C_{13}C_{22}+C_{12}C_{23}})}{C_{13}C_{22} - C_{12}C_{23}}, \\
S_{23} &= \frac{C_{12}(-1 + \frac{C_{12}(C_{23}+\Gamma)}{-C_{13}C_{22}+C_{12}C_{23}})}{C_{13}C_{22} - C_{12}C_{23}}, & S_{33} &= \frac{C_{12}^2(-1 + \frac{C_{12}(C_{23}+\Gamma)}{-C_{13}C_{22}+C_{12}C_{23}})}{c_{13}(C_{13}C_{22} - C_{12}C_{23})}, \\
S_{44} &= \frac{1}{C_{44}}, & S_{55} &= \frac{1}{C_{55}}, S_{66} = \frac{1}{C_{66}},
\end{aligned} \tag{3.129}$$

with

$$\Gamma = \frac{C_{12}C_{13}(C_{23}^2 - C_{22}C_{33})}{C_{13}^2C_{22} - 2C_{12}C_{13}C_{23} + C_{12}^2C_{33}}. \tag{3.130}$$

For orthotropic materials, there are constraints among engineering constants which should be considered. If only one normal stress is applied at a time, the corresponding strain is determined by the diagonal elements of the compliance matrix, (Jones, 1998). Hence, these elements can not be negative which yields to

$$S_{11}, S_{22}, S_{33}, S_{44}, S_{55}, S_{66} > 0, \tag{3.131}$$

and in terms of engineering constant

$$E_1, E_2, E_3, G_{23}, G_{31}, G_{12} > 0. \tag{3.132}$$

Likewise, considering the stress alone, the work is determined by the diagonal elements of the stiffness matrix where these elements should be positive, i.e.

$$C_{11}, C_{22}, C_{33}, C_{44}, C_{55}, C_{66} > 0, \tag{3.133}$$

and

$$1 - \nu_{23}\nu_{32} > 0, \quad 1 - \nu_{13}\nu_{31} > 0, \quad 1 - \nu_{12}\nu_{21} > 0, \tag{3.134}$$

see also (Jones, 1998). Moreover, using Eq.(3.133) and Eq.(3.110), it is possible to write,

$$| S_{23} | < \sqrt{S_{22}S_{33}}, \quad | S_{13} | < \sqrt{S_{11}S_{33}}, \quad | S_{12} | < \sqrt{S_{11}S_{22}}. \tag{3.135}$$

Using Eq.(3.135), Eq.(3.120), and Eq.(3.119), they can be reformulated as

$$\begin{aligned} &| \nu_{21} | < \sqrt{E_2/E_1}, \quad | \nu_{32} | < \sqrt{E_3/E_2}, \quad | \nu_{13} | < \sqrt{E_1/E_3}, \\ &| \nu_{12} | < \sqrt{E_1/E_2}, \quad | \nu_{23} | < \sqrt{E_2/E_3}, \quad | \nu_{31} | < \sqrt{E_3/E_1}. \end{aligned} \tag{3.136}$$

4 Experiments and Material Parameter Identification

Experiments are an essential part of every scientific discipline since they provide necessary information regarding the behavior of a material. The previous chapter served to introduce the material models for isotropic, transverse isotropic, and orthotropic materials. In this chapter, we concentrate on detailed descriptions of different experiments designed for material parameter identification purposes.

4.1 Experimental Investigation

In this work, different tests are performed to obtain the material parameters of isotropy, transversal isotropy, and orthotropy. First, the production process of the specimens is explained. Second, specimens for isotropy, transversal isotropy, and orthotropy for the purpose of determining the parameters of the models are introduced. Moreover, the details of the chosen experiments are discussed. Then, the identification procedure of isotropy, transversal isotropy, and orthotropy are explained in detail.

4.1.1 Glass-Fiber Material

There are different types of fibers that can be used to produce fiber reinforcement composites. It is very common to use E-glass fibers as a reinforcement material in composites, since E-glass fiber is cost-effective and, hence, a very economical reinforcement fiber. The samples used in this work are made of E-glass fibers from HP-Textiles GmbH. According to the manufacturer, the Young's modulus E is $73\,000\ \mathrm{N\,mm^{-2}}$ and the Poisson's ratio ν is 0.22.

4.1.2 Vacuum Assisted Resin Infusion (VARI)

All glass fiber reinforced specimens are made using a VARI process at the Institute for Polymer Materials and Plastics Engineering (PuK) at Clausthal University of Technology. It should be mentioned that VARI is a well-accepted technique for the manufacturing of composites. This method is discussed and utilized in many works, see for instance, (Goren and Atas, 2008; Li et al., 2004; Poodts et al., 2013; Van Oosterom et al., 2019; Zhang et al., 2014). Samples are manufactured using resin RIMR135 with a curing agent RIMH1366, and a weight ratio of 10:3 is needed between the resin and curing agent.

The VARI process requires a setup as shown in Fig. 4.1(a), and the setup is prepared in the following steps. In the first step, a qualitatively good mold is required for vacuum infusion. In addition, the mold should be rigid and properly cleaned. In the second step, the fiber plies are put under a vacuum bag using tacky tape. The bag should be tight enough but still allow space for all the materials, including networks of tubing. Infusion bag that is too large or too small could lead to an improper infusion. Once all the components and materials are in place, the vacuum pump should be attached. Since resin is infused through vacuum pressure, it is beneficial to have a strong pump. Before starting the infusion process, it is necessary to check the setup in order to avoid possible leakage. In the third step, bubbles might occur after mixing resin RIMR135 with the curing agent RIMH1366. Thus, the bubbles can be eliminated by putting the mixture into a vacuum situation so that the bubbles are sucked out, see Fig. 4.2. Two tubes can be seen

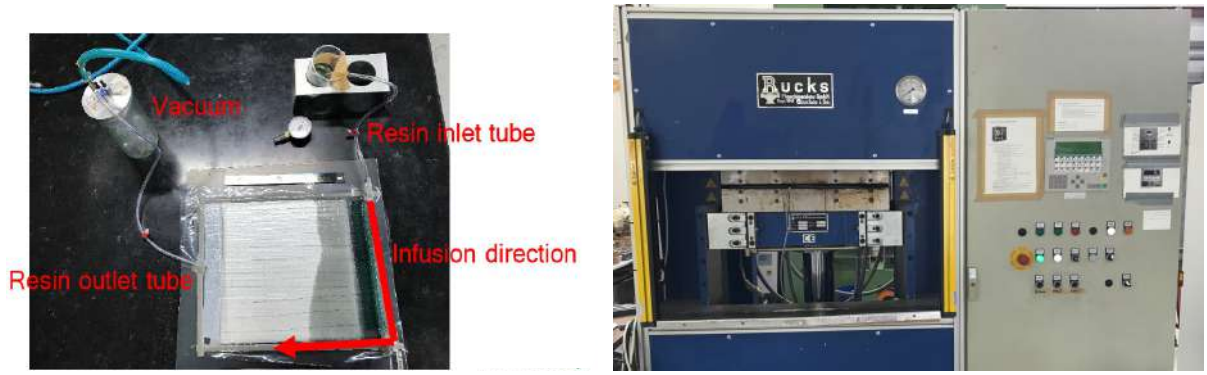

(a) VARI set-up (b) Compression machine

Figure 4.1: Production steps in VARI process

in Fig. 4.1(a). The resin flows through the inlet tube due to the lack of of air generated by the outlet tube. Then, the glass fiber plies are placed under a vacuum bag. The resin should be sucked through the tube into the laminate quickly. It takes a while for the resin to cover all the areas under the vacuum bag, depending on the size of fiber plies, see in Fig. 4.3. After the resin reaches the outlet tube, the setup is placed in a compression machine for one hour with $80\,°\mathrm{C}$, see Fig. 4.1(b). One of the main reasons for using a compression machine is to ensure a constant thickness throughout the plate. In the next step, the setup is placed in an oven for 10 hours with $80\,°\mathrm{C}$ to complete the curing process. After the curing process, a cutting machine is used to cut the plates to the desired dimensions for the samples.

4.1.3 Testing Procedure and Experimental Setup

After the described production process, the samples are ready for the mechanical tests. All tests (except for the compression tests) are performed with a Zwick testing machine Z100, which has a force gauge load maximum of $10\,\mathrm{kN}$ at the Institute of Applied Mechanics, Clausthal University of Technology, see Fig. 4.4(b). The tests are repeated five times at room temperature, and the surface displacements are observed by means of a 3D-digital image correlation system (DIC-

Figure 4.2: Resin in a vacuum atmosphere before starting the infusion process

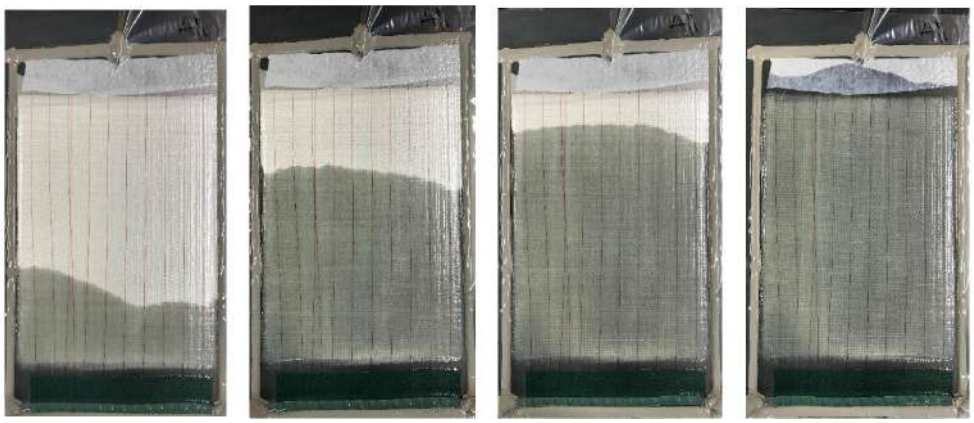

Figure 4.3: Flow process of the resin through the fiber plies

(a) Observing the surface of the sample using a DIC-system

(b) Zwick testing machine (Z100)

Figure 4.4: Experimental setup

system), see Fig. 4.4(a). Here, we use the software Aramis of the company GOM, Braunschweig (Germany), see (GOM, 2011), to calculate the surface deformations. For this purpose, a white background is painted on the surface of the samples using DUPLI-COLOR AQUA spray paint, produced by MOTIP DUPLI GmbH, Haßmersheim (Germany). In addition, a black spray paint (DUPLI-COLOR Deco Matt, from the same company) is used to apply the desired pattern to the white background, see Fig. 4.5(a). The cameras are positioned with respect to the samples by a calibration process, and the images are recorded with a frequency of $1\,\mathrm{Hz}$ for each test. In each test, the detected forces in the testing machine's force gauge are recorded.

Since rigid body motions are observed, one challenge of the experiments is to evaluate the displacements of the specimens. In order to compensate the rigid body movement, two rulers are adapted directly at the clamping system so that they are visible in the pictures. Using a DIC-program, we were then able to compensate the rigid body movements. One ruler is attached to the upper clamp in the Zwick machine, where the displacement should be equal to zero. The second ruler is fixed to the lower clamp, where the displacement is applied to the machine, see Fig. 4.5(a). The rigid body motion is compensated and minimized by determining the displacement of both rulers.

4.1.4 Pure Resin Samples

One set of samples are dog-bone specimens manufactured using resin RIMR135 with the curing agent RIMH1366, see Fig. 4.6 and Fig. 4.7(a), and they are produced according to the German standard (DIN EN ISO 527-2, 1996). The tests for pure resin samples are accomplished with

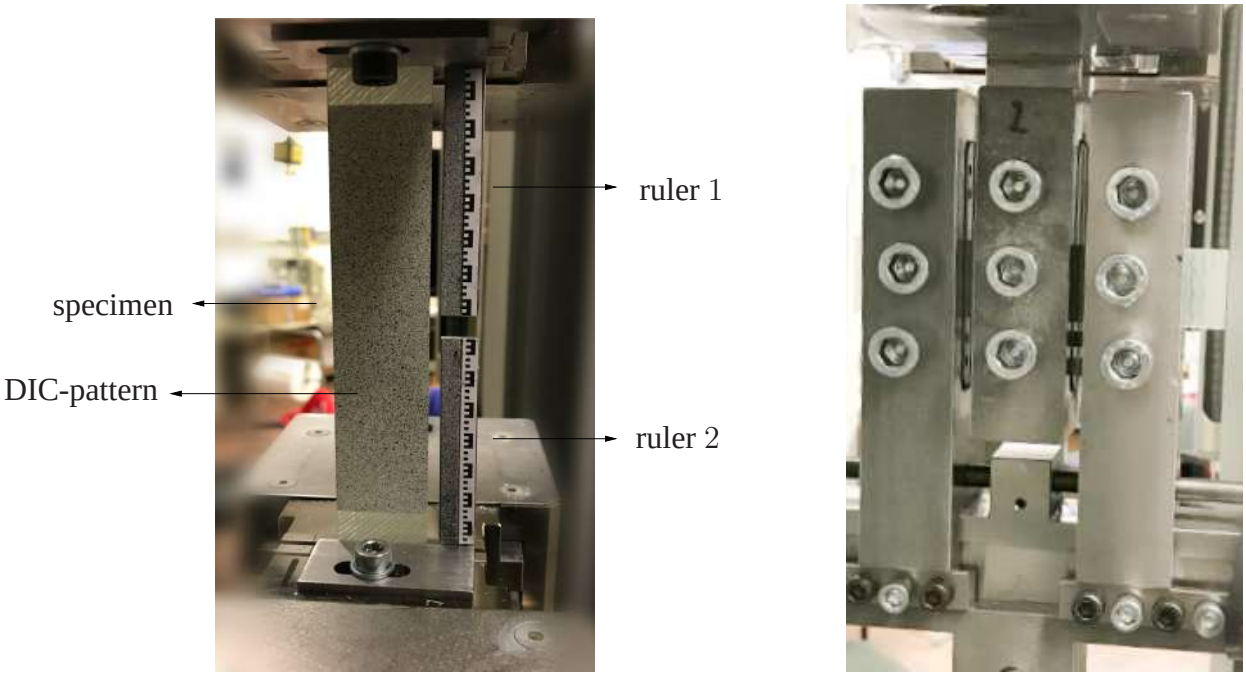

(a) Experimental setup in tensile test (with rulers) (b) Shear tool

Figure 4.5: Experimental tools for tensile and shear tests

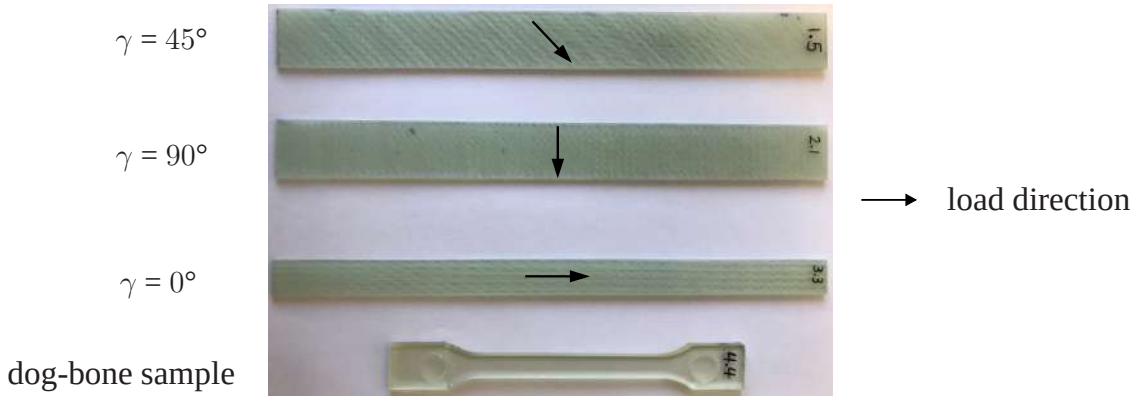

Figure 4.6: Reinforced composite specimens with (45°, 90°, 0°) fiber orientation and dog-bone sample

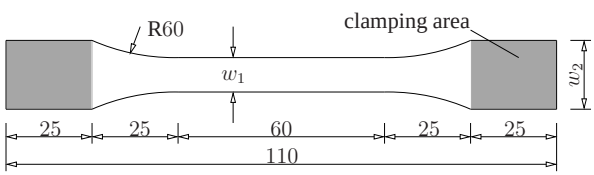

(a) Dog-bone specimens for pure epoxy (thickness $d = 4.1 \pm 0.1\,\mathrm{mm}$, widths $w_1 = 10.18 \pm 0.27\,\mathrm{mm}$ and $w_2 = 20.09 \pm 0.33\,\mathrm{mm}$)

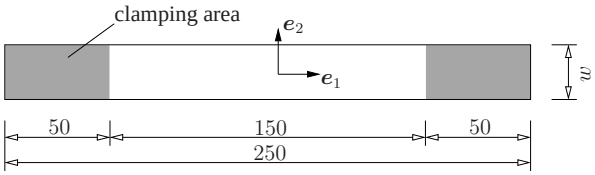

(b) Reinforced composite samples ($\gamma = 0°$: thickness $d = 2.55 \pm 0.15\,\mathrm{mm}$, width $w = 15.7 \pm 0.3\,\mathrm{mm}$; $\gamma = 45°$: thickness $d = 2.55 \pm 0.05\,\mathrm{mm}$, width $w = 25.4 \pm 0.1\,\mathrm{mm}$; $\gamma = 90°$: thickness $d = 2.65 \pm 0.05\,\mathrm{mm}$, width $w = 25.1 \pm 0.3\,\mathrm{mm}$)

Figure 4.7: Geometry of the dog-bone samples and reinforced composite with $0°, 45°$ and $90°$ fiber orientation (in mm) (Hartmann and Kheiri Marghzar, 2018)

a displacement-rate control of $1.65\,\mathrm{mm/min}$. With the help of rulers and by means of digital image correlation system, the displacement is measured in order to compensate the rigid body movement. In addition, the force is obtained using the Zwick device. The force-displacement diagram in the linear region for pure resin samples is shown in Fig. 4.8(a).

4.1.5 Specimens with Unidirectional Fiber Orientation

Specimens with $0°$, $45°$, and $90°$ fiber orientation using VARI process are produced, see Fig. 4.6. The dimensions of the specimens are chosen according to (DIN EN ISO 527-5, 2009), see Fig. 4.7(b). Here, the angle $\gamma = \arccos(\boldsymbol{a} \cdot \boldsymbol{e}_1)$ is presented, where $\boldsymbol{a}$ is the fiber direction in each specimen. For instance, $\gamma = 0°$ means that the fibers are parallel to the load direction, see Fig. 4.6. The specimens have a volume fraction of 55%.

Tensile Tests

Tensile tests are one of the most common tests in mechanical materials testing. We carry out this test for specimens with $0°$, $45°$, and $90°$ fiber orientation. Tensile tests for glass fiber reinforced specimens are accomplished at a displacement rate of $2.25\,\mathrm{mm/min}$ using the Zwick machine. The displacement is applied in $\boldsymbol{e}_1$ direction using the Zwick machine. Moreover, the DIC-system is used to observe the surface deformation of the samples during the tensile experiments. The axial strain distribution of the tensile specimen is shown in Fig. 4.9. Force-displacement curves for samples with $45°$ and $90°$ are obtained, see Fig. 4.8(b) and Fig. 4.8(c). Furthermore, the force-displacement curves for specimens with $0°$ fiber orientation are shown in Fig. 4.8(d). Similar to the resin samples, the displacements are determined using the rulers in order to compensate the rigid body movement. In addition, the force is obtained using a Zwick force gauge.

Shear Tests

The shear behavior is examined using a three-rail shear test, see (ASTM D4255/D4255M-15a, 2002). In these experiments, the middle rail is fixed to the upper clamp of the testing machine,

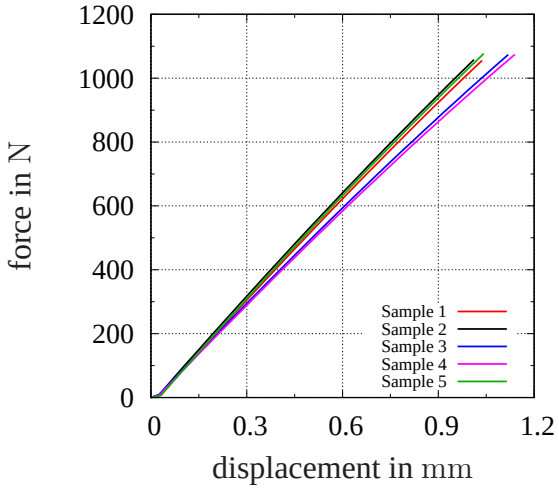

(a) Pure resin samples

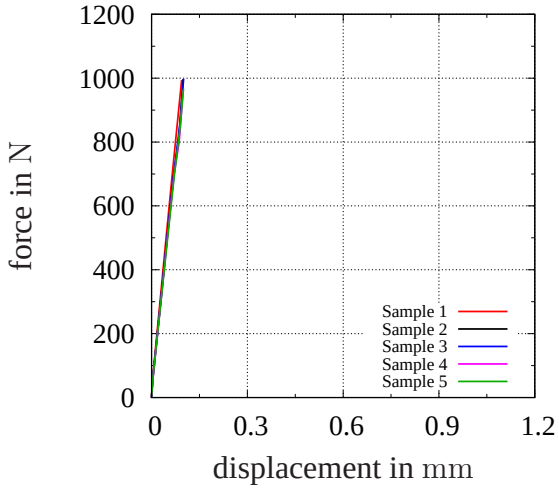

(b) Samples with 0° fiber orientation

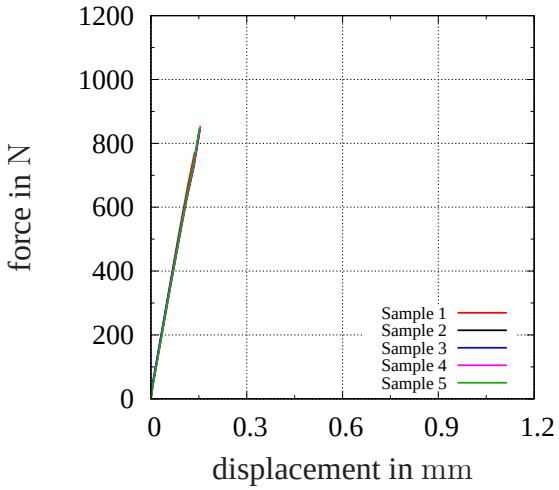

(c) Samples with 45° fiber orientation

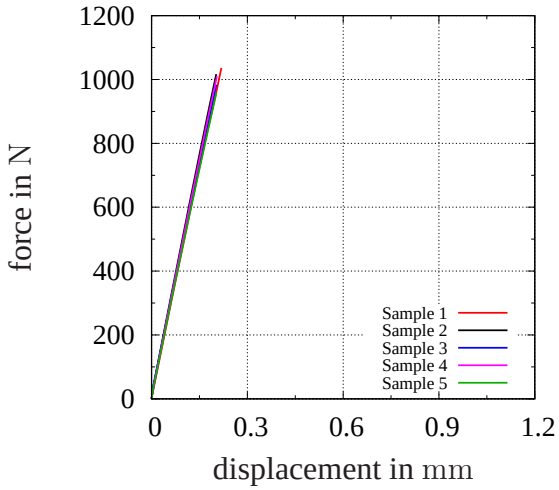

(d) Samples with 90° fiber orientation

Figure 4.8: Force-displacement curves for uni-directional tensile tests

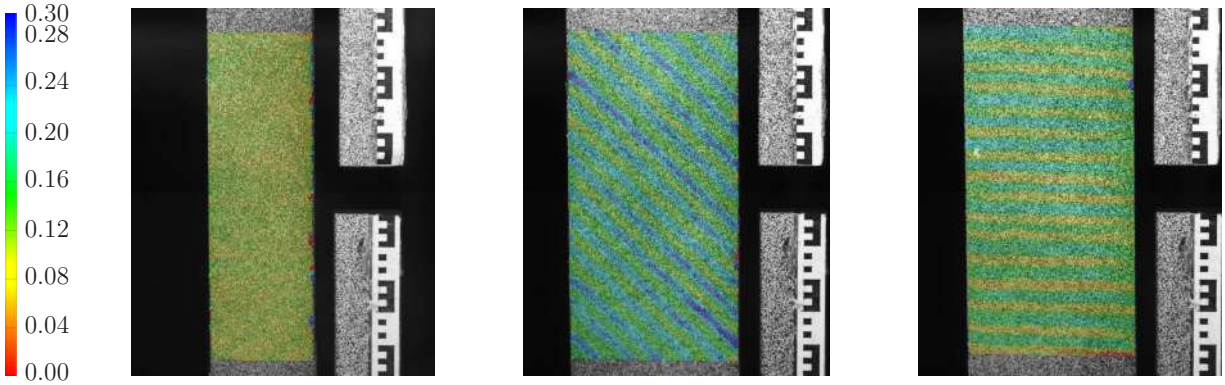

(a) Legend (b) $\gamma = 0°$ (c) $\gamma = 45°$ (d) $\gamma = 90°$

Figure 4.9: DIC-information of axial strains ε_{11}

while the load is applied to the outer rails and transferred to two symmetric regions of the samples. The displacements of the outer rails with respect to the fixed central rail generate a shear deformation in the samples, see (Sguazzo and Hartmann, 2018). The specimens are fixed in the rails by nine bolts, see Fig. 4.5(b). A torque wrench with a torque value of $15\,\mathrm{N\,m}$ is used to tighten the bolts. Due to the limitation of the visible area when using a DIC-system, only one side of the specimen is monitored. Four experiments are carried out with the displacement-rate control $0.75\,\mathrm{mm/min}$. Again, two rulers serve to measure the displacements of the moving and the fixed rails, in order to eliminate rigid body motions. The dimensions and details of the samples are shown in Fig. 4.10(a). The resulting force-displacement curves can be seen in Fig. 4.10(b).

4.1.6 Specimens with Two Fiber Orientations

In this section, the research is extended to the orthotropic case where we have two orthogonal fiber directions.

Tensile Tests

In the case of two orthogonal fiber orientations, the specimens have $0°$ ($\boldsymbol{e}_1$ direction) and $90°$ ($\boldsymbol{e}_2$ direction) fiber orientations and the geometry of the samples for tensile tests can be seen in Fig. 4.11(a). The samples have 8 layers and the volume fraction of the specimens is 60%. The tests for orthotropic glass fiber reinforced specimens are carried out at a displacement-rate of $2.25\,\mathrm{mm/min}$ as the force is applied in $\boldsymbol{e}_1$ direction, see Fig. 4.11(a). Again, the DIC-system is used to observe the surface deformation of the samples during the tensile tests. Additionally, force-displacement curves are obtained, see Fig. 4.11(b).

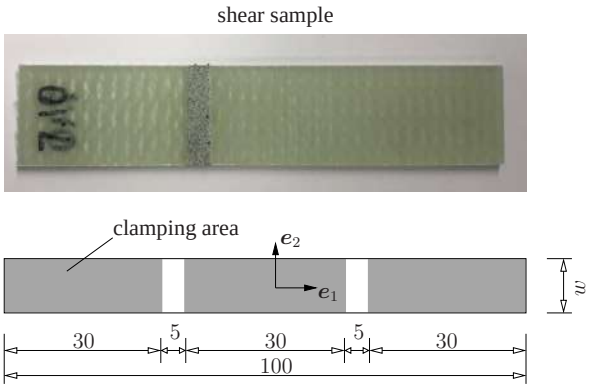

(a) Reinforced composite samples with fiber direction $\boldsymbol{a} = \boldsymbol{e}_2$ (thickness $d = 2.75 \pm 0.25\,\mathrm{mm}$, width $w = 25.4 \pm 0.1\,\mathrm{mm}$)

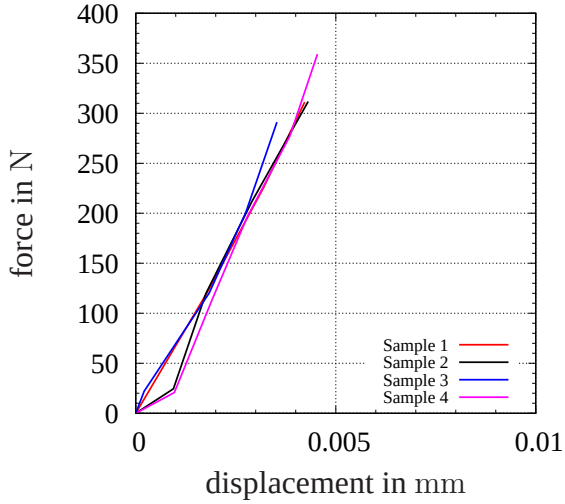

(b) Force-displacement curve for shear test

Figure 4.10: Unidirectional samples for shear test and experimental force-displacement response

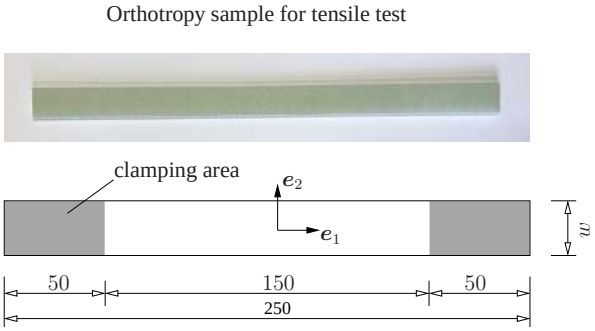

(a) Reinforced composite samples with fiber direction $\boldsymbol{a} = \boldsymbol{e}_2$ and $\boldsymbol{a} = \boldsymbol{e}_1$ (thickness $d = 2.7 \pm 0.1\,\mathrm{mm}$, width $w = 15.3 \pm 0.3\,\mathrm{mm}$)

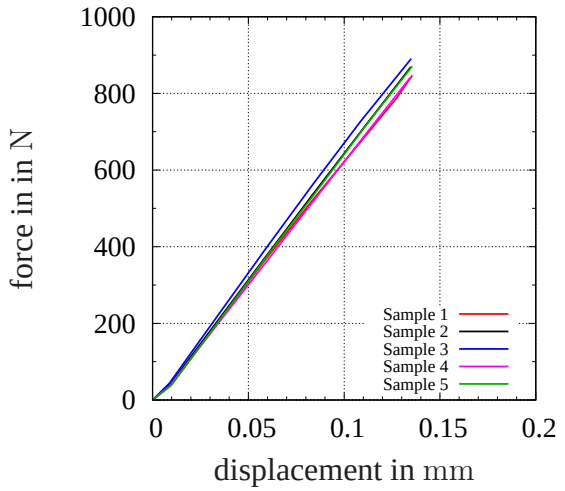

(b) Force-displacement curve for tensile test

Figure 4.11: Sample with two fiber directions for tensile test and experimental force-displacement response

Shear Tests

In the orthotropic case, one aspect of shear mode is investigated using the three-rail shear test. The three-rail shear tests are carried out similarly to the transversal isotropy case in Sect. 4.1.5 where the center rail is fixed to the upper clamp and the displacement is applied to the outer rails. The geometry of specimens can be seen in Fig. 4.12(a). Again, a torque wrench with a torque value of $15\,\mathrm{N\,m}$ is used to tighten the bolts. Furthermore, the experiments are carried out with a displacement-rate control of $0.75\,\mathrm{mm/min}$. Fig. 4.12(b) shows the force-displacement curve.

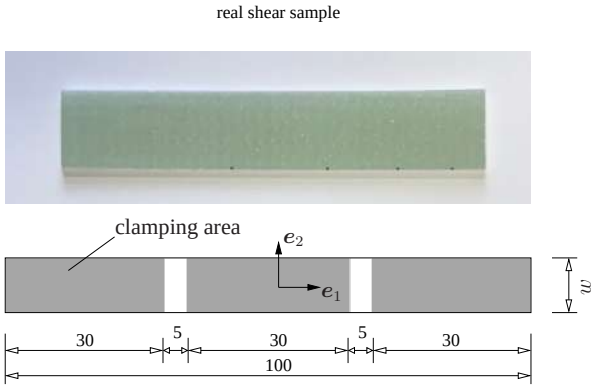

(a) Reinforced orthotropic composite samples with fiber direction $\boldsymbol{a} = \boldsymbol{e}_1$ and $\boldsymbol{b} = \boldsymbol{e}_2$ (thickness $d = 2.65 \pm 0.15\,\mathrm{mm}$, width $w = 25.65 \pm 0.15\,\mathrm{mm}$)

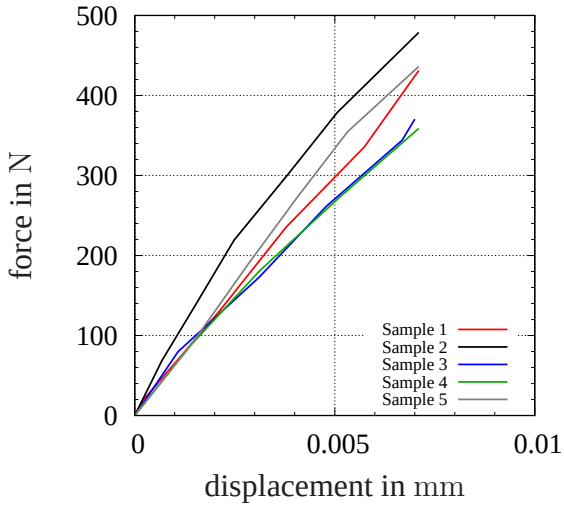

(b) Force-displacement diagram for shear test

Figure 4.12: Sample with two fiber directions for shear tests and experimental force-displacement response

Lap Shear Tests

Lap shear tests including single lap and double lap shear tests are commonly used in adhesive testing. In this work, lap shear tests are used to examine the shear behavior in the in-plane direction. The experiments are carried out with a displacement-rate control of $1.27\,\mathrm{mm/min}$ according to (ASTM D1002-05, 1999), see Fig. 4.13(a) and Fig. 4.13(b). The displacement applied in $\boldsymbol{e}_2$ direction using a Zwick testing machine, see Fig. 4.14. In addition, the displacement in $\boldsymbol{e}_2$ direction is also obtained using the Zwick device. The geometry of the samples can be seen in Fig. 4.14(a). The steel grade S235JR was used to produce the samples.

Since we are interested in the displacement of specimens in the central part, see Fig. 4.14(a), specimen with a given shape, see Fig. 4.14(b), is needed to calibrate the displacement of the ma-

(a) Samples for lap shear test

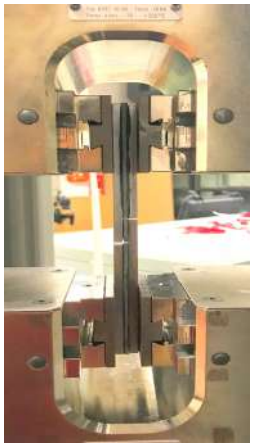

(b) Experimental setup

Figure 4.13: Lap shear test setup

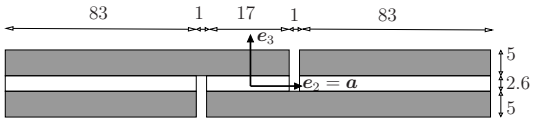

(a) Geometry of samples for lap shear tests (width $w = 10\text{mm}$)

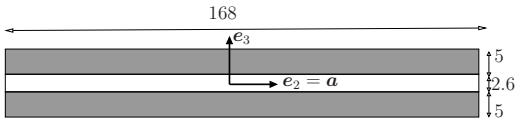

(b) Structure and geometry of sample to compensate rigid body movement (width $w = 10\text{mm}$)

Figure 4.14: Geometry of lap shear test samples

chine and other parts of the samples. This can be done based on the Young's modulus of S235JR, which is $E = 210$ GPa, and the obtained force from the Zwick machine. For this purpose, by considering the force from the Zwick device and having the Young's modulus of S235JR, the displacement of the sample in Fig. 4.14(b) can be calculated. Further, we obtain a displacement from the Zwick device. The difference between the obtained displacement from the Zwick machine and the calculated displacement is considered as a rigid body movement. The lap shear test are also repeated five times, and Fig. 4.15 shows the force-displacement diagrams in linear region. It should be also mentioned that, since the same fibers are used in both directions, the shear behavior in the in-plane direction in both $\boldsymbol{e}_1$ and $\boldsymbol{e}_2$ orientation is the same.

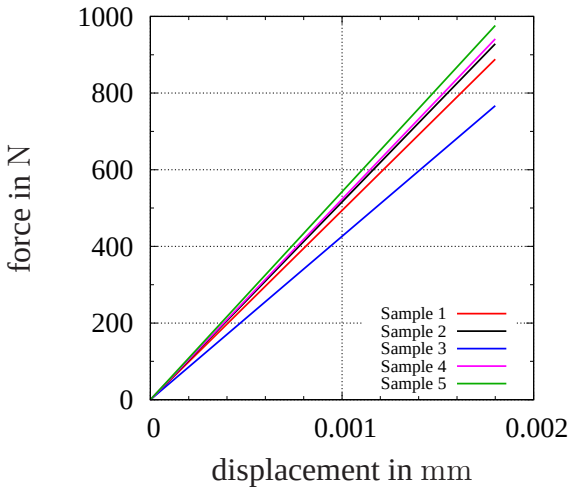

Figure 4.15: Force-displacement curves for lap shear tests

Compression Tests

A compression test is also needed to obtain other material parameters. Compression tests are performed at the Institute of Metallurgy (IMET) at Clausthal University of Technology. A Zwick compression testing machine is used for the experiments. The experiments are carried out with a displacement-rate of $0.3\,\mathrm{mm/min}$. The geometry of the samples are shown in Fig. 4.17(a). In this test, the axial force applied on the upper surface of the sample in $\boldsymbol{e}_3$ direction and the side forces are fixed as the side forces in $\boldsymbol{e}_1$ and $\boldsymbol{e}_2$ directions are measured by the compression tool. Furthermore, the displacement in $\boldsymbol{e}_3$ direction is obtained by the testing machine. In order to compensate the rigid body movement, we performed the compression experiment without any sample. In this case, we expect to obtain no displacement in axial direction though a displacement due to the elongation of the machine is observed. This displacement is considered as the rigid body movement. It should also be mentioned that noises are observed during the compression test. The lateral stress for each sample can be seen in Fig. 4.18(a) and Fig. 4.18(b).

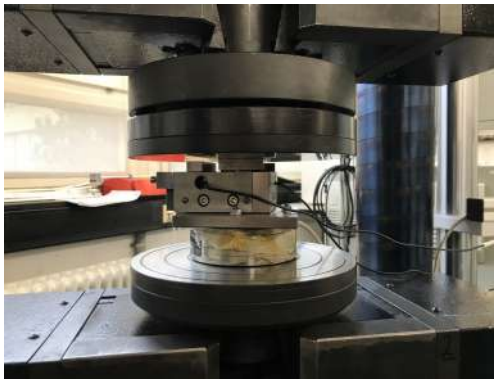

(a) Compression tool

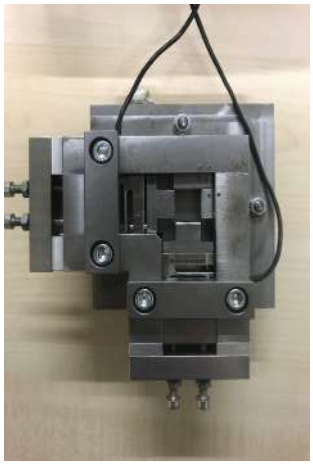

(b) Compression set up

Figure 4.16: Compression test

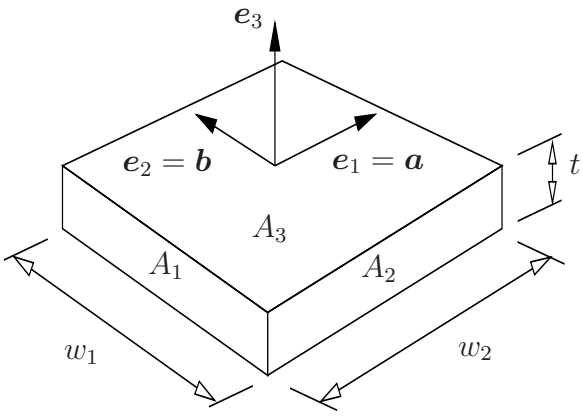

(a) Sketch of samples for compression test (width $w_1 = w_2 = 12.06 \pm 0.01\text{mm}$, thickness $t = 2.51 \pm 0.04\text{mm}$)

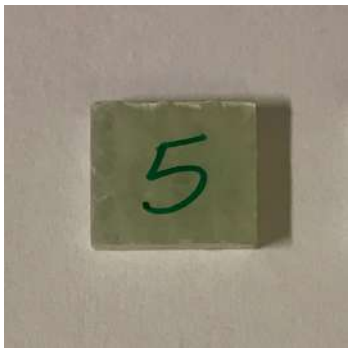

(b) Sample for compression test

Figure 4.17: Compression test

Although a larger dispersion in lateral stresses can be observed in Fig. 4.18(a) in comparison to the Fig. 4.18(b), the mean values of the stresses in both figures are very close to each other. Since the same fibers are used in both directions, it is expected that the side forces will be equal. On the other hand, due to the imperfections in the generated samples and in the compression tool and friction during the tests, there is a small deviation between the lateral stresses. The axial stress of each experiment can be seen in Fig. 4.18(c).

4.2 Material Parameter Identification

This section focuses on a concept to determine the material parameters of the constitutive models presented in Chapter 3. The parameter identification problem is a challenging issue in the theory of materials. The aim of material parameter identification is to find suitable parameters for models calibrated to experimental data. Parameter identification using constitutive models is often discussed by researchers when considering homogeneous and inhomogeneous deformations. Regarding the theory and concept of material parameter identification, works of (Beck and Arnold, 1977; Draper and Smith, 1998; Mahnken, 1998) can be mentioned. There are several optimization methods that can be applied in the scope of identification problem. For the linear least-square problem, this is discussed in (Hartmann, 2001a,b) for the case of hyperelasticity. The main procedure to calculate the material parameters is based on combining the least-square method (which is explained in following section) using the simulation which is carried out based on finite elements, the data from a digital image correlation system, and the force data of the testing machine. This approach follows the works of (Andresen et al., 1996; Mahnken and Stein, 1996).

In this section, a parameter identification procedure is described. Second, the two parameters for pure resin will be identified. Third, according to Eq.(3.60), five parameters are determined for transversal isotropy. In the next step, nine parameters are calibrated to the experimental data for Eq.(3.95), i.e. the orthotropic case.

4.3 Identification Procedure

The aim of material parameter identification is to obtain parameters for a model which is calibrated to experimental results. The parameters of the material models in the cases of isotropy, transversal isotropy, and orthotropy have to be identified in an identification procedure using experimental observations. A least-square approach is chosen to obtain the parameters. For this purpose, the residual $\mathbf{r}(\boldsymbol{\kappa}) = \mathbf{s}(\boldsymbol{\kappa}) - \mathbf{d}$ between the model $\mathbf{s}(\boldsymbol{\kappa}) \in \mathbb{R}^{n_\mathrm{d}}$ and the measured data $\mathbf{d} \in \mathbb{R}^{n_\mathrm{d}}$ is defined. This is given by

$$\mathbf{s} = \left\{ \begin{array}{c} \mathbf{s}^1 \\ \vdots \\ \mathbf{s}^{n_\mathrm{exp}} \end{array} \right\}, \qquad \mathbf{d} = \left\{ \begin{array}{c} \mathbf{d}^1 \\ \vdots \\ \mathbf{d}^{n_\mathrm{exp}} \end{array} \right\}, \tag{4.1}$$

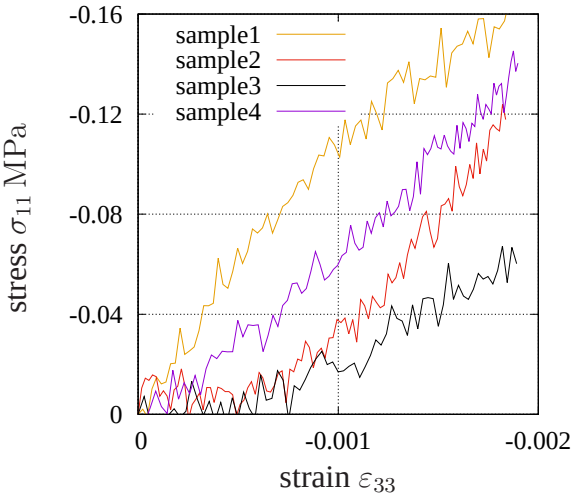

(a) Lateral stress versus strain

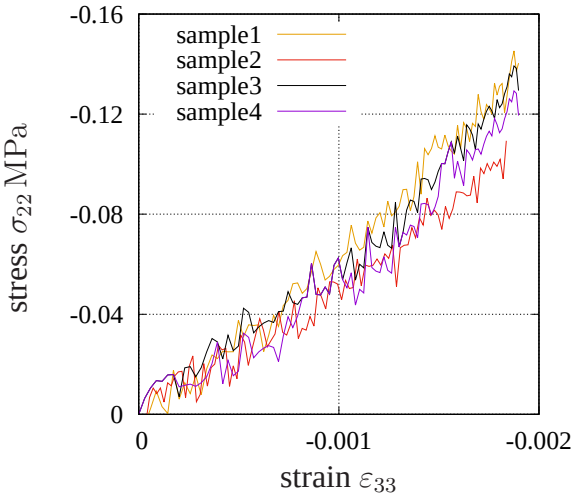

(b) Lateral stress versus strain

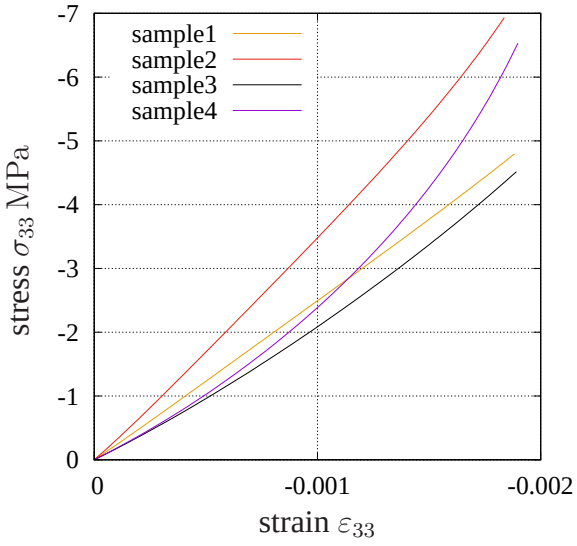

(c) Axial stress versus strain

Figure 4.18: Force-displacement curves for compression tests

where $\mathbf{s}^k$ and $\mathbf{d}^k$ represent the k-th simulation and experiment. Furthermore, n_{exp} corresponds to the number of experiments and n_{d} shows the overall data points used in identification. The parameters $\boldsymbol{\kappa} \in \mathbb{R}^{n_\kappa}$ of the material model have to be identified in the identification procedure. For this purpose, the residual

$$f(\boldsymbol{\kappa}) = \frac{1}{2}\|\boldsymbol{r}(\boldsymbol{\kappa})\|^2 = \frac{1}{2}\boldsymbol{r}^{\mathrm{T}}(\boldsymbol{\kappa})\boldsymbol{r}(\boldsymbol{\kappa}) = \frac{1}{2}\sum_{i=1}^{n_{\text{d}}}(s_i(\boldsymbol{\kappa}) - d_i)^2 \quad \rightarrow \quad \min \tag{4.2}$$

under the inequality constraints

$$\kappa_{\min j} \leq \kappa_j \leq \kappa_{\max j}, \quad j = 1, \ldots, n_\kappa. \tag{4.3}$$

has to be minimized, while each of the material parameters may lie within the specified interval. One of the main questions is what experiments are required to determine hopefully unique material parameters for each model.

The fundamental approach to determine the material parameters is based on combining the least-square method discussed above, where the simulation is carried out by means of finite elements and information from the experiments is determined by both the full-field strain data with the help of a digital image correlation system and the force from Zwick testing machine. This approach can be seen in, for example, (Andresen et al., 1996; Benedix et al., 1998; Cooreman et al., 2007; Kreissig et al., 2001), and the minimum problem is given by

$$\left.\frac{\mathrm{d}f(\boldsymbol{\kappa})}{\mathrm{d}\boldsymbol{\kappa}}\right|_{\boldsymbol{\kappa}=\boldsymbol{\kappa}^*} = \boldsymbol{J}^T(\boldsymbol{\kappa}^*)\{\boldsymbol{s}(\boldsymbol{\kappa}^*) - \boldsymbol{d}\} = \boldsymbol{0}, \tag{4.4}$$

with the Jacobian

$$\boldsymbol{J}(\boldsymbol{\kappa}) := \mathrm{d}\boldsymbol{r}(\boldsymbol{\kappa})/\,\mathrm{d}\boldsymbol{\kappa} = \mathrm{d}\boldsymbol{s}(\boldsymbol{\kappa})/\,\mathrm{d}\boldsymbol{\kappa}, \tag{4.5}$$

where $\boldsymbol{J} \in \mathbb{R}^{n_{\text{d}} \times n_\kappa}$. The result from the optimizer is represented by $\boldsymbol{\kappa}^*$. In the optimization process and under consideration, the simulation data is specified by, see also (Hartmann et al., 2020),

$$\boldsymbol{g}(\boldsymbol{u}(\boldsymbol{\kappa}), \boldsymbol{\kappa}) = \boldsymbol{0}, \tag{4.6}$$

with

$$\boldsymbol{g}(\boldsymbol{u}(\boldsymbol{\kappa}), \boldsymbol{\kappa}) := \boldsymbol{K}(\boldsymbol{\kappa})\boldsymbol{u}(\boldsymbol{\kappa}) + \overline{\boldsymbol{K}}(\boldsymbol{\kappa})\overline{\boldsymbol{u}} - \overline{\boldsymbol{p}}. \tag{4.7}$$

$\boldsymbol{K}$ and $\overline{\boldsymbol{K}}$ are parts of the total finite element stiffness matrix, $\boldsymbol{u}$ shows the unknown nodal displacements, $\overline{\boldsymbol{u}}$ are prescribed nodal displacements, and $\overline{\boldsymbol{p}}$ the given equivalent nodal forces. Using the result of the finite element simulation $\boldsymbol{u}$, the unknown nodal forces

$$\boldsymbol{p}(\boldsymbol{\kappa}) = \overline{\boldsymbol{K}}^T(\boldsymbol{\kappa})\boldsymbol{u}(\boldsymbol{\kappa}) + \overline{\overline{\boldsymbol{K}}}(\boldsymbol{\kappa})\overline{\boldsymbol{u}} \tag{4.8}$$

can be calculated. The model of $\boldsymbol{s}(\boldsymbol{\kappa})$ and the data of $\boldsymbol{d}$ have to be defined in order to determine the Jacobian. The Matlab tool `lsqnonlin.m` is used for this, see (Hartmann and Gilbert, 2018; Hartmann et al., 2018) for further information. Regarding the identification procedure, for finite element computations, points of the strains are analyzed at Gauss-points. Concerning

the curvilinear surfaces in finite element simulations and experiments with DIC-system, strain or displacement computation has to be provided. For a better understanding of the concept and the method to obtain these quantities, see (Hartmann and Rodriguez, 2018; Hartmann and Sguazzo, 2015). Coordinates of each point can be obtained for every time step for a DIC-system and finite element simulations. Furthermore, triangulation approach is used for both sets of data, see (Shewchuk, 2002) for further details. Triangulation is used to project the displacement information of finite element simulation onto the DIC-data. Further, a curvilinear surface approach is used for the strain calculation, see (Hartmann and Rodriguez, 2018).

In the linear least-square problem, we have $\boldsymbol{s}(\boldsymbol{\kappa}) = \boldsymbol{A}\boldsymbol{\kappa}$ with $\boldsymbol{A} \in \mathbb{R}^{n_\mathrm{d} \times n_\kappa}$, i.e. the simulation depends linearly on the parameters and the goal function leads to

$$f(\boldsymbol{\kappa}) = \frac{1}{2}\|\boldsymbol{A}\boldsymbol{\kappa} - \boldsymbol{d}\|^2 = \frac{1}{2}\left(\boldsymbol{\kappa}^T\boldsymbol{A}^T\boldsymbol{A}\boldsymbol{\kappa} - 2\boldsymbol{\kappa}^T\boldsymbol{A}^T\boldsymbol{d} + \boldsymbol{d}^\mathrm{T}\boldsymbol{d}\right) \quad \rightarrow \quad \text{min.} \tag{4.9}$$

The necessary conditions of a minimum in Eq.(4.2) can be calculated by applying the Gâteaux-derivative

$$\mathsf{D}\, f(\boldsymbol{\kappa})[\boldsymbol{h}] = \frac{\mathrm{d}}{\mathrm{d}\lambda} f(\boldsymbol{\kappa} + \lambda\boldsymbol{h})\Big|_{\lambda=0} = \left\{\frac{\mathrm{d}f}{\mathrm{d}\boldsymbol{\kappa}}\right\}^T \boldsymbol{h} = \sum_{k=1}^{n_\kappa} \frac{\partial f}{\partial \kappa_k} h_k = 0, \tag{4.10}$$

i.e. we have

$$\left.\frac{\mathrm{d}f(\boldsymbol{\kappa})}{\mathrm{d}\boldsymbol{\kappa}}\right|_{\boldsymbol{\kappa}=\boldsymbol{\kappa}^*} = \boldsymbol{0} \tag{4.11}$$

at the minimum $\boldsymbol{\kappa}^*$. In the linear least-square problem, this leads to

$$\mathsf{D}\, f(\boldsymbol{\kappa})[\boldsymbol{h}] = \boldsymbol{h}^\mathrm{T}\boldsymbol{A}^T\{\boldsymbol{A}\boldsymbol{\kappa} - \boldsymbol{d}\} = \boldsymbol{h}^\mathrm{T} \underbrace{\left\{\left[\boldsymbol{A}^T\boldsymbol{A}\right]\boldsymbol{\kappa} - \boldsymbol{A}^T\boldsymbol{d}\right\}}_{\mathrm{d}f(\boldsymbol{\kappa})/\,\mathrm{d}\boldsymbol{\kappa}} = 0, \tag{4.12}$$

i.e. for arbitrary directions $\boldsymbol{h}$, the system of linear equations

$$\left[\boldsymbol{A}^T\boldsymbol{A}\right]\boldsymbol{\kappa} = \boldsymbol{A}^T\boldsymbol{d}, \tag{4.13}$$

has to hold, where $\boldsymbol{A} = \boldsymbol{J}(\boldsymbol{\kappa}^*)$, see (Beck and Arnold, 1977; Hartmann and Gilbert, 2018; Lawson and Hanson, 1995), for example.

Confidence Interval

Measuring the quality of identification results is a matter of interest. There exist measures for the quality of an optimization such as the confidence interval, the correlation coefficient, or the coefficient of determination. Considering a linearization over the identified parameters $\boldsymbol{\kappa}^*$

$$\boldsymbol{r}(\boldsymbol{\kappa}) = \boldsymbol{r}(\boldsymbol{\kappa}^*) + \boldsymbol{J}(\boldsymbol{\kappa}^*)\left\{\boldsymbol{\kappa} - \boldsymbol{\kappa}^*\right\}, \tag{4.14}$$

with the Jacobian as $\boldsymbol{J}(\boldsymbol{\kappa}) := \mathrm{d}\boldsymbol{r}(\boldsymbol{\kappa})/\,\mathrm{d}\boldsymbol{\kappa} = \mathrm{d}\boldsymbol{s}(\boldsymbol{\kappa})/\,\mathrm{d}\boldsymbol{\kappa}$. The covariance matrix $\boldsymbol{P}$ can be represented using the Jacobian and standard deviation as s^2, see (Brandt, 1998),

$$\boldsymbol{P} = s^2\left[\boldsymbol{J}^T(\boldsymbol{\kappa}^*)\boldsymbol{J}(\boldsymbol{\kappa}^*)\right]^{-1}, \tag{4.15}$$

where the standard deviation is given by

$$s^2 = \frac{1}{n_\mathrm{d} - 1} \boldsymbol{r}^\mathrm{T}(\boldsymbol{\kappa}^*)\boldsymbol{r}(\boldsymbol{\kappa}^*). \tag{4.16}$$

There is also another approach to approximate the objective function by a quadratic function

$$\hat{f}(\boldsymbol{\kappa}) = f(\boldsymbol{\kappa}^*) + \left\{ \frac{\mathrm{d}f(\boldsymbol{\kappa})}{\mathrm{d}\boldsymbol{\kappa}} \right\}^T \Bigg|_{\boldsymbol{\kappa}=\boldsymbol{\kappa}^*} \Delta\boldsymbol{\kappa} + \frac{1}{2}\Delta\boldsymbol{\kappa}^T \left[\frac{\mathrm{d}^2 f(\boldsymbol{\kappa})}{\mathrm{d}\boldsymbol{\kappa}\,\mathrm{d}\boldsymbol{\kappa}} \right] \Bigg|_{\boldsymbol{\kappa}=\boldsymbol{\kappa}^*} \Delta\boldsymbol{\kappa}, \tag{4.17}$$

$\Delta\boldsymbol{\kappa} = \boldsymbol{\kappa} - \boldsymbol{\kappa}^*$, where the covariance matrix yields

$$\boldsymbol{P} = s^2 \boldsymbol{H}^{-1}(\boldsymbol{\kappa}^*), \tag{4.18}$$

with the Hessian

$$\boldsymbol{H}(\boldsymbol{\kappa}) = \frac{\mathrm{d}^2 f(\boldsymbol{\kappa})}{\mathrm{d}\boldsymbol{\kappa}\,\mathrm{d}\boldsymbol{\kappa}} = \left[\frac{\partial^2 f(\boldsymbol{\kappa})}{\partial\kappa_i \partial\kappa_j} \right] = \left[\sum_{k=1}^{n_\mathrm{d}} \left(\frac{\partial^2 s_k(\boldsymbol{\kappa})}{\partial\kappa_i \partial\kappa_j}(s_k(\boldsymbol{\kappa}) - d_k) + \frac{\partial s_k(\boldsymbol{\kappa})}{\partial\kappa_i} \frac{\partial s_k(\boldsymbol{\kappa})}{\partial\kappa_j} \right) \right]. \tag{4.19}$$

$\mathrm{d}f(\boldsymbol{\kappa})/\,\mathrm{d}\boldsymbol{\kappa}$ is called sensitivity, see (Hartmann and Gilbert, 2018). The confidence interval is calculated by, see (Brandt, 1998),

$$\boldsymbol{\kappa}_\mathrm{conf} = \boldsymbol{\kappa}^* \pm \Delta\boldsymbol{\kappa} \tag{4.20}$$

with

$$\Delta\kappa_i = \sqrt{P_{ii}}, \quad i = 1, \ldots, n_\mathrm{d}. \tag{4.21}$$

Correlation Matrix

The correlation coefficient can be computed as

$$c_{ij} = \frac{P_{ij}}{\sqrt{P_{ii}P_{jj}}}, \tag{4.22}$$

and describes the dependence of two parameters κ_i and κ_j, see (Tarantola, 2005). The correlation coefficient can vary from -1 to 1. Value 1 represents a total correlation, and value -1 means an inverse of total correlation. In addition, value 0 shows no dependence or correlation of parameters.

Coefficient of Determination

Commonly, the R^2-value specifies how well the model fits to the experimental data,

$$R^2 = 1 - \frac{\sum_{i=1}^{n_\mathrm{d}} (d_i - s_i)^2}{\sum_{i=1}^{n_\mathrm{d}} (d_i - \overline{d})^2}, \quad \text{with } \overline{d} = \frac{1}{n_\mathrm{d}} \sum_{i=1}^{n_\mathrm{d}} d_i. \tag{4.23}$$

R^2 can vary between 0 and 1. If $R^2 \approx 1$, it shows that model matches the experimental data very well.

4.4 Identification using Pure Resin Sample

The surface information of the dog-bone specimens in Fig. 4.19* are observed using a DIC-system during each test after compensating rigid body movement. The coordinates of all points at each point in each time-step are acquired, see the maximum principal strains in Fig. 4.19 for example. The surface strain distribution is used, as rigid body motions occurring in the

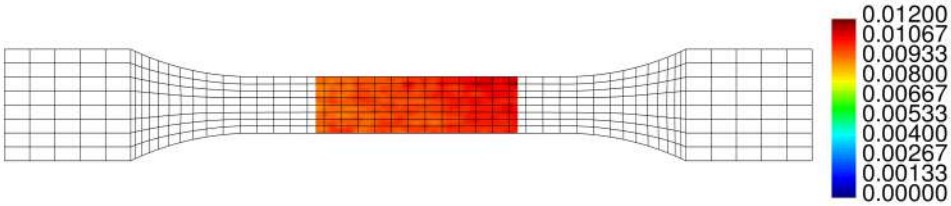

Figure 4.19: Maximum principal strain distribution for a pure resin sample

experiments are compensated. The maximum and minimum principal strains from all the five experiments plus the forces $F(t)$ in Fig. 4.8(a) are needed to identify Young's modulus E and Poisson's ratio ν. The strains from 25 points in x-direction and 12 points in y-direction along with reaction forces of 40 time steps of each experiment are obtained. This information is used to identify the material parameters E and ν. The results of the material parameter identification process regarding Young's modulus E and Poisson's ratio ν can be seen in Tab. 4.1, where the

Table 4.1: Identified parameters of the resin material

parameter	dimension	resin	glass fiber
E	$\mathrm{N\,mm^{-2}}$	1971.42	73 000
ν	$-$	0.39	0.22

material parameters of the glass fiber material are listed according to the manufacturer. The result of the force-displacement curve from the identification procedure is shown in Fig. 4.20(a). The simulation curve has a good prediction as it is within the experimental range. A more exact comparison can be provided since the strains can be calculated at each point of DIC-system. The finite element simulation and the final result of comparison can be seen in Fig. 4.20(b), where a specific area is examined using a DIC-system.

*Figures 4.19- 4.24 are taken from (Hartmann et al., 2020) and Mr. Rose Rogin Gilbert generated these results.

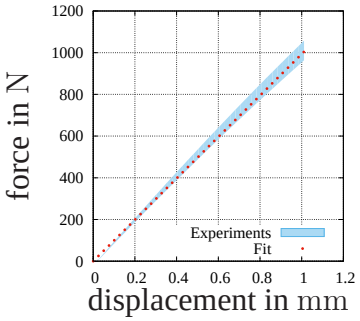

(a) Force-displacement result of pure matrix material

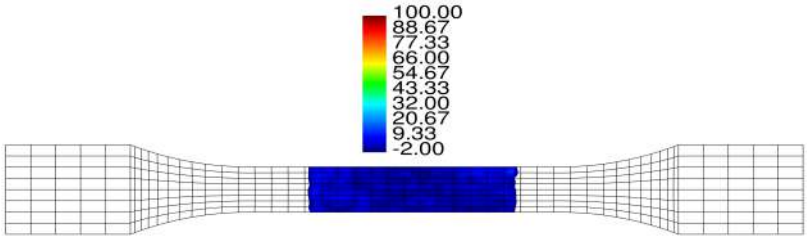

(b) Exemplary representation of (maximum principal) strain error after identification

Figure 4.20: Result of material parameter identification for pure matrix material, (Hartmann et al., 2020)

4.5 Identification of Unidirectional Composites

The aspect of transversal isotropy in this regard is also discussed in (Christensen, 2005). Different experiments are needed to obtain the material parameters. Here, it is assumed that we have a homogeneous deformation. The details are discussed in the following.

4.5.1 Compression Test

Compression test is needed for obtaining parameter Λ as this parameter can not be obtained from tensile tests or shear tests. Tensile tests with $\gamma = 0°, 90°$ do not provide enough information to obtain all parameters. Thus, a compression test is needed, see Fig. 4.21. Due to the lack of a measuring device for this test in the beginning, a numerical "test" is used to obtain parameter Λ in Eq.(4.24). Having the material parameters of the pure resin and the fiber material, see Tab. 4.1, a compression simulation with fiber volume fraction of 55% is carried out, see Fig. 4.21(b), where fibers are shown with blue colour and resin part is shown with green colour. The side parts of this model are fixed and a displacement is applied on the upper surface of this cube. In this compression test, it is assumed that $\gamma_{12} = \gamma_{23} = \gamma_{31} = 0$, and $\varepsilon_{11} = \varepsilon_{22} = 0$. For a known stress T_{11}, it yields to

$$T_{11} = (\Lambda + \alpha)\varepsilon_{33}, \quad T_{22} = \Lambda\varepsilon_{33}, \quad T_{33} = (\Lambda + 2\mu_T)\varepsilon_{33} \tag{4.24}$$

using Eq.(3.61). Using this procedure, Λ can be obtained. Strain ε_{33} in Eq.(4.24) is given as $\varepsilon_{33} = 1\%$. The sum of the nodal forces in $\boldsymbol{e}_2$ direction divided by the cross-section provides a mean stress component T_{22} and with the help of using Eq.(4.24), this leads to Λ in Tab. 4.2.

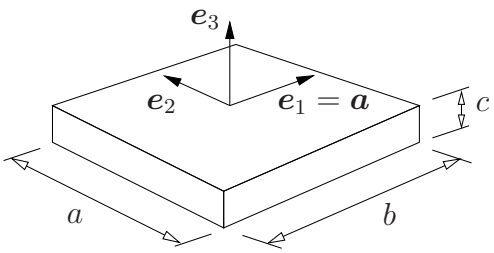

(a) Principle sketch of boundary conditions of the compression test

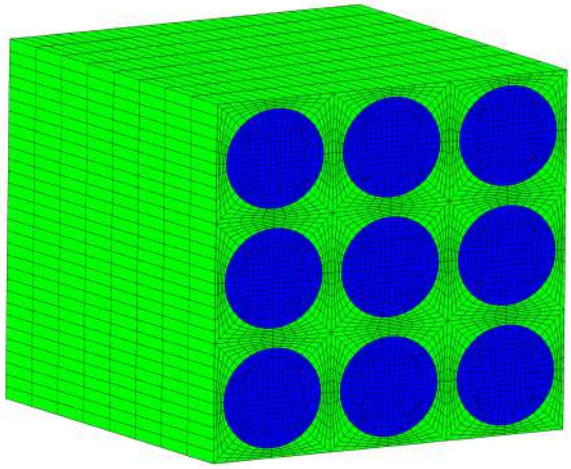

(b) Finite element mesh (20-noded hexahedral elements) for a glass a fiber volume fraction of 55%

Figure 4.21: Compression of a flat specimen

4.5.2 Tensile Test with $\gamma = 0°, 90°$ and Shear Test

After obtaining the material parameter Λ, a least-square method is used through all results of tensile tests with $\gamma = 0°, 90°$ and the results of shear tests using the force measured by the testing machine as well as maximum and minimum principal strains of the DIC-data. Finally, the material parameters $\boldsymbol{\kappa} = \{\mu_L, \alpha, \beta, \mu_T\}$ are obtained, see Tab. 4.2. The maximum principal

Table 4.2: Identified parameters from $0°$, $90°$ fiber orientation and shear tests with $0°$ fiber orientation

parameter	dimension	value
Λ	$\mathrm{N\,mm^{-2}}$	4408.89
α	$\mathrm{N\,mm^{-2}}$	93.55
β	$\mathrm{N\,mm^{-2}}$	$27\,091.83$
μ_L	$\mathrm{N\,mm^{-2}}$	3527.76
μ_T	$\mathrm{N\,mm^{-2}}$	3781.16

strains from all of five experiments with $\gamma = 0°, 90°$ and four experiments of shear tests plus using measured force of testing machine are used to identify the parameters. The maximum principal strain distribution can be seen, for instance, in Fig. 4.22. Fig. 4.23 shows a comparison

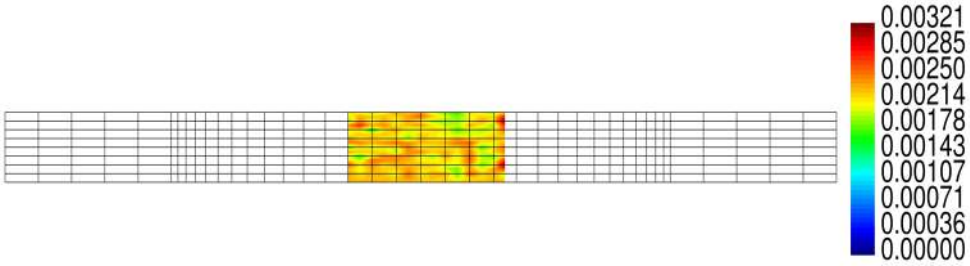

Figure 4.22: Maximum principal strain distribution for $\gamma = 0°$

between the force-displacement of the finite element simulation and the experiments. Fig. 4.24 shows the relative error between the experiment and the simulation. Therefore, all parameters are determined as mentioned above.

4.6 Identification of Orthotropy

This section focuses on identifying the material parameters for the orthotropic model assumed in Section 3.3.3. The compliance matrix $\mathbf{S}$ in Eq.(3.118) is taken into consideration. For this purpose, we need four experiments. Under the assumption of homogeneous deformations, the nine material parameters can be determined uniquely. The main steps will be explained in the following, with detailed information on every single step.

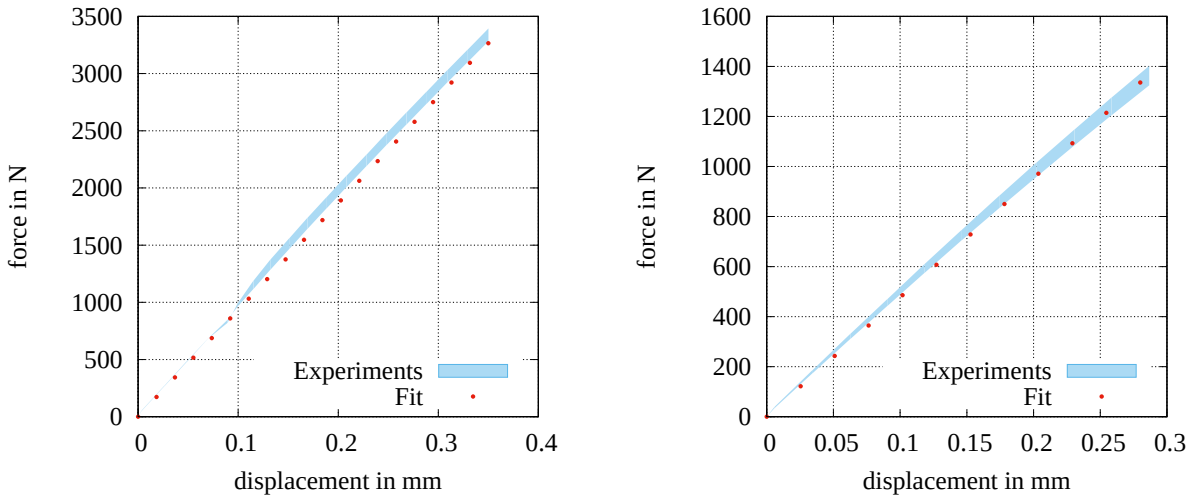

(a) Force vs displacement curve for $0°$ specimens

(b) Force vs displacement curve for $90°$ specimens

Figure 4.23: Calibrated force/displacement diagrams

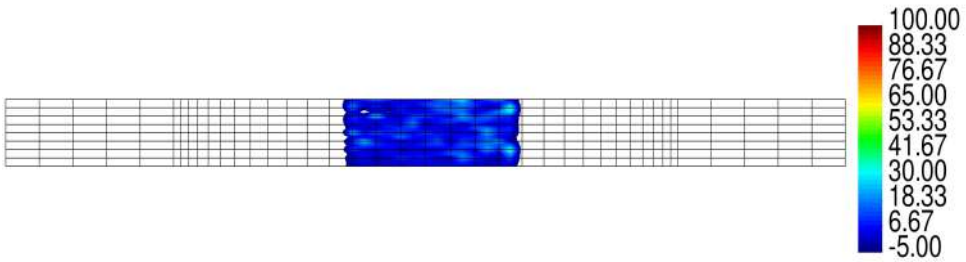

Figure 4.24: Exemplary representation of maximum principal strain error after identification for $\gamma = 0°$, (Hartmann et al., 2020)

1. First, in the tensile tests, $T_{22} = T_{33} = 0$ and for a known T_{11}, we have

$$\varepsilon_{11} = \frac{1}{E_1} T_{11}, \tag{4.25}$$

where E_1 can be obtained by $E_1 = T_{11}/\varepsilon_{11}$. For the tensile tests, using Eq.(3.118), we can write

$$\varepsilon_{22} = -\frac{\nu_{12}}{E_1} T_{11}, \tag{4.26}$$

where ν_{12} can be calculated by

$$\nu_{12} = -\frac{\varepsilon_{22} E_1}{T_{11}} = -\frac{\varepsilon_{22}}{\varepsilon_{11}}. \tag{4.27}$$

A DIC-system is used to determine ε_{11} and ε_{22}. It should be also mentioned that tensile tests also provide another relation as $\varepsilon_{33} = -\frac{\nu_{13}}{E_1} T_{11}$. However, we are not able to read ε_{33} using the DIC-system. Thus, ν_{13} cannot be obtained. Since we assumed that the fiber plies are perpendicular to each other and the same fibers are used in both directions, we obtain $E_1 = E_2$. If the fiber plies are different in both directions, $E_1 \neq E_2$, E_2 should be determined separately in another tensile experiment. In addition, using Eq.(3.119), it can be shown that

$$\nu_{21} = \frac{\nu_{12} E_2}{E_1} = \nu_{12}, \tag{4.28}$$

where ν_{12} is equal to ν_{21}.

2. Second, E_3, ν_{31} and ν_{32} can be obtained by means of a compression test. Considering Eq.(3.118) and Eq.(3.119), we can write,

$$\frac{1}{E_1} T_{11} - \frac{\nu_{21}}{E_2} T_{22} - \frac{\nu_{31}}{E_3} T_{33} = \varepsilon_{11} \tag{4.29}$$

$$-\frac{\nu_{21}}{E_2} T_{11} + \frac{1}{E_2} T_{22} - \frac{\nu_{32}}{E_3} T_{33} = \varepsilon_{22} \tag{4.30}$$

$$-\frac{\nu_{31}}{E_3} T_{11} - \frac{\nu_{32}}{E_3} T_{22} + \frac{1}{E_3} T_{33} = \varepsilon_{33}. \tag{4.31}$$

In the compression tests, a force is applied in $\boldsymbol{e}_3$ direction, see Fig. 4.17(a), and the sides in $\boldsymbol{e}_1 = \boldsymbol{a}$ and $\boldsymbol{e}_2 = \boldsymbol{b}$ are fixed which leads to $\varepsilon_{11} = \varepsilon_{22} = 0$. After obtaining $E_1 = E_2$ and $\nu_{12} = \nu_{21}$ from the tensile tests, the other three parameters are obtained from Eqns.(4.29) - (4.31). This leads to,

$$E_3 = -\frac{E_1 E_2 T_{33}^2}{\Omega} \tag{4.32}$$

$$\nu_{31} = -\frac{(E_2 T_{11} - E_1 \nu_{21} T_{22}) T_{33}}{\Omega} \tag{4.33}$$

$$\nu_{32} = -\frac{(-E_1 \nu_{21} T_{11} + E_1 T_{22}) T_{33}}{\Omega} \tag{4.34}$$

where

$$\Omega = E_2 T_{11}^2 - 2E_1\nu_{21}T_{11}T_{22} + E_1 T_{22}^2 + E_1 E_2 \varepsilon_{33} T_{33}. \tag{4.35}$$

Since we are using the same fiber in both directions, the same dimensions of the specimen, and since the side forces are expected to be the identical, we have $T_{11} = T_{22}$. Thus, it follows that ν_{31} in Eq.(4.33) is equal to ν_{32} in Eq.(4.34).

3. In the third step, G_{12} can be obtained using the three-rail shear test. Considering Eq.(3.118), it follows that

$$\gamma_{12} = \frac{1}{G_{12}} T_{12}, \tag{4.36}$$

where γ_{12} can be obtained using a DIC-system and T_{12} is obtained from the Zwick machine.

4. Fourth, we can address G_{23} using the lap shear test. Again considering Eq.(3.118), we have

$$\gamma_{23} = \frac{1}{G_{23}} T_{23}. \tag{4.37}$$

G_{23} can be obtained by computing γ_{23}, and the testing machine provides T_{23}. Since the fibers are orthogonal in two directions and the same fibers are used in both directions, G_{23} is assumed to be equal to G_{13}. All 9 parameters can be calculated based on these steps.

In following, the details in each step are discussed. In order to obtain E_1 based on a tensile test, Eq.(4.25) leads to

$$E_1 = \frac{1}{\varepsilon_{11}} T_{11}. \tag{4.38}$$

Regarding ε_{11}, it can be computed as follows, see also Fig. 4.25(a),

$$\varepsilon_{11} = \frac{\Delta L}{L_0} = \frac{L - L_0}{L_0} = \frac{(L_0 + U_R - U_L) - L_0}{L_0} = \frac{U_R - U_L}{L_0}. \tag{4.39}$$

In order to calculate the parameters, points are defined in horizontal and vertical lines, see

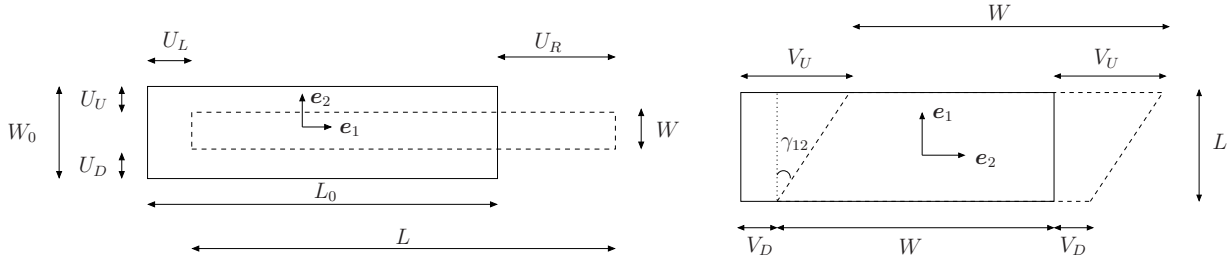

(a) Sketch for calculating ε_{11} and ε_{22}

(b) Sketch for calculating γ_{12} from three-rail shear tests

Figure 4.25: Sketches for measuring (ε_{11}, ε_{22} and γ_{12}) for obtaining parameters

Fig. 4.26. The displacements of each point for every time-step using the DIC-system are obtained. The mean displacement of right set of points in Fig. 4.26 can be represented as $U_R^{(N)}$, and it follows that

$$U_R^{(N)} = \frac{\sum_{i=1}^{n} U_i^{(N)}}{n}, \tag{4.40}$$

where n is equal to the number of points in the right side (in Fig. 4.26 $n = 4$), N is the number of total tensile experiments, $N = 1, \ldots, 5$, and $U_i^{(N)}$ represents the displacement of right points at each time step for experiment number N in $\boldsymbol{e}_1$ direction. Similarly, the mean displacement of the left set of points in $\boldsymbol{e}_1$ direction, $U_L^{(N)}$ can be obtained by

$$U_L^{(N)} = \frac{\sum_{i=1}^{n} U_i^{(N)}}{n}, \tag{4.41}$$

Thus, ε_{11} can be represented as

$$\varepsilon_{11}^{(N)} = \frac{U_R^{(N)} - U_L^{(N)}}{L_0^{(N)}}, \tag{4.42}$$

where $L_0^{(N)}$ is equal to the initial length between these two sets of points. T_{11} can be obtained using the measured force $F^{(N)}$ for each time step (obtained from the Zwick machine). Then, the Young's modulus E_1 in Eq.(4.38) can be calculated as

$$E_1^{(N)} = \frac{F^{(N)}}{A_0^{(N)}} \frac{L_0^{(N)}}{U_R^{(N)} - U_L^{(N)}}. \tag{4.43}$$

In the next step, ν_{21} can be obtained using Eq.(4.27). For ε_{22}, it is possible to calculate as follows, see also Fig. 4.25(a),

$$\varepsilon_{22} = \frac{\Delta W}{W_0} = \frac{W - W_0}{W_0} = \frac{(W_0 - U_U - U_D) - W_0}{W_0} = -\frac{U_U + U_D}{W_0}. \tag{4.44}$$

The mean displacement of the upper and bottom set of points in Fig. 4.26 in vertical direction $\boldsymbol{e}_2$ can be represented as $U_U^{(N)}$ and $U_D^{(N)}$, where the mean displacement of the upper set of points for each time step in Fig. 4.26 can be represented as

$$U_U^{(N)} = \frac{\sum_{i=1}^{n} V_i^{(N)}}{n}, \tag{4.45}$$

and n is equal to the number of points on the upper side (in Fig. 4.26 $n = 18$) and $V_i^{(N)}$ represents the displacement of the points in the upper part for each time step regarding experiment number N in $\boldsymbol{e}_2$ direction. Similarly, the mean displacement of the bottom set of points, $U_D^{(N)}$ can be obtained by

$$U_D^{(N)} = \frac{\sum_{i=1}^{n} V_i^{(N)}}{n}. \tag{4.46}$$

Thus, ε_{22} is equal to

$$\varepsilon_{22} = -\frac{U_U^{(N)} + U_D^{(N)}}{W_0^{(N)}}. \tag{4.47}$$

where $W_0^{(N)}$ is the distance (width) between the upper and the bottom set points in the reference configuration and ε_{11} was already obtained by Eq.(4.42). Thus, ν_{21} can be calculated using Eq.(4.27).

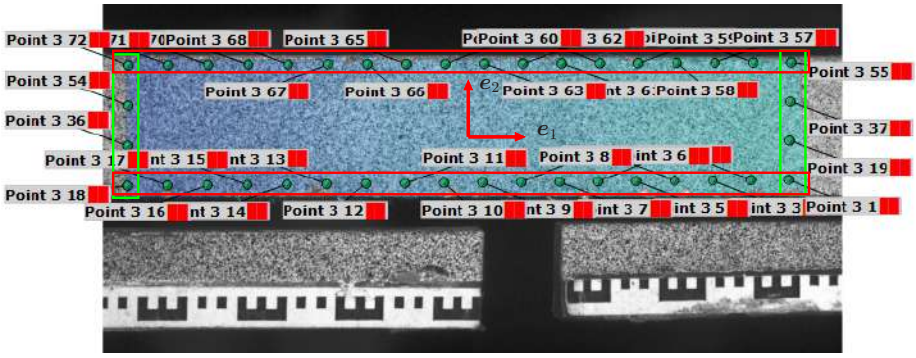

Figure 4.26: Generated points on the surface of tensile test samples

In the second step, using Eqns.(4.32) - (4.34), we obtain E_3, ν_{31}, and ν_{32} are obtained. $E_1 = E_2$ and $\nu_{12} = \nu_{21}$ are known from tensile tests. On the other hand, T_{11}, T_{22}, T_{33} and ε_{33} are unknowns, and the following steps serve to calculate the unknowns.

- In the compression tests, using the force $F_3^{(N)}$ in $\boldsymbol{e}_3$ direction, which is obtained using the compression tool, T_{33} for each time step can be calculated as, see also Fig. 4.17(a),

$$T_{33} = \frac{F_3^{(N)}}{A_3^{(N)}} \tag{4.48}$$

  where $A_3^{(N)} = w_1 w_2$ and N represents the number of experiment.

- Using the force in $\boldsymbol{e}_2$ direction F_2, T_{22} can be obtained using $T_{22} = \frac{F_2^{(N)}}{A_2^{(N)}}, A_2^{(N)} = w_2 t$.

- Similarly, applying the force in $\boldsymbol{e}_1$ direction F_1, T_{11} can be calculated using $T_{11} = \frac{F_1^{(N)}}{A_1^{(N)}}, A_1^{(N)} = w_1 t$, see again Fig. 4.17(a). Since the same fibers are used in both. Both in $\boldsymbol{e}_1$ and $\boldsymbol{e}_2$ direction, the side forces are assumed to be equal, from which follows that $T_{22} = T_{11}$.

- ε_{33} can be obtained by dividing the displacement in $\boldsymbol{e}_3$ direction (with consideration of rigid body movement) to the thickness of sample, which is shown in Fig. 4.17(a) for each experiment.

In the third step, using the three-rail shear test, the shear modulus G_{12} is obtained, see Eq.(4.36). For γ_{12}, the following can be computed, see also Fig. 4.25(b),

$$\gamma_{12} \approx tan\gamma_{12} = \frac{V_U - V_D}{L} \tag{4.49}$$

Points with equal distances are generated on the surface of the samples, as can be seen in Fig. 4.27. The mean value the displacements in $\boldsymbol{e}_2$ direction for each time-step are calculated

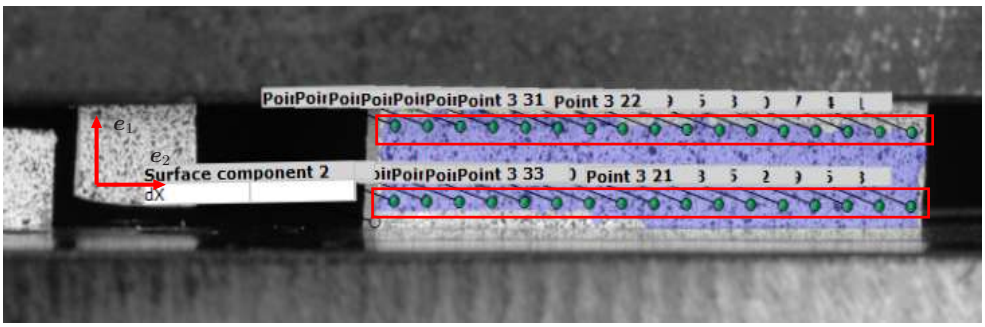

Figure 4.27: Generated points on the surface of shear test samples

for these two sets of points using the DIC-system. The mean displacement of the upper set in $\boldsymbol{e}_2$ direction can be represented as $V_U^{(N)}$,

$$V_U^{(N)} = \frac{\sum_{i=1}^{n} V_i^{(N)}}{n}, \tag{4.50}$$

where n is equal to the number of points on the upper side (in Fig. 4.27 we have $n = 17$) and $V_D^{(N)}$ represents the displacement of bottom points at every time step for experiment number N. Similarly, the mean displacement of the bottom set of points in $\boldsymbol{e}_2$ direction, $V_D^{(N)}$ can be obtained by

$$V_D^{(N)} = \frac{\sum_{i=1}^{n} V_i^{(N)}}{n}. \tag{4.51}$$

The force $F^{(N)}$ is applied in $\boldsymbol{e}_2$ direction, see Fig. 4.12(a), and it can be obtained from the Zwick force gauge. Since we are only considering one part of the three-rail shear test, half of the force is considered in our equation. $L^{(N)}$ is the distance between the upper and bottom set of points in reference configuration. In addition, $A^{(N)}$ is also known for every experiment, see Fig. 4.12(a). For each time step, G_{12} can be computed as

$$G_{12}^{(N)} = \frac{T_{12}}{\gamma_{12}} = \frac{1}{2}\frac{F^{(N)}}{A^{(N)}}\frac{L^{(N)}}{V_U^{(N)} - V_D^{(N)}}. \tag{4.52}$$

In the fourth step, the lap shear test is performed to determine G_{23} using Eq.(4.37). The concept for obtaining the parameter G_{23} is similar to the three-rail shear test. For γ_{23}, it follows that, see also Fig. 4.28,

$$\gamma_{23} \approx tan\gamma_{23} = \frac{V_U - V_D}{T} \tag{4.53}$$

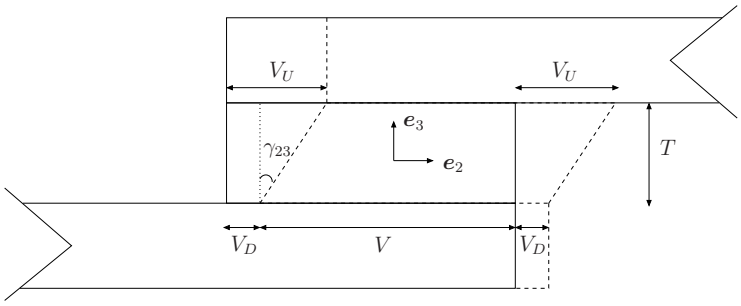

Figure 4.28: Sketch for calculating γ_{23} from lap shear test

Using the displacement generated by the Zwick machine $V_U^{(N)}$ and $V_D^{(N)}$ in $\boldsymbol{e}_2$ direction and the thickness of sample $T^{(N)} = 2.6$ in this test, see Fig. 4.14(a), G_{23} can be obtained using,

$$G_{23}^{(N)} = \frac{F^{(N)}}{A^{(N)}} \frac{T^{(N)}}{V_U^{(N)} - V_D^{(N)}}, \tag{4.54}$$

where $F^{(N)}$ is obtained by the Zwick machine for $N = 1, \ldots, 5$, and $A^{(N)}$ is known, see again Fig. 4.14(a).

In each step, we determine the material parameter from the corresponding five tests using a least-square method. We proceed step by step, as discussed before. Thus, E_1, E_2, and ν_{12} are obtained from the tensile tests. ν_{32}, ν_{31} and E_3 are acquired from the compression tests. G_{12} is obtained from three-rail shear tests. The last two parameters, G_{23} and G_{13} are captured using the lap shear tests. The resulting material parameters $\boldsymbol{\kappa}_{\mathrm{S}} = \{E_1, E_2, E_3, \nu_{12}, \nu_{32}, \nu_{31}, G_{12}, G_{23}, G_{13}\}$ are compiled in Tab. 4.3. The parameters satisfy the conditions in Eqns.(3.131) - (3.136). The results of the identification according to the aforementioned procedure are shown in Fig. 4.29 and Fig. 4.30. In each diagram, the blue region demonstrates experimental results. Since the experiments are repeated five times, an area is obtained for each experiment and this area shows the dispersion within the result of each experiment.

We are also interested in determining the uncertainty of $E_3(E_1, E_2, \nu_{12})$, $\nu_{31}(E_1, E_2, \nu_{12})$ and $\nu_{32}(E_1, E_2, \nu_{12})$, see Eqns.(4.32) - (4.34). To obtain the uncertainty, we draw on the linear error propagation theory, see (Taylor, 1997). A function $f(\boldsymbol{\kappa})$ with the estimated deviation $\Delta\boldsymbol{\kappa}$ yields the uncertainty

$$\delta f = \sqrt{\sum_{k=1}^{n_\kappa} \left(\frac{\partial f}{\partial \kappa_k} \Delta\kappa_k \right)^2}, \tag{4.55}$$

i.e. $f \pm \delta f$, evaluated at the best fit $\boldsymbol{\kappa}$ obtained by the other parameters. Here, $\Delta\kappa_k$ is taken as the standard deviation.

Using the data in Tab. 4.3, the compliance matrix $\mathbf{S}$ in Eq.(3.109) can be calculated. In the next step, $\mathbf{C}$ can be computed using Eq.(3.110) and Eq.(3.111), see Tab. 4.4. The uncertainty of $C_{11}(E_1, E_2, E_3, \nu_{32}, \nu_{31}, \nu_{21})$, $C_{12}(E_1, E_2, E_3, \nu_{32}, \nu_{31}, \nu_{21})$, $C_{13}(E_1, E_2, E_3, \nu_{32}, \nu_{31}, \nu_{21})$, $C_{22}(E_1, E_2, E_3, \nu_{32}, \nu_{31}, \nu_{21})$, $C_{23}(E_1, E_2, E_3, \nu_{32}, \nu_{31}, \nu_{21})$, $C_{33}(E_1, E_2, E_3, \nu_{32}, \nu_{31}, \nu_{21})$, $C_{44}(G_{12})$, $C_{55}(G_{23})$, $C_{66}(G_{31})$ are also determined based on the linear error propagation theory

Table 4.3: Identified parameters $\boldsymbol{\kappa}_{\mathrm{S}}$ for orthotropy laminates from tensile, compression, three-rail shear, and lap shear tests

	parameter	dimension	value	error propagation
	E_1	$\mathrm{N\,mm^{-2}}$	26 808.4	± 130.6
	E_2	$\mathrm{N\,mm^{-2}}$	26 808.4	± 130.6
	E_3	$\mathrm{N\,mm^{-2}}$	2361.6	± 80.7
	ν_{12}	$-$	0.11	± 0.06
$\boldsymbol{\kappa}_{\mathrm{S}}$	ν_{32}	$-$	0.002	± 0.00016
	ν_{31}	$-$	0.002	± 0.00016
	G_{12}	$\mathrm{N\,mm^{-2}}$	6406.8	± 213.7
	G_{23}	$\mathrm{N\,mm^{-2}}$	7841.7	± 21.2
	G_{13}	$\mathrm{N\,mm^{-2}}$	7841.7	± 21.2

by Eq.(4.55), see again Tab. 4.4. In this case, larger errors can be seen in comparison to errors in Tab. 4.3 since $\mathbf{C}$ depends on the elements in the compliance matrix $\mathbf{S}$.

Table 4.4: Identified parameters $\boldsymbol{\kappa}_{\mathrm{C}}$ for orthotropy laminates from tensile, compression, three-rail shear, and lap shear tests

	parameter	dimension	value	error propagation
	C_{11}	$\mathrm{N\,mm^{-2}}$	27 172.3	± 166.7
	C_{12}	$\mathrm{N\,mm^{-2}}$	3138.9	± 102.4
	C_{13}	$\mathrm{N\,mm^{-2}}$	61.5	± 1943.6
	C_{22}	$\mathrm{N\,mm^{-2}}$	27 172.3	± 166.7
$\boldsymbol{\kappa}_{\mathrm{C}}$	C_{23}	$\mathrm{N\,mm^{-2}}$	61.5	± 1943.6
	C_{33}	$\mathrm{N\,mm^{-2}}$	2361.9	± 82.29
	C_{44}	$\mathrm{N\,mm^{-2}}$	6406.8	± 213.7
	C_{55}	$\mathrm{N\,mm^{-2}}$	7841.8	± 21.2
	C_{66}	$\mathrm{N\,mm^{-2}}$	7841.8	± 21.2

Ultimately, the material parameters $\boldsymbol{\kappa}_{\mathrm{SP}} = \{\mu_1, \mu_2, \mu, \Lambda, \alpha_1, \alpha_2, \beta_1, \beta_2, \beta_3\}$ are obtained using Eqns.(3.100) - (3.107) which is required for the fourth order elasticity tensor $\mathcal{C}$ in Eq.(3.95). μ_2 is equal to zero, since C_{66} and C_{55} are equal. These parameters are shown in Tab. 4.5. Again, the uncertainties of $\mu_1(C_{44}, C_{66})$, $\mu_2(C_{55}, C_{66})$, $\mu(C_{44}, C_{55}, C_{66})$, $\Lambda(C_{33}, C_{44}, C_{55}, C_{66})$, $\beta_1(C_{11}, C_{33}, C_{55}, C_{13})$, $\beta_2(C_{22}, C_{33}, C_{44}, C_{23})$, $\beta_3(C_{33}, C_{44}, C_{55}, C_{66}, C_{23}, C_{12}, C_{13})$, $\alpha_1(C_{33}, C_{44}, C_{55}, C_{66}, C_{13})$, $\alpha_2(C_{33}, C_{44}, C_{55}, C_{66}, C_{23})$ are calculated with the help of the linear error propagation theory by Eq.(4.55), see Tab. 4.5.

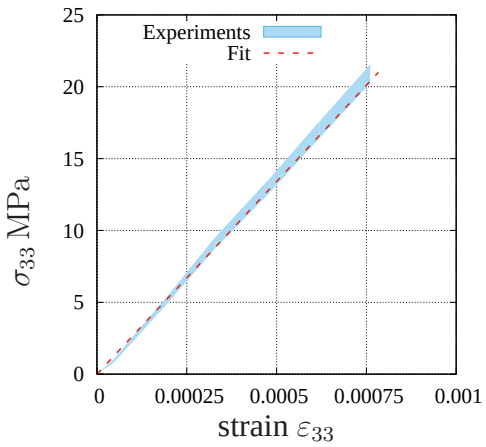

(a) Axial stress vs axial strain for tensile tests

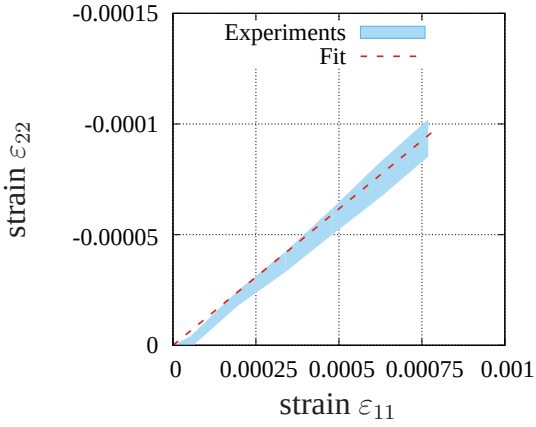

(b) Lateral strain vs axial strain for tensile tests specimens

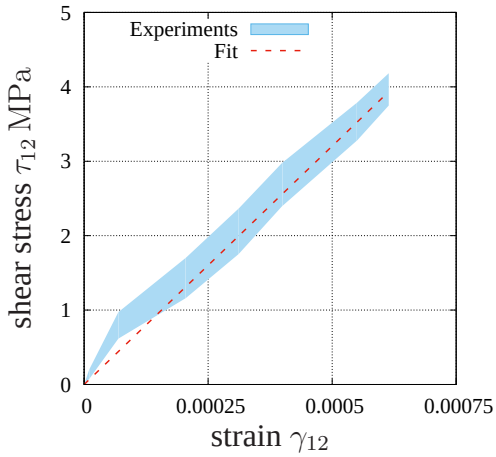

(c) Shear stress vs shear strain for three-rail shear experiments

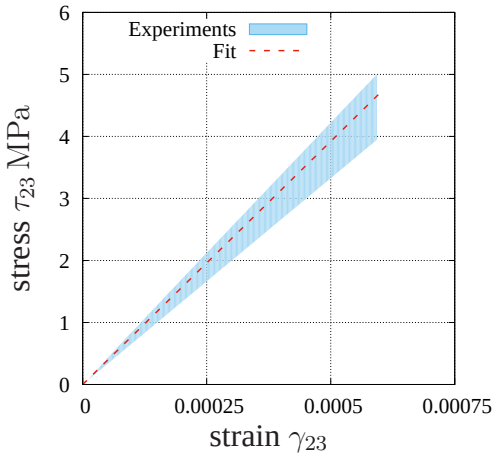

(d) Axial stress vs axial strain for lap shear tests

Figure 4.29: Calibrated experiment-fit diagrams of tensile, three-rail shear, and lap shear tests for orthotropic samples

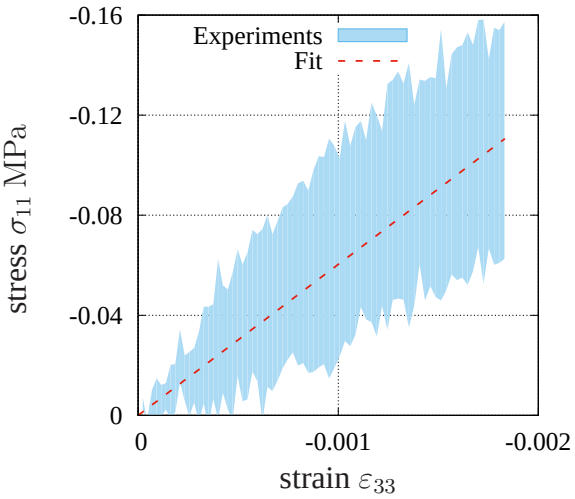

(a) Lateral stress vs axial strain of compression tests

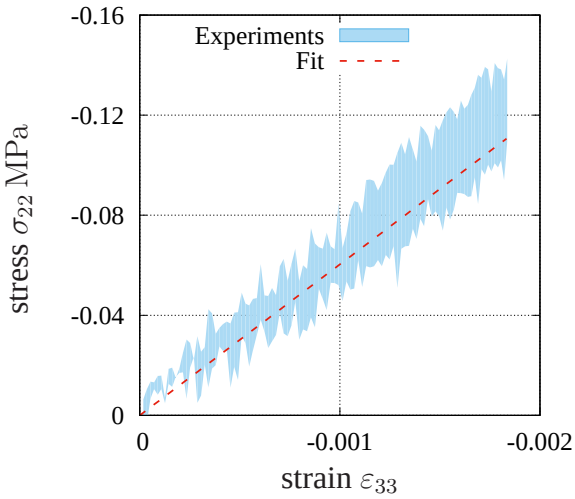

(b) Lateral stress vs axial strain of compression tests

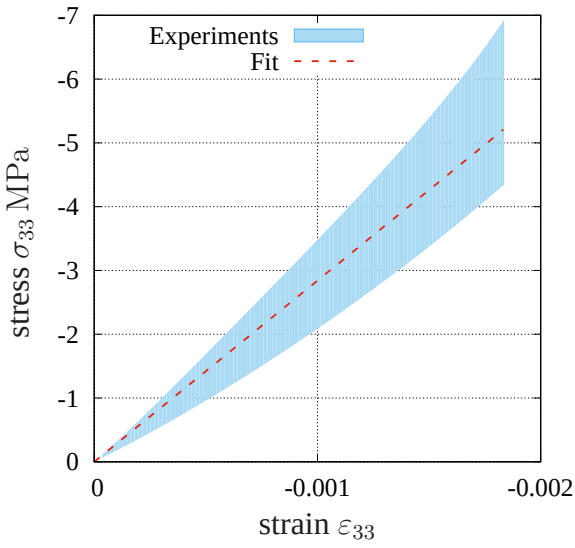

(c) Axial stress vs axial strain of compression tests

Figure 4.30: Calibrated result diagrams of compression tests for samples with two fiber directions

Table 4.5: Identified parameters $\boldsymbol{\kappa}_{\mathrm{SP}}$ for orthotropy laminates from tensile, compression, three-rail shear, and lap shear tests

	parameter	dimension	value	error propagation
$\boldsymbol{\kappa}_{\mathrm{SP}}$	μ_1	$\mathrm{N\,mm^{-2}}$	1435	± 213.7
	μ_2	$\mathrm{N\,mm^{-2}}$	0	± 29.9
	μ	$\mathrm{N\,mm^{-2}}$	6406.8	± 21.2
	Λ	$\mathrm{N\,mm^{-2}}$	$-10\,451.7$	± 435
	β_1	$\mathrm{N\,mm^{-2}}$	-1955.9	± 436.4
	β_2	$\mathrm{N\,mm^{-2}}$	3783.9	± 656.1
	β_3	$\mathrm{N\,mm^{-2}}$	-7435.9	± 1832.7
	α_1	$\mathrm{N\,mm^{-2}}$	$10\,513.2$	± 435
	α_2	$\mathrm{N\,mm^{-2}}$	$10\,513.2$	± 435

5 Geometric Modeling

5.1 Introduction

Over the last decades, geometric modeling has gained increasing attention. B-spline and Bézier curves (which are a special case of B-splines) are the two most commonly used methods for designing shapes. Here, B-spline curves provide more control flexibility than Bézier curves, since the parameters are not dependent on each other. B-spline is a powerful standard method for the representation of different shapes where complex data and physical properties have to be presented and modeled. For instance, the wings of an airplane can be modeled using B-spline patches, see (Brakhage and Lamby, 2008b).

Cutting fibers by drilling a hole in fiber composite laminates can be seen as a common process technology. In another approach, fibers can be bypassed around the hole in order to avoid cutting fibers, see Fig. 4.21. In this work, we need a mathematical function to describe the spatially distributing fiber orientation $\boldsymbol{a} = \boldsymbol{a}(\boldsymbol{x})$ as it is necessary for finite element simulations. Thus, the streamline approach is discussed as a first approach to determine fiber orientation. Furthermore, B-splines are introduced as another suitable method for describing fiber direction due to its high flexibility. This chapter focuses on B-spline properties, and it is shown how surfaces for finite element simulation are generated. In the next step, a unit tangent vector for finite element simulation using B-splines is obtained.

5.2 Streamline Approach

In this section, fiber orientation is presented using a streamline function to obtain continuously distributed fiber directions. In (White, 2009), the streamlines are defined by

$$\Psi = \hat{\Psi}(U_\infty, \theta, r, R, k) = U_\infty \sin\theta \left(r - \frac{R^2}{r} \right) - k \frac{\log r}{R}. \tag{5.1}$$

We define $k = 0$, $a = \Psi / U_\infty$, $x = r\cos\theta$, and $y = r\sin\theta$, which leads to

$$g(x, y, a) = y^3 - ay^2 + (x^2 - R^2)y - ax^2 = 0 \tag{5.2}$$

representing a cubic polynomial in y, where R represents the radius of a hole. Next, we consider the real solution of Eq.(5.2), which can be presented as

$$\hat{y}(x, a) \;=\; \frac{1}{6} \left(2^{2/3} \sqrt[3]{2a^3 + \zeta + 9aR^2 + 18ax^2} + \frac{2\left(a^2 + 3(R - x)(R + x)\right)}{\sqrt[3]{a^3 + \frac{1}{2}\zeta + \frac{9aR^2}{2} + 9ax^2}} + 2a \right). \tag{5.3}$$

with

$$\zeta = \sqrt{\left(2a^3 + 9aR^2 + 18ax^2\right)^2 - 4\left(a^2 + 3(R-x)(R+x)\right)^3}.$$

Fig. 5.1 shows the orientation lines for different a. The arbitrary factor a is constructed in a such

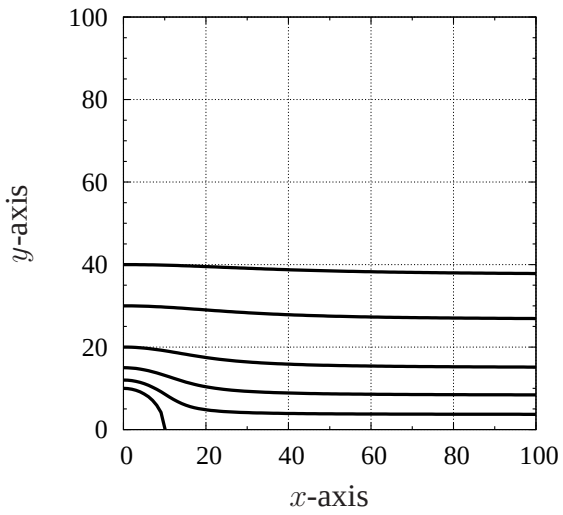

Figure 5.1: Orientation distribution of fibers using streamline functions

way that it has a geometrical meaning, which is studied in the following. Then, Eq.(5.2) can be written as,

$$f(x, y) := g(x, y, a). \tag{5.4}$$

The position vector should be differentiated with respect to x in order to obtain the tangent vector as

$$\boldsymbol{r} = x\boldsymbol{e}_x + \hat{y}(x)\boldsymbol{e}_y, \tag{5.5}$$

$$\hat{y}'(x) = -f_{,x}\,/f_{,y}\,. \tag{5.6}$$

The tangent vector $\boldsymbol{t}(x)$ is equal to

$$\boldsymbol{t}(x) = \frac{\mathrm{d}\boldsymbol{r}}{\mathrm{d}x} = \boldsymbol{e}_x + \hat{y}'(x)\boldsymbol{e}_y = \boldsymbol{e}_x - f_{,x}\,/f_{,y}\,\boldsymbol{e}_y. \tag{5.7}$$

To obtain a unit vector at a point $x = x_1$ and $y = y_1$

$$\boldsymbol{a}(x_1, y_1) = \left.\frac{\boldsymbol{t}(x_1)}{|\boldsymbol{t}(x_1)|}\right|_{x=x_1, y=y_1}, \tag{5.8}$$

with

$$|\boldsymbol{t}(x)| = \sqrt{1 + f_{,x}^{\,2}\, f_{,y}^{\,-2}} = \sqrt{f_{,y}^{\,-2}}\sqrt{f_{,x}^{\,2} + f_{,y}^{\,2}}. \tag{5.9}$$

Then, $\boldsymbol{a}$ can be written as

$$\boldsymbol{a} = \frac{1}{\sqrt{f_{,x}^2 + f_{,y}^2}} \left(\sqrt{f_{,y}^2}\boldsymbol{e}_x - f_{,x} \frac{\sqrt{f_{,y}^2}}{f_{,y}} \boldsymbol{e}_y \right), \tag{5.10}$$

where the unit tangent vector can be obtained at any point like $x = x_1$ and $y = y_1$. Regarding Eq.(5.2), $f_{,x}$ and $f_{,y}$ can be presented as

$$f_{,x} = 2x(y-a), \quad f_{,y} = x^2 - R^2 - 2ay + 3y^2 \tag{5.11}$$

with

$$a = \frac{(x^2 - R^2)y + y^3}{x^2 + y^2}. \tag{5.12}$$

This method is not complicated in comparison to other methods such as B-spline. Considering the streamline approach, there is no need for experimental data. On the other hand, since no real or experimental data are used, it has to be assumed that the fibers are oriented in a certain manner. However, the implementation and the basic concept of the streamline approach are straightforward.

5.3 Definition and Properties of B-Spline Basis Functions

The streamline approach introduced in the previous section is an efficient and fast method to represent fiber orientation but the aim is to find a more precise approach. The mathematical theory of spline approximation is introduced by (Schoenberg, 1959), where he developed splines for creating curves using initial points. Later on, other works such as (De Boor, 1972; Riesenfeld, 1973) promoted the usage of splines for the field of computer-aided design. Using B-splines to obtain curves and surfaces is a very popular approach in the broad field of geometric modeling. This is mainly due to their mathematical properties and their flexibility. For a better understanding, we will first take a closer look at the B-spline curve and the according fundamental relations. In the next step, we will discuss the way B-splines are used to generate surfaces in this work. In this thesis, all of the fiber orientations in the samples are modeled with the help of B-splines where the curvilinear coordinates represent the fibers. The concept of this section is mainly based on books and other literature dealing with NURBS and B-spline, such as (De Boor, 1978; Piegl and Tiller, 1997; Rogers, 2001).

5.4 B-Spline Curve

Having $\boldsymbol{p}(\xi)$ as a position vector, a B-spline curve can be defined as

$$\boldsymbol{p}(\xi) = \sum_{i=1}^{n_c} N_{i,k}(\xi)\boldsymbol{b}_i. \tag{5.13}$$

The number of control points is presented by n_c for a B-spline curve, and it is defined as a polynomial spline function of order k or degree $k-1$ where k must be at least two. In general, a B-spline is considered as a polynomial spline function of order k because it satisfies the following two conditions (Rogers, 2001).

- Each component of $\boldsymbol{p}$ is a polynomial of degree $k-1$ in each interval $\Xi_i \leq \xi < \Xi_{i+1}$.
- $\boldsymbol{p}$ and its derivative of order $1, 2, \ldots, k-2$ are continuous during the whole curve.

$N_{i,k}(\xi)$ represents B-spline basis functions having the index $2 \leq k \leq n_c$. The $\boldsymbol{b}_i$'s are the position vectors of the n_c control polygon vertices, and it can be determined from initial data points. The B-spline basis functions $N_{i,k}(\xi)$ are defined by the Cox-de Boor recursive definition

$$N_{i,k}(\xi) = \frac{\xi - \Xi_i}{\Xi_{i+k-1} - \Xi_i} N_{i,k-1}(\xi) + \frac{\Xi_{i+k} - \xi}{\Xi_{i+k} - \Xi_{i+1}} N_{i+1,k-1}(\xi) \tag{5.14}$$

with the basis

$$N_{i,1}(\xi) = \begin{cases} 1 & \text{if} \quad \Xi_i \leq \xi < \Xi_{i+1}, \\ 0 & \text{otherwise}, \end{cases} \tag{5.15}$$

see (Piegl and Tiller, 1997; Rogers, 2001). In the case of $0/0$ of the fractions in Eq.(5.14), a value of zero is assumed, see (Piegl and Tiller, 1997). A B-spline curve depends on parameters which defines it, determining the order of the curve. These are the knot vector and the control points, which have a significant influence.

5.4.1 Properties of B-Spline Curve

There exist several properties for B-splines in addition to those that were already mentioned.

- Each basis function $N_{i,k}$ cannot be less than zero for all parameters.
- The curve generally follows the shape of the control points, (Rogers, 2001).
- The sum of the B-spline basis functions for any value ξ is

$$\sum_{i=1}^{n_c} N_{i,k}(\xi) = 1, \tag{5.16}$$

  see (De Boor, 1972; Rogers, 2001).

- The curve can be transformed by any change in control points.
- Cox-de Boor relation Eq.(5.14), which is used to define B-spline basis function, is a recursive formula, i.e. a basis function of prescribed order k relies on lower order basis functions down to order one. The calculation of the $k-1$ degree functions leads to a triangular pattern table as follows

$$
\begin{array}{ccccccc}
N_{i,k} & & & & & & \\
N_{i,k-1} & N_{i+1,k-1} & & & & & \\
N_{i,k-2} & N_{i+1,k-2} & N_{i+2,k-2} & & & & \\
N_{i,k-3} & N_{i+1,k-3} & N_{i+2,k-3} & N_{i+3,k-3} & & & \\
\vdots & & & & \vdots & & \\
N_{i,1} & N_{i+1,1} & N_{i+2,1} & N_{i+3,1} & N_{i,k} & \dots & N_{i+k-1,1}
\end{array}
$$

for more details, see (Gopi and Manohar, 1997; Rogers, 2001).

5.4.2 Knot Vector

The knot vector is one of the main parameters to define B-spline basis functions. There is a wide range of research regarding the knot vector. An algorithm has been presented by (Sapidis and Farin, 1990b) for fairing a B-spline curve using the knot vector. A knot removal strategy for splines was presented in (Lyche and Mørken, 1987). The Knot removal strategy is also discussed in (Eck and Hadenfeld, 1995). In (Guo and Li, 2020), a method was provided to obtain adequate geometric shape even for data with considerable noise. Further details on the knot vector can be found in (Cohen et al., 1980; Gordon and Riesenfeld, 1974; Li et al., 2005).

The B-spline basis functions depend on the knot values Ξ_i, $i = 1, \dots, n_{\text{kv}}$, with $n_{\text{kv}} = n_{\text{c}} + k$, and this condition should always be satisfied when used to define B-spline curves. Commonly, theses values are assembled in the knot vector $\boldsymbol{\Xi} = \{\Xi_1, \dots, \Xi_{n_{\text{kv}}}\}$, where the knot values have a significant influence on the shape of the curve (and represent the flexibility of a B-spline function). The only requirement for a knot vector is that it has to satisfy the condition $\Xi_i \leq \Xi_{i+1}$, representing a non-decreasing series of real numbers. Basically, two types of knot vectors can be used: periodic and open. Here, an open and uniform normalized knot vector is used to obtain the knot vector, where the knot entries Ξ_1 and $\Xi_{n_{\text{c}}+1}$ are chosen to have the multiplicity of k so that the first and last control points are equal to the first and the last points of our data, see (Piegl and Tiller, 1987). We choose the knot values as follows: First, we generate the values

$$
\hat{\Xi}_i = \begin{cases} 0 & \text{for } 1 \leq i \leq k \\ i - k & \text{for } k+1 \leq i \leq n_{\text{c}} \\ n_{\text{c}} + 1 - k & \text{for } n_{\text{c}} + 1 \leq i \leq n_{\text{c}} + k \end{cases} \tag{5.17}
$$

and normalize them to $\Xi_i = \hat{\Xi}_i / (n_{\text{c}} + 1 - k)$, $i = 1, \dots, n_{\text{kv}}$. Further discussions on knot vector formulations are provided in (Haron et al., 2012b; Jung and Kim, 2000a; Li et al., 2005; Park and Kim, 1996).

The parameter value ξ for each data point is a measure of the distance of the data point with respect to the B-spline curve, see Fig. 5.2(a). This parameter can be obtained in different ways. Investigations regarding the possibilities of obtaining this parameter can be found, for example, in (Jung and Kim, 2000b). Parameterization methods for calculating this parameter are discussed in (Haron et al., 2012a), while a new methodology is proposed in this work. Many other Parameterization methods have been suggested, see for example, (Cohen and O'dell, 1989; Foley and

Nielson, 1989; Lee, 1989; Rogers and Fog, 1989b). One useful method for defining this parameter is the chord length method, see (Piegl and Tiller, 1997; Rogers, 2001). The distance between the data points is given by

$$d_j = \|\boldsymbol{d}_j - \boldsymbol{d}_{j-1}\|, \quad j = 2, \ldots, n_\mathrm{d}. \tag{5.18}$$

Using $\xi_1 = 0$, the ξ_l can be defined as

$$\xi_l = \frac{\sum_{j=2}^{l} d_j}{\sum_{j=2}^{n_\mathrm{d}} d_j}, \quad \text{for} \quad 2 \leq l \leq n_\mathrm{d} \tag{5.19}$$

and ξ can vary between ξ_{min} and ξ_{max}. In this work, ξ is normalized, while $\xi_{\text{min}} = 0$ and $\xi_{\text{max}} = 1$.

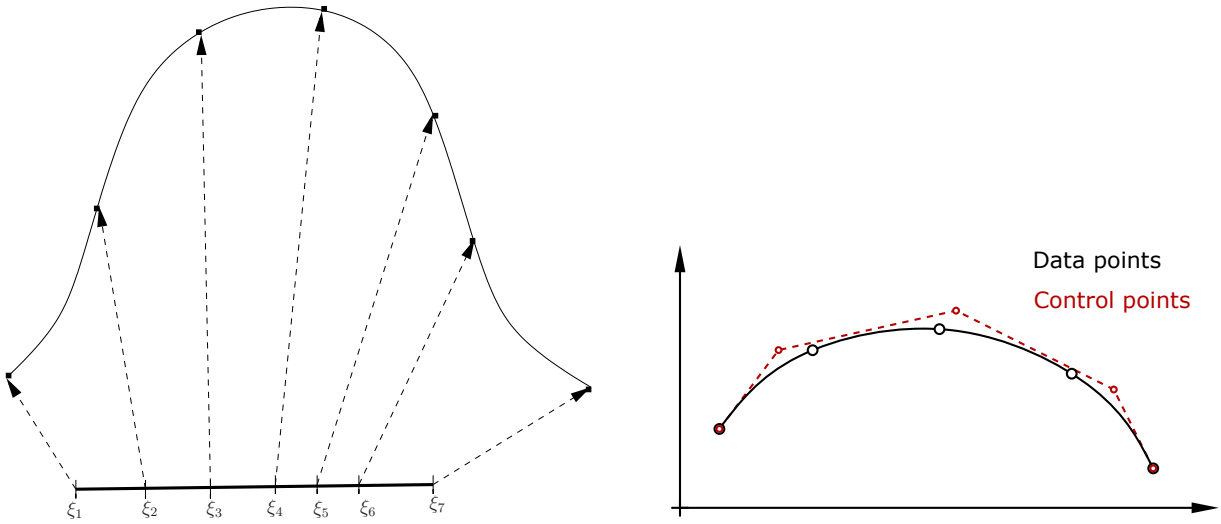

(a) Parameter ξ (b) Data points and control points

Figure 5.2: B-spline basis function

5.4.3 Control Points

Another significant parameter is control point $\boldsymbol{b}_i$, which is needed to generate a B-spline curve, see Fig. 5.2(b). A B-spline curve is strongly influenced by the control points. For this reason, any modification in the control points cause changes in the final curve. There exist many works dealing with control points and all the possibilities to define this parameter. For instance, Yang et al. (2004) proposes a new technique to adjust the control points of a B-spline curve using an optimization scheme to adapt the curve to given data points. Another approach is presented for B-spline curves fitting to a sequence of points while satisfying the desired shape, see (Park and Lee, 2007). The application of control points in shape optimization is investigated in (Hu et al., 2001; Qian, 2010). (Lin et al., 2004; Ma and Kruth, 1998) are further works that draw on different approaches to determine control points.

In this work, it is assumed that the first and the last control point are equal to the first and the last data point,

$$\boldsymbol{p}(0) = \boldsymbol{d}_1, \qquad \text{and} \qquad \boldsymbol{p}(1) = \boldsymbol{d}_{n_\mathrm{d}}, \tag{5.20}$$

or it can be presented like

$$\boldsymbol{b}_1 = \boldsymbol{d}_1 \qquad \text{and} \qquad \boldsymbol{b}_{n_\mathrm{c}} = \boldsymbol{d}_{n_\mathrm{d}}, \tag{5.21}$$

see also (De Boor, 1972; Montemurro and Catapano, 2019; Piegl and Tiller, 1997; Rogers, 2001). Using a least-square method, the curve (5.13) has to be fitted to the given data points. The coefficients of the geometrical vector components of $\boldsymbol{p}(\xi) \in \mathbb{V}^3$ and $\boldsymbol{d}_j \in \mathbb{V}^3$, $j = 1, \ldots, n_\mathrm{d}$, are written into column vectors $\mathbf{p}(\xi) \in \mathbb{R}^3$ and $\mathbf{d}_j \in \mathbb{R}^3$. The residual of each data point is defined by

$$\mathbf{r}_j(\mathbf{b}_2, \mathbf{b}_3, \ldots, \mathbf{b}_{n_\mathrm{c}-1}) = \mathbf{p}(\xi_j) - \mathbf{d}_j. \tag{5.22}$$

Using Eq.(5.21), the polynomial representation of $\mathbf{p}(\xi)$ can be written as

$$\mathbf{p}(\xi) = N_{1,k}(\xi)\mathbf{d}_1 + N_{n_\mathrm{c},k}(\xi)\mathbf{d}_{n_\mathrm{d}} + \sum_{i=2}^{n_\mathrm{c}-1} N_{i,k}(\xi)\mathbf{b}_i = \mathbf{s}(\xi) + \sum_{i=2}^{n_\mathrm{c}-1} N_{i,k}(\xi)\mathbf{b}_i, \tag{5.23}$$

with $\mathbf{s}(\xi) := N_{1,k}(\xi)\mathbf{d}_1 + N_{n_\mathrm{c},k}(\xi)\mathbf{d}_{n_\mathrm{d}}$. The sum of the squares of the residuals (5.22) should be minimized,

$$f(\mathbf{b}_2, \mathbf{b}_3, \ldots, \mathbf{b}_{n_\mathrm{c}-1}) = \frac{1}{2}\sum_{j=2}^{n_\mathrm{d}-1} \|\mathbf{r}_j(\mathbf{b}_2, \mathbf{b}_3, \ldots, \mathbf{b}_{n_\mathrm{c}-1})\|^2 = \frac{1}{2}\sum_{j=2}^{n_\mathrm{d}-1} \mathbf{r}_j^T \mathbf{r}_j \longrightarrow \min. \tag{5.24}$$

All vectors and residuals can be compiled into column vectors

$$\overline{\mathbf{r}} = \left\{ \begin{array}{c} \mathbf{r}_2 \\ \vdots \\ \mathbf{r}_{n_\mathrm{d}-1} \end{array} \right\}, \quad \overline{\mathbf{d}} = \left\{ \begin{array}{c} \mathbf{d}_2 \\ \vdots \\ \mathbf{d}_{n_\mathrm{d}-1} \end{array} \right\}, \quad \overline{\mathbf{p}} = \left\{ \begin{array}{c} \mathbf{p}(\xi_2) \\ \vdots \\ \mathbf{p}(\xi_{n_\mathrm{d}-1}) \end{array} \right\}, \quad \overline{\mathbf{s}} = \left\{ \begin{array}{c} \mathbf{s}(\xi_2) \\ \vdots \\ \mathbf{s}(\xi_{n_\mathrm{d}-1}) \end{array} \right\}, \tag{5.25}$$

$\overline{\mathbf{r}} \in \mathbb{R}^{3(n_\mathrm{d}-2)}$, $\overline{\mathbf{d}} \in \mathbb{R}^{3(n_\mathrm{d}-2)}$, $\overline{\mathbf{p}} \in \mathbb{R}^{3(n_\mathrm{d}-2)}$, $\overline{\mathbf{c}} \in \mathbb{R}^{3(n_\mathrm{d}-2)}$, and $\overline{\mathbf{s}} \in \mathbb{R}^{3(n_\mathrm{d}-2)}$. Then, the problem can be reformulated. Using the control points $\overline{\mathbf{b}}^T = \{\overline{\mathbf{b}}_2^T \ldots \overline{\mathbf{b}}_{n_\mathrm{c}-1}^T\} \in \mathbb{R}^{3(n_\mathrm{c}-2)}$ and Eq.(5.23), we obtain

$$\overline{\mathbf{p}} = \overline{\mathbf{s}} + \overline{\mathbf{N}}\,\overline{\mathbf{b}} \tag{5.26}$$

with

$$\overline{\mathbf{N}} = \begin{bmatrix} N_{2,k}(\xi_2)\mathbf{I} & N_{3,k}(\xi_2)\mathbf{I} & \ldots & N_{n_\mathrm{c}-1,k}(\xi_2)\mathbf{I} \\ N_{2,k}(\xi_3)\mathbf{I} & N_{3,k}(\xi_3)\mathbf{I} & \ldots & N_{n_\mathrm{c}-1,k}(\xi_3)\mathbf{I} \\ \vdots & & & \vdots \\ N_{2,k}(\xi_{n_\mathrm{d}-1})\mathbf{I} & N_{3,k}(\xi_{n_\mathrm{d}-1})\mathbf{I} & \ldots & N_{n_\mathrm{c}-1,k}(\xi_{n_\mathrm{d}-1})\mathbf{I}. \end{bmatrix} \tag{5.27}$$

Here, the identity matrix $\mathbf{I} \in \mathbb{R}^{3\times 3}$ is introduced, $\overline{\mathbf{N}} \in \mathbb{R}^{3(n_\mathrm{d}-2)\times 3(n_\mathrm{c}-2)}$. Then, the minimum problem (5.24) can be reformulated to

$$f(\overline{\mathbf{b}}) = \frac{1}{2}\overline{\mathbf{r}}^T(\overline{\mathbf{b}})\overline{\mathbf{r}}(\overline{\mathbf{b}}) \longrightarrow \min \tag{5.28}$$

with

$$\overline{\mathbf{r}}(\overline{\mathbf{b}}) = \overline{\mathbf{N}}\,\overline{\mathbf{b}} + \overline{\mathbf{s}} - \mathbf{d}. \tag{5.29}$$

In order to obtain all unknown control points $\overline{\mathbf{b}}$, the necessary condition

$$\frac{\mathrm{d}f}{\mathrm{d}\overline{\mathbf{b}}} = \overline{\mathbf{N}}^T\{\overline{\mathbf{N}}\,\overline{\mathbf{b}} + \overline{\mathbf{s}} - \overline{\mathbf{d}}\} = \mathbf{0}, \tag{5.30}$$

has to be fulfilled. This leads to the system of linear equations

$$\left[\overline{\mathbf{N}}^T\overline{\mathbf{N}}\right]\overline{\mathbf{b}} = \overline{\mathbf{N}}^T\{\overline{\mathbf{d}} - \overline{\mathbf{s}}\}. \tag{5.31}$$

Significant advantages of the B-spline approach for the puprose of generating curves are smoothness, continuity, and flexibility. It is possible to create a smoother curve by decreasing the number of control points, which is a significant advantage when generating complex curves. In Appendix 8.4, the concept and effect of control points on the final curve is shown with one example.

5.4.4 Derivatives of B-Spline Curve

The B-spline curve $\boldsymbol{p}(\xi)$ and its derivatives are all continuous over the entire curve. The m^{th} derivative of the B-spline curve is given by

$$\boldsymbol{p}^{(m)}(\xi) = \sum_{i=1}^{n_\mathrm{c}} N_{i,k}^{(m)}(\xi)\boldsymbol{b}_i, \tag{5.32}$$

where $N_{i,k}^{(m)}(\xi)$ can be obtained by

$$N_{i,k}^{(m)}(\xi) = (k-1)\left(\frac{N_{i,k-1}^{(m-1)}(\xi)}{\Xi_{i+k-1} - \Xi_i} - \frac{N_{i+1,k-1}^{(m-1)}(\xi)}{\Xi_{i+k} - \Xi_{i+1}}\right). \tag{5.33}$$

The tangent vector can be obtained by the first derivative of the B-spline curve (5.13) with respect to ξ,

$$\boldsymbol{p}\,'(\xi) = \frac{\mathrm{d}\boldsymbol{p}(\xi)}{\mathrm{d}\xi} = \sum_{i=1}^{n_\mathrm{c}} N'_{i,k}(\xi)\boldsymbol{b}_i. \tag{5.34}$$

$N'_{i,k}(\xi)$ can be computed as

$$N'_{i,k}(\xi) = \frac{k-1}{\Xi_{i+k-1} - \Xi_i}N_{i,k-1}(\xi) - \frac{k-1}{\Xi_{i+k} - \Xi_{i+1}}N_{i+1,k-1}(\xi), \tag{5.35}$$

see (Piegl and Tiller, 1997). Since the B-spline basis function is a recursive formula, the derivative of the B-spline function is also recursive where a basis function of prescribed order k relies on lower order basis functions down to order one.The proof of Eq.(5.35) can be found in (Piegl and Tiller, 1997). The details of the second and third derivative of the B-spline curve are given in Appendix 8.5 and the unit tangent vector reads,

$$\boldsymbol{a}(\xi) = \frac{\boldsymbol{p}\,'(\xi)}{\|\boldsymbol{p}\,'(\xi)\|}. \tag{5.36}$$

5.5 B-Spline Surface

Different methods such as Bezier, B-spline, and NURBS curves and surfaces are mostly used to represent various types of figures in computer-aided design (CAD) systems, see also (Piegl and Tiller, 1997). B-spline surfaces are helpful for sketching any surfaces such as automobile bodies, aircrafts or any other smooth surface. There are many works dealing with B-spline surfaces. (Catmull and Clark, 1978) describes a method for recursively generating surfaces that approximate points lying on a mesh of arbitrary topology. (Eck and Hoppe, 1996) mentions a procedure for reconstructing a tensor product B-spline surface from a set of scanned 3D points. B-spline surfaces are generalized in (Loop and DeRose, 1990) which are capable of capturing surfaces of arbitrary topology. Further works that address the topic of B-spline surfaces are (Hu and Bo, 2020; Piegl and Tiller, 2000b, 2002).

In this section, the B-spline formulation in Section 5.4 is extended to a B-spline surface. The goal of this section is to generate a surface using initial data points that can be obtained from the samples. In Chapter 4, it is shown that the material models depend on structural tensors which represent fiber orientations. In the next step, the unit tangent vector that represents the fiber direction is calculated in order to perform a finite element simulation. Using the B-spline surface, the tangent vectors are obtained for coordinate lines.

A B-spline surface can be defined by

$$\boldsymbol{p}(\xi,\eta)=\sum_{i=1}^{n_{c\xi}}\sum_{j=1}^{n_{c\eta}}N_{i,k}(\xi)M_{j,l}(\eta)\boldsymbol{b}_{ij}, \tag{5.37}$$

and in column vector form, this reads

$$\mathbf{p}(\xi,\eta)=\sum_{i=1}^{n_{c\xi}}\sum_{j=1}^{n_{c\eta}}N_{i,k}(\xi)M_{j,l}(\eta)\mathbf{b}_{ij}, \tag{5.38}$$

where $N_{i,k}(\xi)$ and $M_{j,l}(\eta)$ are the B-spline basis functions in ξ and η direction. They are defined by

$$N_{i,k}(\xi)=\frac{\xi-\Xi_i}{\Xi_{i+k-1}-\Xi_i}N_{i,k-1}(\xi)+\frac{\Xi_{i+k}-\xi}{\Xi_{i+k}-\Xi_{i+1}}N_{i+1,k-1}(\xi), \tag{5.39}$$

with

$$N_{i,1}(\xi)=\begin{cases}1 & \text{if } \Xi_i\leq\xi<\Xi_{i+1},\\ 0 & \text{otherwise},\end{cases} \tag{5.40}$$

and

$$M_{j,l}(\eta)=\frac{\eta-H_j}{H_{j+l-1}-H_j}M_{j,l-1}(\eta)+\frac{H_{j+l}-\eta}{H_{j+l}-H_{j+1}}M_{j+1,l-1}(\eta), \tag{5.41}$$

with

$$M_{j,1}(\eta)=\begin{cases}1 & \text{if } H_j\leq\eta<H_{j+1},\\ 0 & \text{otherwise}.\end{cases} \tag{5.42}$$

The parameters should be determined for the B-spline basis function in ξ and η direction. The numbering for the control points and data points is from left to right and from bottom to top for our computations. The number of data points is given by as $n_{\mathrm{d}\xi}$ and $n_{\mathrm{d}\eta}$, and $n_{\mathrm{c}\xi}$ and $n_{\mathrm{c}\eta}$ are the number of control points in ξ- and η-direction. Another important aspect are the knot values, and the knot values in ξ-direction Ξ_i, $i = 1, \ldots, n_{\mathrm{kv}}$ are independent of the knot values in η-direction H_j, $j = 1, \ldots, n_{\mathrm{kl}}$, see (Piegl and Tiller, 1997; Rogers, 2001). They have both the multiplicity of k at the first and last point in ξ-direction; similarly to Eq.(5.17), they are normalized to 1. The conditions $n_{\mathrm{kv}} = n_{\mathrm{c}\xi} + k$ and $n_{\mathrm{kl}} = n_{\mathrm{c}\eta} + l$ should be satisfied

$$\hat{\Xi}_i = \begin{cases} 0 & \text{for } 1 \leq i \leq k \\ i - k & \text{for } k+1 \leq i \leq n_{\mathrm{c}\xi} \\ n_{\mathrm{c}\xi} + 1 - k & \text{for } n_{\mathrm{c}\xi} + 1 \leq i \leq n_{\mathrm{c}\xi} + k \end{cases} \tag{5.43}$$

where normalization in ξ-direction is done by $\Xi_i = \hat{\Xi}_i / (n_{\mathrm{c}\xi} + 1 - k)$, $i = 1, \ldots, n_{\mathrm{kv}\xi}$,

$$\hat{H}_j = \begin{cases} 0 & \text{for } 1 \leq j \leq l \\ j - l & \text{for } l+1 \leq j \leq n_{\mathrm{c}\eta} \\ n_{\mathrm{c}\eta} + 1 - l & \text{for } n_{\mathrm{c}\eta} + 1 \leq j \leq n_{\mathrm{c}\eta} + l \end{cases} \tag{5.44}$$

and normalization in η-direction is obtained using $H_j = \hat{H}_j / (n_{\mathrm{c}\eta} + 1 - l)$, $j = 1, \ldots, n_{\mathrm{kv}\eta}$. The data points are equal to the control points on the edges, see (Piegl and Tiller, 1987):

$$\mathbf{p}(0,0) = \mathbf{b}_{11}, \quad \mathbf{p}(0,1) = \mathbf{b}_{1 n_{\mathrm{c}\eta}}, \quad \mathbf{p}(1,0) = \mathbf{b}_{n_{\mathrm{c}\xi} 1}, \quad \mathbf{p}(1,1) = \mathbf{b}_{n_{\mathrm{c}\xi} n_{\mathrm{c}\eta}}. \tag{5.45}$$

As before, the parameters ξ_r and η_s are determined according to the chord length approach. Here,

$$d_{j\xi} = \|\mathbf{d}_{j1} - \mathbf{d}_{j-1,1}\|, \quad j = 2, \ldots, n_{\mathrm{d}\xi}, \tag{5.46}$$

and

$$\xi_r = \frac{\sum_{j=2}^{r} d_{j\xi}}{\sum_{j=2}^{n_{\mathrm{d}\xi}} d_{j\xi}}, \quad \text{for} \quad 2 \leq r \leq n_{\mathrm{d}\xi}. \tag{5.47}$$

Accordingly, the parameter η_s can be computed by

$$d_{j\eta} = \|\mathbf{d}_{1j} - \mathbf{d}_{1\,j-1}\|, \quad j = 2, \ldots, n_{\mathrm{d}\eta}, \tag{5.48}$$

and

$$\eta_s = \frac{\sum_{j=2}^{s} d_{j\eta}}{\sum_{j=2}^{n_{\mathrm{d}\eta}} d_{j\eta}}, \quad \text{for} \quad 2 \leq s \leq n_{\mathrm{d}\eta}. \tag{5.49}$$

5.5.1 Control Net

Another important parameter for defining a B-spline surface is the control net $\mathbf{B}$. A B-spline surface is strongly influenced by the control net. Thus, any change in control net leads to changes

in the final surface. There exist many works dealing with the control net and all the possibilities for defining this parameter. (Loop, 1994) provided an algorithm for creating smooth spline surfaces over irregular meshes. (Zhang et al., 2016) presented an iterative and adaptive surface approximation framework using B-splines. This method is able to use any scattered data points with parameterization as input to generate surfaces. Another method to reconstruct surfaces from scattered points is presented in (Gregorski et al., 2000).

In this work, the total number of control points are $n_{\mathrm{c}\xi} n_{\mathrm{c}\eta}$, and the total number of data points are $n_{\mathrm{d}\xi} n_{\mathrm{d}\eta}$. The quantities can be formulated as

$$\mathbf{R} = \begin{bmatrix} \mathbf{r}_{11}^T \\ \vdots \\ \mathbf{r}_{1n_{\mathrm{d}\eta}}^T \\ \mathbf{r}_{21}^T \\ \vdots \\ \mathbf{r}_{2n_{\mathrm{d}\eta}}^T \\ \vdots \\ \mathbf{r}_{n_{\mathrm{d}\xi}1}^T \\ \vdots \\ \mathbf{r}_{n_{\mathrm{d}\xi}n_{\mathrm{d}\eta}}^T \end{bmatrix}, \qquad \mathbf{D} = \begin{bmatrix} \mathbf{d}_{11}^T \\ \vdots \\ \mathbf{d}_{1n_{\mathrm{d}\eta}}^T \\ \mathbf{d}_{21}^T \\ \vdots \\ \mathbf{d}_{2n_{\mathrm{d}\eta}}^T \\ \vdots \\ \mathbf{d}_{n_{\mathrm{d}\xi}1}^T \\ \vdots \\ \mathbf{d}_{n_{\mathrm{d}\xi}n_{\mathrm{d}\eta}}^T \end{bmatrix}, \qquad \mathbf{B} = \begin{bmatrix} \mathbf{b}_{11}^T \\ \vdots \\ \mathbf{b}_{1n_{\mathrm{c}\eta}}^T \\ \mathbf{b}_{21}^T \\ \vdots \\ \mathbf{b}_{2n_{\mathrm{c}\eta}}^T \\ \vdots \\ \mathbf{b}_{n_{\mathrm{c}\xi}1}^T \\ \vdots \\ \mathbf{b}_{n_{\mathrm{c}\xi}n_{\mathrm{c}\eta}}^T \end{bmatrix}, \tag{5.50}$$

with $\mathbf{R} \in \mathbb{R}^{n_{\mathrm{d}\xi} n_{\mathrm{d}\eta} \times 3}$, $\mathbf{D} \in \mathbb{R}^{n_{\mathrm{d}\xi} n_{\mathrm{d}\eta} \times 3}$, $\mathbf{B} \in \mathbb{R}^{n_{\mathrm{c}\xi} n_{\mathrm{c}\eta} \times 3}$. The residual of each data point reads

$$\mathbf{r}_{rs}(\mathbf{B}) = \mathbf{p}(\xi_r, \eta_s) - \mathbf{d}_{rs} = \sum_{i=1}^{n_{\mathrm{c}\xi}} \sum_{j=1}^{n_{\mathrm{c}\eta}} T_{ijrs} \mathbf{b}_{ij} - \mathbf{d}_{rs}, \tag{5.51}$$

with

$$T_{ijrs} = N_{i,k}(\xi_r) M_{j,l}(\eta_s). \tag{5.52}$$

The overall residual can be computed as

$$\mathbf{R}(\mathbf{B}) = \mathbf{T}\mathbf{B} - \mathbf{D} \tag{5.53}$$

where $\mathbf{T}$ is equal to

$$\begin{bmatrix}
T_{1111} & \dots & T_{1n_{c\eta}11} & T_{2111} & \dots & T_{2n_{c\eta}11} & \dots\dots & T_{n_{c\xi}111} & \dots & T_{n_{c\xi}n_{c\eta}11} \\
\vdots & & & & & & & & & \vdots \\
T_{111n_{d\eta}} & \dots & T_{1n_{c\eta}1n_{d\eta}} & T_{211n_{d\eta}} & \dots & T_{2n_{c\eta}1n_{d\eta}} & \dots\dots & T_{n_{c\xi}11n_{d\eta}} & \dots & T_{n_{c\xi}n_{c\eta}1n_{d\eta}} \\
T_{1121} & \dots & T_{1n_{c\eta}21} & T_{2121} & \dots & T_{2n_{c\eta}21} & \dots\dots & T_{n_{c\xi}121} & \dots & T_{n_{c\xi}n_{c\eta}21} \\
\vdots & & & & & & & & & \vdots \\
T_{112n_{d\eta}} & \dots & T_{1n_{c\eta}2n_{d\eta}} & T_{212n_{d\eta}} & \dots & T_{2n_{c\eta}2n_{d\eta}} & \dots\dots & T_{n_{c\xi}12n_{d\eta}} & \dots & T_{n_{c\xi}n_{c\eta}2n_{d\eta}} \\
\vdots & & & & & & & & & \vdots \\
\vdots & & & & & & & & & \vdots \\
T_{11n_{d\xi}1} & \dots & T_{1n_{c\eta}n_{d\xi}1} & T_{21n_{d\xi}1} & \dots & T_{2n_{c\eta}n_{d\xi}1} & \dots\dots & T_{n_{c\xi}1n_{d\xi}1} & \dots & T_{n_{c\xi}n_{c\eta}n_{d\xi}1} \\
\vdots & & & & & & & & & \vdots \\
T_{11n_{d\xi}n_{d\eta}} & \dots & T_{1n_{c\eta}n_{d\xi}n_{d\eta}} & T_{21n_{d\xi}n_{d\eta}} & \dots & T_{2n_{c\eta}n_{d\xi}n_{d\eta}} & \dots\dots & T_{n_{c\xi}1n_{d\xi}n_{d\eta}} & \dots & T_{n_{c\xi}n_{c\eta}n_{d\xi}n_{d\eta}}
\end{bmatrix} \tag{5.54}$$

with $\mathbf{T} \in \mathbb{R}^{(n_{d\xi}n_{d\eta})\times(n_{c\xi}n_{c\eta})}$. The minimization problem reads

$$f(\mathbf{B}) = \frac{1}{2}\mathbf{R}(\mathbf{B}) \cdot \mathbf{R}(\mathbf{B}) \rightarrow \min \tag{5.55}$$

and it yields to, see (Piegl and Tiller, 1997) for more details,

$$\left[\mathbf{T}^T\mathbf{T}\right]\mathbf{B} = \mathbf{T}^T\mathbf{D}. \tag{5.56}$$

It should be mentioned that oscillations are to be expected when using the B-spline method. However, it is possible to minimize these fluctuations by reducing the number of control points or the control net.

5.5.2 Derivatives of B-Spline Surface

A required surface can be obtained using B-spline surface, while curvilinear coordinate lines can be obtained for tangent vectors. We need the unit tangent vector for the constitutive model, representing the fiber orientation. The first derivative of the B-spline surface in ξ direction can be calculated by

$$\boldsymbol{a}^*(\xi,\eta) = \frac{\partial \boldsymbol{p}(\xi,\eta)}{\partial \xi} = \sum_{i=1}^{n_{c\xi}}\sum_{j=1}^{n_{c\eta}} N'_{i,k}(\xi) M_{j,l}(\eta)\boldsymbol{b}_{ij}. \tag{5.57}$$

As mentioned before, the derivatives $N'_{i,k}(\xi)$ can be computed using Eq.(5.35) and the unit tangent vector is equal to

$$\boldsymbol{a}(\xi,\eta) = \frac{\boldsymbol{a}^*(\xi,\eta)}{\|\boldsymbol{a}^*(\xi,\eta)\|}. \tag{5.58}$$

5.5.3 Obtaining Data Points from Experiment

A set of data points is needed to generate a B-spline surface. As shown in Fig. 5.3(a), one quarter of a sample is considered. The required data is obtained using a digital image of a specimen, with manually applied data points on the fibers, see Fig. 5.3(b). Due to the concentration of the fibers, especially around the hole, it is assumed that the shown data points express the fiber directions. It is also presumed that these data points are identical in different experiments. The center of the hole is assumed as the origin of the coordinate system, while the ξ-axis is along the fiber direction and η-axis is perpendicular to the ξ-axis. The coordinates of the data points are estimated using the standard pixel counting method (PCM) and Matlab, and the B-spline surface is determined with Eq.(5.56) using these data points. To obtain horizontal tangents above the

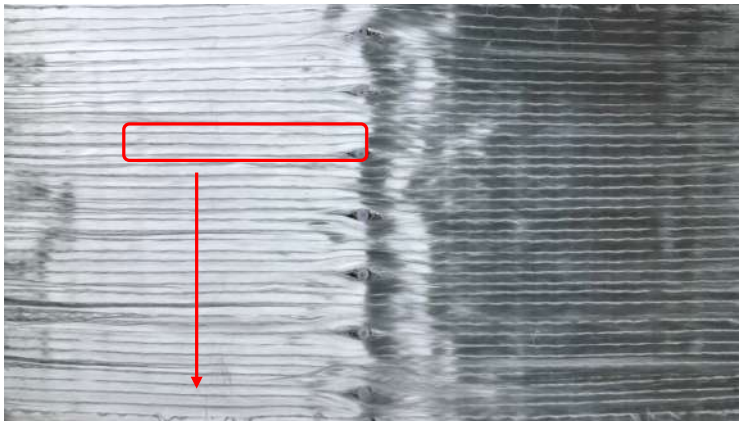

(a) A plate with bypassed fibers around holes and zone of interest for obtaining a set of data points

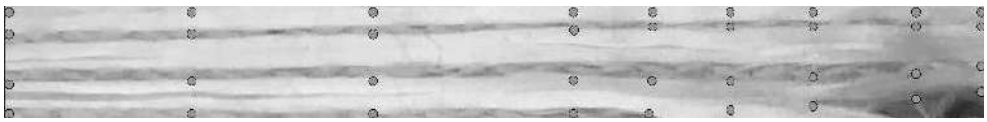

(b) Gray-scale image of data points

Figure 5.3: Orientation distribution of fibers

hole, the points are mirrored with respect to the η-axis. Here, $n_{\mathrm{d}\xi} = 17$ data points and $n_{\mathrm{c}\xi} = 11$ control points with $k = 3$ in ξ-direction are considered. For the η-direction, we choose $n_{\mathrm{c}\eta} = 4$ control points and $n_{\mathrm{d}\eta} = 4$ data points with $l = 4$, see Fig. 5.4.

The B-spline surface is implemented in the in-house finite elements code TASAFEM to perform the simulations, and the spatial distribution of the unit tangent vector $\boldsymbol{a}$ for the constitutive model is calculated by Eq.(5.58).

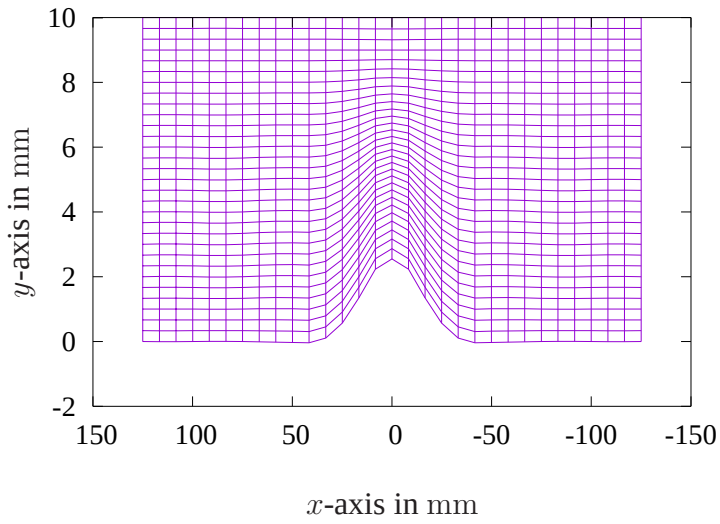

Figure 5.4: Modeling of fiber bypassing around the hole using B-splines

6 Numerical Examples

This chapter includes computations using the constitutive models formulated in the previous chapters, with the help of the obtained material parameters regarding transverse isotropic and orthotropic fiber reinforced composites. GiD software is used as a pre-and post-processor for the numerical investigation, (GiD-Manual, 2012). The computations are carried out using the in-house finite elements code TASAFEM.

To begin with, we present the computations for transverse isotropy, based on the streamline approach of Sect. 5.2 with the help of the parameters calculated in Chapter 4. Furthermore, the computations using this approach are compared with laminates with uni-directional fiber orientation. In addition, the local effect of a rivet in laminates is investigated by finite element simulations.

Second, the computation using the parameters obtained in Chapter 4 and the B-spline approach, which is introduced in Chapter 5, is done for validation cases. In this part, the results of the simulations are compared with validation experiments. The goal of this section is to verify the whole process of modeling, simulation, and material parameter identification using verification tests. Moreover, these computations are again done with the help of streamline approach in Sect. 5.2, and the result of computations are again compared with experimental results. Then, the results of both methods (streamline and B-spline approaches) are compared with each other.

Finally, the validation tests for the orthotropy case are provided. The finite element simulations are performed using the material model presented in Chapter 3 with the parameters calculated in Chapter 4. The main aim of this part is again to verify the entire process of modeling, simulation, and material parameter identification of orthotropy laminates. For this aim, we compare computations of a plate with a hole with experimental results.

6.1 Finite Element Studies - Streamline Approach

This section focuses on the simulations to determine the effect of bypassing the fibers around the hole. For this aim, two computations of a plate with a hole having a radius of $R = 10\,\mathrm{mm}$ are compared while a displacement of $u(100, y) = \overline{u}_x = 0.01\,\mathrm{mm}$ is applied to the plate. The plate is meshed using GiD with 20-noded, hexahedral elements with $(3 \times 3 \times 3)$ Gauss-points. Due to symmetry conditions, only one-eighth of the plate is modeled in this example. For details regarding the symmetry conditions, please refer to Fig. 6.1(a), and to Fig. 6.1(b) for information on the geometry and mesh. In the first computation, the spatially constant *uni-directional* fiber orientation $\boldsymbol{a} = \boldsymbol{e}_x$ is chosen. In the second computation, the fiber orientation of Eq.(5.10) is used, which is indicated by the tangent vectors.

The calculated material parameters in Chapter 4 are used for the computations. Since there

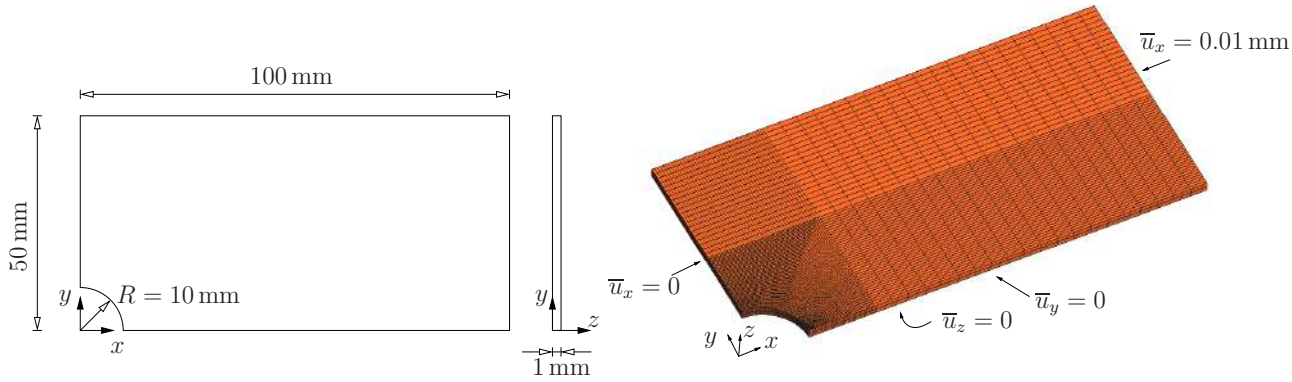

(a) Geometry of one-eighth of the specimen (b) Geometry (mesh and boundary conditions)

Figure 6.1: Geometry, mesh, and boundary conditions

is a small region around the hole where there are no fibers, an improvement is considered, see Fig. 6.7. A polynomial of third order is used to separate this region, as there is no fiber below

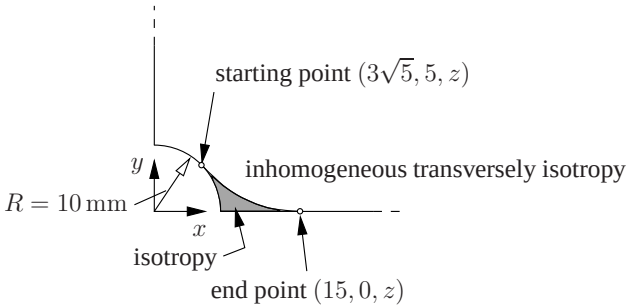

Figure 6.2: Region with purely isotropic material

this polynomial. This case is called *bypass-reduced*. The curve begins at point $(x, y) = (3\sqrt{5}, 5)$ and ends at point $(x, y) = (15, 0)$. The slope of the curve on the right side at $x = 3\sqrt{5}$ is equal to the slope of the circle at this point, and the slope of the curve is zero at the point $x = 15$. Below the polynomial and inside the small region, the isotropic part of the elasticity relation (3.60) is taken.

In the following, the stress and strain states in uni-directional and bypassed-reduced cases are considered. This is followed by calculating the stresses σ_{xx} with respect to vertical axis at $x = 0$ and $z = 1$, $\sigma_{xx}(0, y, 1)$, see Fig. 6.3(a). Furthermore, the stresses in vertical direction at the horizontal symmetry plane, $\sigma_{yy}(x, 0, 1)$ are studied, see Fig. 6.3(b). The plots are generated using GiD as Gauss-point information transfer to nodal points by interpolation schemes.

The highest horizontal stresses can be seen in the uniformly distributed fiber orientation at point $(x, y) = (0, R)$. On the other hand, the simulation for the "bypass-reduced" case does not show high σ_{xx} stresses in this region. In this case, the σ_{xx} stresses are $\approx 60\%$ of σ_{xx} stresses in the uni-directional case.

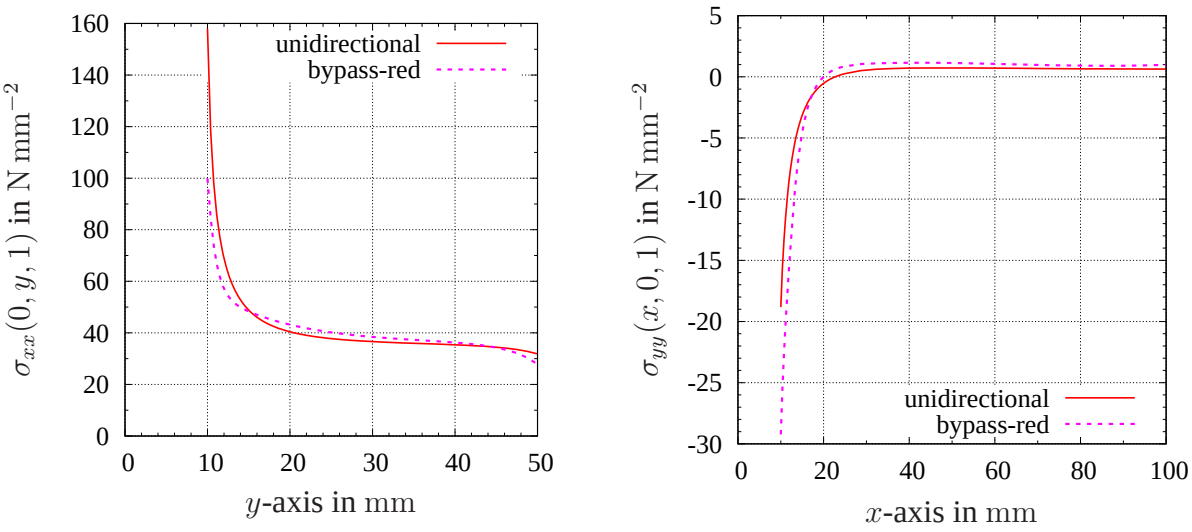

(a) Normal stresses σ_{xx} in the vertical axis

(b) Normal stresses σ_{yy} in the horizontal axis

Figure 6.3: Stresses σ_{xx} and σ_{yy} at the vertical and the horizontal symmetry lines

A similar result is obtained for the strains, see Fig. 6.4. Although very promising results are obtained over σ_{xx} in the "bypass-reduced" case, there are larger compressive strains ε_{yy} for the bypass-reduced computation in comparison to the uni-directional case. In contrast, negative strains are not as critical as tensile strains. Hence, promising results are obtained for the "bypass-reduced" case where the fibers go around the hole. The stress and strain distributions in the uni-directional and the bypass-reduced case are explicated in the following.

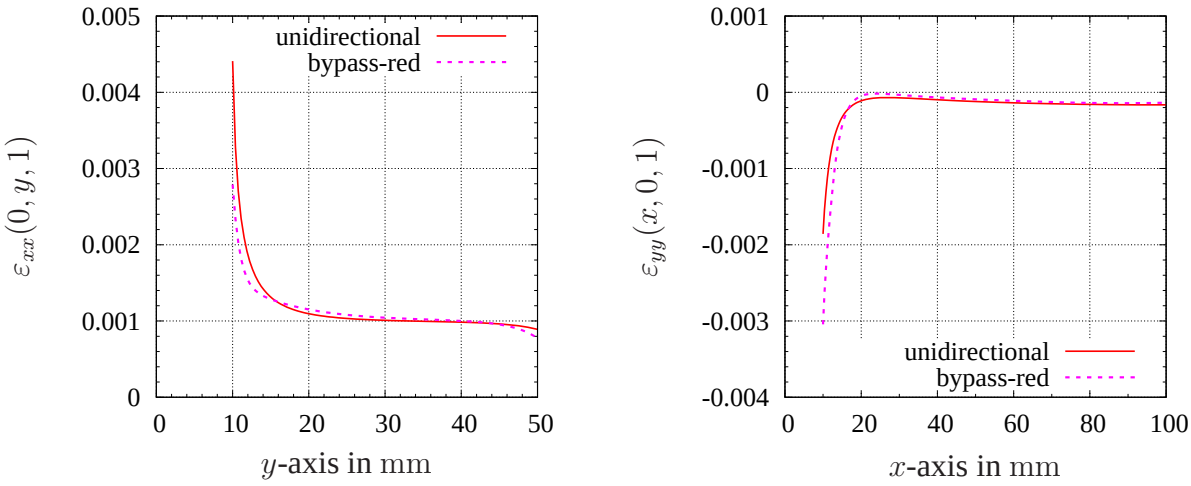

(a) Strain ε_{xx} in the vertical axis

(b) Strain ε_{yy} in the vertical axis

Figure 6.4: Strains ε_{xx} and ε_{yy} at the vertical and the horizontal symmetry lines

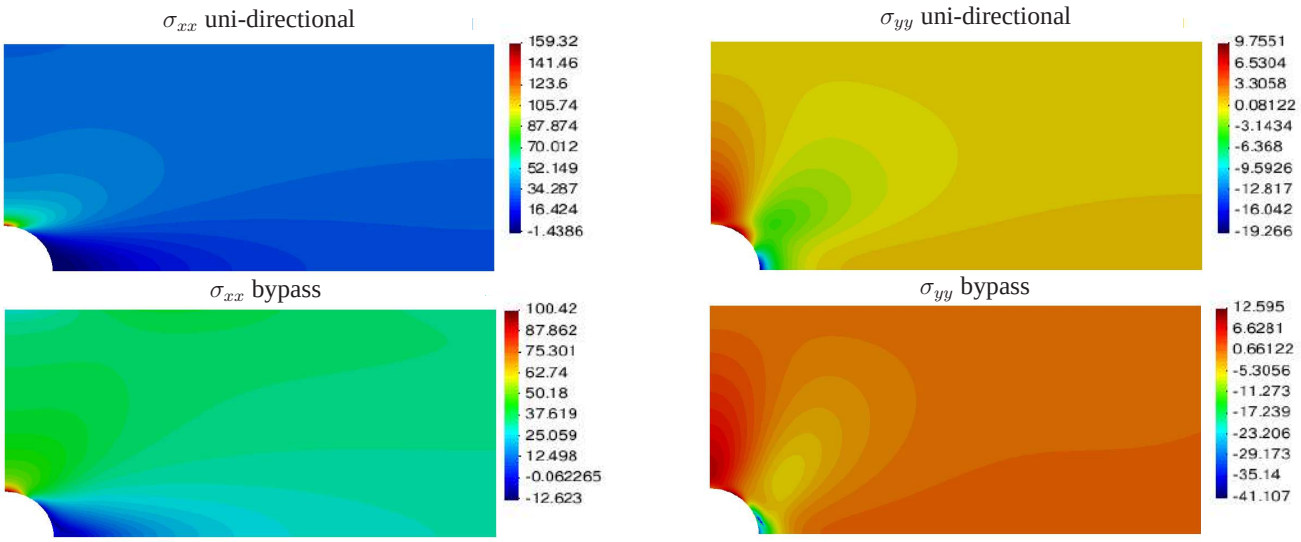

Figure 6.5: σ_{xx} and σ_{yy} in $\mathrm{N\,mm^{-2}}$ for bypass and uni-directional computations

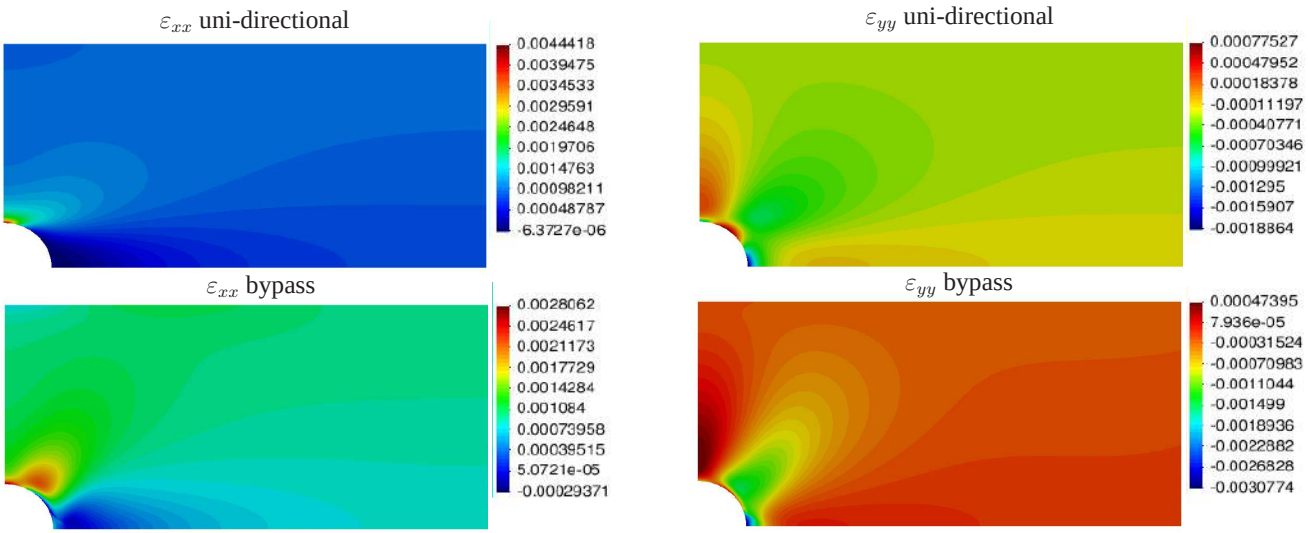

Figure 6.6: ε_{xx} and ε_{yy} for bypass and uni-directional computations

6.2 Projection of FEM Simulation to DIC Results

In order to perform the simulation, the orientation vector $\boldsymbol{a}(\boldsymbol{x})$ of the experimental data, see Eq.(5.58), must be transferred to the finite element program. In this work, it is assumed that $\boldsymbol{a}(\boldsymbol{x})$ is constant within the thickness of the sample. The spatial coordinates $\mathbf{x}_\mathrm{G} = \{x_\mathrm{G}, y_\mathrm{G}\}$ of a Gauss-point are known in a finite element program. These coordinates are equivalent to the position vector (5.38). ξ_G and η_G are the coordinates of spatial points in the B-spline surface. The coordinates ξ_G and η_G can be obtained using the system of two non-linear functions with two unknowns,

$$\mathbf{g}(\xi_\mathrm{G}, \eta_\mathrm{G}) = \mathbf{x}_\mathrm{G} - \mathbf{p}(\xi_\mathrm{G}, \eta_\mathrm{G}) = \mathbf{0}, \quad \rightsquigarrow \xi_\mathrm{G} \text{ and } \eta_\mathrm{G} \tag{6.1}$$

which leads to

$$\left\{ \begin{array}{c} g_1(\xi_\mathrm{G}, \eta_\mathrm{G}) \\ g_2(\xi_\mathrm{G}, \eta_\mathrm{G}) \end{array} \right\} = \left\{ \begin{array}{c} x_\mathrm{G} \\ y_\mathrm{G} \end{array} \right\} - \left\{ \begin{array}{c} p_1(\xi_\mathrm{G}, \eta_\mathrm{G}) \\ p_2(\xi_\mathrm{G}, \eta_\mathrm{G}) \end{array} \right\} = \left\{ \begin{array}{c} 0 \\ 0 \end{array} \right\}. \tag{6.2}$$

In the scope of calculating the tangent vector Eq.(5.58), a Newton-Raphson method is used to find the coordinates ξ_G and η_G for each Gauss-point. The starting values are $(0.1, 0.1)$. It is clear that points are out of field when ξ_G or η_G are not between 0 and 1. There is a region near to the hole where no fibers exist. In this area, a linear isotropic elastic behavior within the resin is assumed, i.e. there is pure resin material in the area below the curve, see Fig. 6.7.

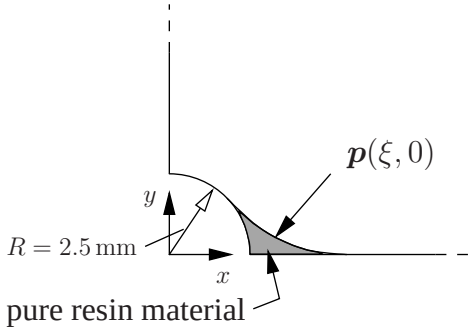

Figure 6.7: Area with matrix material (isotropic elasticity)

6.3 Finite Element Studies of Uni-directional Fiber Laminates with Rivet

In many industrial applications, such as aircraft construction, for example, it is common to use rivets, since they are extremely durable and require no welding, see also (Moroni and Pirondi, 2010). A glance at any airplane or aircraft reveals thousands of rivets in the outer skin, which indicates how important riveting is. Rivets used in the aerospace industry are made of aluminum or steel, see (Wincheski and Namkung, 2004; Yang et al., 2014). Rivets are mainly used to hold different sections in place, to secure fittings, to fasten bracing members, and to attach two or more components, see (Abdelal et al., 2015; Chiou et al., 1991). Quality prediction for riveting is very important, as it can improve the efficiency of a riveting design. Moreover, there are many different riveting method (Kim et al., 2019). Kim et al. (2019) published a literature survey about rivet quality prediction, mainly carried out based on the finite element method to predict deformed shapes, joint strength, and fatigue lifetime for a given material design condition. Simulations can provide better insight into the performance of rivets. Specific requirements in industry for riveting (along with failure mode) are discussed in (Moroni and Pirondi, 2010). A detailed study on the fastening process of small panel assemblies with single and multiple rivets was performed by (Abdelal et al., 2015). In addition, the dimensional growth of aircraft panels while being riveted with stiffeners is also investigated in (Abdelal et al., 2015). A new design of a composite countersunk rivet made of rolled laminates for aeronautical applications is proposed and numerically analyzed in (Leite, 2016). The effect of the riveting process on the residual stress/strain in joints and the stress condition in riveted lap joints is investigated using experimental and finite element methods in (Li et al., 2012). Using rivets brings compression force and friction in an area around a hole, which is critical and significant for us. Rivets can influence the behavior of plates, especially in a region around a hole. Thus, we are interested in studying the effect of compression force generated by rivets in the area around the hole with respect to the fiber orientation.

In this section, simulations are done in order to investigate the local effects of rivets on structure's performance with respect to the fiber orientation. For this purpose, we compare two computations of plates with holes with a radius of $R = 2.5\,\mathrm{mm}$, while a displacement of $\overline{u}_x = 0.1\,\mathrm{mm}$ is applied to the surface of the plate. The plate is meshed using GiD with quadratic, tetrahedral elements. In these examples, two plates are placed on each other, connecting them with a rivet. The distance between the two plates is $10^{-15}\,\mathrm{mm}$. This means that no contact between the two plates is assumed. A rivet with a Young's modulus of $E = 200\mathrm{GPa}$ and a Poisson's ratio of $\nu = 0.3$ is considered. A sketch of such a rivet can be seen in Fig. 6.8(a), and a displacement of $0.005\,\mathrm{mm}$ due to the force of the rivet is applied around the hole (brown area), as shown in Fig. 6.8(b). It is assumed that the force between the plates is transferred through the whole rivet. Due to symmetry conditions, only half of the plate is modeled. The geometry is shown in Fig. 6.9, and the mesh and boundary conditions are pointed out in Fig. 6.10.

In the first computation, the spatially constant fiber orientation $\boldsymbol{a} = \boldsymbol{e}_x$ (uni-directional) is chosen. In the second computation, we model the fiber orientation using the B-spline approach, assuming a spatially varying fiber orientation (which we called bypass). In this case, there is no

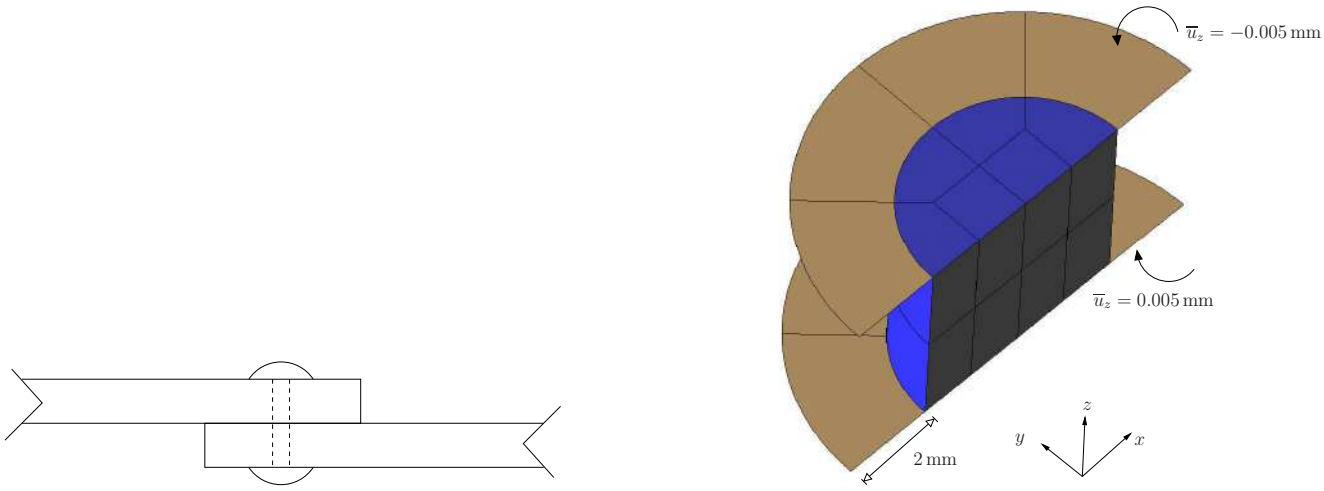

(a) Sketch of rivet

(b) Effect of a rivet on the surface of laminates

Figure 6.8: Rivet considerations for computations

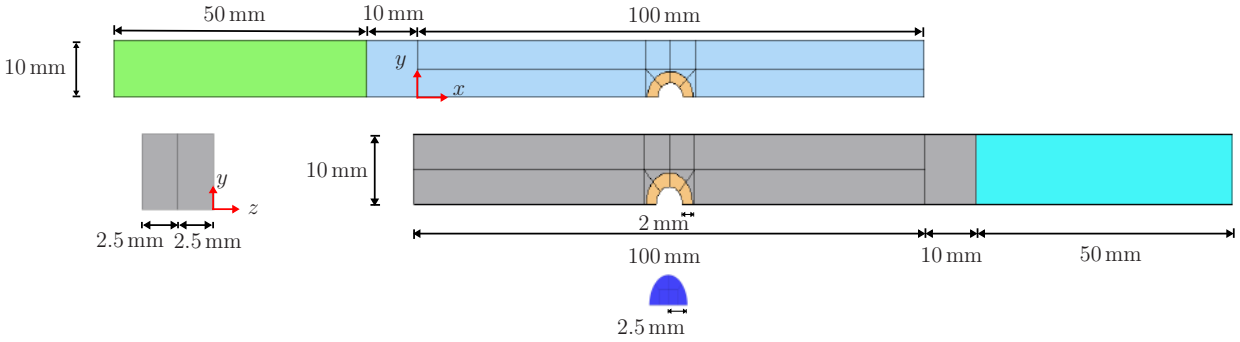

Figure 6.9: Geometry

fiber in a small region around the hole, and isotropic material is considered for this area. In these set of examples, the material parameters determined in Chapter 4 are used.

In the following, the stress and strain states in uni-directional and bypass cases are studied. The stresses $\sigma_{xx}(50, y, -5)$ with respect to the vertical axis at $x = 50\,\text{mm}$ and $z = -5\,\text{mm}$ (in the center of hole) are calculated, see Fig. 6.11(a). Furthermore, the stresses in vertical direction at the horizontal symmetry plane, $\sigma_{yy}(0 < x < 160, 0, -5)$ are studied, see Fig. 6.11(b). Again, the plots are generated using GiD as Gauss-point data transfer to nodal points by interpolation schemes. Since the plate is more critical than the rivet, the plots are generated only for the plate. The simulation results can be seen in Fig. 6.13 - Fig. 6.16.

As mentioned before, the plates are more critical in comparison to the rivets due to their stiffness. If we only consider the plate area, the maximum horizontal stress is generated in uni-directional fiber orientation at point $(x, y) = (0, R)$. The σ_{xx} for the uni-directional case is more than six times larger than that of the bypass case. A similar procedure is carried out for the

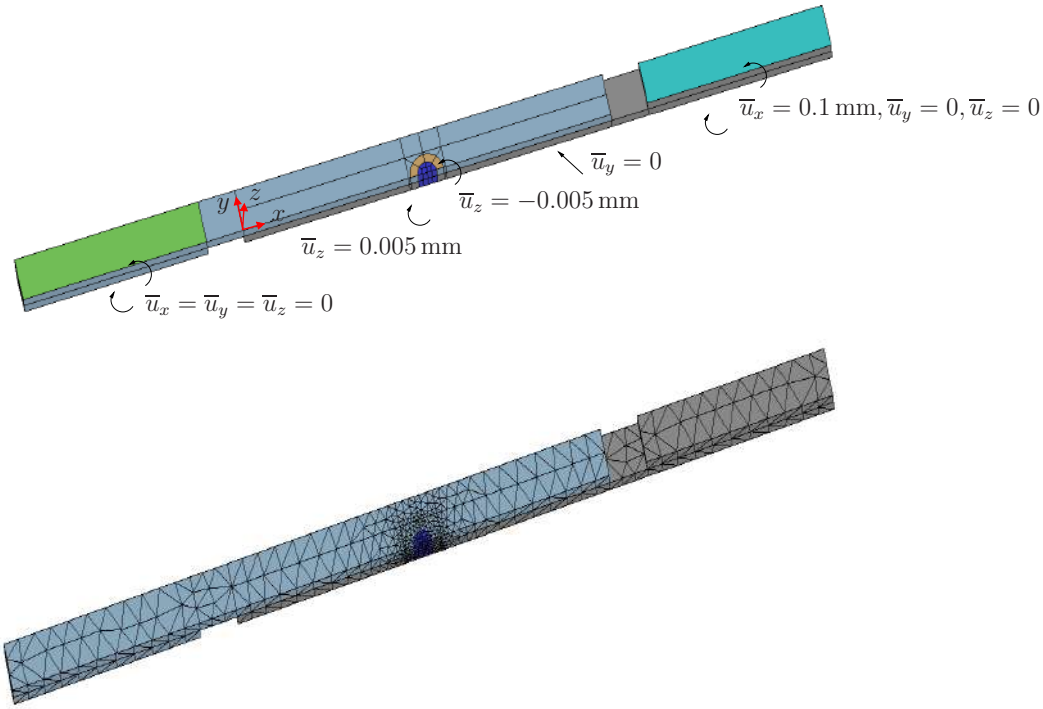

Figure 6.10: Mesh, and boundary conditions

strains, see Fig. 6.12. Even though promising results are obtained over σ_{xx} in the bypass case, larger compressive strains ε_{yy} around the hole, for the bypass computation, can be observed in comparison to the uni-directional case. These larger compressive strains can also be seen in the *bypass-reduced* case in Sect. 6.1 where there are no rivets. Comparing the computations in Sect. 6.1 and Sect. 6.3, it can be seen that bypassing the fibers around the hole reduces the σ_{xx}, although larger compressive strains can be observed around the hole in both cases (with rivets and without). It should be noted that negative strains are not as critical as tensile strains. Thus, positive results are obtained for the bypass case where fibers go around the hole in both cases (with rivet and without). The stress and strain distributions in uni-directional and bypass laminates with rivets are exemplified in the following.

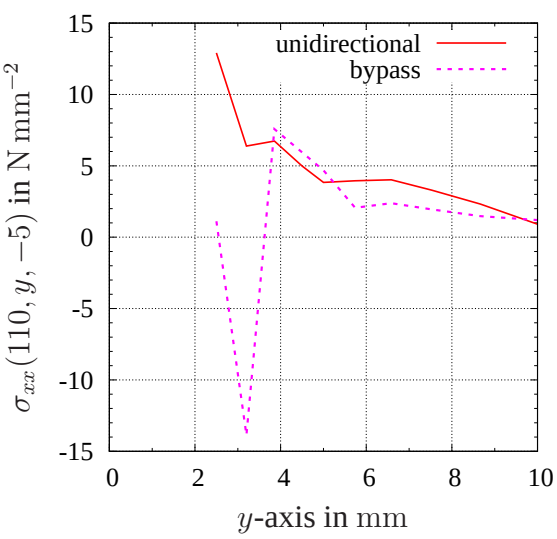

(a) Normal stresses σ_{xx} in the vertical axis

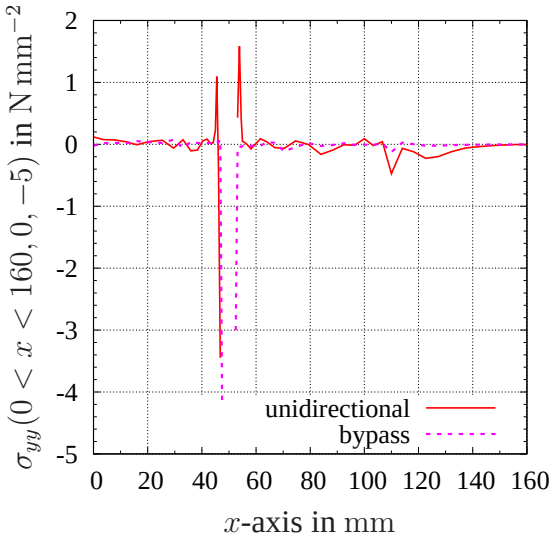

(b) Normal stresses σ_{yy} in the horizontal axis

Figure 6.11: Stresses σ_{xx} and σ_{yy} at the vertical and the horizontal lines

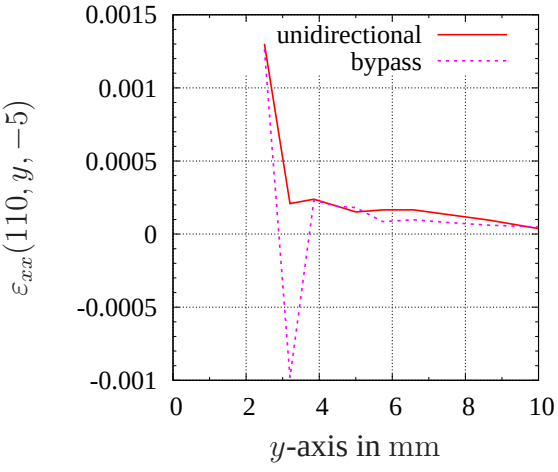

(a) Strain ε_{xx} in the vertical axis

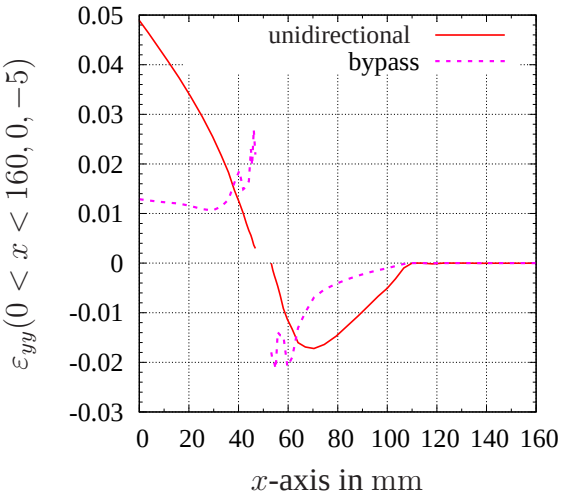

(b) Strain ε_{yy} in the vertical axis

Figure 6.12: Strains ε_{xx} and ε_{yy} at the vertical and the horizontal lines

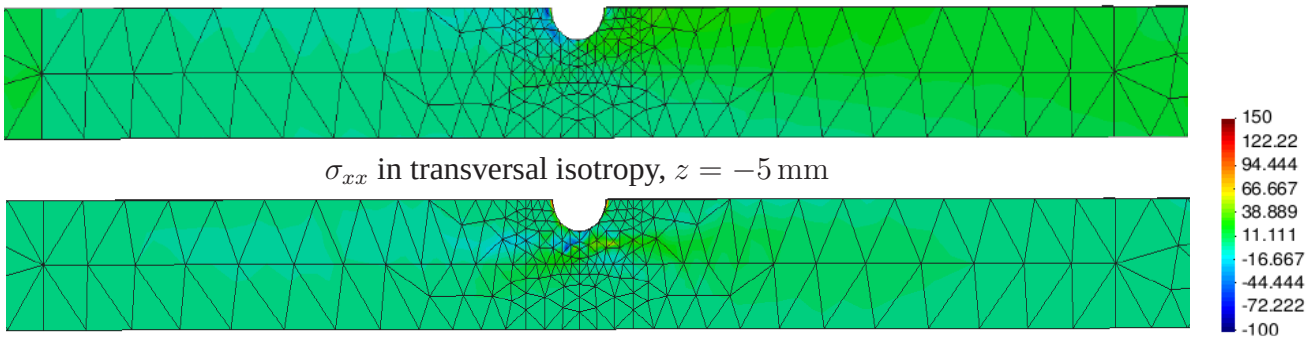

σ_{xx} in transversal isotropy, $z = -5\,\mathrm{mm}$

σ_{xx} in bypass case, $z = -5\,\mathrm{mm}$

Figure 6.13: Stress distributions

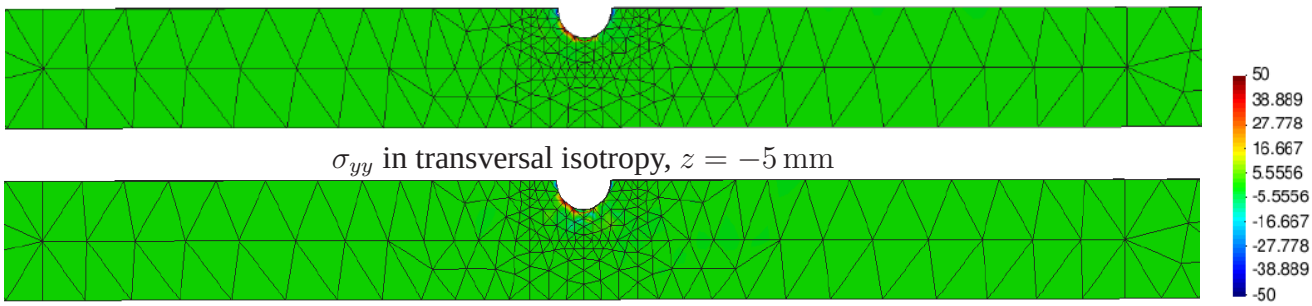

σ_{yy} in transversal isotropy, $z = -5\,\mathrm{mm}$

σ_{yy} in bypass case, $z = -5\,\mathrm{mm}$

Figure 6.14: Stress distributions

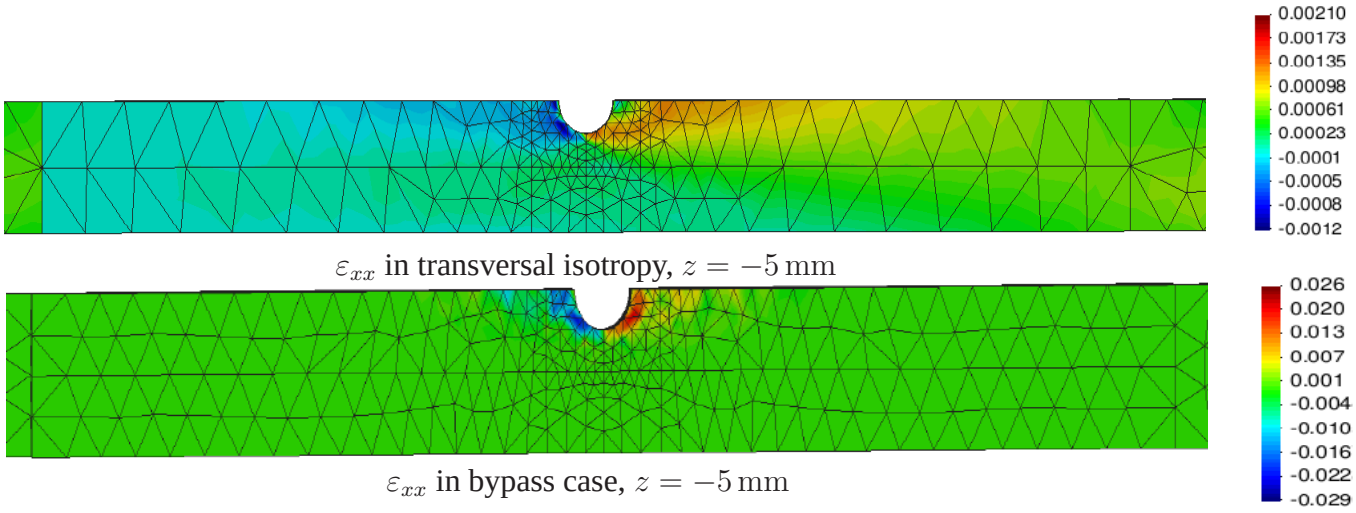

ε_{xx} in transversal isotropy, $z = -5\,\mathrm{mm}$

ε_{xx} in bypass case, $z = -5\,\mathrm{mm}$

Figure 6.15: Strain distributions

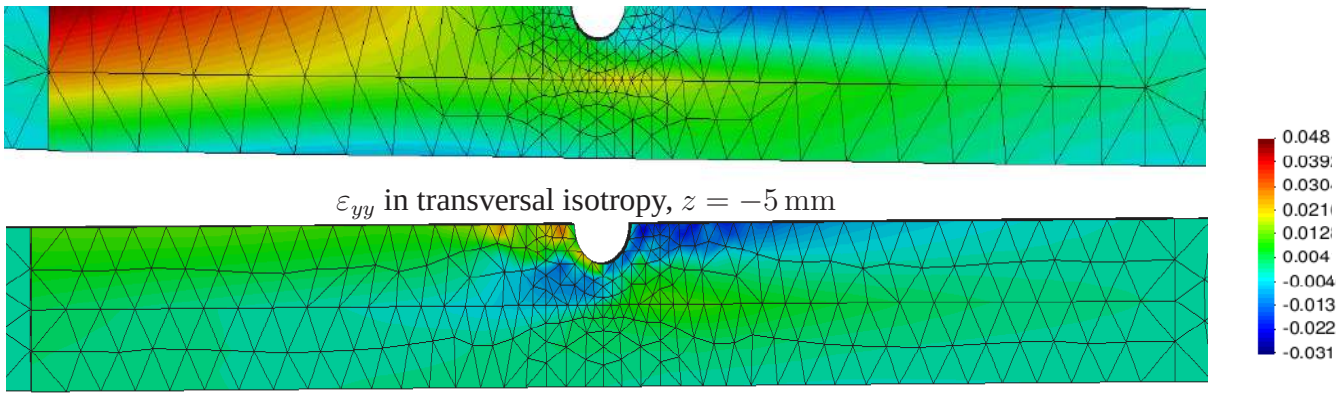

ε_{yy} in transversal isotropy, $z = -5\,\mathrm{mm}$

ε_{yy} in bypass case, $z = -5\,\mathrm{mm}$

Figure 6.16: Strain distributions

6.4 Validation Examples

The material models for isotropy, uni-directional fiber orientation, and orthotropy laminates are discussed in Chapter 3. In Chapter 4, the parameters for isotropy, transversal isotropy, and orthotropy are obtained. One question we are aiming to answer is how well we are able to predict the behavior of these laminates. In order to answer this question, we have to compare the simulation and the experiments. In the following, validation experiments will be introduced. In addition, we will take a look at a comparison between the simulation and the experiment data for the cases of transversal isotropy and orthotropy.

6.5 Transversal Isotropy

6.5.1 Experimental Results

Two sets of experiments are considered. In the first set, the fibers are cut after the production process by drilling a hole into the laminates. In the second set, the fibers are bypassed around the hole. The aim of this section is to validate the entire process of the experiments, the modeling, and the material parameter identification. Two sets of specimens are manufactured using resin RIMR135 with the curing agent RIMH1366, similar to the samples for identification purposes in Chapter 4, see. Fig. 6.17(a). Each set of experiments is repeated five times. The geometry is shown in Fig. 6.17(b).

6.5.2 Comparison of Experiments and Simulations

Due to symmetry conditions, we can compare the experimental results with the finite element computations of one-eighth of the plate with a hole with a radius of $R = 2.5\,\mathrm{mm}$, see Fig. 6.18(a). A displacement of $\bar{u}_x = 0.26\,\mathrm{mm}$ is applied to the plate at the clamping part, see the blue area in Fig. 6.18(b). The model is meshed using 20-noded hexahedral elements, see Fig. 6.18(b). GID software (GiD-Manual, 2012) is used as a pre-and post-processor for the finite element simulation. Further, the in-house finite element program TASAFEM is used to perform three-dimensional computations for the small strain case using 20-noded hexahedral elements with $3 \times 3 \times 3$ Gauss-point.

First, a uni-directional fiber orientation computation with $\boldsymbol{a} = \boldsymbol{e}_1$ is performed. In the second simulation, the fiber bypassing simulation, the tangent vectors are determined using the B-spline approach, see Eq.(5.58). A comparison between the experiments and the simulations regarding the force-displacement curves can be seen in Fig. 6.19* with the mean-value and the blue-scaled standard deviation. A force-displacement curve represents the force determined by finite element computations. From the results, we can see a deviation in the stiffness. The force-displacement plots for both cases indicate that there is a deviation of nearly $8 - 10\%$ between the simulations and the experiments. Let us compare the computations and the experimental values for the

*Figures 6.19- 6.22 and Tab. 6.1 are taken from (Hartmann et al., 2020) and Mr. Rose Rogin Gilbert generated these pictures.

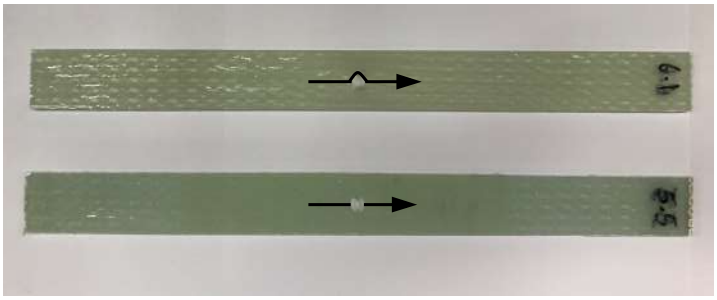

(a) Specimens with bypassed and cut fibers with hole radius of $r = 2.5\,\mathrm{mm}$

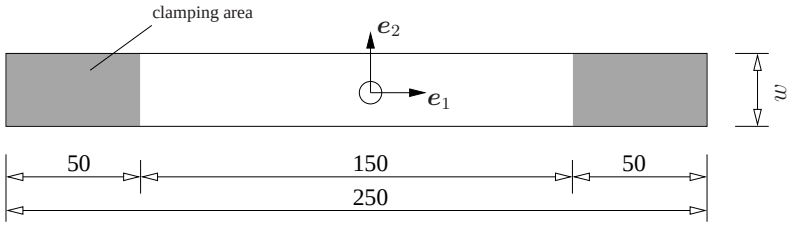

(b) Bypass specimens: thickness $d = 2.5 \pm 0.1\,\mathrm{mm}$, width $w = 19.7 \pm 0.4\,\mathrm{mm}$; uni-directional specimens: thickness $d = 2.4 \pm 0.1\,\mathrm{mm}$, width $w = 19.95 \pm 0.45\,\mathrm{mm}$ (with a hole having a radius of $R = 2.5\,\mathrm{mm}$)

Figure 6.17: Samples for validation purposes

maximum principal strain in the middle of the samples, which is significant and critical. The maximum principal strain of the simulations around the hole can be seen in Fig. 6.20. The division between the purely isotropic and anisotropic regions can be noticed in Fig. 6.20(b), i.e. the discontinuity of the material is recognizable in the simulation.

Here, the maximum principal strain distributions are obtained for the uni-directional fibers and the fiber bypassing samples, see Fig. 6.21. The DIC-system is not able to present data in the white regions. This might be due to the spray-paint pattern on the surface of samples, since some big black dots can be seen on the surface of the samples. Moreover, if the surface of specimen is not smooth enough or has any defects, this can also lead to problems for DIC-systems. On the other hand, the principle strain distribution is relatively close to the numerical results.

The introduction of relative errors is provided to allow for a better comparison of the results from the simulation and the experiments,

$$e = \frac{|\varepsilon_{1,\mathrm{exp}} - \varepsilon_{1,\mathrm{sim}}|}{|\varepsilon_{1,\mathrm{exp}}|} \times 100. \tag{6.3}$$

The experimental maximum principal strains are represented with $\varepsilon_{1,\mathrm{exp}}$, and $\varepsilon_{1,\mathrm{sim}}$ correspond to the numerical results. The relative error for the five validation experiments with uni-directional fibers and fiber bypassing specimens are provided in Fig. 6.22. In order to evaluate the results, the mean-values of all data of the evaluation points are determined. The mean relative errors of all the five uni-directional and fiber bypassing samples are listed in Tab. 6.1, (Hartmann et al.,

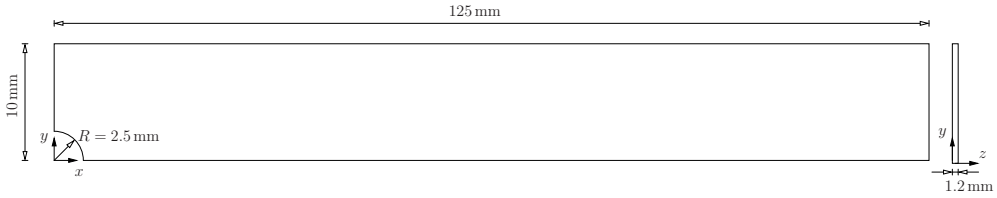

(a) Geometry of one-eighth of the specimen

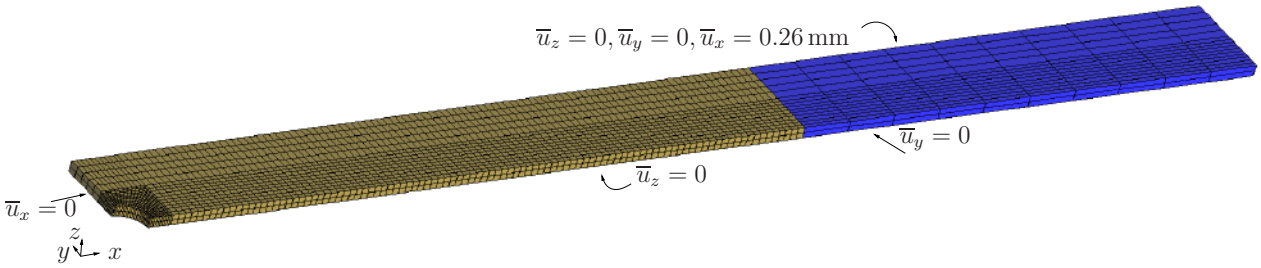

(b) Geometry (mesh and boundary conditions)

Figure 6.18: Geometry, mesh, and boundary conditions

2020). The prediction of the entire region based on finite element simulation has a deviation of

Table 6.1: Mean relative error of uni-directional and bypassing fiber samples

sample no.	uni-directional fiber		fiber bypassing	
	mean relative error - full field (in %)	mean relative error - ROI (in %)	mean relative error - full field (in %)	mean relative error - ROI (in %)
1	20.79	29.50	24.53	30.72
2	15.44	18.65	26.52	35.44
3	16.45	26.11	22.97	35.75
4	17.76	27.58	23.40	32.01
5	17.95	28.43	22.59	30.32

$\approx 18\%$ for the uni-directional fiber direction and $\approx 24\%$ for the bypass case. If we concentrate only on the region around the hole, the errors are higher. This becomes more noticeable if we specify a "region of interest" (ROI). For this aim, an area of $6\,\mathrm{mm} \times 6\,\mathrm{mm}$ around the center of the hole is chosen. For the specified area, a mean relative error of 26% can be observed for the uni-directional samples and only 33% for the bypass samples. Nevertheless, there are much higher errors in the uni-directional case locally, while the mean relative errors are larger in the bypass case. In this regard, quality measures of heterogeneous material calculations are still an open matter.

Since it is possible to address the fiber direction using two methods, the difference between the streamline and the B-spline approaches is of interest. For this aim, the computations are

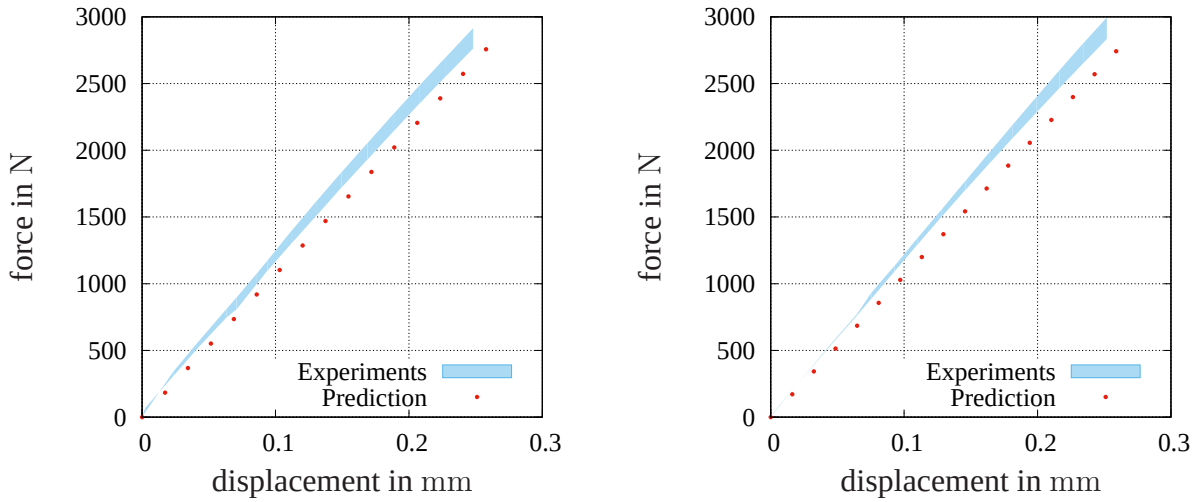

(a) Samples with uni-directional fiber orientation

(b) Samples with fibers bypassing the hole

Figure 6.19: Force-displacement curves of validation examples

again done using the obtained parameters for transversal isotropy in Chapter 4 with the geometry and mesh in Fig. 6.18. Again, a displacement of $\bar{u}_x = 0.26\,\mathrm{mm}$ is applied to the plate at the clamping part, see the blue area in Fig. 6.18(b). Fiber orientation $\boldsymbol{a}$ is determined using the streamline approach, with the help of Eq.(5.10). There is an area where no fibers exist, see Fig. 6.23(a). Regarding this area, the first and the end points are obtained from the experiment pictures, see Fig. 5.3. A polynomial of third order is used to define the area. This polynomial is defined with the help of coordinates and the first derivative of the start and end points, which is assumed to be zero.

A force-displacement curve shows the resulting force from the finite element computations, see Fig. 6.23(b). The force-displacement plots indicate that there is a deviation of around $6 - 12\%$ between the simulations and the experiments. Again, a comparison between the maximum principal strains of the computations and the experiments is provided with regard to the center of the samples. Fig. 6.24 shows the maximum principal strain of the simulations for the area around the hole. The relative error of the five validation experiments for the fiber-bypassing specimens are provided in Fig. 6.25.

To get a better understanding of the results, the mean-values of all data of the evaluation points are calculated. The mean relative errors of all the five fiber-bypassing samples are compiled in Tab. 6.2. The prediction of the entire region based on a finite element simulation has a deviation of $\approx 23\%$. In addition, the finite element simulation for an area of $6\,\mathrm{mm} \times 6\,\mathrm{mm}$ around the center of the hole, which is again referred to as a ROI, has a deviation of $\approx 43\%$. Comparing Tab. 6.1 and Tab. 6.2, it can be seen that finite element simulations using the streamline approach have a larger deviation, $\approx 1\%$ for the entire plate and $\approx 10\%$ for the ROI, in comparison to the

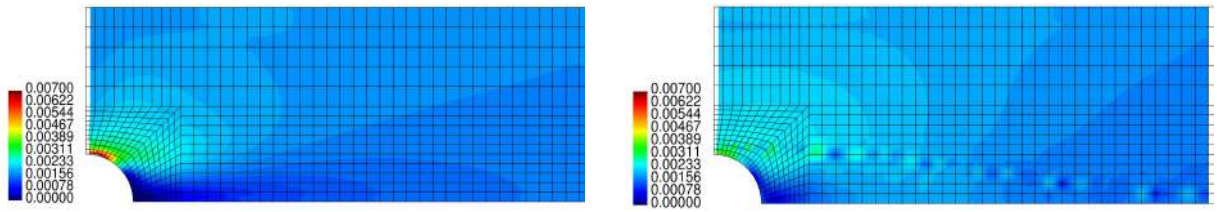

(a) Uni-directional fiber orientation (b) Curvilinear fiber orientation

Figure 6.20: FEM prediction of uni-directional and fiber circumplacement computations using B-spline approach

Table 6.2: Mean relative error of validation samples with the streamline approach

sample no.	mean relative error - full field (in $\%$)	mean relative error - ROI (in $\%$)
1	21.65	38.77
2	22.34	43.45
3	24.59	49.17
4	22.99	43.98
5	21.50	40.99

finite element simulation based on the B-spline approach. The differences in the ROI result from the fiber directions around the hole. Clearly, since the unit tangent vector has different values, the most pronounced difference between the streamline method and the B-spline method is to be found in the area around the hole. It is obvious that computations using a B-spline approach show less deviation, since the experimental data represents the fiber orientations more accurately. On the other hand, the behavior of the entire plate is very similar in the two methods.l A direct comparison does not show huge differences between the force-displacement curves of the two computation methods; both have an average deviation of $\approx 9\%$.

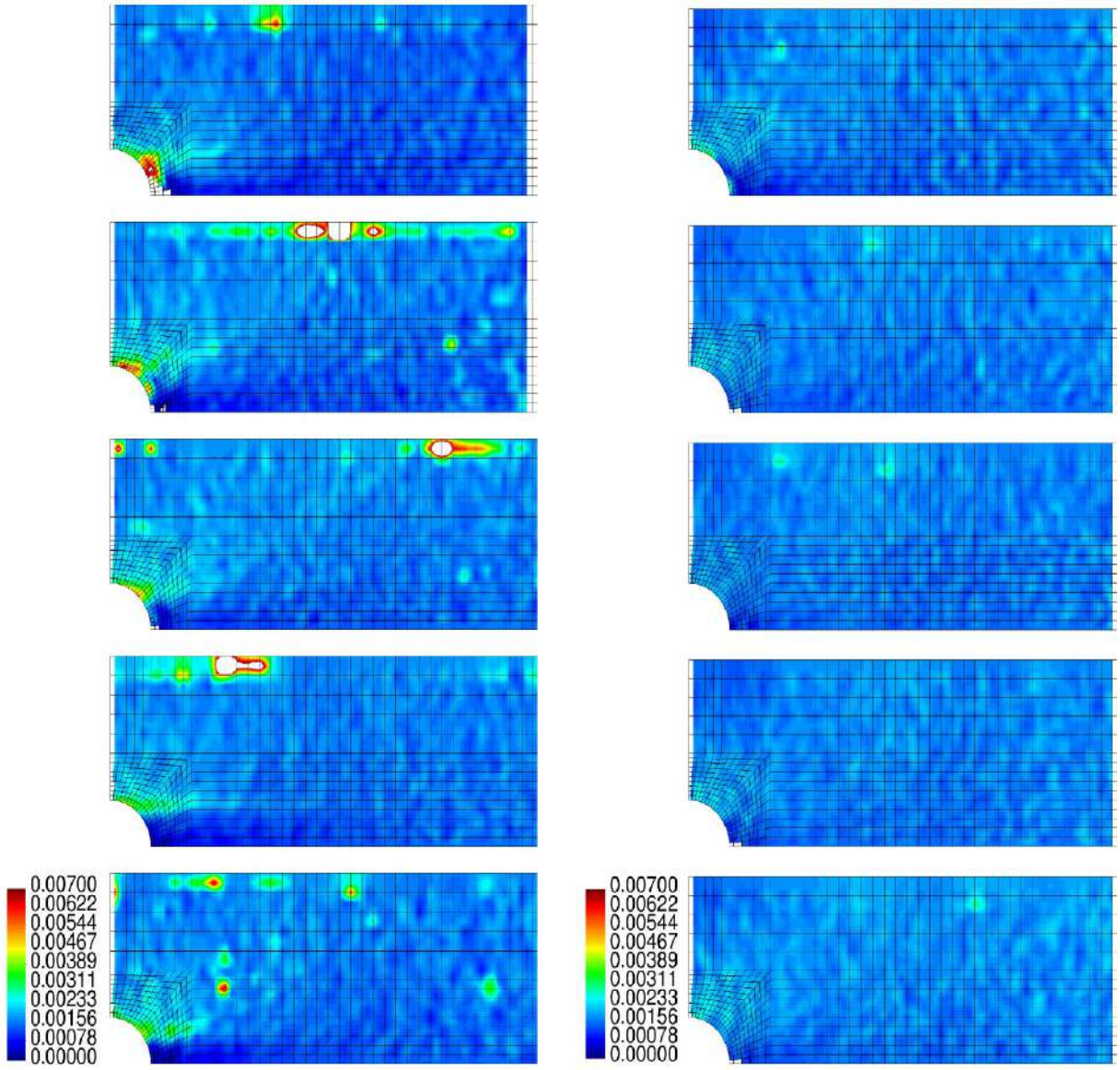

(a) Maximum principal strains for uni-directional fiber orientation

(b) Maximum principal strains for fiber bypassing orientation

Figure 6.21: Maximum principal strain distribution in validation examples

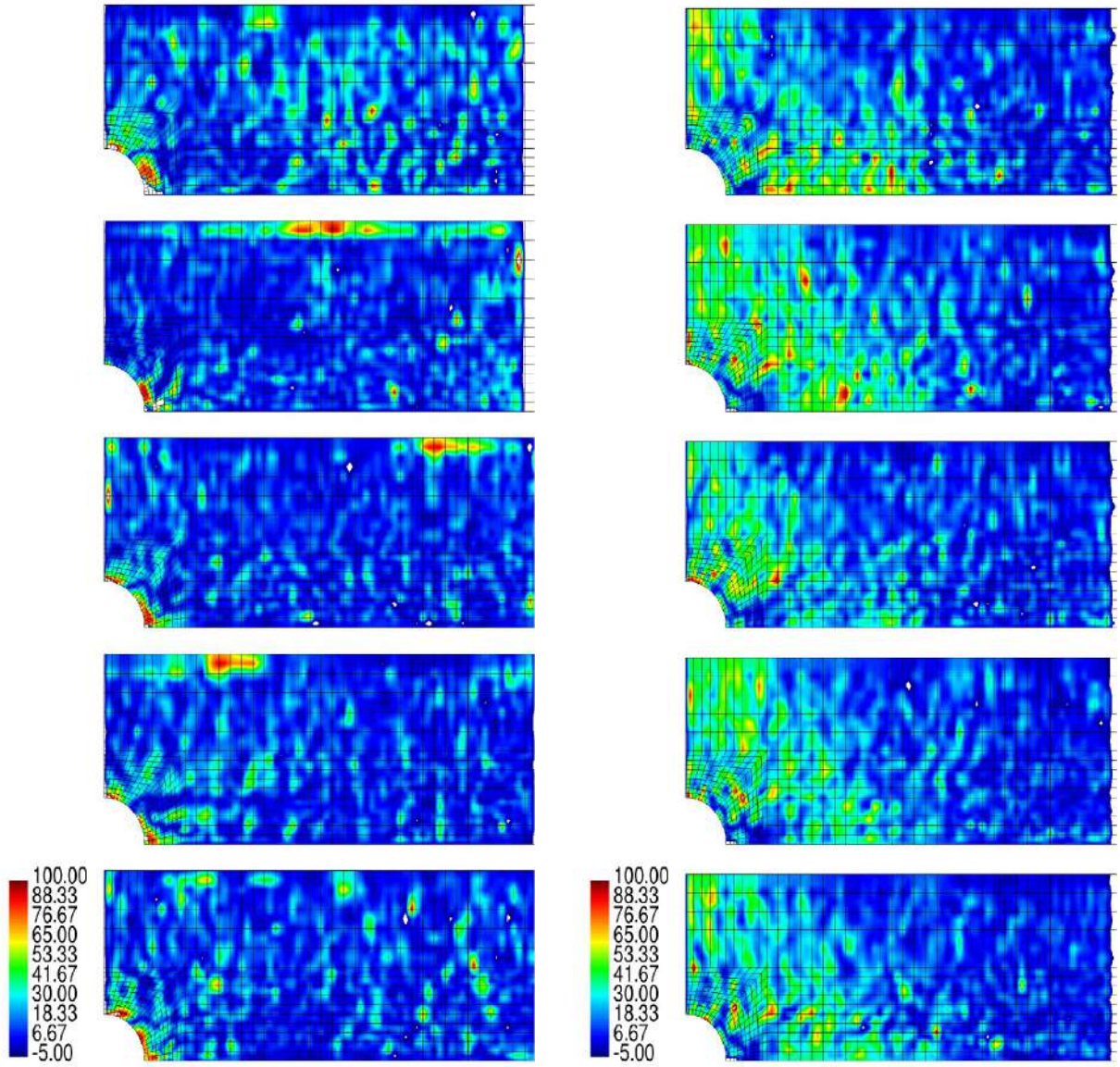

(a) Relative error for uni-directional fiber orientation (b) Relative error for fiber bypassing orientation

Figure 6.22: Relative error for uni-directional fiber orientation and fiber bypassing orientation with respect to experimental results

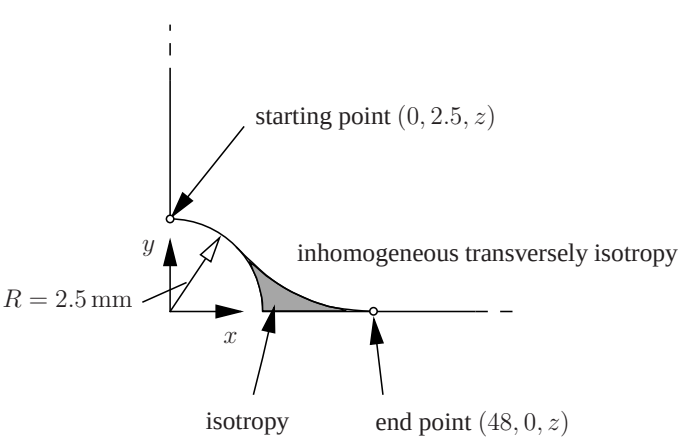

(a) Region with isotropic material

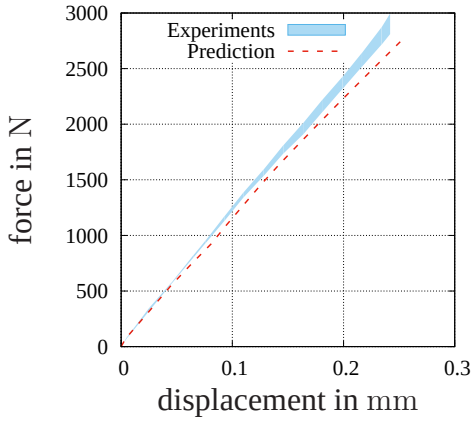

(b) Force-displacement curves of validation examples

Figure 6.23: Region with isotropic material and force-displacement curves of validation examples with fiber bypassing orientation for transversal isotropy laminates

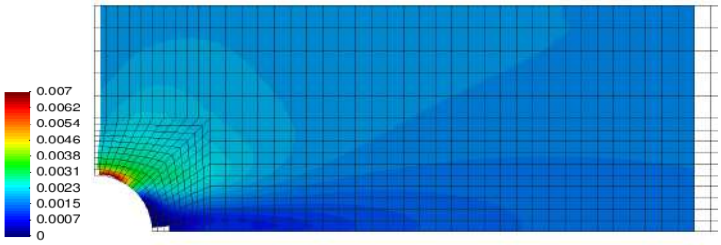

(a)

Figure 6.24: FEM prediction of fiber circumplacement computations using the streamline approach

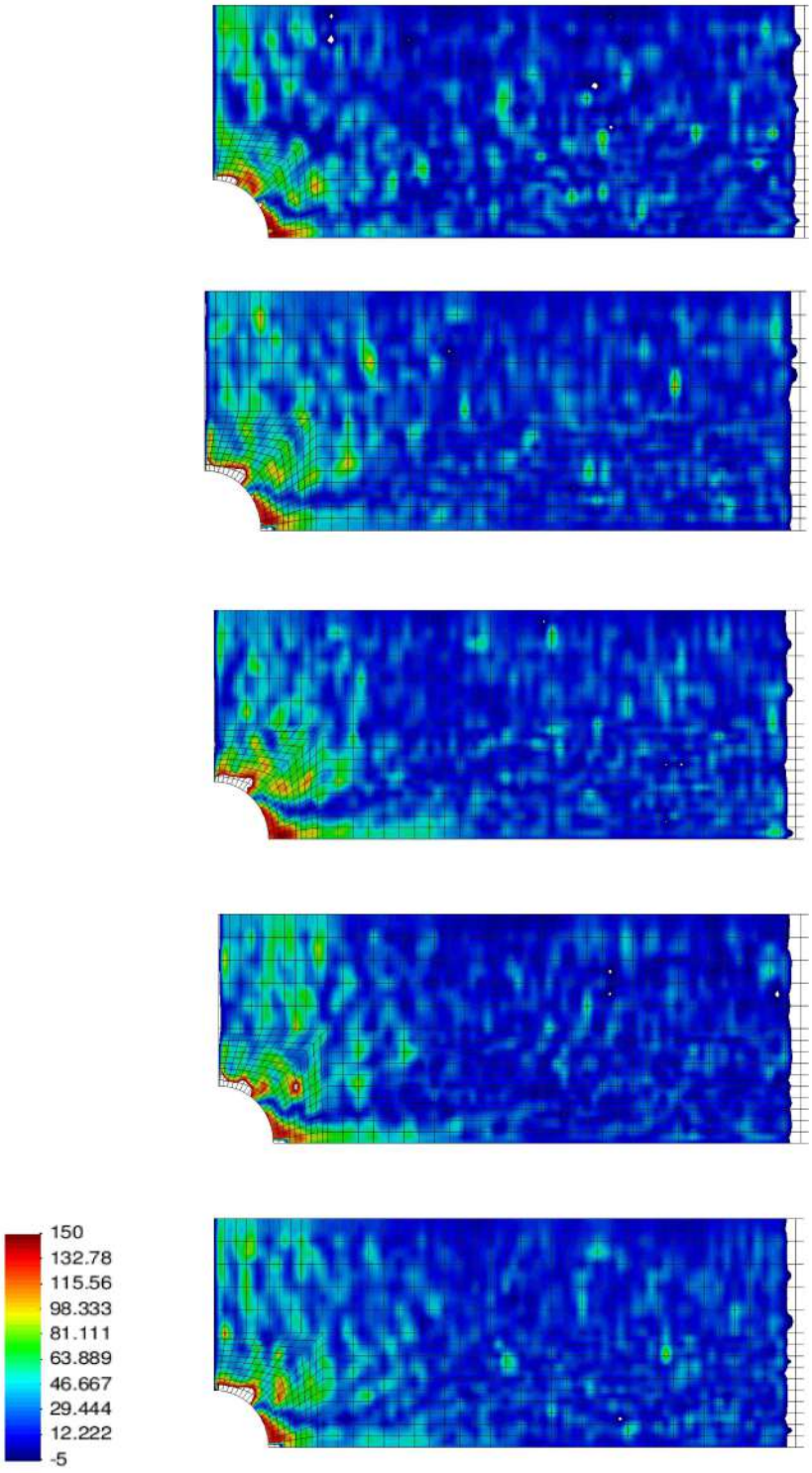

Figure 6.25: Relative error of validation examples using the streamline approach

6.6 Orthotropy

6.6.1 Experimental Results

A set of bi-directional fiber laminate experiments is carried out. In this set, the fibers are cut after the production process by drilling a hole into the laminates. The set of specimens was made using resin RIMR135 with the curing agent RIMH1366, similar to the sample for identification purposes in Chapter 4, see Fig. 6.26(a). This experiment is again repeated five times, and the geometry is shown in Fig. 6.26(b). It should also be mentioned that, in this case, bypassing the

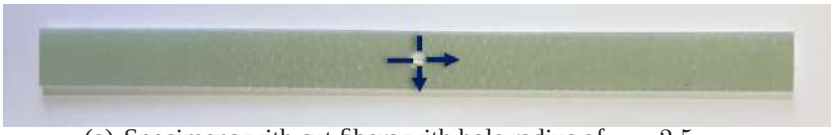

(a) Specimens with cut fibers with hole radius of $r = 2.5\,\mathrm{mm}$

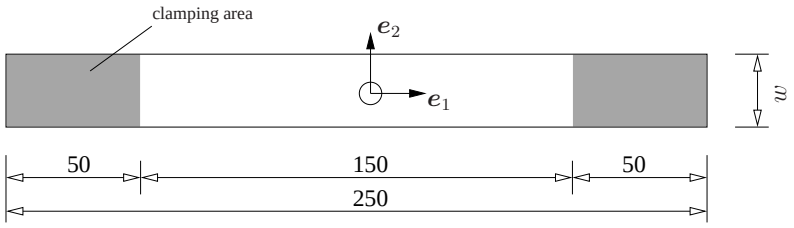

(b) Reinforced composite samples with fiber direction $\boldsymbol{a} = \boldsymbol{e}_2$ and $\boldsymbol{a} = \boldsymbol{e}_1$ (thickness $d = 2.5 \pm 0.1\,\mathrm{mm}$, width $w = 20.4 \pm 0.4\,\mathrm{mm}$, with hole radius of $r = 2.5\,\mathrm{mm}$)

Figure 6.26: Orthotropy samples for validation purpose

fibers around the hole generates an area around the hole where the fibers are not perpendicular to each other. Thus, the laminate is not orthotropic anymore, and it is not considered for the validation experiments. In this section, the entire process of experiments, modeling of fiber-bypassing, and material parameter identification for the orthotropy material is validated.

6.6.2 Comparison of Experiments and Simulations

Due to symmetry conditions, we can again compare the finite element computations of one-eighth of the plate with a hole with a radius of $R = 2.5\,\mathrm{mm}$ to the experimental results, see Fig. 6.27. The model is meshed using 20-noded hexahedral elements. A displacement of $\bar{u}_x = 0.19\,\mathrm{mm}$ is applied to the plate at the clamping part, see the blue area in Fig. 6.27(b).

Orthotropic laminates with two fiber orientations, $\boldsymbol{a} = \boldsymbol{e}_1$ and $\boldsymbol{b} = \boldsymbol{e}_2$, are considered. A comparison between the experiments and simulations with respect to the force-displacements can be seen in Fig. 6.28. The results clearly show the deviations regarding the stiffness. The force-displacement plots for both cases indicate that, using Eq.(6.3), there is a deviation of nearly $7 - 13\%$ between the simulations and the experiments.

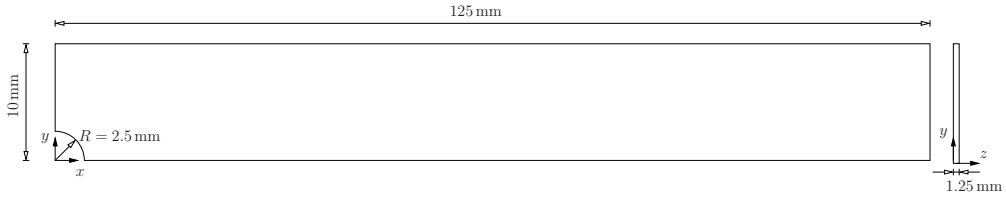

(a) Geometry of one-eighth of the specimen

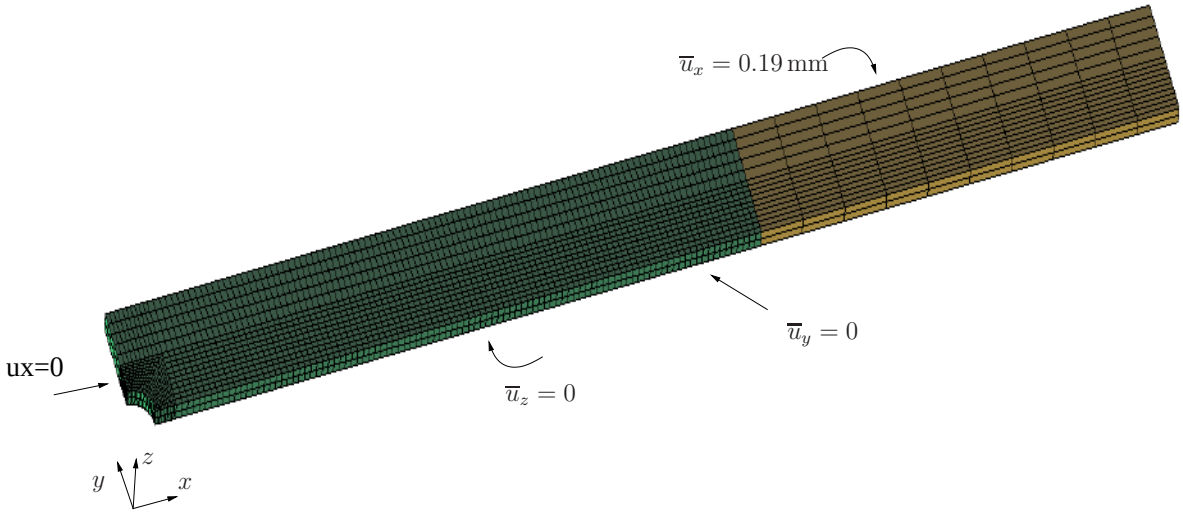

(b) Geometry (mesh and boundary conditions)

Figure 6.27: Geometry, mesh, and boundary conditions of orthotropy laminates for computations

Since the center of the samples is significant and crucial for us, a comparison between the maximum principal strains of the computations and the experiments is provided. The maximum principal strains of the simulations around the hole can be seen in Fig. 6.29. Here, the maximum principal strain distributions of the orthotropy samples for the five validation experiments are obtained, see in Fig. 6.30(a). The DIC-system is not able to represent data for the white regions. On the other hand, the principle strain distribution is in good agreement with the numerical results.

To allow for a better comparison between the results of the simulation and the experiments, the relative errors using Eq.(6.3) are provided. The experimental maximum principal strains are represented with $\varepsilon_{1,\text{exp}}$, and $\varepsilon_{1,\text{sim}}$ correspond to the numerical results. The relative error for the five validation experiments in the orthotropic samples are provided in Fig. 6.30(b). In order to evaluate the results, the mean-values of all data of the evaluation points are determined. The mean relative error of all the five uni-directional and fiber-bypassing samples are compiled in Tab. 6.3. The prediction of the entire region using finite element simulation shows a deviation of $\approx 32\%$ for the orthotropic case. Moreover, finite element computations for an area of $6\,\mathrm{mm} \times 6\,\mathrm{mm}$ from the center of the hole, which is again referred to as ROI, has a deviation of $\approx 35.5\%$.

Considering the uni-directional samples in Tab. 6.1 and Tab. 6.3, it can be seen that finite element simulations for orthotropic plates have higher deviations, $\approx 14\%$ for the entire plate and

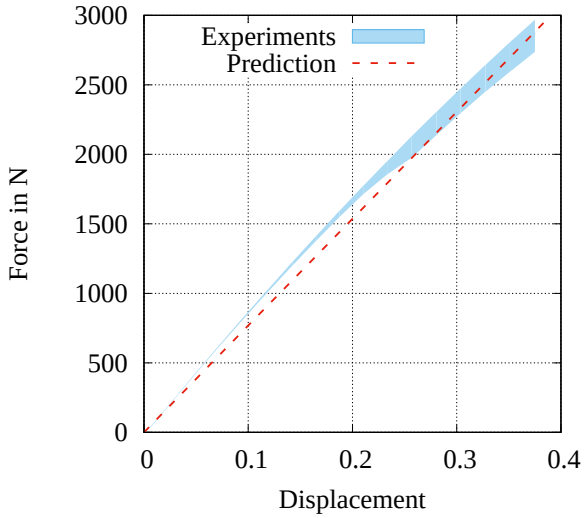

Figure 6.28: Force-displacement curves of orthotropy validation examples

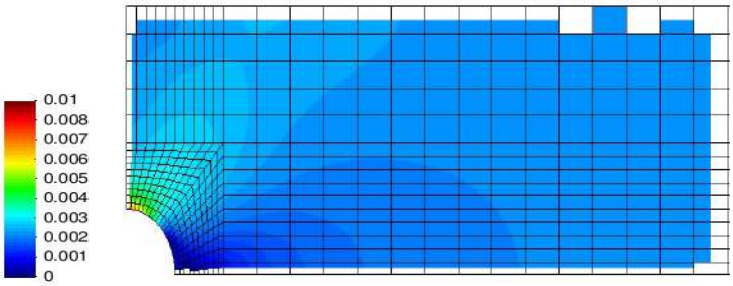

Figure 6.29: FEM prediction of orthotropy computations

$\approx 10.5\%$ for the ROI. In the orthotropy case, more parameters are involved in the computations. Therefore, the uncertainty of each parameter causes a disagreement, and this increases the deviation between the simulations and the experiments in the orthotropy case. A comparison between the force-displacement curves of the computations for orthotropy and the transversal isotropy laminates shows almost the same mean deviations: $\approx 9 - 10\%$ on the average.

Table 6.3: Mean relative error of orthotropy samples

sample no.	mean relative error - full field (in %)	mean relative error - ROI (in %)
1	29.64	32.64
2	32.61	35.20
3	29.26	32.10
4	36.13	42.35
5	32.13	35.37

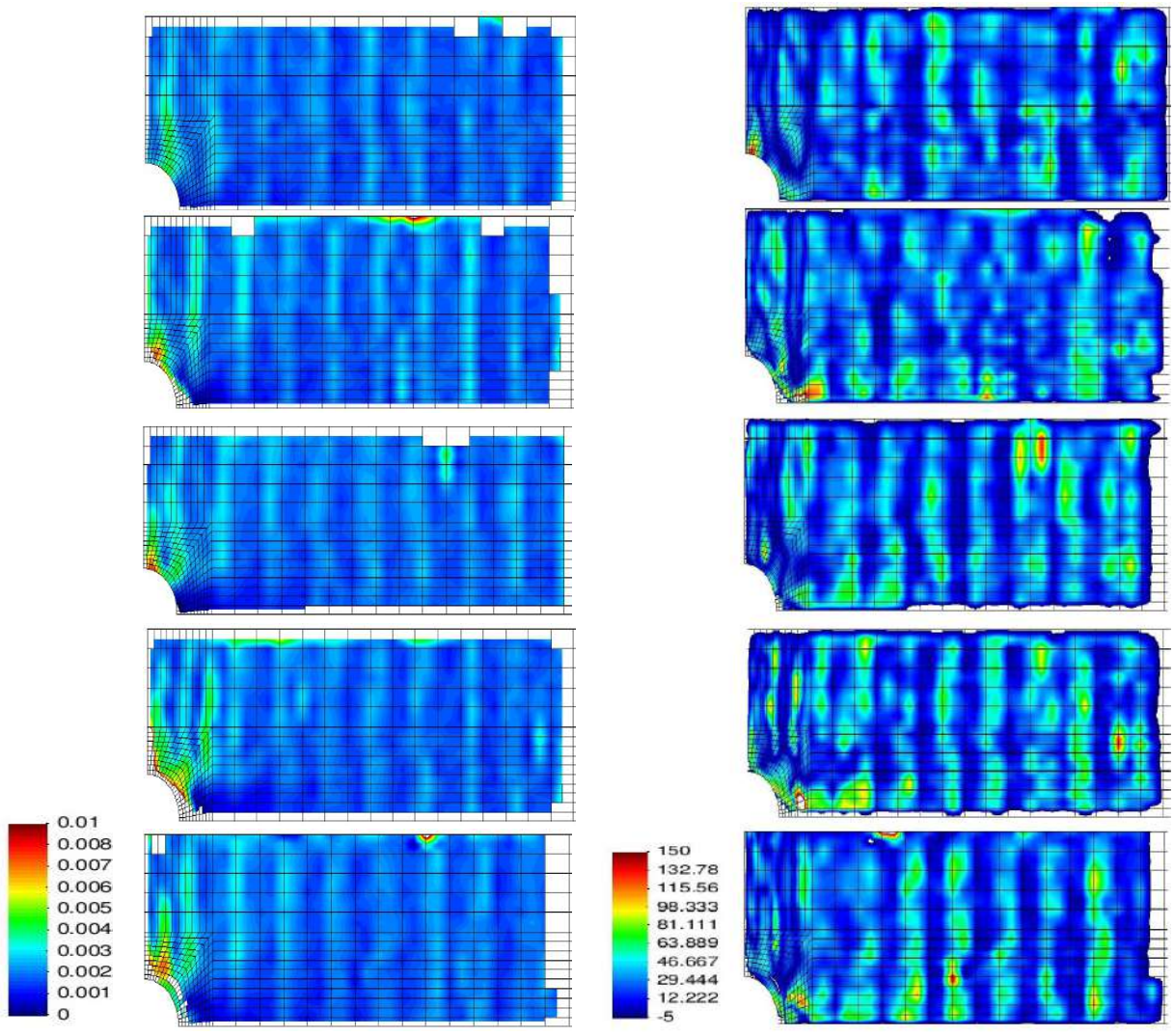

(a) Maximum principal strains for orthotropy samples using DIC-system

(b) Relative error for orthotropy samples

Figure 6.30: Maximum principal strain distribution and relative error in validation samples

7 Conclusions and Outlook

One major aim of this thesis is to study, simulate, and predict the behavior of transverse isotropic laminates where the fiber orientation is spatially inhomogeneous. This is modeled using a B-spline approach. It is also investigated what effect it has if a specimen is designed in such a way that the fibers bypass a hole. In both cases, special focus is placed on determining the material parameters from experimental investigations.

Composite laminate specimens with a hole can be obtained by producing a fiber-reinforced composite plate and, subsequently, drilling the borehole. Another approach is to bypass the fibers around the hole before injecting the matrix material. In the first case, the spatial distribution of the axis of anisotropy and the structural tensor concerned are spatially constant. In the second case, i.e. the fiber circumplacement around the hole, yields a space-dependent area of anisotropy. Thus, the possibility of bypassing the fibers around a hole in order to improve the structure performance is one of the aspects addressed in this work. For this purpose, it is necessary to investigate the stress and strain distribution of uni-directional and inhomogeneous fiber directions around a hole. A mathematical function serves to model the fiber distribution in a plate. In the first step, the circumplacement of the fibers is modeled using a streamline function to obtain the inhomogeneous fiber direction, which can be used in finite element simulations of transversely isotropic material. The calculated material parameters are then used for the computations. A comparison between the two described cases showed promising results, namely that the stresses are essentially reduced around the hole. There are, however, higher compressive strains, vertical to the loading direction, but they are not as problematic as the tensile strains. In addition, the computations are also performed for plates with rivets in order to investigate the local effect of rivets around the hole. It is observed that bypassing the fibers reduces the stress around the hole, however with higher compressive strains. Thus, positive results are obtained, as compressive strains are not as critical as tensile strains in these cases.

It turns out that further investigations and comparisons to experimental data have to follow. For this purpose, the aim is to find a more precise way to define fiber orientation, although the streamline approach is an efficient and fast way to represent fiber directions. B-splines are powerful when it comes to representing curves and surfaces. It should also be mentioned that the precision of the continuous description of the spatially inhomogeneous fiber distribution in the B-spline approach is a remarkable advantage, although this method is much more complicated than the streamline approach. Thus, with regard to determining of the continuous fiber distribution, a new concept of interpolating data points regarding experimental fiber directions using B-splines surfaces is proposed. This approach leads to a smooth approximation in comparison to classical discrete approaches. The function is implemented into the finite element program (TASAFEM) so that the fiber orientation can be computed at each Gauss-point of the finite element. An important aspect is the formulations of computing the control points from experimental data,

where a consistent matrix notation is applied.

The next challenge is to obtain the material parameters to perform the finite element simulations. Five material parameters of linear elastic, transverse isotropy have to be identified for the material model. The material parameter identification process is performed based on a least-square approach combining finite element simulations and both sets of surface strain information from a digital image correlation system as well as force data from the testing machine. Specific experiments have to be carried out to obtain the material parameters, namely uniaxial tension for the fiber orientations of $0°$ and $90°$, a shear test, and a computational compression test.

The material model is evaluated using the parameters obtained for the transverse isotropic samples. For this, it is necessary to validate the numerical approach by means of experimental observations. Two types of specimens are used for the validation examples: one with a hole that was drilled after the production process, with a uniform fiber distribution, and one with a hole where the fibers were bypassed around the hole before the matrix material was injected. All the solutions are treated using finite elements. Validation experiments are performed, and real errors between the computations and the experimental results of the digital image correlation system are shown. This is commonly circumvented in the literature. It turns out that, firstly, the strain scattering of the samples dominates the evaluation and, secondly, that it is possible to determine a region of interest. The computations for the bypassing case are performed based on B-spline and streamline approaches, and the streamline method showed higher deviations with respect to the experiments.

The investigation is extended to orthotropy laminates with two fiber directions. One goal is to predict the behavior of orthotropy laminates based on the calculated material parameters. In the first step, a constitutive model of orthotropy for the small strain case is derived from large strain theory. The model is implemented in the in-house finite element program TASAFEM. The constitutive model of orthotropy is based on strain energy function with seven invariants. Nine material parameters of linear elastic, orthotropy are identified. In order to obtain the material parameters, various samples based on the VARI production process are manufactured, and different experiments such as tension, compression, three-rail shear, and lap shear tests are carried out. Furthermore, the material parameters are identified within a least-square approach with the help of optical results from a digital image correlation system.

In the following step, the material model is evaluated using the obtained material parameters for specimens with bi-directional fiber orientations. For this purpose, it is necessary to validate the numerical approach with experimental observations. Then, validation experiments are performed with specimens with fibers in two perpendicular directions and with a hole (drilled after the production process). To estimate the final stress and strain state for an orthotropic composite plate, finite element simulations are again accomplished. Regarding the validation experiments, a real error can again be shown between the computation and the experimental results of the digital image correlation system. A comparison between the finite element simulations and the experiment results shows promising results. The computations for bi-directional fiber orientation show higher deviations with respect to the experimental data in comparison to the uni-directional case, because more material parameters had to be considered for the predictions.

There are aspects that could be investigated more thoroughly in the future. The scope of this work is restricted to the linear elasticity, but the approach could be extended to the non-linear

problem in future work. Further, it could be promising to develop a model to represent bypassed fibers in samples with bi-directional fiber orientations.

8 Appendix

8.1 Relation of the Invariants of the Green Strain and the Right Cauchy-Green Tensor

Using $\mathbf{E} = (1/2)(\mathbf{C} - \mathbf{I})$ or $\mathbf{C} = 2\mathbf{E} + \mathbf{I}$, the invariants of the Green strain and right Cauchy-Green tensor are related to each other as

$$\begin{aligned}
\operatorname{tr}\mathbf{C} &= \operatorname{tr} 2\mathbf{E} + \mathbf{I} = 2\operatorname{tr}\mathbf{E} + 3 = 2\mathrm{I}_{\mathbf{E}} + 3, && (8.1)\\
\operatorname{tr}\mathbf{C}^2 &= \operatorname{tr}((2\mathbf{E} + \mathbf{I})(2\mathbf{E} + \mathbf{I})) = \operatorname{tr}(4\mathbf{E}^2 + 4\mathbf{E} + \mathbf{I}) = 4\operatorname{tr}\mathbf{E}^2 + 4\operatorname{tr}\mathbf{E} + 3\\
&= 4\mathrm{II}_{\mathbf{E}} + 4\mathrm{I}_{\mathbf{E}} + 3, && (8.2)\\
\operatorname{tr}\mathbf{C}^3 &= \operatorname{tr}((4\operatorname{tr}\mathbf{E}^2 + 4\operatorname{tr}\mathbf{E} + 3)(2\mathbf{E} + \mathbf{I})) = \operatorname{tr}(8\mathbf{E}^3 + 12\mathbf{E}^2 + 6\mathbf{E} + \mathbf{I})\\
&= 8\operatorname{tr}\mathbf{E}^3 + 12\operatorname{tr}\mathbf{E}^2 + 6\operatorname{tr}\mathbf{E} + 3 = 8\mathrm{III}_{\mathbf{E}} + 12\mathrm{II}_{\mathbf{E}} + 6\mathrm{I}_{\mathbf{E}} + 3, && (8.3)\\
\operatorname{tr}\mathbf{C}\mathbf{M}_1 &= \operatorname{tr}(\mathbf{C}(\boldsymbol{a}\otimes\boldsymbol{a})) = \boldsymbol{a}\cdot\mathbf{C}\boldsymbol{a} = \boldsymbol{a}\cdot(2\mathbf{E} + \mathbf{I})\boldsymbol{a} = 2\boldsymbol{a}\cdot\mathbf{E}\boldsymbol{a} + \boldsymbol{a}\cdot\boldsymbol{a} = 2\boldsymbol{a}\cdot\mathbf{E}\boldsymbol{a} + 1\\
&= 2\mathrm{IV}_{\mathbf{E}} + 1, && (8.4)\\
\operatorname{tr}\mathbf{C}^2\mathbf{M}_1 &= \operatorname{tr}(\mathbf{C}^2(\boldsymbol{a}\otimes\boldsymbol{a})) = \mathbf{C}\boldsymbol{a}\cdot\mathbf{C}\boldsymbol{a} = (2\mathbf{E} + \mathbf{I})\boldsymbol{a}\cdot(2\mathbf{E} + \mathbf{I})\boldsymbol{a} = (2\mathbf{E}\boldsymbol{a} + \boldsymbol{a})\cdot(2\mathbf{E}\boldsymbol{a} + \boldsymbol{a})\\
&= 4\mathbf{E}\boldsymbol{a}\cdot\mathbf{E}\boldsymbol{a} + 4\mathbf{E}\boldsymbol{a}\cdot\boldsymbol{a} + 1 = 4\mathrm{V}_{\mathbf{E}} + 4\mathrm{IV}_{\mathbf{E}} + 1. && (8.5)
\end{aligned}$$

Similarly to Eq.(8.4) and Eq.(8.5), it can be written that

$$\begin{aligned}
\operatorname{tr}\mathbf{C}\mathbf{M}_2 &= \operatorname{tr}(\mathbf{C}(\boldsymbol{b}\otimes\boldsymbol{b})) = 2\mathrm{VI}_{\mathbf{E}} + 1, && (8.6)\\
\operatorname{tr}\mathbf{C}^2\mathbf{M}_2 &= \operatorname{tr}(\mathbf{C}^2(\boldsymbol{b}\otimes\boldsymbol{b})) = 4\mathbf{E}\boldsymbol{b}\cdot\mathbf{E}\boldsymbol{b} + 4\mathbf{E}\boldsymbol{b}\cdot\boldsymbol{b} + 1 = 4\mathrm{VII}_{\mathbf{E}} + 4\mathrm{VI}_{\mathbf{E}} + 1. && (8.7)
\end{aligned}$$

8.2 Calculation of Second Piola-Kirchhoff Stress Tensor in Orthotropic Case

The calculation of the second Piola-Kirchhoff in Eq.(3.89) requires a chain rule which is applied on Eq.(3.87). The Gateaux-derivative is required within the chain rule. The details of the calculation of the Gateaux-derivative for invariants is provided in the following. The first invariant is $\mathrm{I}_{\mathbf{E}} = \operatorname{tr}\mathbf{E}$, and by applying the Gateaux-derivative, it yields

$$\frac{\partial \mathrm{I}_{\mathbf{E}}}{\partial \mathbf{E}}\mathbf{H} = \mathsf{D}_{\mathbf{E}}\,\mathrm{I}_{\mathbf{E}}(\mathbf{E})[\mathbf{H}] = \frac{\partial \operatorname{tr}(\mathbf{E} + \lambda\mathbf{H})}{\partial\lambda}|_{\lambda=0} = \operatorname{tr}(\mathbf{H}) = \mathbf{I}\cdot\mathbf{H}, \tag{8.8}$$

which results in

$$\frac{\partial \mathrm{I}_{\mathbf{E}}}{\partial \mathbf{E}} = \mathbf{I}. \tag{8.9}$$

The second invariant is $\mathrm{II}_{\mathbf{E}} = \operatorname{tr} \mathbf{E}^2$

$$\frac{\mathrm{d}\mathrm{II}_{\mathbf{E}}}{\mathrm{d}\mathbf{E}}\mathbf{H} = \mathsf{D}_{\mathbf{E}}\, \mathrm{II}_{\mathbf{E}}(\mathbf{E})[\mathbf{H}] = \frac{\mathrm{d}\operatorname{tr}(\mathbf{E}+\lambda\mathbf{H})^2}{\mathrm{d}\lambda}|_{\lambda=0} = 2\mathbf{E}\cdot\mathbf{H}, \tag{8.10}$$

and yields to

$$\frac{\partial \mathrm{II}_{\mathbf{E}}}{\partial \mathbf{E}} = 2\mathbf{E}. \tag{8.11}$$

The third invariant is $\mathrm{I}_{\mathbf{E}} = \operatorname{tr} \mathbf{E}^3$

$$\begin{aligned}\frac{\partial \mathrm{III}_{\mathbf{E}}}{\partial \mathbf{E}}\mathbf{H} = \mathsf{D}_{\mathbf{E}}\, \mathrm{III}_{\mathbf{E}}(\mathbf{E})[\mathbf{H}] = \frac{\mathrm{d}\operatorname{tr}(\mathbf{E}+\lambda\mathbf{H})^3}{\mathrm{d}\lambda}|_{\lambda=0} &= \frac{\mathrm{d}\operatorname{tr}(\mathbf{E}^3+3\mathbf{E}^2\lambda\mathbf{H}+3\mathbf{E}\lambda^2\mathbf{H}^2+\lambda^3\mathbf{H}^3)}{\mathrm{d}\lambda}|_{\lambda=0} \\ &= 3\mathbf{E}^2\cdot\mathbf{H},\end{aligned} \tag{8.12}$$

and it follows that

$$\frac{\partial \mathrm{III}_{\mathbf{E}}}{\partial \mathbf{E}} = 3\mathbf{E}^2. \tag{8.13}$$

The fourth invariant is $\mathrm{IV}_{\mathbf{E}} = \operatorname{tr}(\mathbf{E}\mathbf{M}_1)$

$$\frac{\partial \mathrm{IV}_{\mathbf{E}}}{\partial \mathbf{E}}\mathbf{H} = \mathsf{D}_{\mathbf{E}}\, \mathrm{V}_{\mathbf{E}}(\mathbf{E},\mathbf{M}_1)[\mathbf{H}] = \mathbf{H}\cdot\mathbf{M}_1, \tag{8.14}$$

and it is equal to

$$\frac{\partial \mathrm{IV}_{\mathbf{E}}}{\partial \mathbf{E}} = \mathbf{M}_1. \tag{8.15}$$

Correspondingly, for the sixth invariant $\mathrm{VI}_{\mathbf{E}} = \operatorname{tr}(\mathbf{E}^2\mathbf{M}_1)$, it can be shown that

$$\frac{\partial \mathrm{VI}_{\mathbf{E}}}{\partial \mathbf{E}} = \mathbf{M}_2, \tag{8.16}$$

The fifth invariant is $\mathrm{V}_{\mathbf{E}} = \operatorname{tr}(\mathbf{E}^2\mathbf{M}_1)$

$$\frac{\partial \mathrm{V}_{\mathbf{E}}}{\partial \mathbf{E}}\mathbf{H} = \mathsf{D}_{\mathbf{E}}\, \mathrm{V}_{\mathbf{E}}(\mathbf{E},\mathbf{M}_1)[\mathbf{H}] = \mathbf{H}\mathbf{E}\cdot\mathbf{M}_1 + \mathbf{E}\mathbf{H}\cdot\mathbf{M}_1 = \mathbf{H}\cdot(\mathbf{M}_1\mathbf{E}+\mathbf{E}\mathbf{M}_1), \tag{8.17}$$

from which follows

$$\frac{\partial \mathrm{V}_{\mathbf{E}}}{\partial \mathbf{E}} = \mathbf{M}_1\mathbf{E}+\mathbf{E}\mathbf{M}_1. \tag{8.18}$$

Similarly, for the seventh invariant $\mathrm{VII}_{\mathbf{E}} = \operatorname{tr}(\mathbf{E}^2\mathbf{M}_2)$, it is possible to write

$$\frac{\partial \mathrm{VII}_{\mathbf{E}}}{\partial \mathbf{E}} = \mathbf{M}_2\mathbf{E}+\mathbf{E}\mathbf{M}_2. \tag{8.19}$$

8.3 Calculation of the Fourth Order Elasticity Tensor $\mathcal{C}$ for the Orthotropic Model

In order to obtain Eq.(3.95), the following steps have to be taken: The second Piola-Kirchhoff stress tensor $\tilde{\mathbf{T}}$ can be written as

$$\tilde{\mathbf{T}} = \mathbf{h}(\mathbf{E}, \mathbf{M}_1, \mathbf{M}_2) \tag{8.20}$$

where the fourth order elasticity tensor $\mathcal{C}$ can be obtained by applying the Gateaux-derivative as

$$\mathcal{C}\mathbf{H} = \mathsf{D}_{\mathbf{E}}\, \mathsf{I}_{\mathbf{E}}(\mathbf{h})[\mathbf{E}, \mathbf{M}_1, \mathbf{M}_2]\mathbf{H} \tag{8.21}$$

which follows with the help of Eq.(3.93) as

$$\begin{aligned}\mathcal{C}\mathbf{H} = \Big(&(\lambda(\mathbf{H}\cdot\mathbf{I}) + \alpha_1(\mathbf{M}_1\cdot\mathbf{H}) + \alpha_2(\mathbf{M}_2\cdot\mathbf{H}))\mathbf{I} + 2\mu\mathbf{H} + \Big(\alpha_1(\mathbf{H}\cdot\mathbf{I}) + \beta_1(\mathbf{M}_1\cdot\mathbf{H}) \\ &+ \beta_3(\mathbf{M}_2\cdot\mathbf{H})\Big)\mathbf{M}_1 + 2\mu_1(\mathbf{EH}+\mathbf{HE}) + 2\mu_2(\mathbf{EH}+\mathbf{HE}) + \Big(\alpha_2(\mathbf{H}\cdot\mathbf{I}) + \\ &\beta_2(\mathbf{M}_2\cdot\mathbf{H}) + \beta_3(\mathbf{M}_1\cdot\mathbf{H})\Big)\mathbf{M}_2\Big),\end{aligned} \tag{8.22}$$

and it leads to

$$\begin{aligned}\mathcal{C}\mathbf{H} = \Big[&\lambda\mathbf{I}\otimes\mathbf{I} + \alpha_1\mathbf{I}\otimes\mathbf{M}_1 + \alpha_2\mathbf{I}\otimes\mathbf{M}_2 + 2\mu\mathcal{I} + \alpha_1\mathbf{M}_1\otimes\mathbf{I} + \beta_1\mathbf{M}_1\otimes\mathbf{M}_1 \\ &+ \beta_3\mathbf{M}_1\otimes\mathbf{M}_2 + 2\mu_1\Big[\mathbf{I}\otimes\mathbf{M}_1 + \mathbf{M}_1\otimes\mathbf{I}\Big]^{T_{23}} + \alpha_2\mathbf{M}_2\otimes\mathbf{I} + \beta_2\mathbf{M}_2\otimes\mathbf{M}_2 \\ &+ \beta_3\mathbf{M}_2\otimes\mathbf{M}_1 + 2\mu_2\Big[\mathbf{I}\otimes\mathbf{M}_2 + \mathbf{M}_2\otimes\mathbf{I}\Big]^{T_{23}}\Big]\mathbf{H}.\end{aligned} \tag{8.23}$$

Finally, the elasticity tensor reads

$$\begin{aligned}\mathcal{C} = &\lambda\mathbf{I}\otimes\mathbf{I} + \alpha_1\Big[\mathbf{I}\otimes\mathbf{M}_1 + \mathbf{M}_1\otimes\mathbf{I}\Big] + \alpha_2\Big[\mathbf{I}\otimes\mathbf{M}_2 + \mathbf{M}_2\otimes\mathbf{I}\Big] + 2\mu\mathcal{I} + \beta_1\mathbf{M}_1\otimes\mathbf{M}_1 \\ &+ \beta_2\mathbf{M}_2\otimes\mathbf{M}_2 + \beta_3\Big[\mathbf{M}_1\otimes\mathbf{M}_2 + \mathbf{M}_2\otimes\mathbf{M}_1\Big] + 2\mu_1\Big[\mathbf{I}\otimes\mathbf{M}_1 + \mathbf{M}_1\otimes\mathbf{I}\Big]^{T_{23}} \\ &+ 2\mu_2\Big[\mathbf{I}\otimes\mathbf{M}_2 + \mathbf{M}_2\otimes\mathbf{I}\Big]^{T_{23}}.\end{aligned} \tag{8.24}$$

8.4 Control Points

Here, two examples are provided to show the influence of the control points on the final curve. In the first example, the number of data points and control points are the same, as the curve goes through all data points, see Fig. 8.1(a). In the second example, the number of control points is reduced to 4, and the curve goes only through the first and the last data point. In this case, the first and the last data point are equal to the first and the last control point.

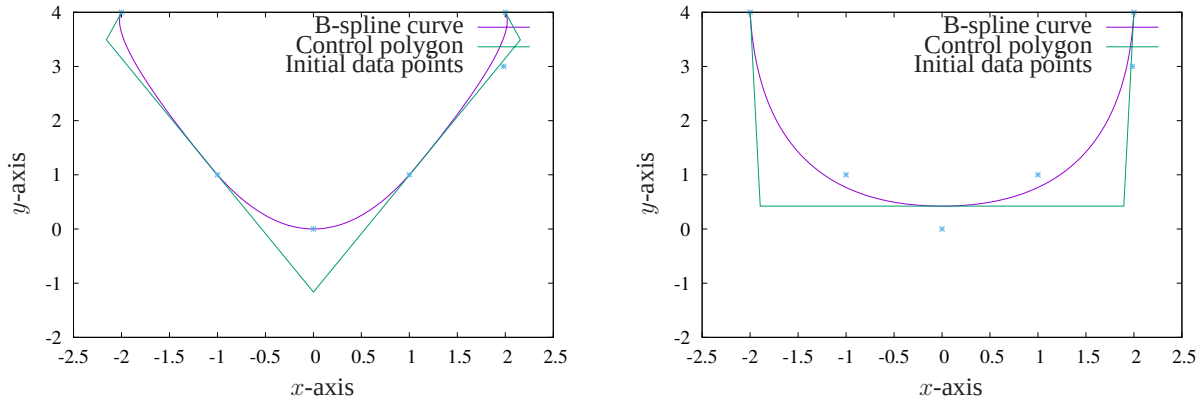

(a) 5 data points and 5 control points

(b) 5 data points and 4 control points

Figure 8.1: The impact of number of control points on the curve

8.5 Investigation Regarding Second and Third Derivatives of the B-Spline Curve

A derivative of higher order for the B-spline curve can be obtained as well. Generally speaking, second and third derivatives are of interest in most curve representations since they provide information about the characteristics and the quality of curves. The second derivative corresponds to the curvature of a curve, and the third derivative is connected to the torsion of a curve, which is a fundamental property of curves in three dimensions. Differentiating Eq.(5.35) yields

$$\begin{aligned} N^{(2)}_{i,k}(\xi) &= \frac{k-1}{\Xi_{i+k-1}-\Xi_i} N^{(1)}_{i,k-1}(\xi) - \frac{k-1}{\Xi_{i+k}-\Xi_{i+1}} N^{(1)}_{i+1,k-1}(\xi) \\ &= \frac{k-1}{\Xi_{i+k-1}-\Xi_i}\left(\frac{k-2}{\Xi_{i+k-2}-\Xi_i} N_{i,k-2}(\xi) - \frac{k-2}{\Xi_{i+k-1}-\Xi_{i+1}} N_{i+1,k-2}(\xi)\right) \\ &\quad - \frac{k-1}{\Xi_{i+k}-\Xi_{i+1}}\left(\frac{k-2}{\Xi_{i+k-1}-\Xi_{i+1}} N_{i+1,k-2}(\xi) - \frac{k-2}{\Xi_{i+k}-\Xi_{i+2}} N_{i+2,k-2}(\xi)\right). \end{aligned} \tag{8.25}$$

The third derivative of a B-spline basis function can also be calculated. Using Eqns.(5.33) and

(8.25), the third derivative $N_{i,k}^{(3)}(\xi)$ reads

$$
\begin{aligned}
N_{i,k}^{(3)}(\xi) &= \frac{k-1}{\Xi_{i+k-1}-\Xi_i} N_{i,k-1}^{(2)}(\xi) - \frac{k-1}{\Xi_{i+k}-\Xi_{i+1}} N_{i+1,k-1}^{(2)}(\xi) \\
&= \frac{k-1}{\Xi_{i+k-1}-\Xi_i} \left[\frac{k-2}{\Xi_{i+k-2}-\Xi_i} \left(\frac{k-3}{\Xi_{i+k-3}-\Xi_i} N_{i,k-3}(\xi) - \frac{k-3}{\Xi_{i+k-2}-\Xi_{i+1}} N_{i+1,k-3}(\xi) \right) \right. \\
&\quad \left. - \frac{k-2}{\Xi_{i+k-1}-\Xi_{i+1}} \left(\frac{k-3}{\Xi_{i+k-2}-\Xi_{i+1}} N_{i+1,k-3}(\xi) - \frac{k-3}{\Xi_{i+k-1}-\Xi_{i+2}} N_{i+2,k-3}(\xi) \right) \right] \\
&\quad - \frac{k-1}{\Xi_{i+k}-\Xi_{i+1}} \left[\frac{k-2}{\Xi_{i+k-1}-\Xi_{i+1}} \left(\frac{k-3}{\Xi_{i+k-2}-\Xi_{i+1}} N_{i+1,k-3}(\xi) - \frac{k-3}{\Xi_{i+k-1}-\Xi_{i+2}} N_{i+2,k-3}(\xi) \right) \right. \\
&\quad \left. - \frac{k-2}{\Xi_{i+k}-\Xi_{i+2}} \left(\frac{k-3}{\Xi_{i+k-1}-\Xi_{i+2}} N_{i+2,k-3}(\xi) - \frac{k-3}{\Xi_{i+k}-\Xi_{i+3}} N_{i+3,k-3}(\xi) \right) \right] . \qquad (8.26)
\end{aligned}
$$

9 List of symbols

9.1 Scalars

Δt_n	Time step size of intervall reaching from t_n until t_{n+1}
c_{ij}	Material parameters of generalized polynomial elasticity
C_{ijkl}	Component of fourth order tensor
ϱ	Density in the current configuration
ϱ_{R}	Density in the reference configuration
$\mathrm{d}V$	Material volume element in the reference configuration
$\mathrm{d}v$	Material volume element in the current configuration
d	Internal dissipation
d^{h}	Discretized internal dissipation
E_{ij}	Components of Green strain tensors given as vector
$E(\mathcal{B},t)$	Internal energy
e	Mass specific internal energy
η	Viscosity of material body
η_0	Initial viscosity
F_{ij}	Components of deformation gradient
G	Shear modulus
g	Step length in line search
γ	Entropy production density
γ_{ij}	Shear angles
$\Gamma(\mathcal{B},t)$	Volume distributed entropy production
$H(\mathcal{B},t)$	Entropy exchange
$\mathrm{I}_{\mathbf{C}}$	First invariant of tensor $\mathbf{C}$
$\mathrm{II}_{\mathbf{C}}$	Second invariant of tensor $\mathbf{C}$
$\mathrm{III}_{\mathbf{C}}$	Third invariant of tensor $\mathbf{C}$
J	Determinant of deformation gradient
J_{M}	Mechanic part of deformation gradient
K	Bulk modulus
k	Order of a curve or surface
$k-1$	Degree a curve or surface
$K(\mathcal{B},t)$	Kinetic energy
$L(\mathcal{B},t)$	Power of external forces
$m(\mathcal{B},t)$	Mass of a material body
μ	Material parameter

ψ	Helmholtz free energy
$S(\mathcal{B}, t)$	Entropy content of a material body
$\mathrm{I}_{\mathbf{E}}, \mathrm{II}_{\mathbf{E}}, \mathrm{III}_{\mathbf{E}}$	Invariants
$\mathrm{IV}_{\mathbf{E}}, \mathrm{V}_{\mathbf{E}}, \mathrm{VI}_{\mathbf{E}}$	Invariants
$\mathrm{VII}_{\mathbf{E}}$	Invariants
Λ, μ_T, μ_L	Material parameter of transversal isotropy model
α, β	Material parameter of transversal isotropy model
$\mathrm{I}_{\mathbf{C}}, \mathrm{II}_{\mathbf{C}}, \mathrm{III}_{\mathbf{C}}$	Invariants of transversal isotropy model
$\mathrm{IV}_{\mathbf{C}}, \mathrm{V}_{\mathbf{C}}, \mathrm{VI}_{\mathbf{C}}$	Invariants of transversal isotropy model
$\mathrm{VII}_{\mathbf{C}}$	Invariants
t	Time
X, Y, Z	Component of coordinates of material point in reference configuration
x, y, z	Component of coordinates of material point in current configuration
α_1, α_2	Material parameter in orthotropy case
$\beta_1, \beta_2, \beta_3$	Material parameter in orthotropy case
μ, μ_1, μ_2	Material parameter in orthotropy case
E_i	Young's modulus
ν_{ij}	Poisson ratios
s^2	Standard deviation
$\boldsymbol{\kappa}_{\mathrm{conf}}$	Confidence interval
c_{ij}	Correlation coefficient
R^2	Coefficient of determination
N	Number of experiments
A_0	Intended surface of sample in the current configuration
n_{c}	Number of control points
$N_{i,k}(\xi)$	B-spline basis function
ξ	Parameter value in B-spline
n_{kv}	number of knot values as it is in ξ-direction
n_{kl}	number of knot values as it is in η-direction
$n_{\mathrm{d}\xi}$	The number of data points in ξ-direction
$n_{\mathrm{d}\eta}$	The number of data points in eta-direction
$n_{\mathrm{c}\xi}$	The number of control points in ξ-direction
$n_{\mathrm{c}\eta}$	The number of control points in eta-direction
$N_{i,k}^{(m)}(\xi)$	m^{th} derivative of B-spline basis function
l	Order of a curve or surface

9.2 Vector Valued Quantities

$\boldsymbol{\chi}$	Arbitrary configuration of material body
$\boldsymbol{\chi}_t$	Current configuration of material body
$\boldsymbol{\chi}_{\mathrm{R}}$	Motion of a material body

$\boldsymbol{\chi}^e$	Mapping from unit element to reference configuration
$\delta\boldsymbol{u}$	Virtual displacement
$\mathrm{d}\boldsymbol{X}$	Material line element in the reference configuration
$\mathrm{d}\boldsymbol{x}$	Material line element in the current configuration
$\mathrm{d}\boldsymbol{A}$	Material surface element in the reference configuration
$\mathrm{d}\boldsymbol{a}$	Material surface element in the current configuration
$\boldsymbol{e}_x$,$\boldsymbol{e}_y$,$\boldsymbol{e}_z$	Base vectors of cartesian coordinates
$\boldsymbol{E}_i$	Parametric curve description for curve i of the reference element
$\boldsymbol{m}(\mathcal{B},t)$	Rotational momentum
$\boldsymbol{n}_\mathrm{R}$	Surface unit normal in the reference configuration
$\boldsymbol{n}$	Surface unit normal in the current configuration
$\boldsymbol{\phi}$	Entropy flux vector
$\boldsymbol{p}(\mathcal{B},t)$	Linear momentum
$\boldsymbol{q}$	Cauchy heat flux vector
$\boldsymbol{p}(\xi)$	Position vector over B-spline curve
$\boldsymbol{q}_\mathrm{R}$	Piola-Kirchhoff heat flux vector
$\boldsymbol{t}$	Cauchy stress vector
$\boldsymbol{t}_\mathrm{R}$	Piola stress vector
$\boldsymbol{u}$	Displacement of material point
$\boldsymbol{v}$	Velocity of material point with respect to the current configuration
$\boldsymbol{x}$	Position of a material point at time t
$\boldsymbol{X}$	Position of a material point in reference configuration
$\boldsymbol{X}_0$	Position of a specific material point in reference configuration
$\boldsymbol{\xi}$	Coordinates of the reference element
$\boldsymbol{e}_1,\boldsymbol{e}_2,\boldsymbol{e}_3$	Fiber orientations in laminates
$\boldsymbol{a},\boldsymbol{b},\boldsymbol{c}$	Fiber orientations in laminates
$\boldsymbol{t}(x)$	The tangent vector
Ξ, H	Knot vector
ξ,η	Parameter vectcor for defining B-spline functions
$\overline{\mathbf{p}}$	Contro points vector
$\boldsymbol{a}^*(\xi,\eta)$	Tangent vector of B-spline surface
$\boldsymbol{p}^{(m)}(\xi)$	m^{th} derivative of B-spline curve
$\boldsymbol{a}(\xi,\eta)$	Unit tangent vector

9.3 Second and Higher Order Tensor Quantities

$\mathbf{B}$	Left Cauchy-Green tensor
$\mathbf{C}$	Right Cauchy-Green tensor
$\bar{\mathbf{C}}$	Volume-preserving part of right Cauchy-Green tensor
$\mathbf{D}$	Symmetric part of spatial velocity gradient
$\mathbf{E}$	Green strain tensor

$\mathbf{F}$	Deformation gradient
$\hat{\mathbf{F}}$	Isochoric part of deformation gradient
$\bar{\mathbf{F}}$	Volume changing part deformation gradient
$\mathbf{H}$	Displacement gradient
$\mathbf{I}$	Second order identity tensor
$\mathcal{I}$	$= [\mathbf{I} \otimes \mathbf{I}]^{T_{23}}$, fourth order identity tensor
$\mathbf{L}$	Spatial velocity gradients
$\mathbf{M}_i$	Structural tensor
$\mathbf{S}$	Weighted Cauchy stress tensor, Kirchhoff stress tensor
$\mathbf{T}$	Cauchy stress tensor
$\mathbf{T}_{\text{eq}}$	Cauchy stress tensor of equilibrium part
$\mathbf{T}_{\text{R}}$	First Piola-Kirchhoff stress tensor
$\tilde{\mathbf{T}}$	Second Piola-Kirchhoff stress tensor
$\tilde{\mathbf{T}}_{\text{eq}}$	Equilibrium part of second Piola-Kirchhoff stress tensor
$\tilde{\mathbf{T}}_{\text{ov}}$	Overstress part of second Piola-Kirchhoff stress tensor
$\mathbf{W}$	Skew symmetric part of spatial velocity gradient

9.4 Matrices and Column Matrices

$\boldsymbol{K}$	parts of the total finite element stiffness matrix
$\overline{\boldsymbol{K}}$	parts of the total finite element stiffness matrix
$\boldsymbol{J}$	Jacobian matrix
$\boldsymbol{P}$	Covariance matrix
$\boldsymbol{s}(\boldsymbol{\kappa})$	Matrix containing simulation data
$\boldsymbol{d}$	Matrix containing experiment data
$\boldsymbol{A}$	$\in \mathbb{R}^{n_{\text{d}} \times n_{\kappa}}$ coefficient matrix for least-square problem
$\boldsymbol{u}$	Matrix containing the coefficients associated with unknown displacement coefficients
$\overline{\boldsymbol{u}}$	Matrix containing the coefficients associated with prescribed displacement coefficients
$\overline{\boldsymbol{p}}$	Matrix of given equivalent nodal forces
$\boldsymbol{h}$	Arbitrary directions in system of linear equations
$\mathbf{R}$	The residual of data points
$\mathbf{D}$	Total number of data nets
$\mathbf{B}$	Total number of control nets
$\mathbf{r}_{rs}(\mathbf{B})$	The residual of each data point

9.5 Mathematical Operators

$\det$	Determinant of a second order tensor
div	Divergence with respect to coordinates of the current configuration
Div	Divergence with respect to coordinates of the reference configuration
grad	$= \frac{\partial()^i}{\partial x^j} \boldsymbol{e}_i \otimes \boldsymbol{e}^j$, gradient of a vector field with respect to coordinates of the current configuration
Grad	$= \frac{\partial()^i}{\partial X^j} \boldsymbol{e}_i \otimes \boldsymbol{e}^j$, gradient of a vector field with respect to coordinates of the current configuration
$\mathbf{A} \cdot \mathbf{B}$	Inner product of two second order tensors
$\mathbf{A} \otimes \mathbf{B}$	Dyadic product of two second order tensors
$\mathrm{tr}\,\mathbf{A}$	Trace of a second order tensor
$\mathbf{A}^{-1}$	Invers of a second order tensor
$\frac{\partial x}{\partial y}$	Partial derivative of x with respect to y
$\frac{\mathrm{d}x}{\mathrm{d}y}$	Total derivative of x with respect to y
adj	Adjugate of a tensor field
$\det$	Determinant of a tensor field
cof	Cofactor of a tensor field

9.6 Short Notations

CAD	Computer Aided Design
FEM	Finite element method
VARI	Vacuum Assisted Resin Infusion
DIC	Digital image correlation
NURBS	Non-Uniform Rational B-spline
PCM	pixcel counting method

9.7 Miscellaneous

$\mathcal{B}$	Material body
$\partial\mathcal{B}$	Surface of a material body
$\varphi(\boldsymbol{x}, t)$	Production density of physical quantity in the current configuration
$\boldsymbol{\Psi}$	Physical quantity in the current configuration
$\boldsymbol{\Phi}$	Flux of physical quantity in the current configuration
$\partial\Omega$	Boundary of a body in the reference configuration
$\partial\omega$	Boundary of a body in the current configuration

Ω_{st}^{h}	Volume of unit element (3-D)
$\mathcal{P}$	Material point or particle
$\boldsymbol{\mathcal{S}}_{ps}^{p_\xi,p_\eta}(\Omega_{st}^{q})$	Tensor-product-space (2-D)
$\boldsymbol{\mathcal{R}}$	Reference configuration of material body
$(\bullet)^*$	Quantity associated with an orthogonal transformation

Bibliography

Abdelal, G. F., Georgiou, G., Cooper, J., Robotham, A., Levers, A., and Lunt, P. (2015). Numerical and experimental investigation of aircraft panel deformations during riveting process. *Journal of Manufacturing Science and Engineering*, 137(1).

Aboudi, J. (2013). *Mechanics of Composite Materials: A Unified Micromechanical Approach*. Studies in Applied Mechanics. Elsevier Science.

Aboudi, J., Arnold, S., and Bednarcyk, B. (2012). *Micromechanics of Composite Materials: A Generalized Multiscale Analysis Approach*. Elsevier Science.

Agarwal, B., Broutman, L., and Chandrashekhara, K. (2006). *Analysis and Performance of Fiber Composites*. Wiley.

Almeida, E. S. and Spilker, R. L. (1998). Finite elements formulations for hyperelastic transversely isotropic biphasic soft tissues. *Computer Methods of Applied Mechanics and Engineering*, 151:513–538.

Altenbach, H. (2000a). An alternative determination of transverse shear stiffnesses for sandwich and laminated plates. *International Journal of Solids and Structures*, 37(25):3503 – 3520.

Altenbach, H. (2000b). On the determination of transverse shear stiffnesses of orthotropic plates. *Zeitschrift für angewandte Mathematik und Physik ZAMP*, 51(4):629–649.

Altenbach, H. (2012). *Kontinuumsmechanik*. Springer.

Altenbach, H. and Altenbach, J. (2004). *Mechanics of composite structural elements*. Springer.

Altenbach, H. and Becker, W. (2003). *Modern trends in composite laminates mechanics*, volume 448. Springer Science & Business Media.

Altenbach, J. and Altenbach, H. (1994). *Einführung in die Kontinuumsmechanik*. Teubner, Stuttgart.

Andresen, K., Dannemeyer, S., Friebe, H., Mahnken, R., Ritter, R., and Stein, E. (1996). Parameteridentifikation für ein plastisches Stoffgesetz mit FE-Methoden und Rasterverfahren. *Bauingenieur*, 71:21–31.

ASTM D1002-05 (1999). Standard test method for apparent shear strength of single-lap-joint adhesively bonded metal specimens by tension loading (metal-to-metal). www.astm.org.

ASTM D4255/D4255M-15a (2002). Standard test method for in-plane shear properties of polymer matrix composite materials by the rail shear method. www.astm.org.

Auger, D., Wang, Q., Trevelyan, J., Huang, S., and Zhao, W. (2018). Investigating the quality inspection process of offshore wind turbine blades using B-spline surfaces. *Measurement*, 115:162 – 172.

Balzani, D., Neff, P., Schröder, J., and Holzapfel, G. A. (2006). A polyconvex framework for soft biological tissues. adjustment to experimental data. *International Journal of Solids and Structures*, 43:6052–6070.

Banichuk, N. (1981). Optimization problems for elastic anisotropic bodies. *Arch. Mech*, 33(3):347–363.

Beck, J. V. and Arnold, K. J. (1977). *Parameter estimation in engineering and science*. John Wiley & Sons, New York.

Benedix, U., Görke, U.-J., Kreißig, R., and Kretzschmar, S. (1998). Local and global analysis of inhomogeneous displacement fields for the identification of material parameters. In Hoa, S. V., De Wilde, W. P., and Blain, W. R., editors, *Computer Methods in Composite Materials VI (CADCOMP 98)*, pages 159–168.

Bentamy, A., Guibault, F., and Trépanier, J. Y. (2005). Cross-sectional design with curvature constraints. *Computer-Aided Design*, 37(14):1499 – 1508.

Bischoff, J., Arruda, E., and Grosh, K. (2002). A microstructurally based orthotropic hyperelastic constitutive law. *J. Appl. Mech.*, 69(5):570–579.

Blom, A. W., Abdalla, M. M., and Gürdal, Z. (2010). Optimization of course locations in fiber-placed panels for general fiber angle distributions. *Composites Science and Technology*, 70(4):564 – 570.

Böhlke, T., Henning, F., Hrymak, A., Kärger, L., Weidenmann, K., and Wood, J. T. (2019). *Continuous–Discontinuous Fiber-Reinforced Polymers: An Integrated Engineering Approach*. Carl Hanser Verlag GmbH Co KG.

Brakhage, K.-H. and Lamby, P. (2008a). Application of B-spline techniques to the modeling of airplane wings and numerical grid generation. *Computer Aided Geometric Design*, 25(9):738 – 750. Classical Techniques for Applied Geometry.

Brakhage, K.-H. and Lamby, P. (2008b). Application of b-spline techniques to the modeling of airplane wings and numerical grid generation. *Computer Aided Geometric Design*, 25(9):738 – 750. Classical Techniques for Applied Geometry.

Brandt, J. (1998). FE-simulation of compaction and solid state sintering of cemented carbides. *Mechanics of Cohesive-frictional Materials*, 3(1):181–205.

Bronzino, J. D. (2006). *Biomedical Engineering Fundamentals*. Taylor & Francis, Boca Raton, Florida.

Catmull, E. and Clark, J. (1978). Recursively generated b-spline surfaces on arbitrary topological meshes. *Computer-aided design*, 10(6):350–355.

Chiou, C.-P., Margetan, F. J., and Rose, J. H. (1991). Ultrasonic detection of cracks below bolts in aircraft skins. In *Review of progress in quantitative nondestructive evaluation*, pages 1891–1898. Springer.

Christensen, R. M. (2005). *Mechanics of composite materials*. Dover Publication, Mineoly, N.Y.

Cohen, E., Lyche, T., and Riesenfeld, R. (1980). Discrete b-splines and subdivision techniques in computer-aided geometric design and computer graphics. *Computer graphics and image processing*, 14(2):87–111.

Cohen, E. and O'dell, C. (1989). A data dependent parametrization for spline approximation. In *Mathematical methods in computer aided geometric design*, pages 155–166. Elsevier.

Colasante, G. (2014). *Tensile structures: biaxial testing and constitutive modelling of coated fabrics at finite strains*. PhD thesis.

Cooreman, S., Lecompte, D., Sol, H., Vantomme, J., and Debruyne, D. (2007). Elasto-plastic material parameter identification by inverse methods: Calculation of the sensitivity matrix. *International Journal of Solids and Structures*, 44:4329–4341.

Criscione, J. C., Douglas, A. S., and Hunter, W. C. (2001). Physically based strain invariant set for materials exhibiting transversely isotropic behavior. *Journal of the Mechanics and Physics of Solids*, 49(4):871–897.

de Boer, R. (1982). *Vektor- und Tensorrechnung für Ingenieure*. Springer, Berlin, 1st edition.

De Boor, C. (1972). On calculating with B-splines. *Journal of Approximation Theory*, 6:50–62.

De Boor, C. (1978). *A practical guide to splines*, volume 27. springer-verlag New York.

DIN EN ISO 527-2 (1996). Plastics - determination of tensile properties - Part 2: Test conditions for molding and extrusion plastics (ISO 527-2: 1993 including Corr 1: 1994). www.beuth.de.

DIN EN ISO 527-5 (2009). Plastics - determination of tensile properties - part 5: Test conditions for unidirectional fibre-reinforced plastic composites. www.beuth.de.

Draper, N. R. and Smith, H. (1998). *Applied regression analysis*. John Wiley & Sons, Inc., New York, 3 edition.

Duong, M. T. and Itskov, U. D.-I. R. M. (2015). *Hyperelastic modeling and soft-tissue growth integrated with the smoothed finite element method-SFEM*. PhD thesis, Universitätsbibliothek der RWTH Aachen.

Duvaut, G., Terrel, G., Léné, F., and Verijenko, V. (2000). Optimization of fiber reinforced composites. *Composite Structures*, 48(1-3):83–89.

Eck, M. and Hadenfeld, J. (1995). Knot removal for b-spline curves. *Computer Aided Geometric Design*, 12(3):259–282.

Eck, M. and Hoppe, H. (1996). Automatic reconstruction of b-spline surfaces of arbitrary topological type. In *Proceedings of the 23rd annual conference on Computer graphics and interactive techniques*, pages 325–334.

Fiolka, M. (2008). *Theorie und Numerik volumetrischer Schalenelemente zur Delaminationsanalyse von Faserverbundlaminaten*. Report no. 2/2008, Institute of Mechanics, University of Kassel.

Foley, T. A. and Nielson, G. M. (1989). Knot selection for parametric spline interpolation. In *Mathematical methods in computer aided geometric design*, pages 261–CP4. Elsevier.

Frederiksen, P. S. (1997a). Application of an improved model for the identification of material parameters. *Mechanics Of Composite Materials And Structures An International Journal*, 4(4):297–316.

Frederiksen, P. S. (1997b). Experimental procedure and results for the identification of elastic constants of thick orthotropic plates. *Journal of Composite Materials*, 31(4):360–382.

Gibson, R. (2011). *Principles of Composite Material Mechanics, Third Edition*. Mechanical Engineering. CRC Press.

GiD-Manual (2012). *GiD: Reference Manual*. GiD.

GOM (2011). *Aramis – User Manual: The basics of strain*. GOM – Gesellschaft für optische Messtechnik, Braunschweig, Germany.

Gopi, M. and Manohar, S. (1997). A unified architecture for the computation of b-spline curves and surfaces. *IEEE Transactions on Parallel and Distributed Systems*, 8(12):1275–1287.

Gordon, W. J. and Riesenfeld, R. F. (1974). B-spline curves and surfaces. In *Computer aided geometric design*, pages 95–126. Elsevier.

Goren, A. and Atas, C. (2008). Manufacturing of polymer matrix composites using vacuum assisted resin infusion molding. *Archives of materials Science and Engineering*, 34(2):117–120.

Gregorski, B. F., Hamann, B., and Joy, K. I. (2000). Reconstruction of b-spline surfaces from scattered data points. In *Proceedings computer graphics international 2000*, pages 163–170. IEEE.

Grossman, M. (1971). Parametric curve fitting. *The Computer Journal*, 14(2):169–172.

Guo, M. and Li, C. (2020). Curve reconstruction algorithm based on discrete data points and normal vectors. *Journal of Mathematical Research with Applications*, 40(1):87–100.

Haron, H., Rehman, A., Adi, D., Lim, S., and Saba, T. (2012a). Parameterization method on b-spline curve. *Mathematical Problems in Engineering*, 2012.

Haron, H., Rehman, A., Adi, D. I. S., Lim, S. P., and Saba, T. (2012b). Parameterization method on B-spline curve. *Mathematical Problems in Engineering*, 2012.

Hartmann, S. (2001a). Numerical studies on the identification of the material parameters of Rivlin's hyperelasticity using tension-torsion tests. *Acta Mechanica*, 148:129–155.

Hartmann, S. (2001b). Parameter estimation of hyperelasticity relations of generalized polynomial-type with constraint conditions. *International Journal of Solids and Structures*, 38(44-45):7999–8018.

Hartmann, S. (2003). *Finite-Elemente Berechnung inelastischer Kontinua. Interpretation als Algebro-Differentialgleichungssysteme*. Habilitation, University of Kassel, Institute of Mechanics. Report No. 1/2003.

Hartmann, S. (2017). A remark on material parameter identification using finite elements based on constitutive models of evolutionary-type. *Computer Assisted Methods in Engineering and Science*, 24:113 – 126.

Hartmann, S. and Gilbert, R. R. (2018). Identifiability of material parameters in solid mechanics. *Archive of Applied Mechanics*, 88(1):3–26.

Hartmann, S., Gilbert, R. R., and Sguazzo, C. (2018). Basic studies in biaxial tensile tests. *GAMM-Mitteilungen*, 41:e201800004.

Hartmann, S. and Kheiri Marghzar, A. (2018). Modeling of fiber circumplacement around a hole using a streamline approach. *Universal Journal of Mathematics and Applications*, 1:17 – 28.

Hartmann, S., Kheiri Marghzar, A., Rogin Gilbert, R., Pangboonyanon, W., and Meiners, D. (2020). Experiment, modeling and simulation of bypassing holes in composites. *Composite Structures*, 234:111666.

Hartmann, S. and Rodriguez, S. (2018). Verification examples for strain and strain-rate determination of digital image correlation systems. In Altenbach, H., Jablonski, F., Müller, W., Naumenko, K., and Schneider, P., editors, *Advances in Mechanics of Materials and Structural Analysis. Advanced Structured Materials*, number 80 in Advanced Structured Materials, pages 135 – 174. Springer International Publishing, Cham.

Hartmann, S. and Sguazzo, C. (2015). Strain analysis in sandwich structures using digital image correlation. In für Materialtechnik, C. Z., editor, *Berichtsband Clausthaler Zentrum für Materialtechnik. Zeitraum 2013-2015*, volume 1 of *Fortschrittsberichte der Materialforschung und Werkstofftechnik / Bulletin of Materials Research and Engineering*, pages 61–71, Aachen. Clausthaler Zentrum für Materialtechnik, Shaker Verlag.

Hartmann, S., Tschöpe, T., Schreiber, L., and Haupt, P. (2003). Large deformations of a carbon black-filled rubber. Experiment, optical measurement and parameter identification using finite elements. *European Journal of Mechanics, Series A/Solids*, 22:309–324.

Haupt, P. (2000). *Continuum Mechanics and Theory of Materials*. Springer-Verlag Berlin Heidelberg.

Holbery, J. and Houston, D. (2006). Natural-fiber-reinforced polymer composites in automotive applications. *JOM: the Journal of the Minerals, Metals and Materials Society*, 58:80–86.

Holzapfel, G. (2008). *Nonlinear Solid Mechanics: A Continuum Approach for Engineering*. John Wiley & Sons, 5th edition.

Holzapfel, G. and Ogden, R. (2010). Constitutive modelling of arterials. *Proceedings of the Royal Society of London A*, 466:1551–1597.

Holzapfel, G. A., Gasser, T. C., and Ogden, R. W. (2000). A new constitutive framework for arterial wall mechanics and a comparative study of material models. *Journal of Elasticity*, 61:1–48.

Hu, S.-M., Li, Y.-F., Ju, T., and Zhu, X. (2001). Modifying the shape of nurbs surfaces with geometric constraints. *Computer-Aided Design*, 33(12):903–912.

Hu, Z. and Bo, P. (2020). Developable b-spline surface generation from control rulings. *arXiv preprint arXiv:2004.09038*.

Huang, J. and Haftka, R. (2005). Optimization of fiber orientations near a hole for increased load-carrying capacity of composite laminates. *Structural and Multidisciplinary Optimization*, 30(5):335–341.

Huang, L., Sun, X., Liu, Y., and Cen, Z. (2004). Parameter identification for two-dimensional orthotropic material bodies by the boundary element method. *Engineering Analysis with Boundary Elements*, 28(2):109–121.

Huber, N. and Tsakmakis, C. (1999a). Determination of constitutive properties from spherical indentation data using neural networks, Part I: plasticity with nonlinear and kinematic hardening. *Journal of the Mechanics and Physics of Solids*, 47:1589–1607.

Huber, N. and Tsakmakis, C. (1999b). Determination of constitutive properties from spherical indentation data using neural networks, Part II: the case of pure kinematic hardening in plasticity laws. *Journal of the Mechanics and Physics of Solids*, 47:1569–1588.

Hufenbach, W., Böhm, R., Thieme, M., Winkler, A., Mäder, E., Rausch, J., and Schade, M. (2011). Polypropylene/glass fibre 3d-textile reinforced composites for automotive applications. *Materials & Design*, 32(3):1468–1476.

Hyer, M. and Lee, H. (1991). The use of curvilinear fiber format to improve buckling resistance of composite plates with central circular holes. *Composite Structures*, 18(3):239 – 261.

Hyer, M. W. and Charette, R. F. (1991). Use of curvilinear fiber format in composite structure design. *AIAA Journal*, 125:1011 – 1015.

Itskov, M. (2001). A generalized orthotropic hyperelastic material model with application to incompressible shells. *International Journal for Numerical Methods in Engineering*, 50(8):1777–1799.

Itskov, M. (2007). *Tensor algebra and tensor analysis for engineers*. Springer, Berlin.

Itskov, M. and Aksel, N. (2004). A class of orthotropic and transversely isotropic hyperelastic constitutive models based on a polyconvex strain energy function. *International Journal of Solids and Structures*, 41:3833–3848.

Jones, R. M. (1998). *Mechanics of composite materials*. CRC press.

Jung, H. and Kim, K. (2000a). A new parameterisation method for NURBS surface interpolation. *The International Journal of Advanced Manufacturing Technology*, 16(11):784–790.

Jung, H. and Kim, K. (2000b). A new parameterisation method for nurbs surface interpolation. *The International Journal of Advanced Manufacturing Technology*, 16(11):784–790.

Kaliske, M. (1999). *Zur Theorie und Numerik von Strukturen aus Faserverbundmaterial*. Mitteilung nr. 49-99, Universität Hannover.

Kim, K.-Y., Sim, J., Jannat, N.-E., Ahmed, F., and Ameri, S. (2019). Challenges in riveting quality prediction: a literature survey. *Procedia Manufacturing*, 38:1143–1150.

Koricho, E. G., Khomenko, A., Fristedt, T., and Haq, M. (2015). Innovative tailored fiber placement technique for enhanced damage resistance in notched composite laminate. *Composite Structures*, 120:378 – 385.

Krämer, S. (2016). *Einfluss von Unsicherheiten in Materialparametern auf Finite-Elemente Simulationen*. Phd-thesis, report no. 5/2016, Institute of Applied Mechanics, Clausthal University of Technology, Clausthal-Zellerfeld.

Krawietz, A. (2013). *Materialtheorie: mathematische Beschreibung des phänomenologischen thermomechanischen Verhaltens*. Springer-Verlag.

Kreissig, R., Benedix, U., and Goerke, U.-J. (2001). Statistical aspects of the identification of material parameters for elasto-plastic models. *AAM*, 71:123–134.

Lawson, C. L. and Hanson, R. J. (1995). *Solving least squares problems*. Siam Society for Industrial and Applied Mathematics, Philadelphia.

Lecompte, D., Sol, H., Vantomme, J., and Habraken, A. (2005). Identification of elastic orthotropic material parameters based on espi measurements. In *Proc., SEM Annual Conf. and Exposition on Experimental and Applied Mechanics*.

Lee, E. T. (1989). Choosing nodes in parametric curve interpolation. *Computer-Aided Design*, 21(6):363–370.

Lehmann, K. S. (2001). Addendum:bspline inteerpolation in medical image processing. *IEEE Transactions on Medical Imaging*, 20.

Leite, A. M. (2016). Modelling and analysis of composite joint reinforced by composite fastener.

Li, G., Shi, G., and Bellinger, N. C. (2012). Assessing the riveting process and the quality of riveted joints in aerospace and other applications. In *Welding and joining of aerospace materials*, pages 181–214. Elsevier.

Li, W., Krehl, J., Gillespie Jr, J., Heider, D., Endrulat, M., Hochrein, K., Dunham, M., and Dubois, C. (2004). Process and performance evaluation of the vacuum-assisted process. *Journal of composite materials*, 38(20):1803–1814.

Li, W., Xu, S., Zhao, G., and Goh, L. P. (2005). Adaptive knot placement in B-spline curve approximation. *Computer-Aided Design*, 37(8):791 – 797. CAD '04 Special Issue: Modelling and Geometry Representations for CAD.

Lin, H., Wang, G., and Dong, C. (2004). Constructing iterative non-uniform b-spline curve and surface to fit data points. *Science in China Series: Information Sciences*, 47(3):315–331.

Loop, C. (1994). Smooth spline surfaces over irregular meshes. In *Proceedings of the 21st annual conference on Computer graphics and interactive techniques*, pages 303–310.

Loop, C. and DeRose, T. D. (1990). Generalized b-spline surfaces of arbitrary topology. In *Proceedings of the 17th annual conference on Computer graphics and interactive techniques*, pages 347–356.

Lozano, G. G., Tiwari, A., Turner, C., and Astwood, S. (2016). A review on design for manufacture of variable stiffness composite laminates. *Proceedings of the Institution of Mechanical Engineers, Part B: Journal of Engineering Manufacture*, 230(6):981–992.

Lüth, H. and Ibach, H. (2003). *Solid-state physics: an introduction to principles of materials science*. Springer-Verlag Berlin Heidelberg.

Lyche, T. and Mørken, K. (1987). Knot removal for parametric b-spline curves and surfaces. *Computer Aided Geometric Design*, 4(3):217–230.

Ma, W. and Kruth, J.-P. (1998). Nurbs curve and surface fitting for reverse engineering. *The International Journal of Advanced Manufacturing Technology*, 14(12):918–927.

Mahnken, R. (1998). *Theoretische und numerische Aspekte zur Parameteridentifikation und Modellierung bei metallischen Werkstoffen*. Bericht nr. f 98/2, Universität Hannover.

Mahnken, R. and Stein, E. (1996). A unified approach for parameter identification of inelastic material models in the frame of the finite element method. *Computer Methods in Applied Mechanics and Engineering*, 136:225–258.

Mäkelä, P. and Östlund, S. (2003). Orthotropic elastic–plastic material model for paper materials. *International Journal of Solids and Structures*, 40(21):5599–5620.

Malakhov, A. and Polilov, A. (2016). Design of composite structures reinforced curvilinear fibres using fem. *Composites Part A: Applied Science and Manufacturing*, 87:23 – 28.

Malakhov, A. V. and Polilov, A. N. (2013). Construction of trajectories of the fibers which bypass a hole and their comparison with the structure of wood in the vicinity of a knot. *Journal of Machinery Manufacture and Reliability*, 42(4):306–311.

Malvern, L. E. (1969). *Introduction to the Mechanics of a Continuous Medium*. Prentice-Hall, Englewood Cliffs.

Montemurro, M. and Catapano, A. (2019). A general b-spline surfaces theoretical framework for optimisation of variable angle-tow laminates. *Composite Structures*, 209:561–578.

Moroni, F. and Pirondi, A. (2010). Technology of rivet: adhesive joints. In *Hybrid adhesive joints*, pages 79–108. Springer.

Motevalli, M., Uhlemann, J., Stranghoener, N., and Balzani, D. (2019). A new nonlinear polyconvex orthotropic material model for the robust simulation of technical fabrics in civil engineering applications at large strains-validation with large-scale experiment. *BAUINGENIEUR*, 94(12):488–497.

Nagendra, S., Kodiyalam, S., and Davis, J. (1995). Optimization of tow fiber paths for composite design. *Proceedings of the 36th AIAA/ASME/ASCE/AHS/ASC conference on structures, structural dynamics, and materials and AIAA/ASME forum on adaptive structures, New Orleans, LA*.

Niu, X. J., Yang, T., Du, Y., and Xue, Z. Q. (2016). Tensile properties of variable stiffness composite laminates with circular holes based on potential flow functions. *Archive of Applied Mechanics*, 86(9):1551–1563.

Ogden, R. W. (1984). *Non-Linear Elastic Deformations*. Ellis Horwood, Chichester.

Park, H. and Kim, K. (1996). Smooth surface approximation to serial cross-sections. *Computer-Aided Design*, 28(12):995 – 1005.

Park, H. and Lee, J.-H. (2007). B-spline curve fitting based on adaptive curve refinement using dominant points. *Computer-Aided Design*, 39(6):439–451.

Parton, V. and Kudryavtsev, B. (1993). *Engineering Mechanics of Composite Structures*. CRC Press, Inc.

Pedersen, P. (1991). On thickness and orientational design with orthotropic materials. *Structural Optimization*, 3(2):69–78.

Peeters, D. M. J., Hesse, S., and Abdalla, M. M. (2015). Stacking sequence optimisation of variable stiffness laminates with manufacturing constraints. *Composite Structures*, 125:596 – 604.

Piegl, L. and Tiller, W. (1987). Curve and surface constructions using rational B-splines. *Computer-Aided Design*, 19(9):485 – 498.

Piegl, L. and Tiller, W. (1997). *The NURBS Book*. Springer Verlag, 2nd edition.

Piegl, L. A. and Tiller, W. (2000a). Least-squares B-spline curve approximation with arbitrary end derivatives. *Engineering Computation*, 16(2):109–116.

Piegl, L. A. and Tiller, W. (2000b). Surface approximation to scanned data. *The visual computer*, 16(7):386–395.

Piegl, L. A. and Tiller, W. (2002). Surface skinning revisited. *The Visual Computer*, 18(4):273–283.

Poodts, E., Minak, G., Dolcini, E., and Donati, L. (2013). Fe analysis and production experience of a sandwich structure component manufactured by means of vacuum assisted resin infusion process. *Composites Part B: Engineering*, 53:179–186.

Powell, M. J. D. (1998). Direct search algorithms for optimization calculations. *Acta Numerica*, 7:287–336. (see internet address: http://plato.la.asu.edu/topics/problems/nlores.html).

Prot, V., Skallerud, B., and Holzapfel, G. (2007). Transversely isotropic membrane shells with application to mitral valve mechanics. constitutive modelling and finite element implementation. *International journal for numerical methods in engineering*, 71(8):987–1008.

Qian, X. (2010). Full analytical sensitivities in nurbs based isogeometric shape optimization. *Computer Methods in Applied Mechanics and Engineering*, 199(29-32):2059–2071.

Reddy, J. (2003). *Mechanics of Laminated Composite Plates and Shells: Theory and Analysis, Second Edition*. CRC Press.

Reese, S., Raible, T., and Wriggers, P. (2001). Finite element modelling of orthotropic material behaviour in pneumatic membranes. *International journal of solids and structures*, 38(52):9525–9544.

Ribeiro, P., Akhavan, H., Teter, A., and Warmiński, J. (2014). A review on the mechanical behaviour of curvilinear fibre composite laminated panels. *Journal of Composite Materials*, 48(22):2761–2777.

Riesenfeld, R. F. (1973). *Applications of B-spline approximation to geometric problems of computer-aided design*. PhD thesis, Syracuse University New York.

Rogers, D. and Fog, N. (1989a). Constrained B-spline curve and surface fitting. *Computer-Aided Design*, 21(10):641 – 648.

Rogers, D. F. (1977). B-spline curves and surfaces for ship hull definition.

Rogers, D. F. (2001). *An Introduction to NURBS: With Historical Perspective*. Morgan Kaufmann Publishers Inc., San Francisco, CA, USA.

Rogers, D. F. and Fog, N. (1989b). Constrained b-spline curve and surface fitting. *Computer-Aided Design*, 21(10):641–648.

Roth, S., Pracisnore, F., Coutandin, S., and Fleischer, J. (2020). A new approach for modelling the fibre path in bolted joints of continuous fibre reinforced composites. *Composite Structures*, page 112184.

Rowlands, R. E., Daniel, I. M., and Whiteside, J. B. (1973). Stress and failure analysis of a glass-epoxy composite plate with a circular hole. *Experimental Mechanics*, 13(1):31–37.

Rüter, M. and Stein, E. (2000). Analysis, finite element computation and error estimation in transversely isotropic nearly incompressible finite elasticity. *Computer methods in applied mechanics and engineering*, 190(5-7):519–541.

Sansour, C. (2008). On the physical assumptions underlying the volumetric-isochoric split and the case of anisotropy. *European Journal of Mechanics - A/Solids*, 27:28–39.

Sapidis, N. and Farin, G. (1990a). Automatic fairing algorithm for b-spline curves. *Computer-Aided Design*, 22(2):121 – 129.

Sapidis, N. and Farin, G. (1990b). Automatic fairing algorithm for b-spline curves. *Computer-aided design*, 22(2):121–129.

Schmid, H., Nash, M., Young, A., and Hunter, P. (2006). Myocardial material parameter estimation—a comparative study for simple shear.

Schoenberg, I. J. (1959). On variation diminishing approximation methods. *Numerical Approximation*, pages 249–274.

Schröder, J. (1996). *Theoretische und algorithmische Konzepte zur phänomenologischen Beschreibung anisotropen Materialverhaltens*. PhD thesis.

Schröder, J. and Neff, P. (2003). Invariant formulation of hyperelastic transverse isotropy based on polyconvex free energy functions. *International journal of solids and structures*, 40(2):401–445.

Schröder, J. and Neff, P. (2003). Invariant formulation of hyperelasticity transverse isotropy based on polyconvex free energy functions. *International Journal of Solids and Structures*, 40:401–445.

Schröder, J., Neff, P., and Balzani, D. (2005). A variational approach for materially stable anisotropic hyperelasticity. *International Journal of Solids and Structures*, 42:4352–4371.

Sepahia, O., Radtke, L., Debus, S., and Düster, A. (2018). Anisotropic hierarchic solid finite elements for the simulation of passive-active arterial wall models. *Computers & Mathematics with Applications*.

Sguazzo, C. and Hartmann, S. (2018). Tensile and shear experiments using polypropylene/polyethylene foils at different temperatures. *Technische Mechanik. Scientific Journal for Fundamentals and Applications of Engineering Mechanics*, 38(2):166–190.

Shewchuk, J. R. (2002). Delaunay refinement algorithms for triangular mesh generation. *Computational Geometry: Theory and Applications*, 22(1-3):21–74.

Skordos, A., Chan, P. H., Vincent, J. F. V., and Jeronimidis, G. (2002). A novel strain sensor based on the campaniform sensillum of insects. *Philosophical Transactions of the Royal Society of London A: Mathematical, Physical and Engineering Sciences*, 360(1791):239–253.

Spencer, A. J. M. (1971). Theory of invariants. In Eringen, C., editor, *Continuum Physics*, pages 239–353. Academic Press New York.

Spencer, A. J. M. (1984). Constitutive theory for strongly anisotropic solids. In Spencer, A. J. M., editor, *Continuum theory of the mechanics of fibre-reinforced composites*, number 282 in Courses and lectures - International Centre for Mechanical Sciences, pages 1–32. Springer-Verlag, Wien.

Tarantola, A. (2005). *Inverse problem theory and methods for model parameter estimation*. SIAM.

Taylor, J. R. (1997). *An introduction to Error Analysis*. University Science Books, California.

Toubal, L., Karama, M., and Lorrain, B. (2005). Stress concentration in a circular hole in composite plate. *Composite Structures*, 68(1):31 – 36.

Truesdell, C. and Noll, W. (1965). *The Non-Linear Field Theories of Mechanics*. Handbuch der Physik III/3. Springer, Berlin.

Van Oosterom, S., Allen, T., Battley, M., and Bickerton, S. (2019). An objective comparison of common vacuum assisted resin infusion processes. *Composites Part A: Applied Science and Manufacturing*, 125:105528.

Vannucci, P. (2018). *Anisotropic elasticity*, volume 85 of *Lecture Notes in Applied an Computational Mechanics*. Springer Nature, Singapore, 1 edition.

Vogler, M., Kolling, S., and Rolfes, R. (2007). Transversely isotropic plasticity with application to fiber-reinforced plastics. *LS-DYNA Anwenderforum Frankenthal*, pages 55–74.

Wall, W. A., Frenzel, M. A., and Cyron, C. (2008). Isogeometric structural shape optimization. *Computer Methods in Applied Mechanics and Engineering*, 197(33):2976 – 2988.

Weise, M. and Meyer, A. (2003). Grundgleichungen für transversal isotropes Materialverhalten. Preprint CSC/10-03, TU Chemnitz, Fakultät für Mathematik, Chemnitz (Germany).

Weiss, J. A., Maker, B. N., and Govindjee, S. (1996a). Finite element implementation of incompressible, transversely isotropic hyperelasticity. *Computer Methods in Applied Mechanics and Engineering*, 135:107–128.

Weiss, J. A., Maker, B. N., and Govindjee, S. (1996b). Finite element implementation of incompressible, transversely isotropic hyperelasticity. *Computer Methods in Applied Mechanics and Engineering*, 135(1):107 – 128.

White, F. (2009). *Fluid Mechanics*. McGraw-Hill.

Wincheski, B. and Namkung, M. (2004). Electromagnetic detection of fatigue cracks under protruding head ferromagnetic fasteners.

Wriggers, P., Schröder, J., and Auricchio, F. (2016). Finite element formulations for large strain anisotropic material with inextensible fibers. *Advanced Modeling and Simulation in Engineering Sciences*, 3:1–18.

Yang, G., Dib, G., Udpa, L., Tamburrino, A., and Udpa, S. S. (2014). Rotating field ec-gmr sensor for crack detection at fastener site in layered structures. *IEEE Sensors Journal*, 15(1):463–470.

Yang, H., Wang, W., and Sun, J. (2004). Control point adjustment for b-spline curve approximation. *Computer-Aided Design*, 36(7):639–652.

Yau, S.-S. and Chou, T.-W. (1988). Strength of woven-fabric composites with drilled and molded holes. In *Composite Materials: Testing and Design (Eighth Conference)*. ASTM International.

Zdunek, A., Rachowicz, W., and Eriksson, T. (2014). A novel computational formulation for nearly incompressible and nearly inextensible finite hyperelasticity. *Computer Methods in Applied Mechanics and Engineering*, 281:220–249.

Zhang, K., Gu, Y., Zhang, Z., et al. (2014). Effect of rapid curing process on the properties of carbon fiber/epoxy composite fabricated using vacuum assisted resin infusion molding. *Materials & Design (1980-2015)*, 54:624–631.

Zhang, Y., Cao, J., Chen, Z., Li, X., and Zeng, X.-M. (2016). B-spline surface fitting with knot position optimization. *Computers & Graphics*, 58:73–83.

Zhu, Y., Liu, J., Liu, D., Xu, H., Yan, C., Huang, B., and Hui, D. (2017). Fiber path optimization based on a family of curves in composite laminate with a center hole. *Composites Part B: Engineering*, 111:91 – 102.

List of Publications

1. Hartmann, S. and Kheiri Marghzar, A. (2018). Modeling of fiber circumplacement around a hole using a streamline approach. *Universal Journal of Mathematics and Applications*, 1:17 – 28.

2. Hartmann, S., Kheiri Marghzar, A., Rogin Gilbert, R., Pangboonyanon, W., and Meiners, D. (2020). Experiment, modeling and simulation of bypassing holes in composites. *Composite Structures*, 234:111666.

3. Hartmann, S., Rogin Gilbert, R., Kheiri Marghzar, A., Leistner, C., and Kumar Dileep, P., (2020). Material Parameter Identification of Unidirectional Fiber-Reinforced Composites. *Archive of Applied Mechanics*, (submitted).